ROTORDYNAMIC FORCES GENERATED BY DISCHARGE-TO-SUCTION LEAKAGE FLOWS IN CENTRIFUGAL PUMPS

Thesis by

Adiel Guinzburg

In Partial Fulfillment of the Requirements

for the Degree of

Doctor of Philosophy

California Institute of Technology

Pasadena, California

1992

(Submitted December 10, 1991)

ACKNOWLEDGEMENTS

I must first thank my advisor, Professor Christopher Brennen, for his support and guidance. I am indebted to him for his constructive criticism. I would also like to thank my co-advisors, Professors Allan Acosta and Thomas Caughey for their technical assistance and continued interest in this research. I am thankful to have been at Caltech, which provided me with the opportunity to discuss my project with other faculty members. A partial list includes Professors Anatol Roshko, Steve Wiggins, and Edward Zukoski. A special thanks needs to go to Professor Hans Liepmann who helped guide me to my project and provided me with much counsel during the course of my stay at Caltech.

Several other people were involved in the process. I wish to thank M. Gerfen from Central Engineering Services for help with the installation of the apparatus. Thanks also go to M. Gould from the Mechanical Engineering Shop for his help with design of some of the mechanical components.

The assistance provided by F. Zhuang, A. Bhattacharyya, F. Rahman and Sandor Nagy with the experimental program is greatly appreciated. The help of C. Lin with the graphics and Dana Young and Jackie Beard with the administrative tasks is also appreciated.

Interaction with fellow students is essential during a graduate program. In particular, I would like to thank my friend Regina Dugan. She taught me so much and not just in areas confined to engineering. I also want to thank Julia Hodge for biking with me and all those enjoyable discussions, which we had at the top of the San Gabriel mountains overlooking the smog.

I would also like to thank NASA George Marshall Space Flight Center for support under Grant NAG8-118.

ABSTRACT

In recent years, increasing attention has been given to fluid-structure interaction problems in turbomachines. The present research focuses on just one such fluid-structure interaction problem, namely the role played by fluid forces in determining the rotordynamic stability and characteristics of a centrifugal pump. While the geometry of the impeller shroud/pump casing annulus varies considerably, previous studies indicate that the contributions from the leakage flow can be of the same order as the contributions from the nonuniform pressure acting on the impeller discharge. Thus, the emphasis of this study is to investigate the contributions to the rotordynamic forces from the discharge-to-suction leakage flows between the front shroud of the rotating impeller and the stationary pump casing. An experiment was designed to measure the rotordynamic shroud forces due to simulated leakage flows for different parameters such as flow rate, shroud clearance, face-seal clearance and eccentricity. The data demonstrates substantial rotordynamic effects and a destabilizing tangential force for small positive whirl ratios; this force decreased with increasing flow rate. The rotordynamic forces appear to be inversely proportional to the clearance and change significantly with the flow rate. Two sets of data taken at different eccentricities yielded quite similar nondimensional rotordynamic forces indicating that the experiments lie within the linear regime of eccentricity.

Like earlier measurements of the total fluid induced rotordynamic forces on impellers [Chamieh et al. (1985), Jery et al. (1985), Adkins et al. (1988)], the forces measured in these experiments scaled with the square of the rotor speed. The functional dependence on the ratio of whirl frequency to rotating frequency (termed the whirl ratio) is very similar to that measured in experiments and similar to that predicted by the theoretical work of Childs. Childs' bulk flow model yielded some unusual results including peaks in the rotordynamic forces at particular positive whirl ratios, a phenomenon which Childs tentatively described as a "resonance" of the leakage flow. This unexpected phenomenon developed at small positive whirl ratios when the inlet swirl velocity ratio exceeded about 0.5. Childs points out that a typical

swirl velocity ratio at inlet (pump discharge) would be about 0.5 and may not therefore be large enough for the resonance to be manifest. To explore whether this effect occurs, an inlet guide vane was constructed which introduced a known amount of swirl into the flow upstream of the leakage flow inlet. A detailed comparison of model predictions with the present experimental program is presented. The experimental results showed no evidence of the "resonances", even at much larger swirl inlet velocities than explored by Childs.

TABLE OF CONTENTS

NOMENCLATURE

[A]	rotordynamic matrix, normalized by $\rho\pi\omega^2R_2^3L$
B	depth of inlet guide vane
b	width of impeller discharge
C,c	rotordynamic damping coefficients, normalized by $\rho\pi\omega R_2^2L$
C_{de}	exit-seal pressure loss coefficient
F(t)	hydrodynamic forces, normalized by $\rho\pi\omega^2R_2^3L\varepsilon/R_2$
$F_x(t),F_y(t)$	lateral forces on the rotating shroud in the stationary laboratory frame, normalized by $\rho\pi\omega^2R_2^3L\varepsilon/R_2$
F_{ox},F_{oy}	steady hydrodynamic forces, normalized by $\rho\pi\omega^2R_2^3L$
$F_n(t),F_t(t)$	unsteady hydrodynamic forces, normalized by $\rho\pi\omega^2R_2^3L\varepsilon/R_2$
$F_1(t),F_2(t)$	lateral forces in the rotating dynamometer frame, normalized by $\rho\pi\omega^2R_2^3L\varepsilon/R_2$
H	shroud clearance between rotor and casing
h	nondimensionalized shroud clearance between rotor and casing
H_s	seal clearance
i	$\sqrt{-1}$
j	$\sqrt{-1}$
K,k	rotordynamic stiffness coefficients, normalized by $\rho\pi\omega^2R_2^2L$

L	axial length of the shroud
L_s	meridional length of the shroud
M,m	rotordynamic inertial coefficients, normalized by $\rho\pi R_2^2 L$
P	pressure in the leakage path
p	nondimensionalized pressure in the leakage path
Pe	exit pressure for the leakage flow
Ps	supply pressure for the leakage flow
$P(L)$	pressure at the annulus of the leakage exit
Q	volume flow rate
r,θ	polar coordinate system
R	shroud radius
r	nondimensionalized shroud radius
Re_ω	Reynolds number based on tip speed, $\omega R_2^2/\nu$
Re_ϕ	Reynolds number based on meridional velocity, $\frac{2 H U_s}{\nu}$
s	meridional coordinate defined along the leakage path
t	time
$U_s(L)$	bulk leakage velocity at the annulus of the leakage exit
u_s	bulk leakage velocity, normalized by inlet tip speed ωR_2.

U_θ	bulk flow tangential velocity
u_θ	bulk flow tangential velocity, normalized by inlet tip speed ωR_2.
$x(t)$	instantaneous displacement in the x direction, normalized by R_2.
$y(t)$	instantaneous displacement in the y direction, normalized by R_2.
z	axial coordinate
t	time
α	swirl turning angle
Γ	mean inlet swirl or ratio of inlet fluid tangential velocity to rotor velocity.
δ	offset or distance between the center of the whirl orbit and the center of the stationary casing.
ε	eccentricity or radius of the whirl motion.
$\lambda s, \lambda r$	friction factors which account for the shear stresses
ν	dynamic viscosity of the fluid
ξ	inlet loss coefficient, typically 0.1
ρ	density of the fluid
ϕ	flow coefficient, $Q/2\pi R_2^2 H\omega$
ω	rotor frequency
Ω	whirl frequency

Subscripts

0	steady or time averaged component
1	leakage flow discharge (pump inlet)
2	leakage flow inlet (pump outlet)
n	normal to the whirl orbit
t	tangential to the whirl orbit
x	along the x axis
y	along the y axis

Superscripts

*	dimensional quantity
0	denotes zeroth order perturbation variable
1	denotes first order perturbation variable

LIST OF FIGURES

Figure 3.15 Dimensionless steady forces as a function of the flow coefficient at 1000 RPM, an eccentricity ε = 0.118 cm, a clearance H = 0.140 cm, offset δ = O and a seal clearance of 0.051 cm.

Figure 3.16 Pressure distribution along the shroud for different whirl positions at 1000 RPM, a flow of 10 GPM, an eccentricity ε = 0.0254 cm, a clearance H = 0.140 cm, offset δ = O and a seal clearance of 0.051 cm. The measurements are from each set of pressure taps along the meridional direction and are 120° apart.

Figure 3.17 Pressure distribution along the shroud for different whirl positions at 1000 RPM, a flow of 20 GPM, an eccentricity ε = 0.0254 cm, a clearance H = 0.140 cm, offset δ = O and a seal clearance of 0.051 cm. The measurements are from each set of pressure taps along the meridional direction and are 120° apart.

Figure 3.18 Pressure distribution along the shroud for different whirl positions at 1000 RPM, a flow of 30 GPM, an eccentricity ε = 0.0254 cm, a clearance H = 0.140 cm, offset δ = O and a seal clearance of 0.051 cm. The measurements are from each set of pressure taps along the meridional direction and are 120° apart.

Figure 4.1 Dimensionless normal and tangential forces at 1000 RPM, an eccentricity ε = 0.0254 cm, a clearance H = 0.140 cm, offset δ = O and various flow rates as follows: O ℓ/sec, 0.631 ℓ/sec, 1.262 ℓ/sec, 1.892 ℓ/sec.

Figure 4.2 Dimensionless normal and tangential forces at 500 RPM, an eccentricity ε = 0.0254 cm, a clearance H = 0.140 cm, offset δ = O and various flow rates as follows: O ℓ/sec, 0.631 ℓ/sec, 1.262 ℓ/sec, 1.892 ℓ/sec.

Figure 4.3 Dimensionless normal and tangential forces at 2000 RPM, an eccentricity ε = 0.0254 cm, a clearance H = 0.140 cm, offset δ = O and various flow rates as follows: O ℓ/sec, 0.631 ℓ/sec, 1.262 ℓ/sec.

Figure 4.4 Dimensionless normal and tangential forces at 1000 RPM, an eccentricity ε = 0.118 cm, a clearance H = 0.140 cm, offset δ = O and various flow rates as follows: 0 ℓ/sec, 0.631 ℓ/sec, 1.262 ℓ/sec, 1.892 ℓ/sec.

Figure 7.3 Numerical predictions of the normal and tangential forces, as a function of whirl ratio for the following conditions: inlet swirl, $\Gamma = 0$, seal clearance = 0.5 mm, 1000 RPM, 20 GPM, H=4.24cm. Both curves show the results for the detailed seal geometry included in calculation. The solid line is with C_{de} from the calculation, C_{de}=-0.2. The dashed line uses the loss coefficient from the partial geometry in which the seal is approximated by the exit loss coefficient alone, Cde=109. .

Figure 7.4 Numerical predictions of the normal and tangential forces, as a function of whirl ratio for the following conditions: inlet swirl, $\Gamma = 0$, seal clearance = 0.5 mm, 1000 RPM, 20 GPM, H=4.24cm. The solid line is obtained with the detailed seal geometry included in the calculation, using C_{de} from the partial geometry without the seal, C_{de}=109. The dashed line is obtained with the partial geometry and the seal is approximated by the exit loss coefficient alone, C_{de}=109.

Figure 7.5 Numerical predictions of the normal and tangential forces, as a function of whirl ratio for the following conditions: inlet swirl, Γ=0, seal clearance= 0.5 mm, 1000 RPM, 20 GPM. All the curves are obtained with the seal approximated by the exit loss coefficient alone. The solid line is for the clearance, H=4.24 cm, C_{de}=109. The other curves are for the clearance, H=1.4 cm and two different total pressure drops.

Figure 7.6 Numerical predictions of the normal and tangential forces, as a function of whirl ratio for the following conditions: seal clearance= 0.5 mm, 1000 RPM, 20 GPM, clearance, H=4.24cm and three different inlet swirl ratios, 0, 0.5, and 0.8.

Figure 7.7 Numerical predictions of the normal and tangential forces, as a function of whirl ratio for the following conditions: Γ=0.5, seal clearance= 0.5 mm, 1000 RPM, 20 GPM. The solid line is for a clearance, H=4.24 cm and the dotted line is for a clearance, H=1.4 cm.

Figure 7.8 Numerical predictions of the normal and tangential forces, as a function of whirl ratio for the following conditions: seal clearance= 0.5 mm, 1000 RPM, 20 GPM H=1.4 cm and three different inlet swirl ratios, 0, 0.5, and 0.8.

LIST OF TABLES

CHAPTER ONE

INTRODUCTION

1.1 Background

In turbomachinery, the trend toward higher speeds and higher power densities has led to an increase in the number and variety of fluid-structure interaction problems in pumps, compressors, turbines and other machines. Fundamentally this occurs because the typical fluid forces scale like the square of the speed and thus become increasingly important relative to the structural strength. This becomes particularly acute in rocket engine turbopumps where demands to minimize the turbopump mass may also lead to reductions in the structural strength. Consequently, it is natural for designers and manufacturers to be concerned with the fluid induced rotordynamic forces on impellers in turbomachines, specifically centrifugal pumps. Knowledge of the steady and unsteady forces and the associated rotordynamic coefficients is required to effectively model the rotordynamics of high speed turbopumps such as the High Pressure Oxygen Turbopump(HPOTP) and the High Pressure Fuel Turbopump(HPFTP) of the Space Shuttle Main Engine (SSME).

1.2 Literature survey

The forces that act on a rotating impeller can be divided into two categories: those that arise from the mechanical components of the pump and those that are a result of the working fluid. This thesis is concerned with the latter. It has been recognized for some time that asymmetries in the flow through an impeller can cause significant radial loads (Iverson et al, 1960; Chamieh et al., 1985). The forces result in a deflection of the center line of the rotor. As a result asymmetrical variations of pressure in the working fluid become apparent especially where the radial clearances are small. However, the fluid-induced rotordynamic forces and force matrices have not been investigated until recently. The interaction of the impeller and the working

fluid induce forces on the rotor. These induced forces cause self-excited whirl where the axis of rotation moves along a trajectory eccentric to the undeflected position. When designing turbomachinery it is important to be able to predict these fluid induced forces.

Rotordynamic forces imposed on a centrifugal pump by the fluid flow through it were first measured by Domm and Hergt (1970), Hergt and Krieger (1969-70), Chamieh et al. (1985) and Jery et al. (1985). In the Rotor Force Test Facility (RFTF) at Caltech (Jery et al., 1985; Adkins et al., 1988; Franz et al., 1989) known whirl motions over a full range of frequencies (subsynchronous, supersynchronous as well as reverse whirl) are superimposed on the normal motion of an impeller. The unsteady forces imposed by the fluid on the impeller are then measured by means of a six-component dynamic force balance onto which the impellers are directly mounted (Jery et al., 1986). These measurements are processed to find not only the steady forces due to volute asymmetry, but also the unsteady rotordynamic forces and matrices.

1.3 Research objective

This research focuses on a fluid-structure interaction problem, namely the role played by fluid forces in determining the rotordynamic stability and characteristics of a turbopump. More specifically, the emphasis of this study is to investigate the contributions to the rotordynamic forces from the fluid flow through centrifugal pump impellers and the discharge-to-suction leakage flows external to the impeller. The leakage flow occurs between the front shroud of the rotating impeller and the stationary pump casing. The objective of this research was to evaluate the fluid induced forces acting on the shroud of an impeller of a centrifugal pump due to the leakage flow. The thesis begins with a description of experimental facility. This will be followed by an analysis of the nature of these leakage flow contributions, which involved measurements of forces and pressures.

1.4 Notation

The hydrodynamic force on a rotating shroud or impeller (see figure 1.1) which is whirling can be expressed in the stationary laboratory frame in linear form as:

$$\begin{bmatrix} F^*_x(t) \\ F^*_y(t) \end{bmatrix} = \begin{bmatrix} F^*_{ox} \\ F^*_{oy} \end{bmatrix} + [A^*] \begin{bmatrix} x^*(t) \\ y^*(t) \end{bmatrix} \tag{1.1}$$

The first term on the right hand side represents the radial force in the absence of whirl motion. So F^*_{ox}, F^*_{oy} are the steady, time-averaged forces in a stationary frame which result from flow asymmetries in the volute or in the inlet duct. The steady radial forces are discussed in detail elsewhere (Iversen et al. [1960], Domm and Hergt [1970], Chamieh [1983], Chamieh et al. [1985], Adkins [1985]). The matrix $[A^*]$ is the rotordynamic matrix which operates on the instantaneous displacement $[x^*]$ of the rotor center. The x^* and y^* coordinates are nondimensionalized by the leakage inlet radius, R_2. Note that $[A^*]$ will in general be a function not only of the mean flow conditions and pump geometry but also of the frequency of whirl, Ω. If outside the linear range, it may also be a function of the amplitude of the whirl motion, ε. At small, linear amplitudes $[A^*]$ should be independent of ε and presented as a function of the whirl ratio Ω/ω where ω is the impeller rotation frequency. In the case of a circular whirl orbit $x^* = \varepsilon \cos \Omega t$, $y^* = \varepsilon \sin \Omega t$.

$$\begin{bmatrix} F^*_x(t) \\ F^*_y(t) \end{bmatrix} = \begin{bmatrix} F^*_{ox} \\ F^*_{oy} \end{bmatrix} + \left[A^*\left(\frac{\Omega}{\omega}\right)\right] \begin{bmatrix} x^*(t) \\ y^*(t) \end{bmatrix} \tag{1.2}$$

The forces normal and tangential to the imposed circular whirl orbit are related to the matrix elements as follows:

$$F_n^*(t) = \frac{1}{2}\left(A^*_{xx} + A^*_{yy}\right)\varepsilon$$

$$F_t^*(t) = \frac{1}{2}\left(-A^*_{xy} + A^*_{yx}\right)\varepsilon \tag{1.3}$$

The reader is referred to Jery et al (1985) and Franz et al. (1989) for details. In the analysis which follows, the above equations will be expressed in nondimensional terms. The unsteady forces, Fn* and Ft*, are nondimensionalized by $\rho\pi\omega^2 R_2^3 b_2 \varepsilon / R_2$ and $[A^*]$ by $\rho\pi\omega^2 R_2^3 b_2$, where ρ is the fluid density and b_2, R_2 are respectively the width and radius of the impeller discharge.) If [A] is to be rotationally invariant, then

$$A_{xx} = A_{yy} = Fn$$

$$A_{xy} = -A_{yx} = Ft \tag{1.4}$$

Zhuang (1989) also found the hydrodynamic force matrices for the present experiment to be skew-symmetric and virtually all of the experimental results confirm the fact that the matrix [A] is rotationally invariant for these flows.

The forces $F_1(t)$ and $F_2(t)$ are detected in the rotating frame by the dynamometer (Franz(1990)) and are related to the forces in the laboratory frame (see figure 1.2) as follows:

$$F_x(t) = - F_1(t) \sin \omega t - F_2(t) \cos \omega t$$

$$F_y(t) = F_1(t) \cos \omega t - F_2(t) \sin \omega t \tag{1.5}$$

Combining equations (1.2) and (1.5) yields

$$- F_1(t) \sin \omega t - F_2(t) \cos \omega t = F_{ox} + A_{xx} \cos \Omega t + A_{xy} \sin \Omega t$$

$$F_1(t) \cos \omega t - F_2(t) \sin \omega t = F_{oy} + A_{yx} \cos \Omega t + A_{yy} \sin \Omega t$$

(1.6)

The components of the steady force are obtained by averaging over time. In the present experiment, this involves taking a long record of data and ensemble averaging over this period:

$$F_{ox}(t) = \frac{1}{T} \int_0^T \{ - F_1(t) \sin \omega t - F_2(t) \cos \omega t \} dt$$

$$F_{oy}(t) = \frac{1}{T} \int_0^T \{ F_1(t) \cos \omega t - F_2(t) \sin \omega t \} dt \tag{1.7}$$

The elements of the hydrodynamic force matrix are obtained by the following manipulations. To obtain $A_{xx}(t)$ and $A_{yx}(t)$, equation (1.6) is multiplied by cos Ωt and then averaged over time:

$$A_{xx}(t) = \frac{2}{T}\int_0^T \{- F_1(t) \sin \omega t \cos \Omega t - F_2(t) \cos \omega t \cos \Omega t\} dt$$

$$= \frac{2}{T}\int_0^T - \frac{1}{2} \{F_1(t) \sin (\omega-\Omega)t + F_2(t) \sin (\omega+\Omega)t + F_2(t) \cos (\omega-\Omega)t + F_2(t) \cos (\omega+\Omega)t\} dt$$

$$A_{yx}(t) = \frac{2}{T}\int_0^T \{F_1(t) \cos \omega t \cos \Omega t - F_2(t) \sin \omega t \cos \Omega t\} dt$$

$$= \frac{2}{T}\int_0^T \frac{1}{2} \{F_1(t) \cos (\omega-\Omega)t + F_1(t) \cos (\omega+\Omega)t - F_2(t) \sin (\omega+\Omega)t - F_2(t) \sin (\omega-\Omega)t\} dt$$

To obtain $A_{xy}(t)$ and $A_{yy}(t)$, equation 1.6 is multiplied by sin Ωt and then averaged over time:

$$A_{xy}(t) = \frac{2}{T}\int_0^T \{- F_1(t) \sin \omega t \sin \Omega t - F_2(t) \cos \omega t \sin \Omega t\} dt$$

$$= \frac{2}{T}\int_0^T - \frac{1}{2} \{F_1 (t) \cos (\omega-\Omega)t - F_1(t) \cos (\omega+\Omega)t + F_2(t) \sin (\omega+\Omega)t - F_2(t) \sin (\omega-\Omega)t\} dt$$

$$A_{yy}(t) = \frac{2}{T}\int_0^T \{F_1(t) \cos \omega t \sin \Omega t - F_2(t) \sin \omega t \sin \Omega t\} dt$$

$$= \frac{2}{T}\int_0^T \frac{1}{2} \{F_1(t) \sin (\omega+\Omega)t - F_1(t) \sin (\omega-\Omega)t + F_2(t) \cos (\omega+\Omega)t - F_2(t) \cos (\omega-\Omega)t\} dt$$

(1.8)

Conventionally, rotordynamicists represent the force matrix by sub-dividing into components which depend on the orbit position (x,y), the orbit velocity $(\dot{x},\dot{y})$ and the orbit acceleration $(\ddot{x},\ddot{y})$. In other words, a simple stiffness, damping and mass model for the fluid forces is used.

$$\begin{pmatrix} F_x \\ F_y \end{pmatrix} = \begin{pmatrix} F_{ox} \\ F_{oy} \end{pmatrix} - [K] \begin{pmatrix} x \\ y \end{pmatrix} - [C] \begin{pmatrix} \dot{x} \\ \dot{y} \end{pmatrix} - [M] \begin{pmatrix} \ddot{x} \\ \ddot{y} \end{pmatrix} \tag{1.9}$$

where the matrices [M], [C], [K] are the hydrodynamically-induced mass, damping and stiffness matrices. Although measurements indicate that the force elements may depart from this quadratic form, it is convenient for analytical purposes to evaluate [M], [C], [K], by fitting quadratics to the experimental data.

$$\begin{aligned} A_{xx} &= - K_{xx} - (\Omega/\omega)\, C_{xy} + (\Omega^2/\omega^2)\, M_{xx} \\ -A_{xy} &= - K_{xy} + (\Omega/\omega)\, C_{xx} + (\Omega^2/\omega^2)\, M_{xy} \\ A_{yx} &= - K_{yx} - (\Omega/\omega)\, C_{yy} + (\Omega^2/\omega^2)\, M_{yx} \\ A_{yy} &= - K_{yy} + (\Omega/\omega)\, C_{yx} + (\Omega^2/\omega^2)\, M_{yy} \end{aligned} \tag{1.10}$$

It is experimentally shown that the hydrodynamic matrix is skew symmetric. Skew-symmetry is also a result of the rotational-invariance of the matrix [A]. Thus, the coefficients simplify as follows:

$$\begin{aligned} K_{xx} &= K_{yy} = K \\ K_{xy} &= -K_{yx} = -k \\ - C_{xx} &= C_{yy} = -C \\ C_{xy} &= C_{xy} = c \\ M_{xx} &= M_{yy} = M \\ M_{xy} &= -M_{yx} = -m \end{aligned} \tag{1.11}$$

The present experimental results will be presented in terms of the so-called "direct" coefficients K, C and M and the so-called "cross-coupled" coefficients k, c and m. Finally note that the normal and tangential forces are related to the rotordynamic coefficients by:

$$F_n = - K - (\Omega/\omega)\, c + (\Omega^2/\omega^2)\, M$$

$$F_t = k - (\Omega/\omega)\, C + (\Omega^2/\omega^2)\, m \qquad (1.12)$$

1.5 Experimental Background

Typical experimental measurements of the dimensionless normal and tangential forces, Fn and Ft, (Fn*,Ft* nondimensionalized by $\rho\pi\omega^2 R_2{}^3 b_2 \varepsilon / R_2$, where ρ is the fluid density and b_2, R_2 are respectively the width and radius of the impeller discharge) from the work of Jery (1986) are shown in figure 1.4. These particular results are for a typical five-bladed centrifugal pump impeller made by Byron-Jackson for a specific speed of 0.57 (referred to as Impeller X) and installed in a well-matched spiral volute in the manner shown in figure 1.3 (for more detail see Jery (1986)). One of the most significant features of these results is the range of positive whirl ratios within which the tangential force is positive and therefore potentially destabilizing rotordynamically. A positive normal force is directed outward and would tend to increase the displacement of the impeller.

Moreover, the work of Jery et al. (1985) and Adkins et al. (1988) on centrifugal pump impellers demonstrated that there are two sources for these fluid-induced forces. By shortening the front shroud of the casing, both the steady and the unsteady forces on the impeller were reduced, as was, the region of destabilizing whirl. Adkins (1986) made steady pressure measurements at two axial locations on the stationary casing facing the rotating impeller shroud. It was recognized that contributions to the rotordynamic forces could arise not only from azimuthally nonuniform pressures in the discharge flow acting on the impeller discharge area but also from similar nonuniform pressures acting on the exterior of the impeller front shroud as a result of the leakage flow passing between this shroud and the pump casing. Consequently, Jery (1986) also made measurements using a

solid "impeller" (Impeller S) with the same exterior profile as Impeller X. The leakage flow was simulated by a remote auxiliary pump which generated the same discharge to inlet pressure differences as occurred with Impeller X operating at a given flow coefficient. The normal and tangential forces obtained are included in figure 1.4. If one assumes that the solid impeller experiences the same leakage flow contributions to F_n, F_t as Impeller X but does not experience the main throughflow contributions, the tentative conclusion could be drawn that the leakage flow contribution to the normal force was about 70% of the total and the contribution to the tangential force was about 30% of the total. This tentative conclusion indicating the substantial contribution of the leakage flow to rotordynamic forces motivated the present study.

Adkins et al. (1988) demonstrated both analytically and experimentally that the leakage flow from the discharge through the gap outside the impeller shroud to the inlet was responsible for significant nonuniformity in the pressure acting on the exterior of the shroud and that this contributed to both the radial forces and rotordynamic matrices. Parallel to the experimental investigation, a fluid mechanical model of the complicated unsteady throughflow generated when a rotating impeller whirls was developed by Adkins (1986). It is quasi-one-dimensional and requires only the geometry of the impeller and volute and the impeller/volute performance curve. The model allowed evaluation of the pressure perturbations in the impeller discharge which compared well with the experimental measurements of these perturbations. It therefore permitted evaluation of the contribution to the rotordynamic forces from these pressure perturbations and typical results for a limited range of whirl ratios are presented in figure 1.5 along with experimental measurements of the total F_n, F_t under the same conditions. The conclusions are crudely consistent with the early remarks; the pressures in the main discharge flow contribute about one half of the rotordynamic forces. To confirm this Adkins (1986) made pressure perturbation measurements in both the main discharge and the leakage flow. These allowed evaluation of the rotordynamic stiffness, namely the rotordynamic forces at zero whirl ratio, $F_n(0)$ and $F_t(0)$ as can be seen from equation (1.14). Experimental results of Adkins (1986), showed that the fluid in the annular gap region was

responsible for a hydrodynamic stiffness given by

$$[K] = \begin{pmatrix} -1.6 & 0.3 \\ -0.3 & -1.6 \end{pmatrix} \tag{1.13}$$

The following hydrodynamic stiffness is from Chamieh's (1983) direct measurements of the total hydrodynamic stiffness on the same impeller.

$$[K] = \begin{pmatrix} -2.0 & 0.9 \\ -0.9 & -2.0 \end{pmatrix} \tag{1.14}$$

When the above hydrodynamic stiffness in equation (1.15) is compared to Chamieh's (1983) direct measurements of the total hydrodynamic stiffness given in equation (1.16), it can be seen that the contribution to the gap is significant

The above-mentioned experiments suggested fractional contributions similar to those in Jery's work, namely that the leakage flow component of $F_n(0)$ was about 80% while the component of $F_t(0)$ was more than 30%. Adkins (1986) also concluded that changes in the geometry of the leakage pathway resulted in significant changes in these rotordynamic contributions. The measurements of Adkins (1986) were for a large annular gap. Arndt and Franz (1986) and Franz et al. (1986) made measurements without the enlarged annular region and demonstrated that the large shroud clearances reduce the rotordynamic forces. Since the geometry used in these tests was not typical of that in prototype pumps it was also concluded that further work on the rotordynamic characteristics of leakage flows was clearly indicated and this led to the fabrication of the experiment described in this thesis.

There are several other indications which suggest the importance of leakage flows to the fluid-induced rotordynamic forces. It is striking that the total rotordynamic forces measured by Bolleter et al. (1987) from Sulzer Brothers, Ltd., for a conventional centrifugal pump configuration are about twice the magnitude of those measured by Jery (1986) or Adkins (1986) at Caltech. Both test programs used a radial face seal to minimize the forces which would be developed by the wear-ring seals. So the measured hydrodynamic forces are due to a combination of the impeller-volute and the impeller-shroud interaction. It now seems sensible to suggest that this

difference is due to the fact that the clearance in Bolleter's leakage flow annulus is substantially smaller than in the experiments of Jery and Adkins.

The force generated by fluid in the annular seals separating the high pressure discharge of the pump from the low pressure inlet has been explored by Childs (1983b) and Black (1969). They basically extended the analysis of Lomakin (1958) for seals. When it became apparent that leakage flows could contribute significantly to the rotordynamics of a pump, Childs (1989) adapted the bulk-flow model which was developed for the analysis of fluid-induced forces in seals (Childs [1983a,b]) to evaluate the rotordynamic forces, Fn and Ft, due to these leakage flows. The model was applied to several pump geometries; typical results for the conventional centrifugal pump configuration tested by Bolleter et al. (1987) are shown in figure 1.6. The results have been scaled to conform with the nondimensionalization used in this research. Data is shown for three different inlet swirl velocity conditions in which the swirl velocity is assumed to be 0.5, 0.6 or 0.7 of the impeller tip speed. Note that Childs (1989) presents qualitatively similar results for quite a different leakage flow path geometry.

Several general conclusions may be drawn from Childs work. First the magnitude and overall form of the model predictions are consistent with the experimental data. In particular, the model also predicts positive, rotordynamically destabilizing tangential forces over a range of positive whirl ratios. Moreover, Childs' theory yielded some unusual results including peaks in the rotordynamic forces at particular positive whirl ratios, a phenomenon which Childs tentatively described as a "resonance" of the leakage flow. This unexpected phenomenon develops at small positive whirl ratios when the inlet swirl velocity ratio exceeds about 0.5. It remains to be seen whether such "resonances" occur in practice. Childs (1986) points out that a typical swirl velocity ratio at inlet (pump discharge) would be about 0.5 and may not therefore be large enough for the resonance to be manifest. There have been reports that SSME impellers fitted with anti-swirl vanes in the leakage flow annulus have had noticeably different rotordynamic characteristics (Childs et al. [1990a,b]). It is clear that a detailed comparison of model predictions with experimental measurement remains to be made and is one of the purposes of the present program.

1.6 Fluid force effects

In this section, some general fluid induced rotordynamic effects will be reviewed. Further discussion on this subject can be found in Vance (1988).

A variation of the clearance between the blade tip and the the housing can induce tip forces (Alford [1965]). The Alford effect describes the force which results from a circumferential variation of blade tip clearance. The lift of the blade increases because the gap decreases and this results in a force in a direction opposite to the rotation of the pump, as follows:

$$F_n = 0$$

$$F_t = -\frac{2K''}{\pi\rho R^2\omega^2} \tag{1.15}$$

where K'' is a constant. This is a constant force and would be stabilizing for positive whirl and destabilizing for negative whirl. Vance (1982) performed experimental measurements to verify Alford's force in axial-flow machinery and showed a linear variation with the rotor eccentricity. The form of these forces support the nondimensionalization in the present research. It should be noted that the Alford force neglects any swirl or viscous effects.

A variation in the speed of the blades can induce blade forces. Thompson (1978) estimates the tangential force as proportional to the speed of the tangential blade tip speed.

$$F_t = -\frac{2K'''\Omega}{\pi\rho R^2\omega^2} \tag{1.16}$$

where K''' is a constant. Note that this force is always stabilizing.

The operation of a bearing is typically associated with an eccentricity. The fluid velocity is increased where the clearance is reduced and this gives rise to a normal force which is proportional to the speed, namely:

$$F_n = \frac{2K'}{\pi\rho R^2\omega}\left(1 - \frac{\Omega}{\omega}\right) \tag{1.17}$$

where K' is a constant. This is a restoring force and occurs when the flow is dominated by viscous effects. In seals, the axial length to radius is small. So, this would be a predominant effect. Lomakin (1958) originally recognized the significance of the forces arising in the seal gaps of hydraulic high pressure machines.

An added mass effect occurs when the blade tip approaches the casing. This results in a force which is proportional to $(\Omega - \omega)^2$ as follows:

$$F_n = \frac{2K}{\pi\rho R^2\omega}\left(1 - \frac{\Omega}{\omega}\right)^2 \tag{1.18}$$

This inertia effect or Bernoulli effect competes with the Lomakin (1958) effect.

Brennen (1976) investigated Couette flow in an annulus of gap width H, surrounding a whirling cylinder and obtained asymptotic solutions for various Reynolds number regimes. A summary of the findings will be given here because it is possible to consider the present experiment as Couette flow in an annulus surrounding a cone.

Inviscid high Re:

$$F_n = -\left(\frac{\Omega}{\omega}\right)^2 + \frac{2\gamma^2}{\gamma^2 - 1}\left(\frac{\Omega}{\omega} - K_a\right)\left(\frac{\Omega}{\omega} - K_b\right)$$

$$F_t = 0 \tag{1.19}$$

where K_a, K_b are the relative tangential speeds near the inner and outer cylinders respectively.

Laminar mean flow :

Very low Reynolds number :

$$F_n = \frac{9R^5}{4H^5}\left(2\frac{\Omega}{\omega} - 1\right)$$

$$F_t = -\frac{6R^3}{Re\ H^3}\left(2\frac{\Omega}{\omega} - 1\right) \tag{1.20}$$

where the Reynolds number is defined based on the gap width as follows:

$$Re = \frac{\omega R H}{\nu} \tag{1.21}$$

the above equations are valid for very low $Re < (H/R)^3$. For slightly higher Re, such that $(H/R)^3 < Re < (H/R)$ then the following equations apply:

Low Reynolds number :

$$F_n = \frac{16\nu^2}{\omega^2 HR}\left(2\frac{\Omega}{\omega} - 1\right)$$

$$F_t = \frac{128H\nu^3}{3R^4\omega^3}\left(2\frac{\Omega}{\omega} - 1\right) \tag{1.22}$$

A schematic of these forces is shown qualitatively in figure 1.7. It is important to understand whether the flow is dominated by viscous effects or inertia effects. As can be seen, each contribution has a different result on the induced forces. These effects which induce forces on an impeller play an important role, as it is important to understand how these forces acting on the rotor will either dampen or amplify the whirl motion.

1.7 Summary

The current knowledge of the forces which act on a rotating impeller has been the subject of this chapter. This thesis is specifically concerned with the shroud forces which result from the discharge-to-suction leakage flows in a centrifugal impeller. In the next chapter, the experimental method for obtaining these fluid forces will be discussed.

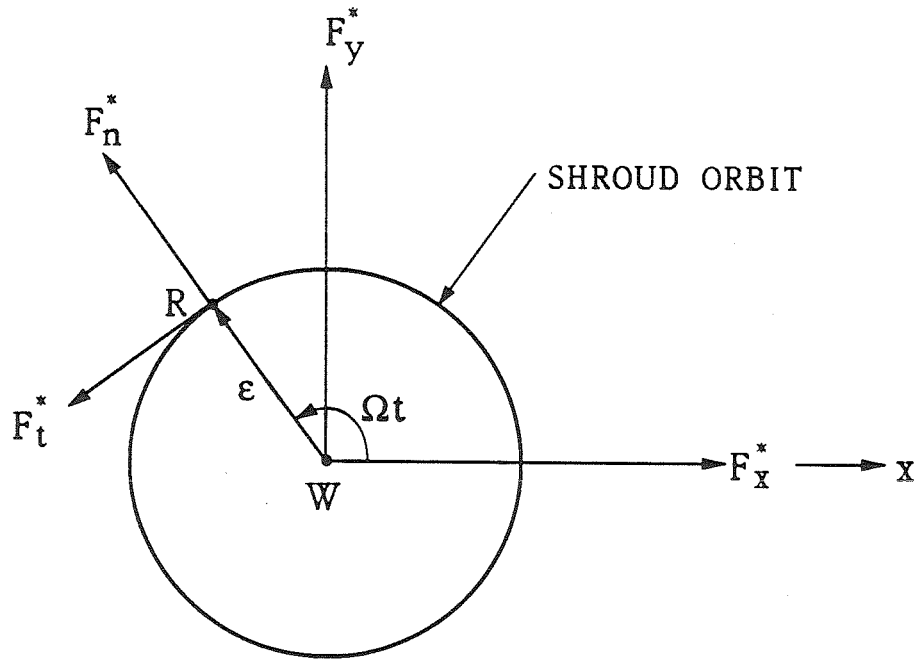

Figure 1.1. Schematic of the fluid-induced radial forces acting on an impeller whirling in a circular orbit. F_x^* and F_y^* represent the instantaneous forces in the stationary laboratory frame. F_n^* and F_t^* are the forces normal and tangential to the whirl orbit where Ω is the whirl frequency.

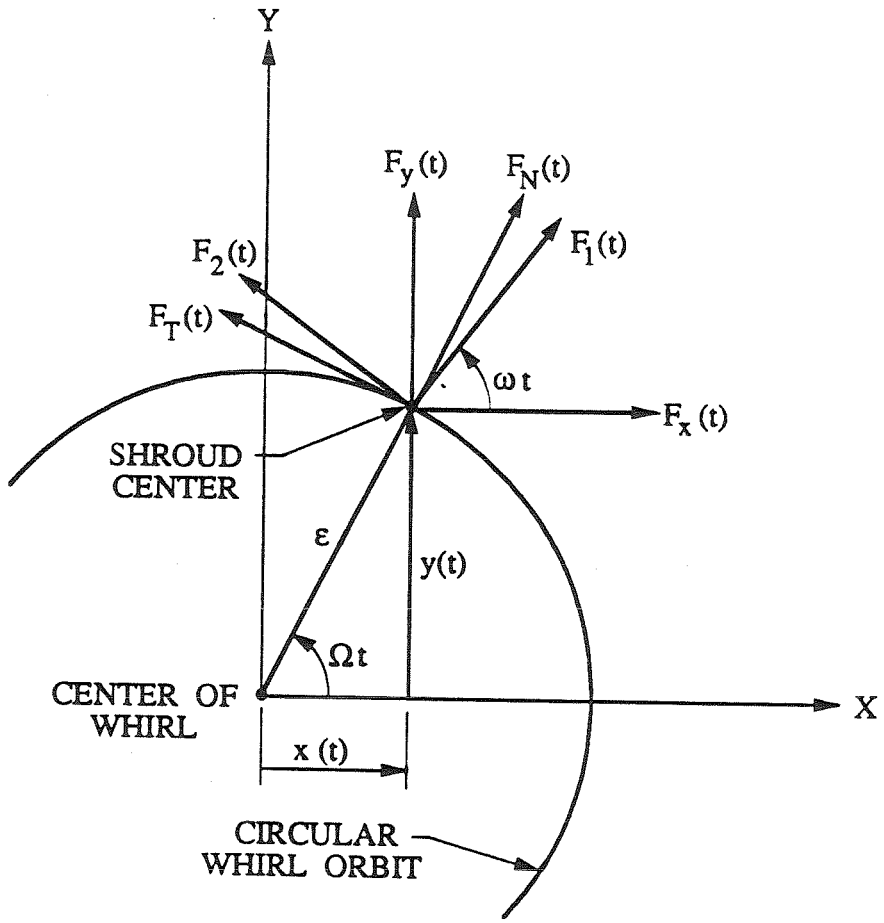

Figure 1.2. Schematic of the fluid-induced radial forces acting on an impeller whirling in a circular orbit. $F_1^*(t), F_2^*(t)$ represent the instantaneous forces in the rotating dynamometer frame. F_n^* and F_t^* are the forces normal and tangential to the whirl orbit where Ω is the whirl frequency.

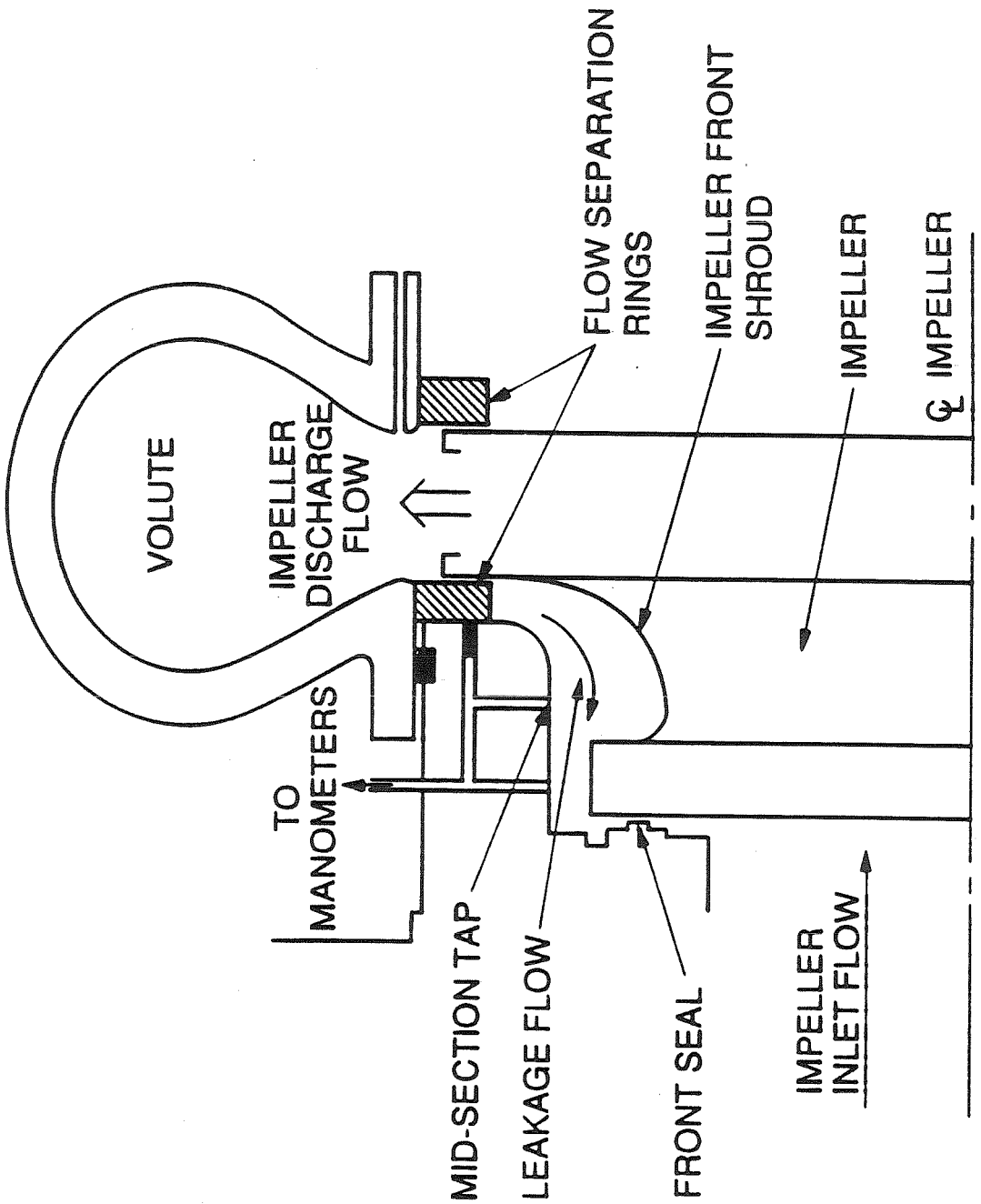

Figure 1.3. Schematic showing the impeller/volute arrangement for the experiments of Jery (1986) and Adkins (1986).

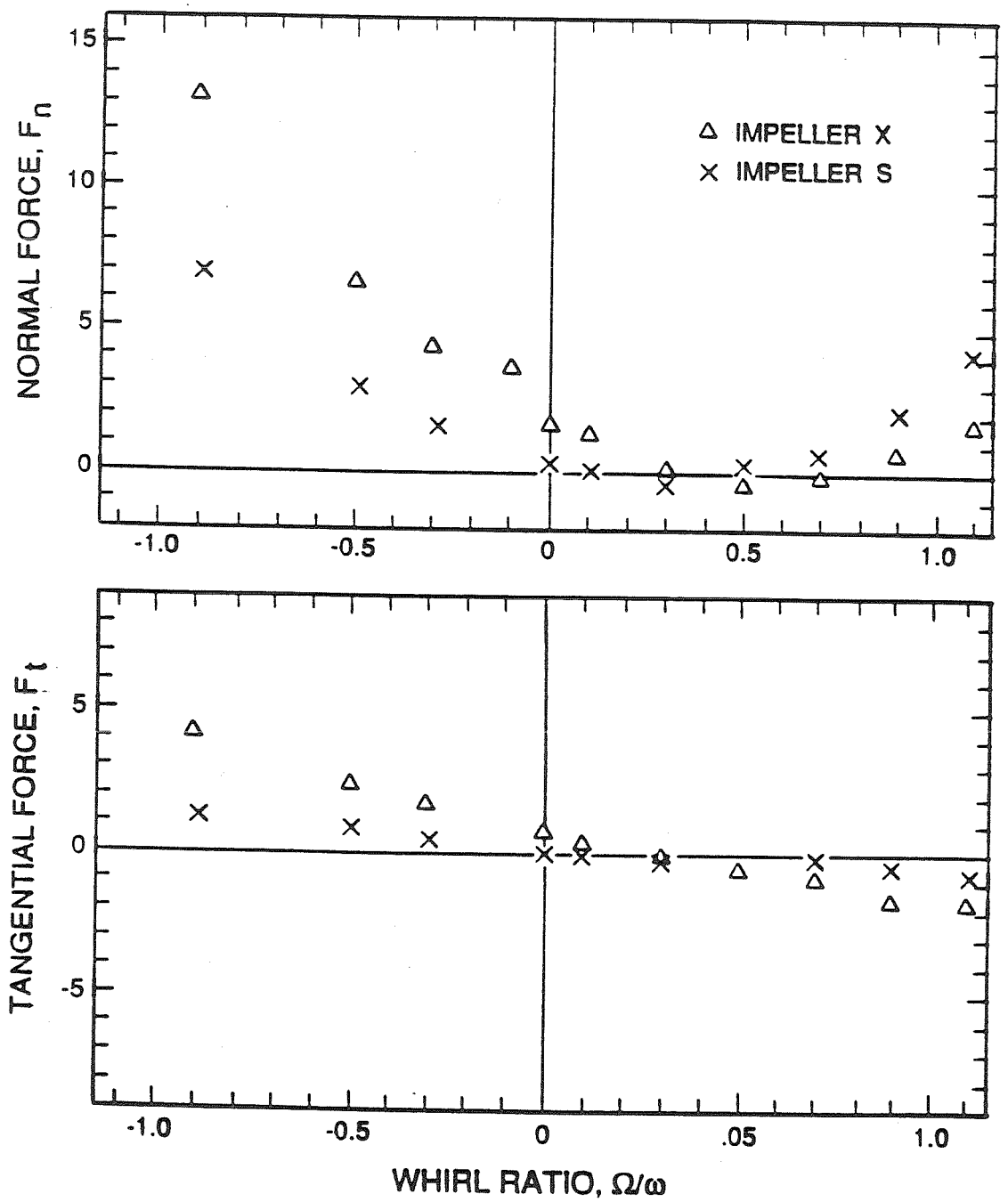

Figure 1.4. Dimensionless normal and tangential forces, F_n and F_t, as a function of whirl ratio from Jery (1986) for a typical centrifugal impeller/volute combination (Impeller X and Volute A at 1000 rpm and a flow coefficient $\phi = 0.092$) are shown by squares. The dummy Impeller S results with an externally imposed pressure rise are shown by x.

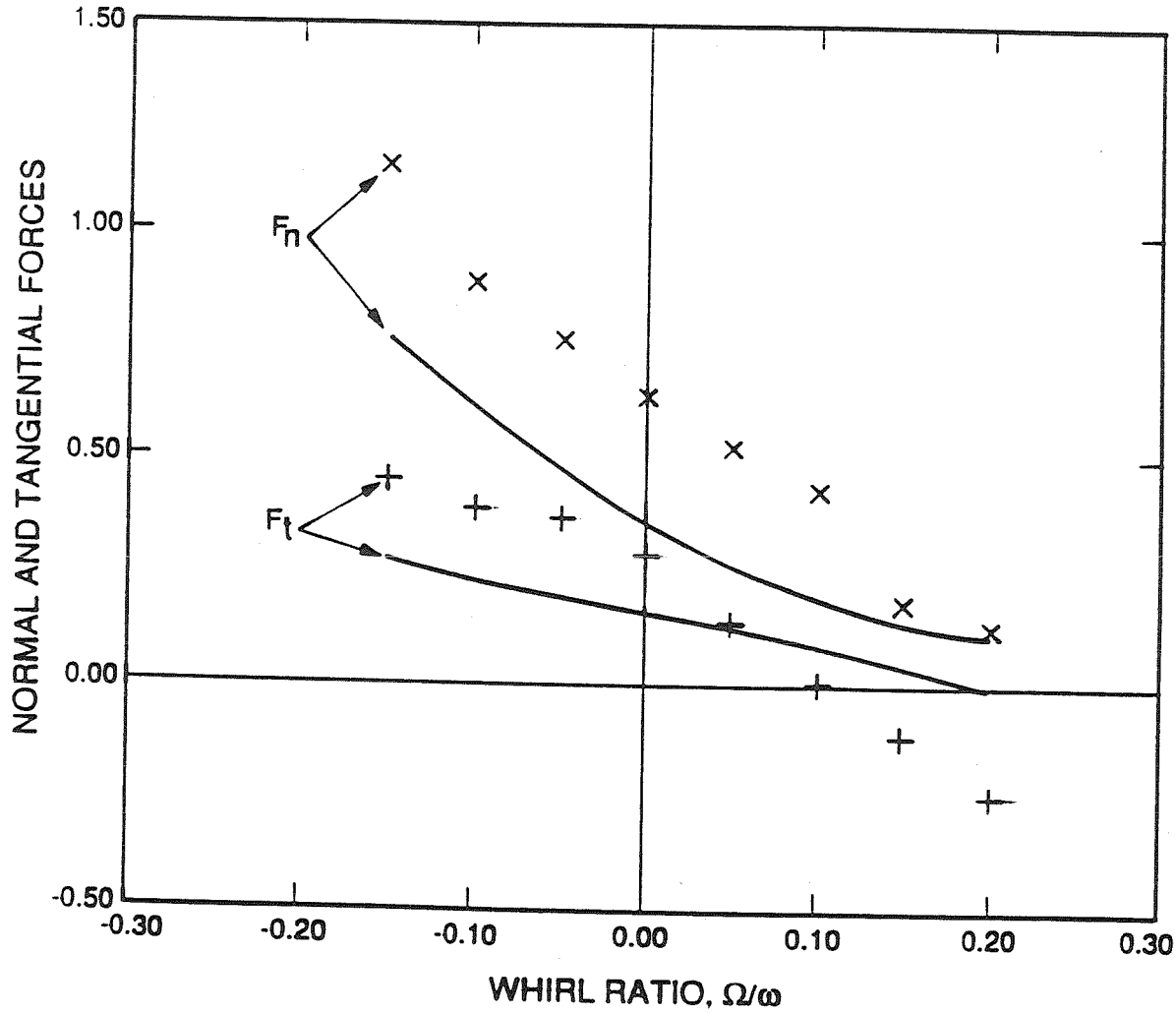

Figure 1.5. Comparison of the dimensionless normal and tangential forces according to Adkins (1986) theory (solid lines) with the experimental values for Impeller X at ϕ = 0.092.

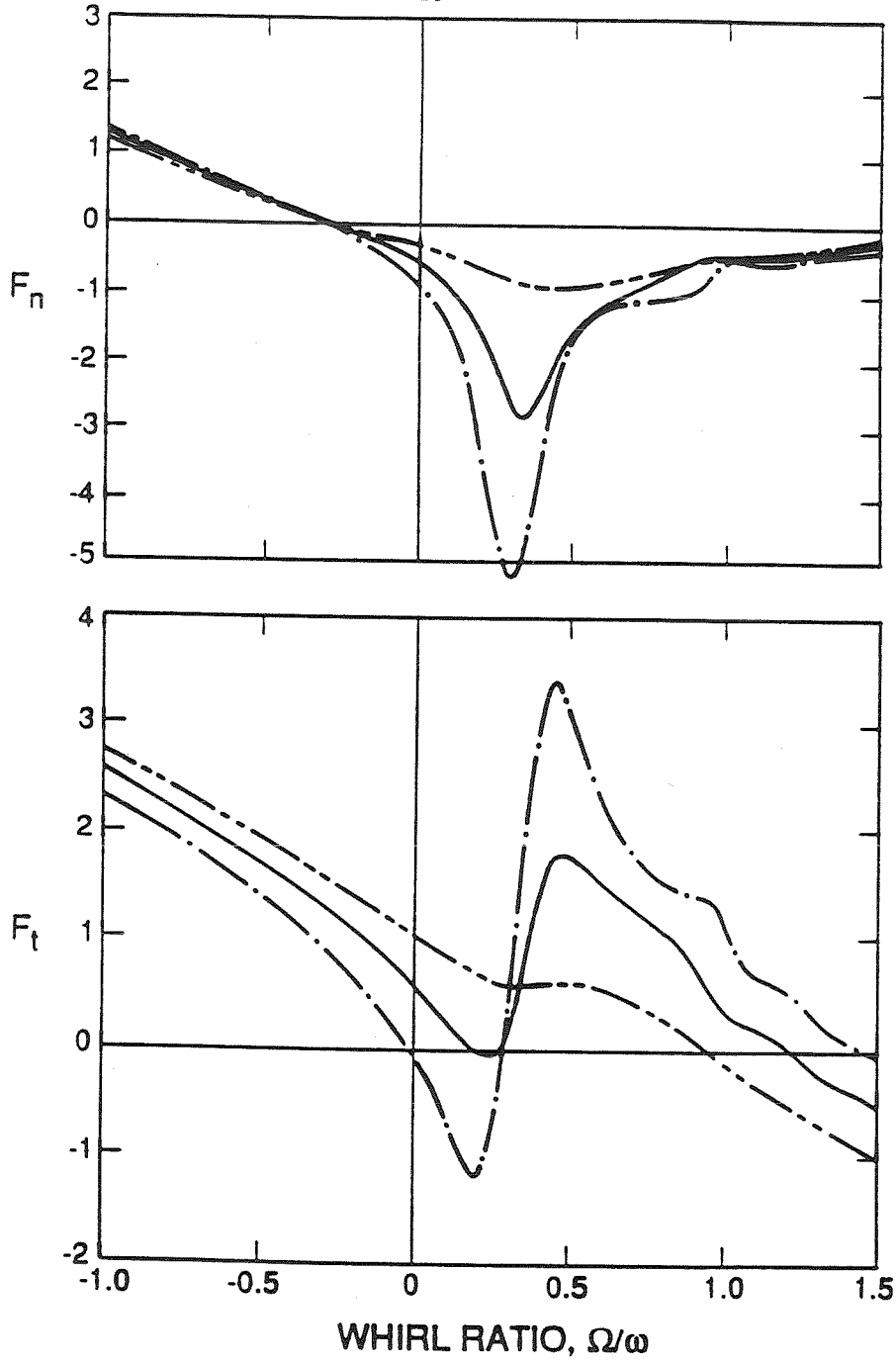

Figure 1.6. Theoretical predictions from Childs (1986) on the F_n and F_t resulting from the conventional leakage path geometry used in the tests of Bolleter et al. (1985). Results are shown for three different inlet swirl velocity conditions in which that swirl velocity is assumed to be 0.5 , 0.6, and 0.7 of the shroud inlet rotating velocity.

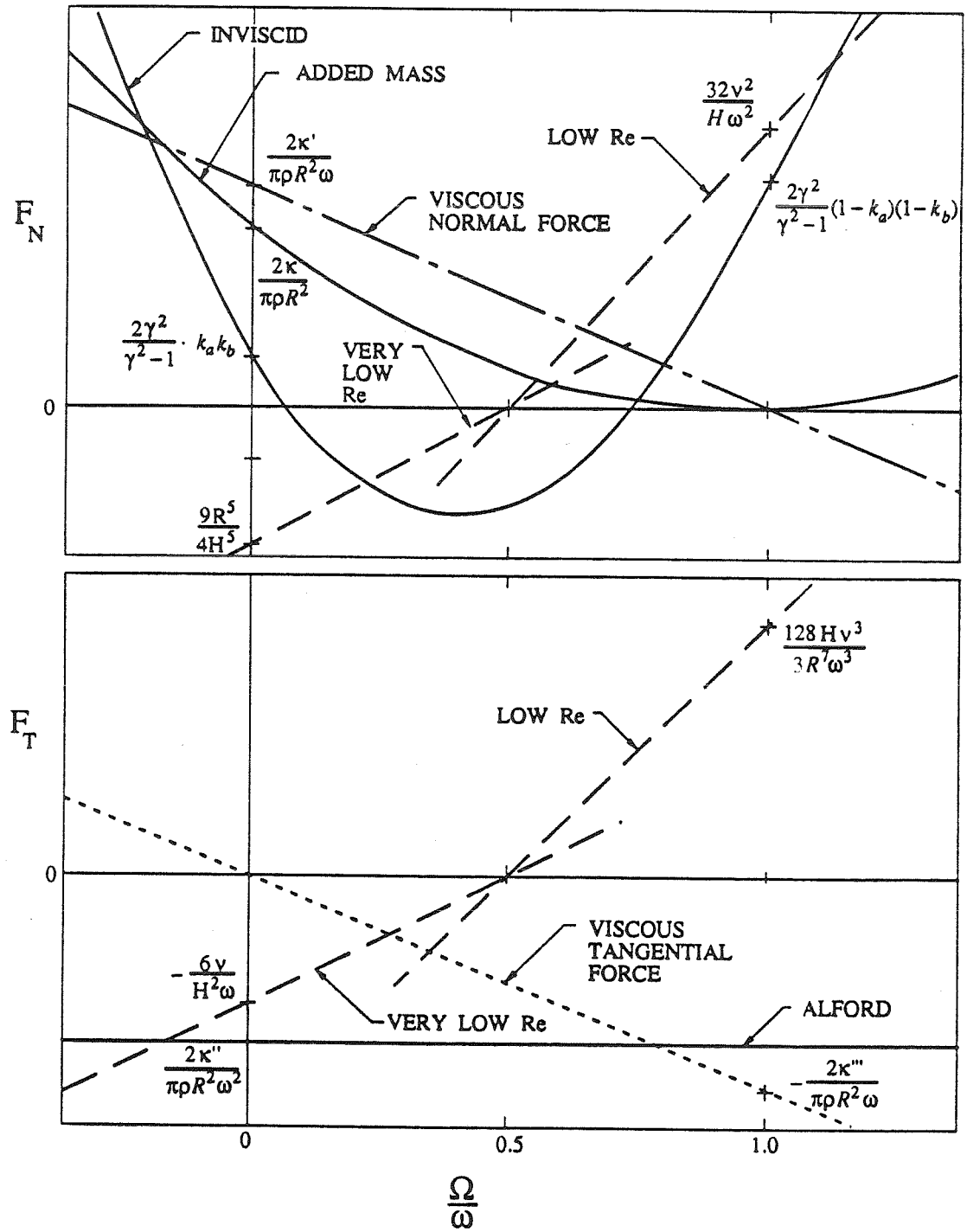

Figure 1.7 Qualitative schematic of some fluid-induced forces.which result from various effects.

CHAPTER 2

LEAKAGE FLOW TEST APPARATUS

2.1 Rotor force test facility

A detailed description of the test facility, can be found in many of the references (Chamieh [1983], Adkins [1986], Jery [1986], Arndt [1988], Franz [1989]), so only a brief description will be given here. The experiments were conducted in the Rotor Force Test Facility (RFTF) shown in figure 2.1, which was constructed to study fluid induced forces due to imposed whirl motions. It is an experiment in forced vibration in that the rotor is forced to move in a circular whirl orbit of prescribed frequency and amplitude (eccentricity). A schematic of the installation in the RFTF is shown in Figure 2.2. Briefly, the RFTF consists of a cast housing which was designed to hold different impeller/volute (diffuser) configurations in the closed recirculating loop. The overall system can be regulated by an airbag and a heat exchanger maintains constant water temperature. The experimental objective was to impose well controlled rotations and whirl motions on a very stiff impeller/shaft system and to measure directly the resulting force on the impeller. This is accomplished by the eccentric drive mechanism which superposes a circular orbit on the basic rotation. A rotating shroud is mounted on a spindle attached to the rotating force balance (Jery et al. [1985], Franz et al. [1989]), which measures the forces directly on the shroud. The four-post design of this rotating dynamometer involved nine strain-gage bridges which measure all six force components on the impeller and is discussed in detail by Jery (1986). The output of the bridges is amplified by a rack of Vishay Model 2310 signal conditioning amplifiers. These amplifiers are connected to a data taker which stored the force measurements as a series of voltages on a desk top computer. The relationship between the strains and the forces were found by static calibration tests. Existing software exists for most of the stages from taking the data to processing the data and performing the mathematical manipulations described in section 1. The rotating dynamometer permits measurements of the rotordynamic force matrix due to the shroud fluid forces.

Closed loop controls for the main motor and for the whirl motor synchronized the orientation and position of the dynamometer with the data acquisition system. The orientation and location of the impeller along its orbit was imparted to the data acquisition system. The data acquisition system sampled 128 points per bridge per cycle and typically 256 cycles of data were taken to average the data. Each cycle corresponds to an integral number of revolutions of the whirl motor. A frequency multiplier/divider was used to provide command signals.

2.2 Experimental apparatus

The experimental apparatus sketched in figures 2.2 and 2.3 was designed and constructed to simulate the leakage flow along the shroud from the impeller discharge to the impeller inlet (Zhuang [1989], Guinzburg et al. [1990], Guinzburg et al. [1992]). The clearance between the rotating shroud and the stationary casing can be varied by both axial and radial adjustment of the stationary casing. For the present experiment, the initial geometric configuration consists of a straight annular gap inclined at an angle of 45° to the axis of rotation. The schematic in figure 2.3 shows the clearance in the centered position when the centers of the shroud and the casing both coincide. The magnitude of the clearance can be adjusted by moving the stationary shroud axially by as much as 7mm. In figure 2.4, the concept of an offset is illustrated. Although no offsets were used in this research, the possibility existed of moving the stationary shroud in the radial direction by as much as 7 mm. The allowable offset (to avoid rubbing between the stationary shroud and rotating shroud) depends on the clearance and the eccentricity, since the rotating shroud moves along a circular orbit with a radius of the eccentricity. In order to model losses in the flow, an adjustable face seal ring was used to give a clearance of up to 7mm (refer to figure 2.2). The face seal clearance in this experiment permits the pressure drop to be adjusted separately from the flow. In an impeller, there are two seals for the following purposes: either to reduce the leakage flow along the front surface of the impeller or to reduce the leakage from the inlet back along the shaft to the previous inlet. The flow through the leakage path is generated by an auxiliary pump (Flotec F2P4-1062 pump) and is described in detail elsewhere (Andrews[1988]); a schematic of the loop in which it was installed is included

in appendix A.

The selection of the flow rates through the leakage path (see appendix A) was based on performance characteristics of a typical centrifugal pump. For the centrifugal pumps examined by Sherzer (1924), the internal leakage was determined to be 6% of the capacity of the pump. However, larger values could be expected for clearance increases due to wear. So, this order of magnitude of leakage was considered for the present experiments. The flow coefficient of a centrifugal pump is usually on the order of ϕ = 0.15. So a leakage flow rate of 10 GPM would correspond to approximately 7% of the flow rate through a centrifugal pump with the dimensions of the present experiment. This sample calculation is given in appendix A.

Both the main motor and the whirl motor are driven through position and velocity feedback systems which are coupled to a data acquisition system which records the position in both rotation cycles at which radial force measurements are taken. Descriptions of the force balance, data processing and other details are contained in Jery (1986), Franz (1989). The main rotational motion is driven by a 20hp DC main motor through the main pump shaft and the shroud can be driven at speeds up to 3500 RPM. A 2hp DC whirl motor produces the eccentric motion. A circular whirl motion with a frequency up to 1800 RPM can be superimposed on the basic rotation. The eccentric drive mechanism permits testing with the amplitude of the whirl motion or eccentricity, ε adjustable from 0.000 cm. to 0.152 cm (0.060 in). In these experiments two eccentricities were used, one with a radius of 0.0254cm and the other 0.118cm. The distance from the center of the whirl orbit to the center of the casing, termed the fixed offset, δ is also variable. So concentric and nonconcentric circular whirl orbits could be investigated. However, in the present experiments there was no offset, so the center of the shroud rotates about the center of the casing.

2.3 Inlet guide-vane

As was mentioned previously, the inlet tangential velocity to the leakage path was shown by Childs (1989) to have an effect on the rotordynamic forces. Consequently, the effect of inlet swirl was investigated by installing an inlet

guide vane that was used to introduce swirl in the direction of shaft rotation at the leakage flow inlet. This was accomplished by constraining the flow in a logarithmic spiral channel.

The fluid was assumed to be constrained to flow along the installed vane, which is shown schematically in figure 2.5. Assuming conservation of circulation and a continuity relation, it is possible to relate the turning angle, α, with the inlet swirl, Γ as follows:

$$\Gamma = \frac{Q}{B} \frac{1}{2\pi R_2^2 \omega} \frac{1}{\tan \alpha} \tag{2.1}$$

More explanation of how this equation was arrived at can be found in appendix B. This expression assumes that the flow discharging from the inlet swirl vane is parallel with that vane. However, this was not confirmed by measurement of the inlet swirl. It is also important to note that the inlet swirl could not be varied arbitrarily as it depends on the leakage flow rate. Recalling that the flow coefficient, ϕ, is given by,

$$\phi = Q/2\pi R_2^2 H\omega \tag{2.2}$$

it follows that,

$$\frac{\Gamma}{\phi} = \frac{H}{B \, \mathrm{Tan} \, \alpha} \tag{2.3}$$

Therefore the only way to vary the inlet swirl ratio independently of the flow coefficient would be to vary the depth of the inlet guide vane, B or the turning angle, α. Varying the clearance between the shroud and the stationary casing is clearly not an option as this factor introduces its own effects on the results.

Based on the above simple geometry and continuity considerations, the turning angle was chosen to be 2°. This allowed a range of swirl ratios, defined as the ratio of the inlet tangential velocity to the rotor velocity. Thus, as the leakage flow rate and therefore tangential velocity was increased, the swirl ratio could be increased for a fixed rotor speed. Various views of the device are shown in figure 2.6. Note that the flow may only enter the spiral guide because the back of the plate is sealed by foam rubber to prevent undirected flow from

entering the leakage path.

2.4 Calibration of the rotating dynamometer

The basic design features and fabrication of the rotating dynamometer are discussed by Jery (1986). Briefly the dynamometer is instrumented with strain gages which form wheatstone bridges. This section will be limited to the procedure involved with the calibration of the dynamometer. Greater detail can be found in Jery (1986), Franz (1989) and Zhuang (1989). The purpose of the calibration was to produce a six-by six calibration matrix, [B], which includes all possible dynamometer reactions. The six-component force vector, [F], can then be obtained from the measured bridge output voltages by use of the relation $[F] = [B]\ [V]$, where [V] is the six-component voltage vector. The matrix vector [B] is simply the inverse of the matrix of slopes, [S], in which an element S_{ij}, represents the output, V_i of bridge i under a unit load of the force component F_j. The slopes are determined by six individual force loadings, one for each generalized force component. The slopes have been recently checked for the lateral forces by Zhuang (1989) and typical calibration curves are presented therein. Due to the dynamic nature of the primary forces to be measured, the above static calibration was supplemented by testing the dynamic characteristics of the dynamometer (Zhuang [1989]). By rotating the main shaft in air without whirl motion, the weight of the shroud will be sensed by the dynamometer as a periodic lateral force. The magnitude and phase of this force was evaluated by Zhuang[1989] up to speeds of 3000 RPM and remained unchanged. A lateral impulse load was applied to the rotating shroud. The natural frequency of the dynamometer (200 Hz) with the rotating shroud mounted was the outcome of this test and was found to be much higher than the shaft frequencies planned for the present experiment. Because of the success of the dynamic tests, the static calibration matrices were sufficient to process the dynamic measurements.

2.5 Pressure measurement

In addition to steady radial forces and rotordynamic forces which are obtained from the force balance measurements, arrays of pressure taps are located on the surface of the stationary casing. Static pressure manometer taps

were placed along meridians in the leakage flow passage at three different circumferential locations, spaced equally apart. Along each meridional direction, there was a set of ten equally spaced taps. The meridional directions are 120° apart. At the inlet of the leakage path there are nine taps, which includes the three from the set along the meridians, equally spaced along the circumferance. In addition, two sets of pressure taps (six for each set) were placed 90° apart so that high frequency (250kHz) and good resolution piezoelectric dynamic pressure transducers could be installed. They are flush-mounted and a seal box protects them from contact with water. The installation of the taps is shown in figure 2.2. The rotating shroud was positioned at various offsets which enabled steady pressure measurements to be made. The zero whirl frequency rotordynamic forces were evaluated by integration of the measured pressure differences. Zhuang (1989) compared these results with the force balance measurements from the same experiments.

2.6 Experimental method

The investigation of the radial forces and rotordynamic matrices was conducted for a wide range of flow, shroud clearance, eccentricity, face seal clearance, shaft rotating speed, and whirl rotating speed. A matrix of the tests can be found in appendix C. The results from these experiments will be presented nondimensionally by dividing the forces by $\rho\pi\omega^2 R_2^3 L\varepsilon/R_2$. This differs from the factor used to nondimensionalize the impeller forces presented earlier in that the axial length, L of the leakage flow passage (figure 2.3) has replaced b_2, the impeller discharge width. In most pumps L and b_2 are comparable and hence, to evaluate the significance of the results, the dimensionless data from the leakage flow tests may be directly compared with that from the impeller tests.

The measured forces include forces associated with the weight and the buoyancy of the rotor. To extract the fluid-induced forces at a given whirl ratio and operating condition, two identical tests must be performed. One with the rotor operating in air (a "dry" run) and another operating in water (a "wet" run.) Thus each data point resulted from the following subtraction: {"wet" run - "dry" run.). The dry runs account for the force of gravity and the centrifugal force on the impeller. The buoyancy force is also subtracted, so

that only the fluid induced rotordynamic forces are left.

Therefore, the experimental measurements include:

(i) the overall radial forces and rotordynamic matrices acting on the rotating shroud measured using the force balance.

(ii) the steady and unsteady pressure profiles in the leakage path.

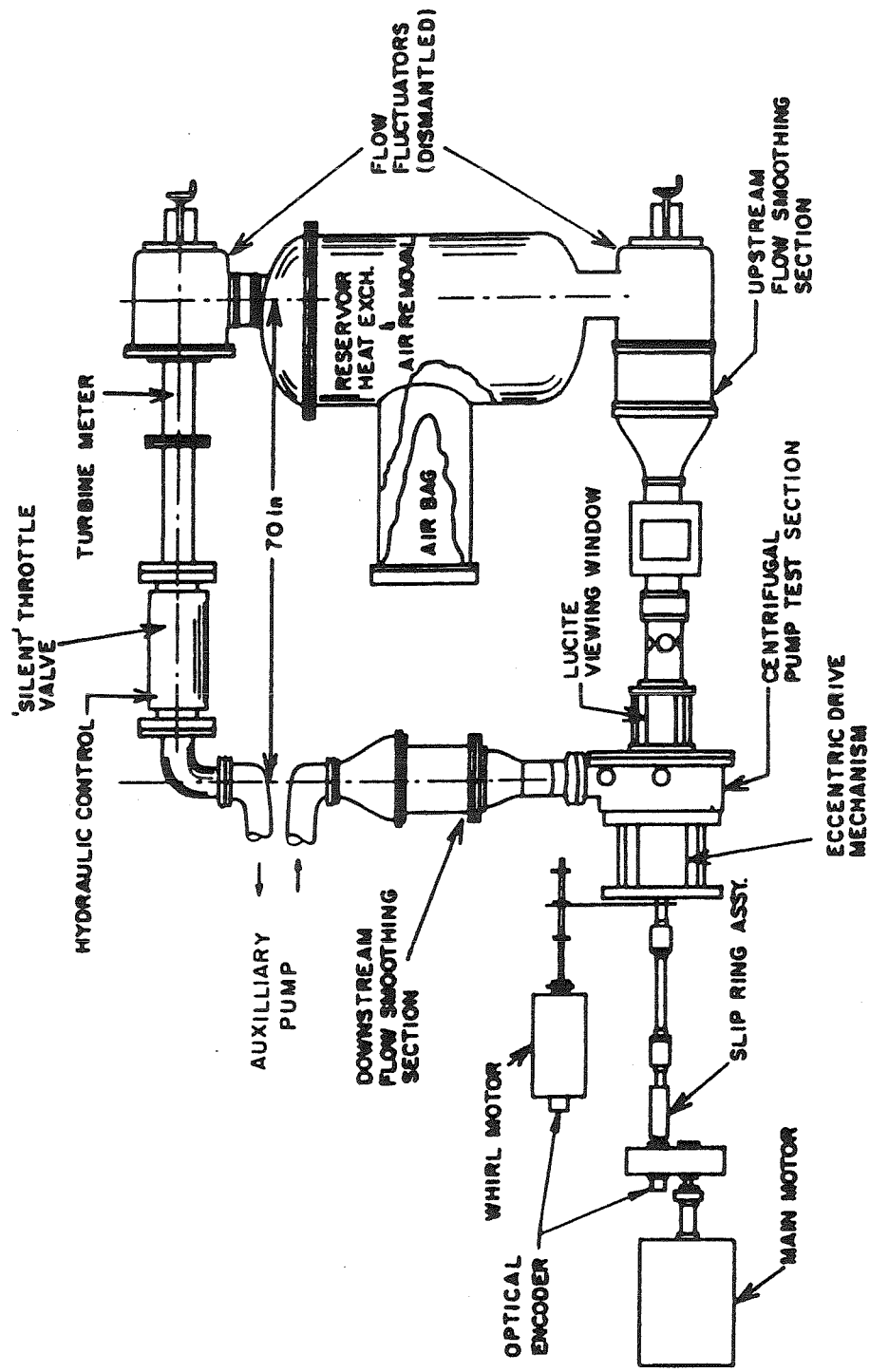

Figure 2.1. Schematic of the Rotor Test Facility (RFTF).

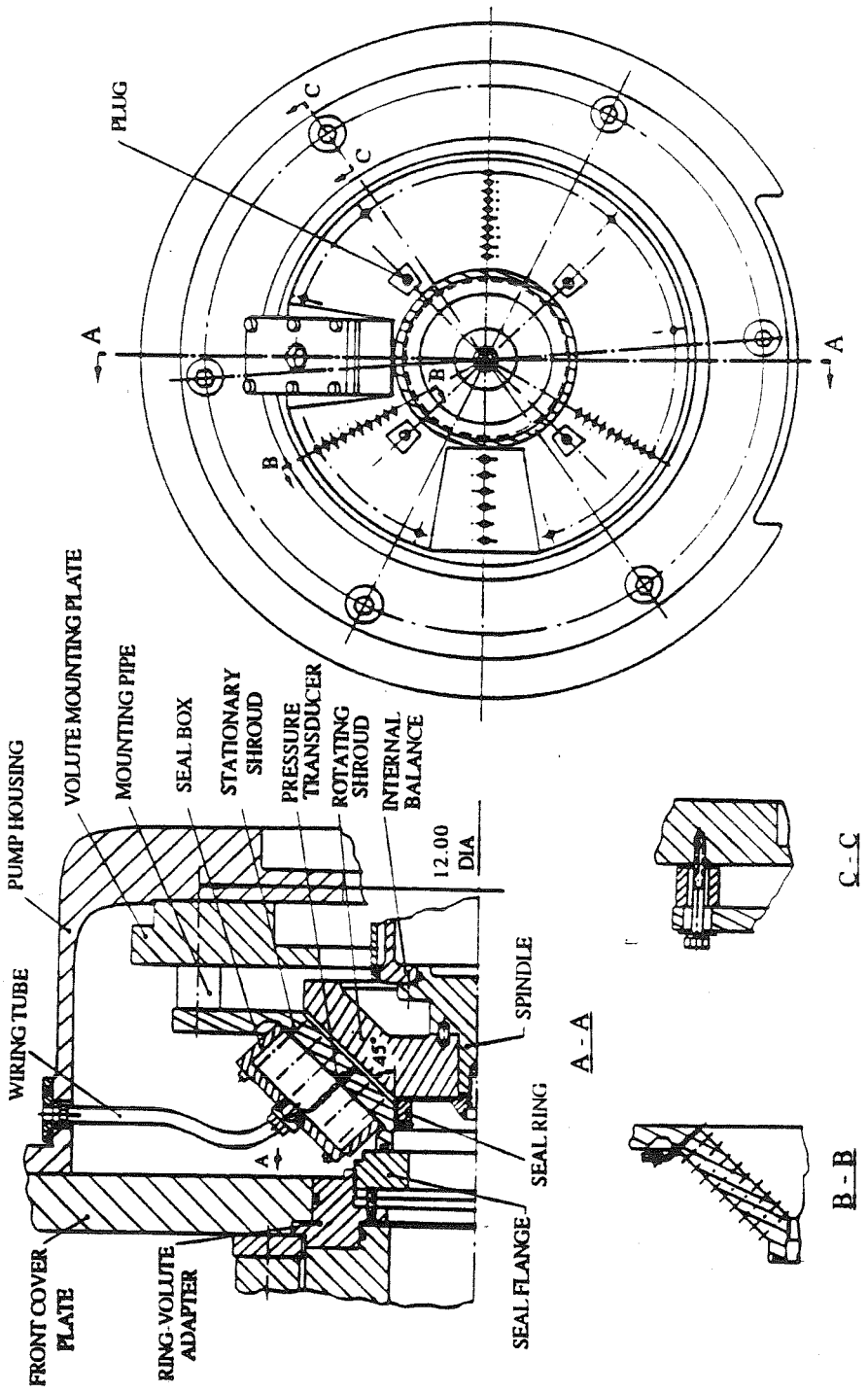

Figure 2.2 Layout of the leakage flow test apparatus for installation in the RFTF. (Zhuang [1989]).

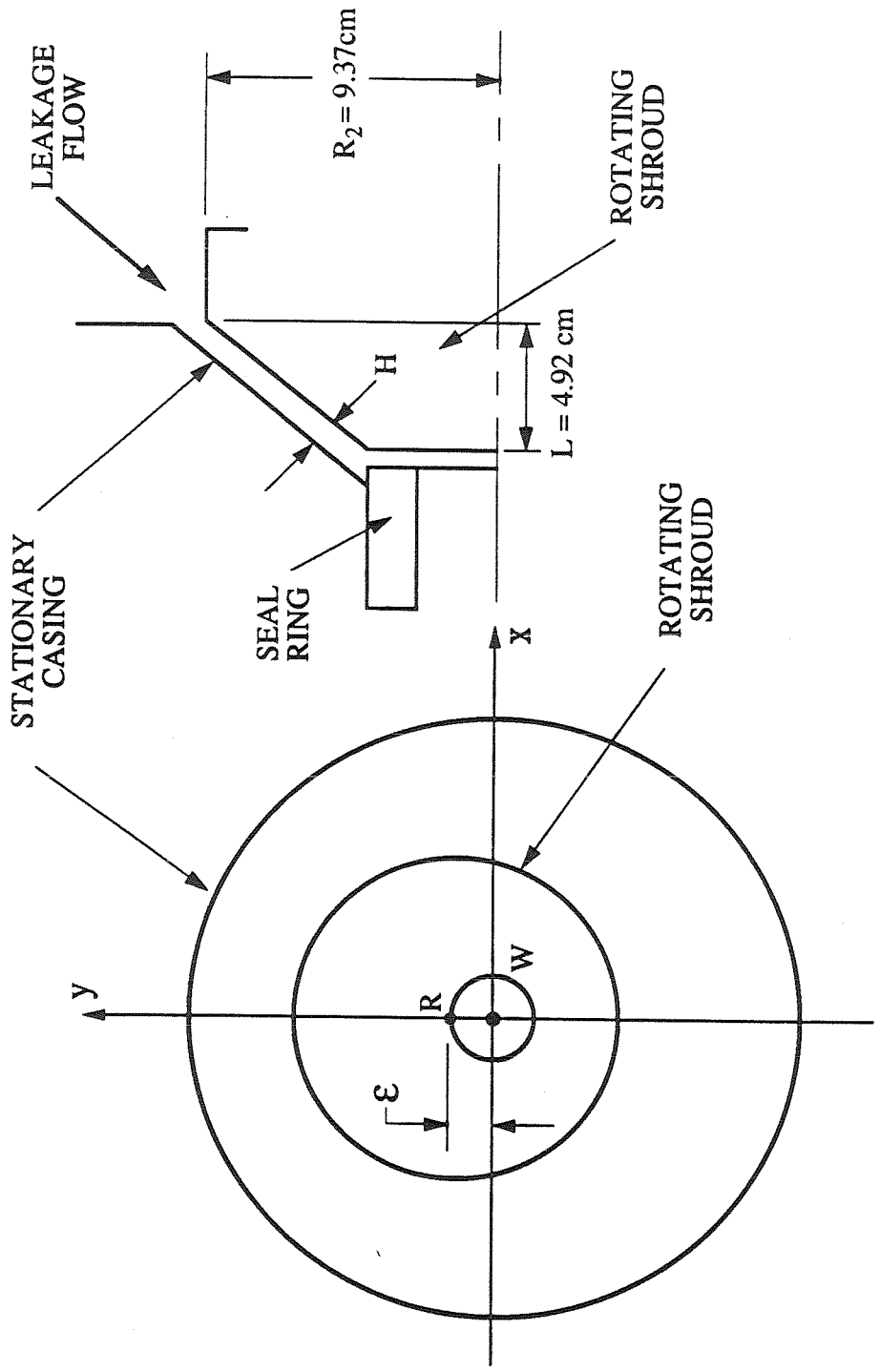

Figure 2.3 Schematic of the whirling shroud, R is the center of the rotating shroud, W is the center of the whirl orbit along which R travels and also the center of the stationary casing, WR = ε is the eccentricity.

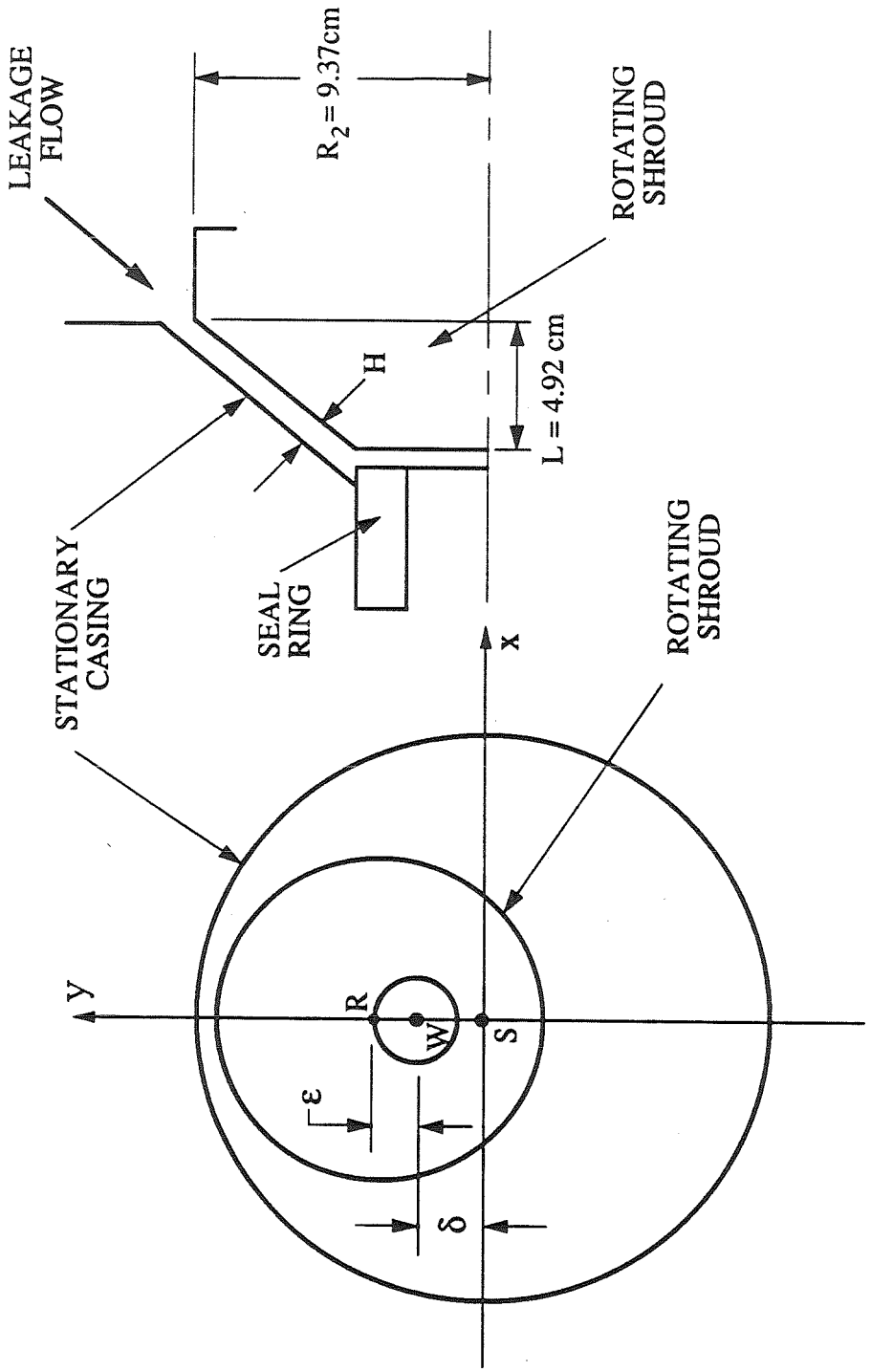

Figure 2.4 Schematic of the whirling shroud with offset, where S is the center of the stationary casing and WS = δ is the offset.

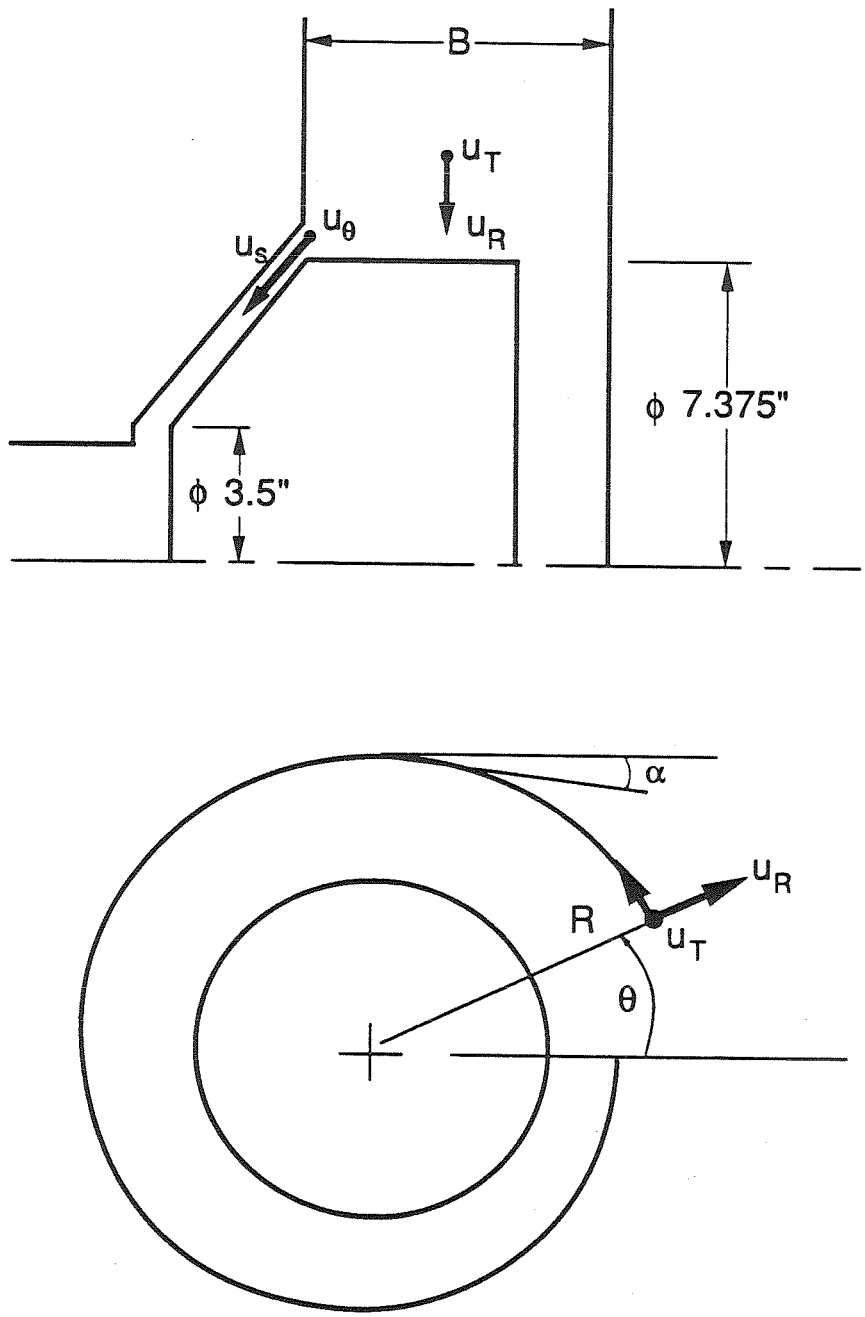

Figure 2.5 Description of the inlet swirl geometry.

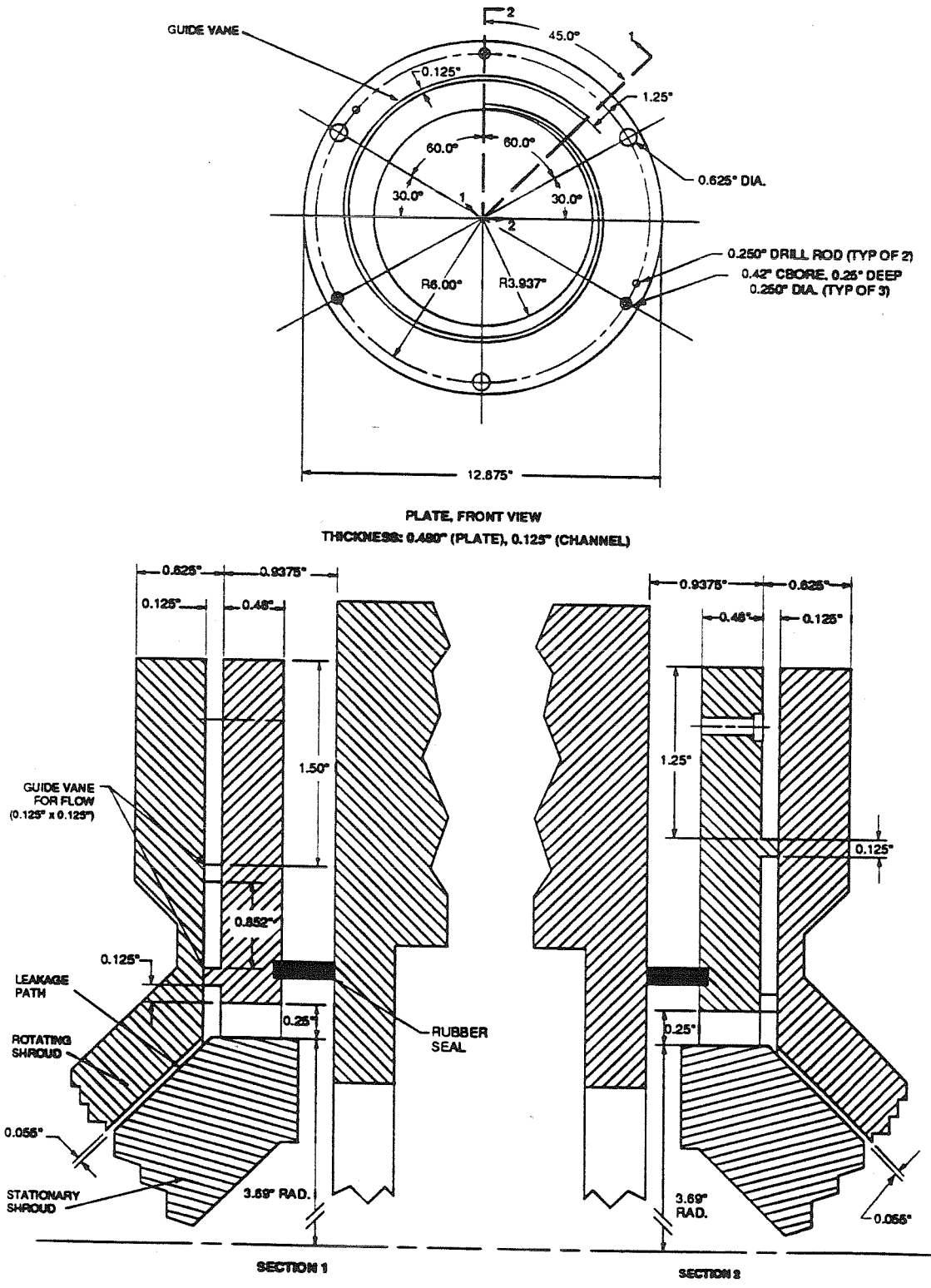

Figure 2.6 Installation of the inlet swirl vane in the leakage flow test apparatus.

CHAPTER 3

PRELIMINARY RESULTS

3.1 Force measurements with no whirl.

Preliminary results from this experimental apparatus were obtained for zero whirl frequency using static offsets (Zhuang [1989]). Typical results for zero flow rate and a particular offset are presented in figure 3.1 which illustrates a number of general features in the data. Note first that the data at rotating speeds of 1000 rpm and 1500 rpm are in good agreement which provides some evidence that the Reynolds number effects are not too significant. Secondly the forces calculated from the measured pressure distributions in the leakage annulus agree well with those measured directly with the force balance. This confirms the fact that the forces arise from the pressure variations in the leakage flow and not from the viscous shear stresses or the stresses on the other surfaces of the rotating shroud. Finally, figure 3.1 clearly demonstrates that the forces are a strong function of the clearance, H; indeed the dependence is close to inverse proportionality.

3.2 Steady force measurements with whirl

The steady forces F_{ox} and F_{oy} are temporal and spatial averages of the lateral forces sensed by the dynamometer. Hence they should be independent of the whirl ratio. This is evident from the steady forces for the entire matrix of experiments shown in figures 3.2-3.14. As mentioned in chapter 2, to extract the fluid-induced forces, the graphs are the result after subtracting the weight and the buoyancy. The nondimensional magnitudes of the steady forces are small compared to the nondimensionalized unsteady forces, however this is deceiving because they are not dimensionalized in the same way as F_n and F_t (which are nondimensionalized by the eccentricity ratio also).[1] Perhaps an

---

[1] Thus the steady forces need to be multiplied by 79 for the larger eccentricity and 369 for the smaller eccentricity in order to compare them to the unsteady forces.

indication of the magnitude of these forces is to compare the steady forces to those for an impeller housed in a volute. For example for Impeller X housed in Volute A, Jery (1986) obtained forces on the order of 28.5 N for shut-off, 3 N for a flow coefficient of 0.092 (the design point), and -7 N for a flow coefficient of 0.0132. Clearly the further from the design point that the pump is operated at, the stronger are the distortions. The conclusion which can be made is that the steady forces for the shroud[1] are not significant compared with those arising from an entire impeller. In the idealized case where the rotating shroud is perfectly centered, the steady forces would be zero. Nevertheless, the steady forces occur due to an offset or other minor asymmetry which would result from the way in which the apparatus is assembled. It is interesting to note that as a general trend the steady forces increase as the leakage flow increases. The nondimensional forces decrease with increasing rotational speeds, indicating that there is a steady force independent of rotational speed (since they are nondimensionalized by rotational speed.) The rotational speed does not affect the steady forces. This is noted by comparing figures 3.2, 3.3, 3.4 (which were obtained for an eccentricity of 0.0254 cm) or figures 3.5, 3.6, 3.7 (which were obtained for an eccentricity of 0.118 cm). The magnitude of F_{ox} is the same irrespective of the eccentricity. The magnitude of F_{oy} increases slightly with eccentricity, as demonstrated by figures 3.2, 3.5 or 3.3, 3.6 or 3.4, 3.7. The effect of decreasing the clearance is to increase the forces, which is shown by figures 3.5, 3.10 and 3.11 or figures 3.6,3.9. Comparison of figure 3.5 with 3.12 and 3.13 shows no effect of seal clearance on the steady forces. The general conclusion which can be made from the above discussion is that the steady forces for leakage flows is clearly not significant. The results are summarised in figure 3.15, which presents the steady forces as a function of flow-coefficient.

3.3 Pressure measurements

The pressure in the annular gap is measured from the taps located on the surface of the stationary shroud. (see section 2.4). These pressure taps were connected to a bank of 36 manometers. Two additional manometers were used to measure the downstream pressure and the pressure on the wall of the pump

---

[1] In the present graphs for 1000 RPM, unity corresponds to 1392 N.

housing. As was seen in figure 3.1, the steady pressure measurements from the manometers could yield only steady radial forces and stiffness matrices [K], because of the limited frequency response of the water manometers.

Figures 3.16-3.18 show typical pressure distributions along the meridional direction of the rotating shroud. The horizontal axis is normalized by the shroud length and begins at the leakage inlet. Pressure distributions along the shroud were obtained for different whirl positions at 1000 RPM, an eccentricity $\varepsilon = 0.0254$ cm, a clearance H = 0.140 cm, an offset δ = O and a seal clearance of 0.051 cm. The measurements are from each set of pressure taps along the meridional direction and are 120° apart. The pressure is normalized by the dynamic head at the inlet to the leakage path, ρv_2^2. Figures 3.16, 3.17, and 3.18 were obtained for flows of 10 GPM, 20 GPM, and 30 GPM respectively. The variation in the pressure distribution of each meridional set can be expained as follows. For a particular circumferential location, the clearance between the stationary shroud and the rotating shroud varies. Thus the pressure taps sense different pressure drops due to a different clearance. It can be seen in the last figure of each series, that when the pressures from the each whirl position are averaged, the results are similar in magnitude. Use of these distributions will be made later in the discussion of a theoretical model.

Unsteady pressure measurements (using the PCB piezoelectric pressure transducers) were taken synchronously with the force measurements. The signals from the piezoelectric transducers were sampled on a 16 channel data acquisition system similar to the one which was used for the force measurements. For each revolution of the shroud, 1024 data points were taken. Since 4 transducers were available, this enabled them to be sampled at 256 points/channel/cycle. In order to average, 256 cycles of data were taken. Both instantaneous and ensemble averaged data were stored. The average is obtained for measurements made at identical orientations of the rotating shroud. The transducers were split among the two sets of pressure taps, placed 90° apart (see figure 2.2).The objective was to look for eddy cells or other unsteady flow patterns. The motivation for this study is from the work on disk-friction flow by Stafford et al. (1975). In that work, the disc/wall diameter ratio was an important parameter which would produce pulsating flow at a

particular disc/wall diameter ratio. The pulse frequency was in the range of $\frac{1}{10}$ to $\frac{1}{2}$ of the shaft frequency. The spectra that were obtained for each individual transducer showed no frequencies different from the whirl frequencies. (It is known that these frequencies are associated with the rotordynamic forces.) Thus, it was not thought useful to cross-correlate the pressure signals.

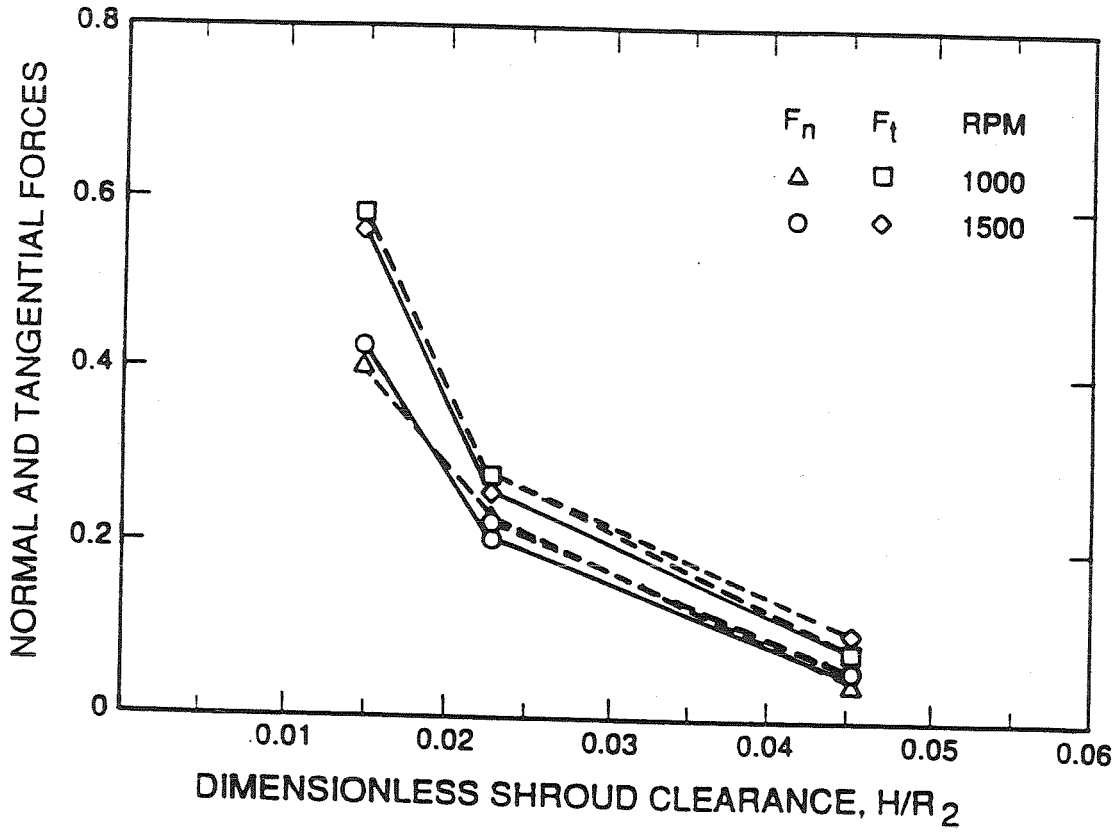

Figure 3.1 Dimensionless normal and tangential forces at zero whirl frequency, $F_n(O)$ and $F_t(0)$, as a function of the dimensionless shroud clearance, H/R_2 for an eccentricity ε = 0.096 cm, zero flow rate and two rotating speeds as indicated. Results obtained from pressure measurements and direct measurements with the force balance are both shown (Zhuang [1989]).

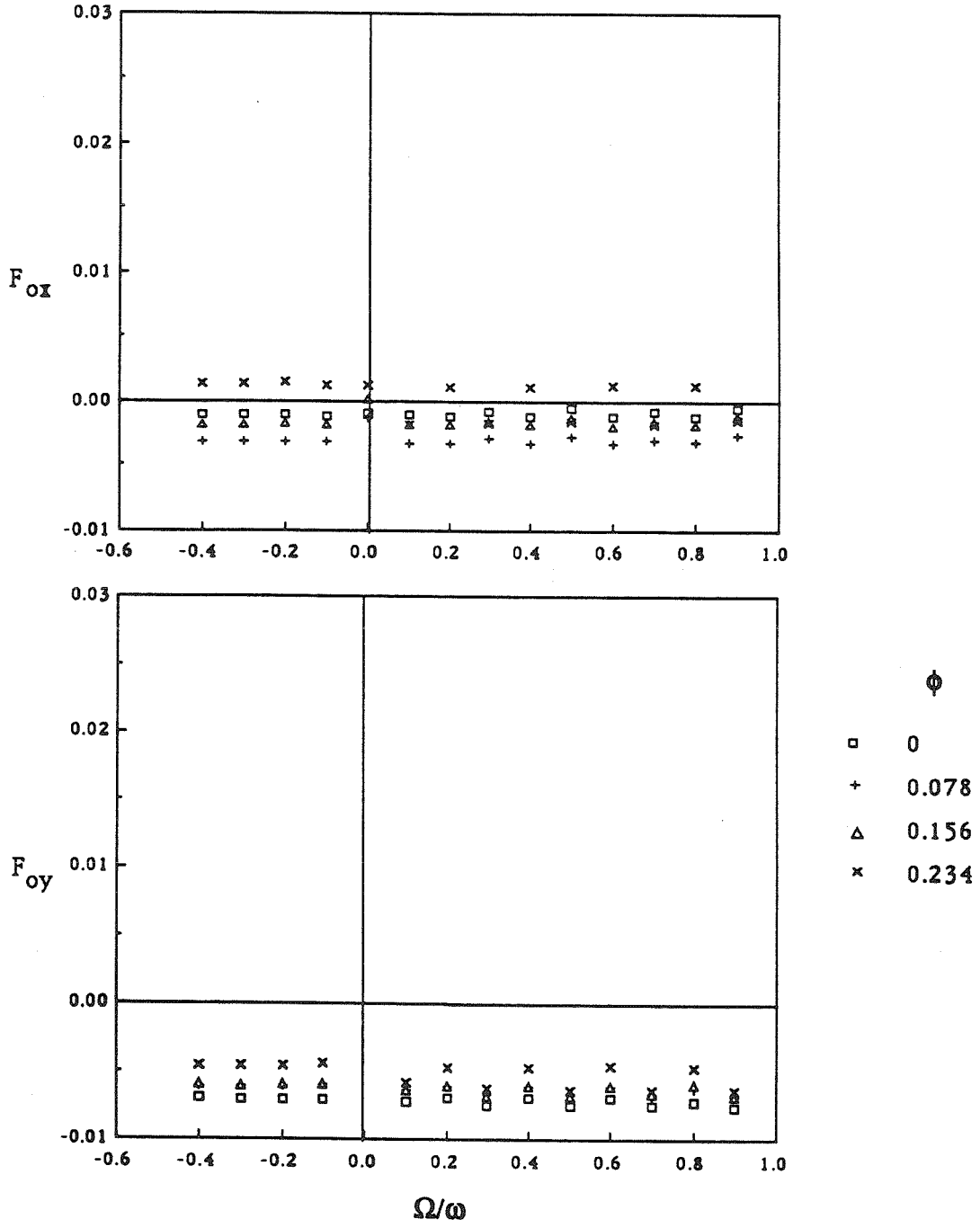

Figure 3.2 Dimensionless steady forces at 1000 RPM, an eccentricity ε = 0.0254 cm, a clearance H = 0.140 cm, offset δ = 0 and various flow rates as follows: 0 ℓ/sec, 0.631 ℓ/sec, 1.262 ℓ/sec, 1.892 ℓ/sec.

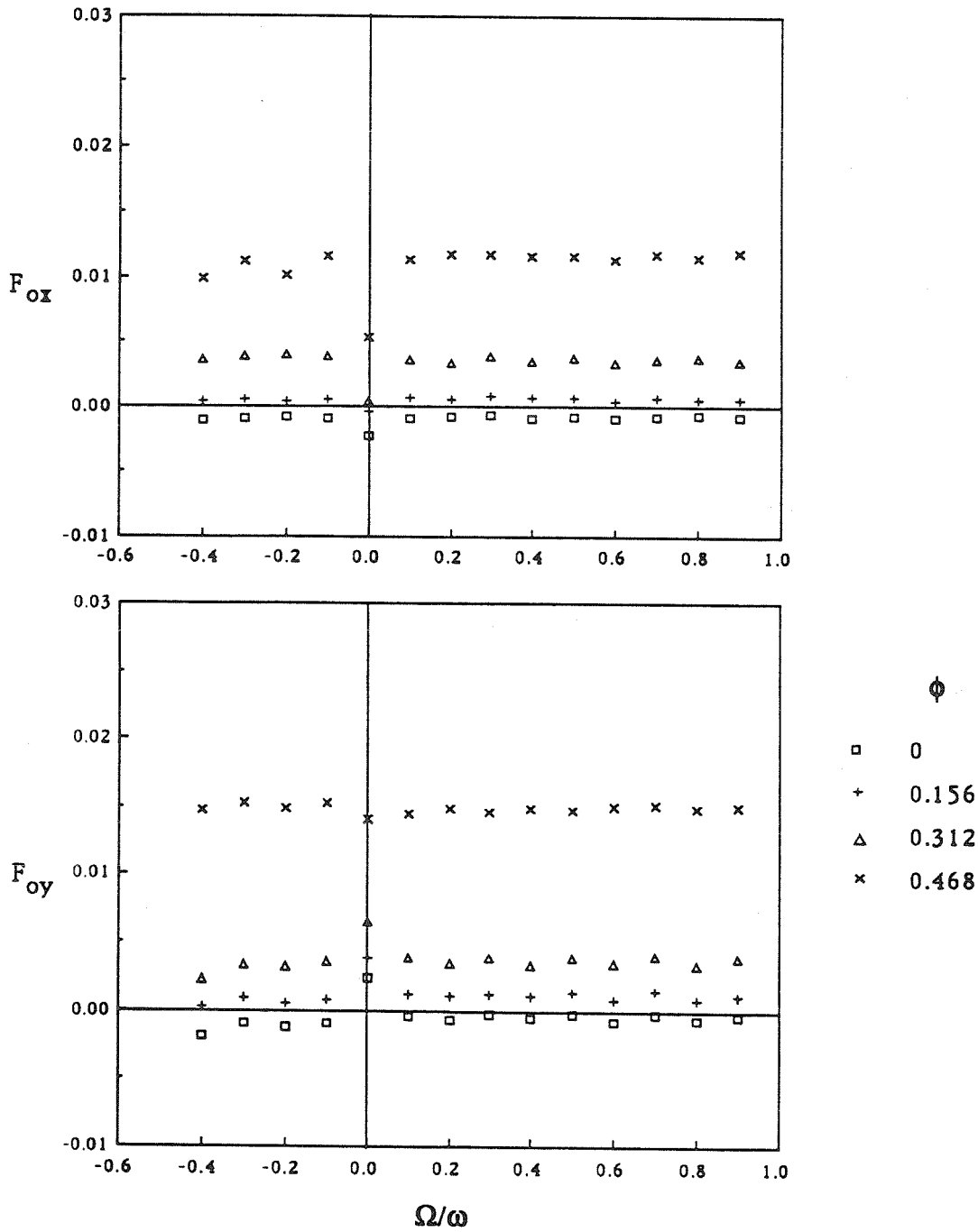

Figure 3.3 Dimensionless steady forces at 500 RPM, an eccentricity ε = 0.0254 cm, a clearance H = 0.140 cm, offset δ = 0 and various flow rates as follows: 0 ℓ/sec, 0.631ℓ/sec, 1.262 ℓ/sec, 1.892ℓ/sec.

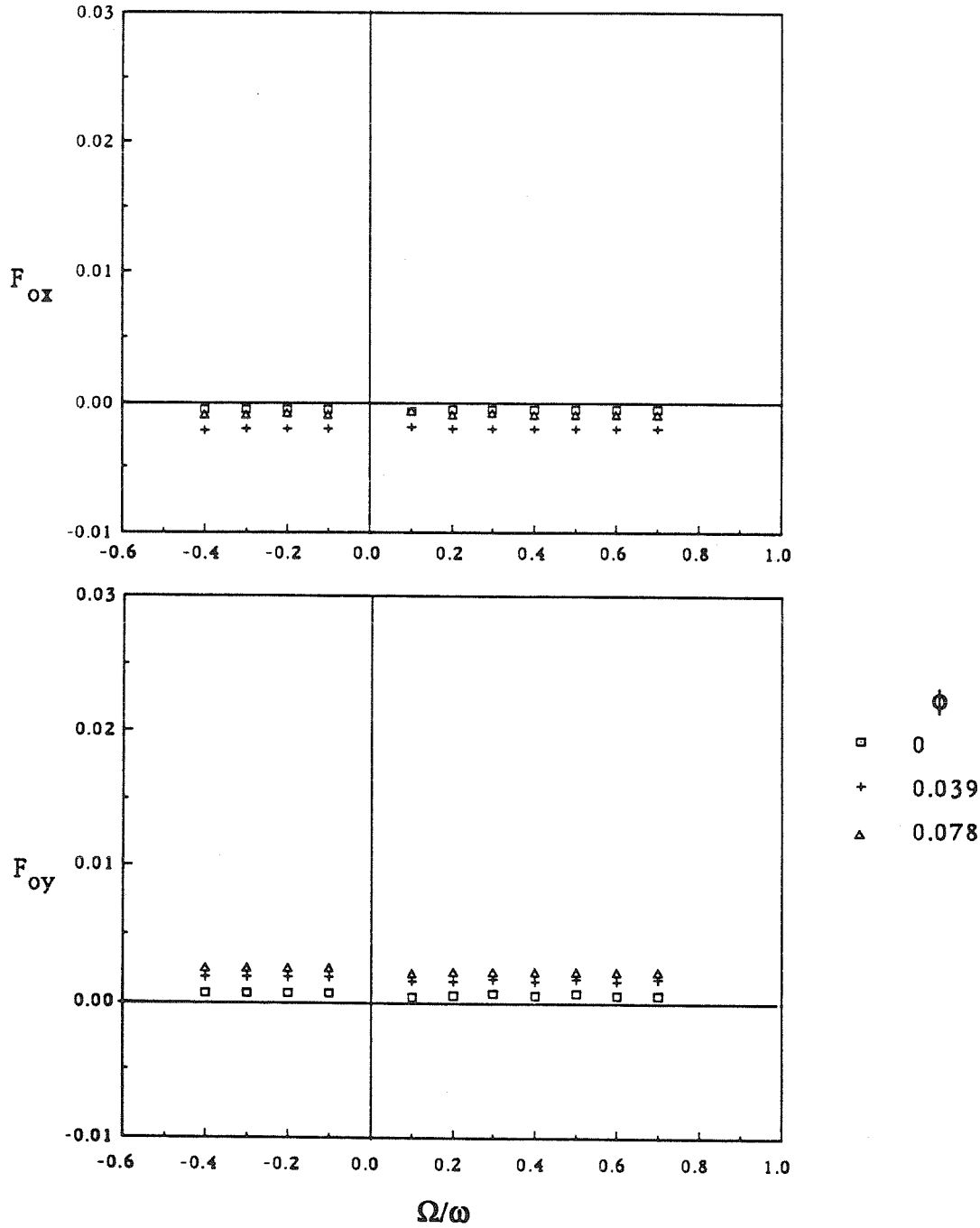

Figure 3.4 Dimensionless steady forces at 2000 RPM, an eccentricity ε = 0.0254 cm, a clearance H = 0.140 cm, offset δ = 0 and various flow rates as follows: 0 ℓ/sec, 0.631 ℓ/sec, 1.262 ℓ/sec.

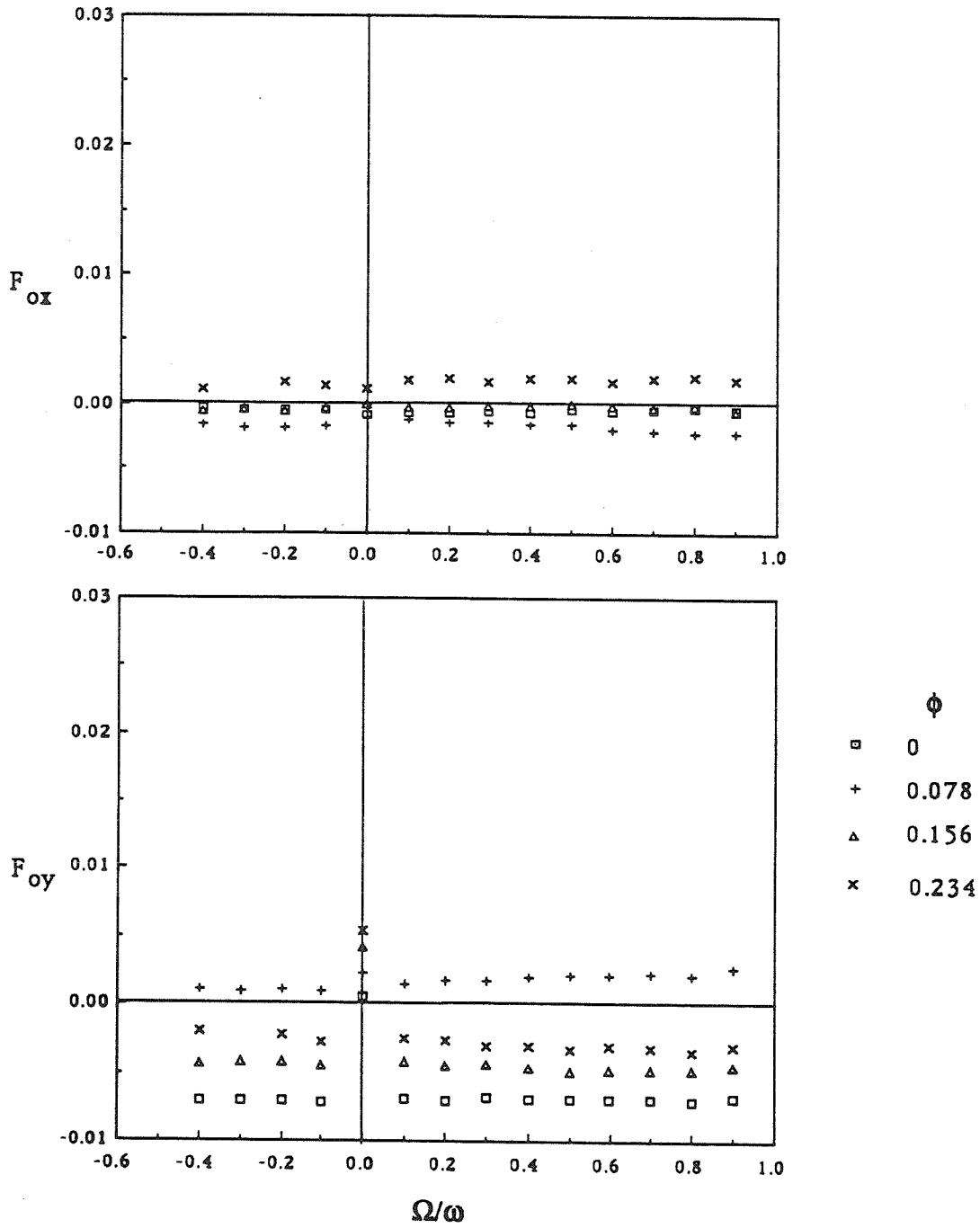

Figure 3.5 Dimensionless steady forces at 1000 RPM, an eccentricity ε = 0.118 cm, a clearance H = 0.140 cm, offset δ = 0 and various flow rates as follows: 0 ℓ/sec, 0.631 ℓ/sec, 1.262 ℓ/sec, 1.892 ℓ/sec. The seal clearance is 0.0508cm.

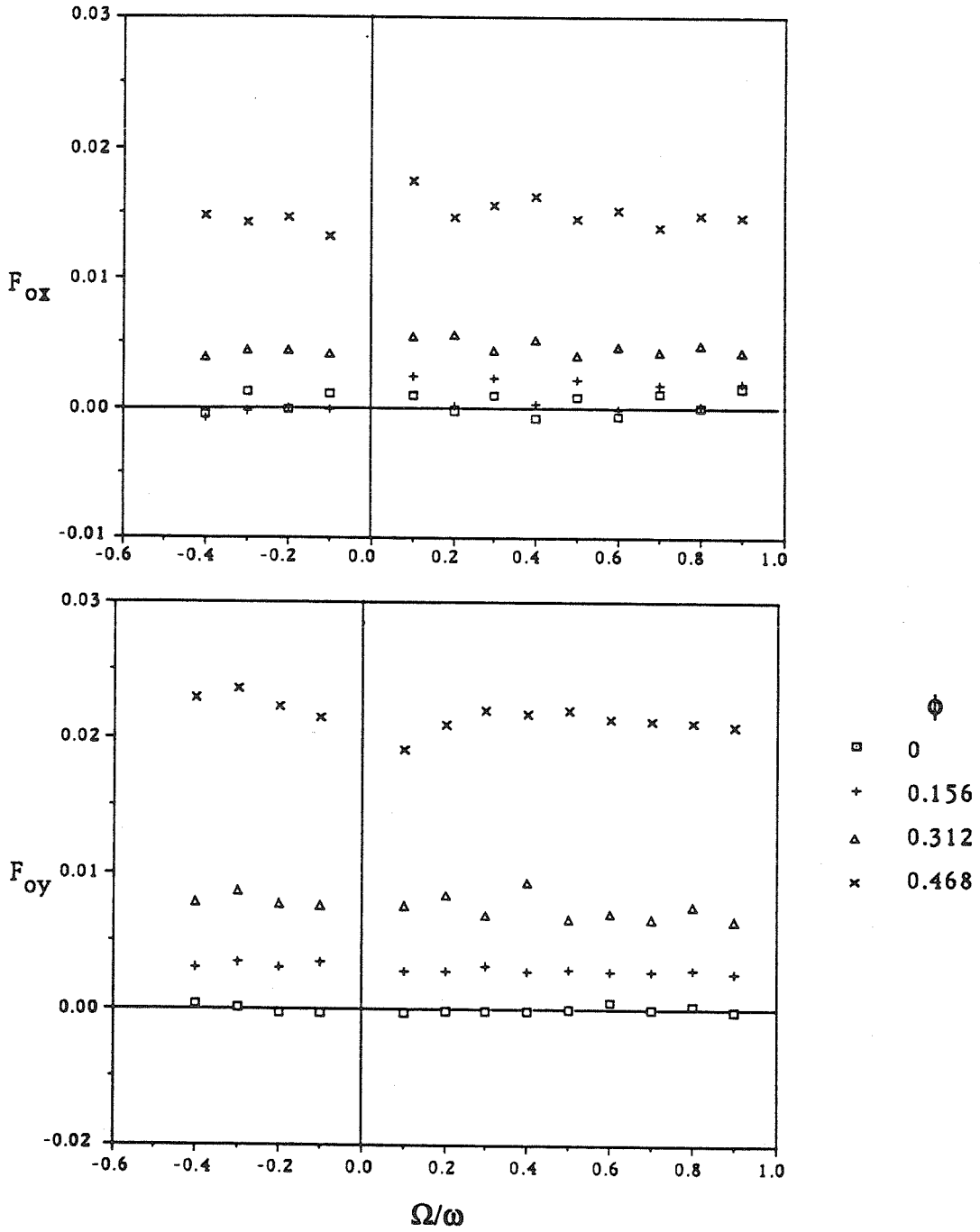

Figure 3.6 Dimensionless steady forces at 500 RPM, an eccentricity ε = 0.118 cm, a clearance H = 0.140 cm, offset δ = 0 and various flow rates as follows: 0 ℓ/sec, 0.631 ℓ/sec, 1.262 ℓ/sec, 1.892 ℓ/sec.

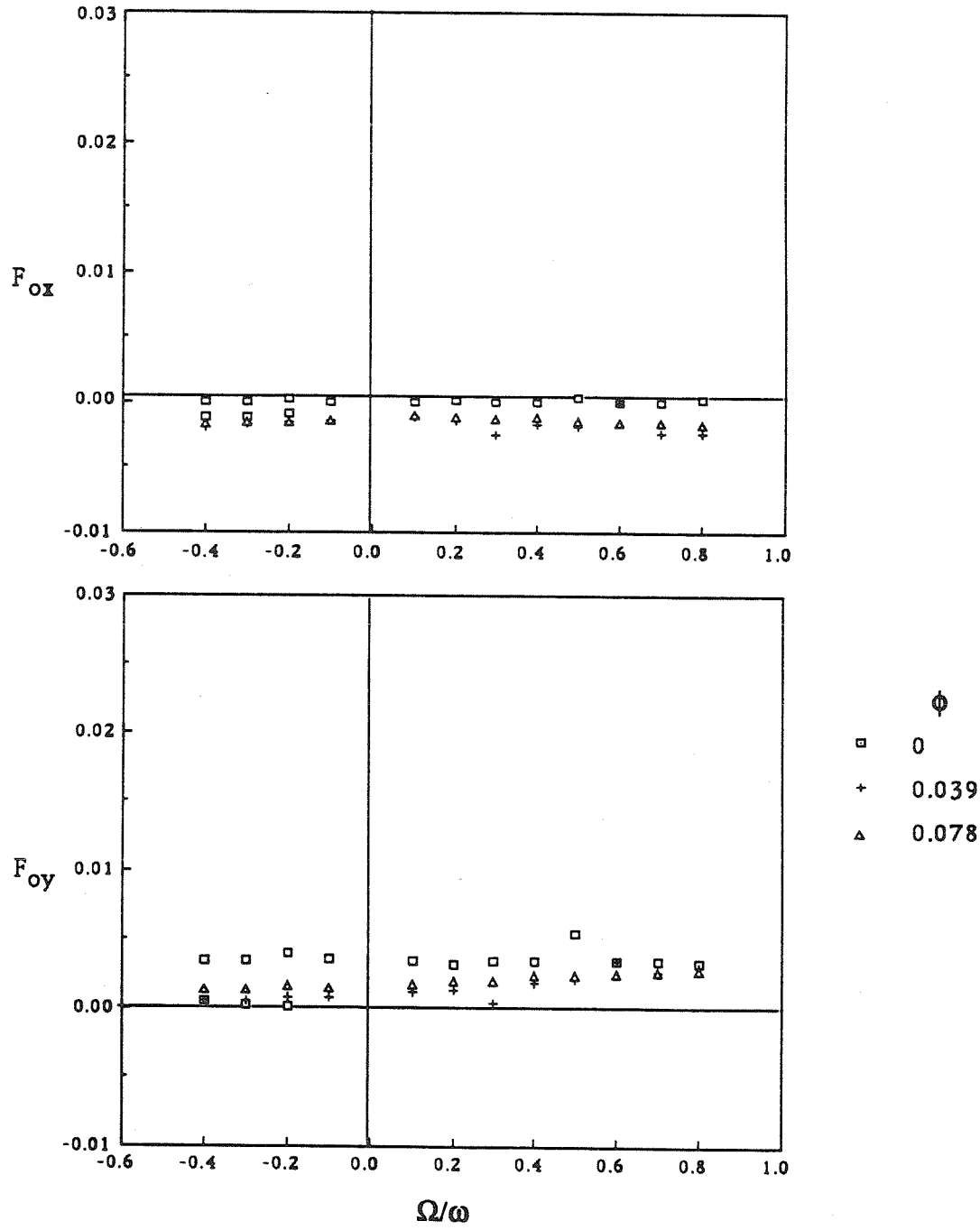

Figure 3.7 Dimensionless steady forces at 2000 RPM, an eccentricity ε = 0.118 cm, a clearance H = 0.140 cm, offset δ = 0 and various flow rates as follows: 0 ℓ/sec, 0.631 ℓ/sec, 1.262 ℓ/sec.

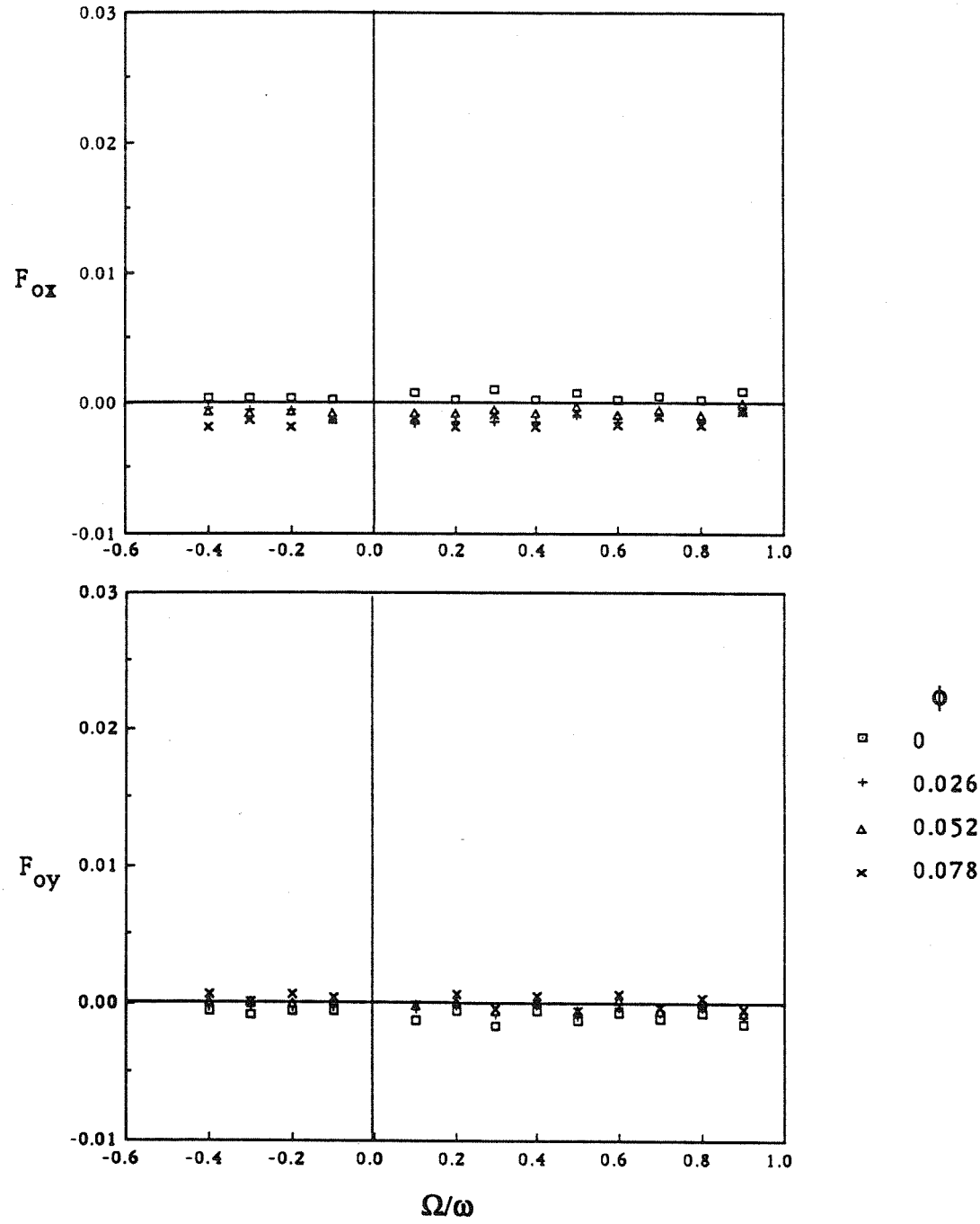

Figure 3.8. Dimensionless steady forces at 1000 RPM, an eccentricity ε = 0.0254 cm, a clearance H = 0.424 cm, offset δ = 0 and various flow rates as follows: 0 ℓ/sec, 0.631 ℓ/sec, 1.262 ℓ/sec, 1.892 ℓ/sec.

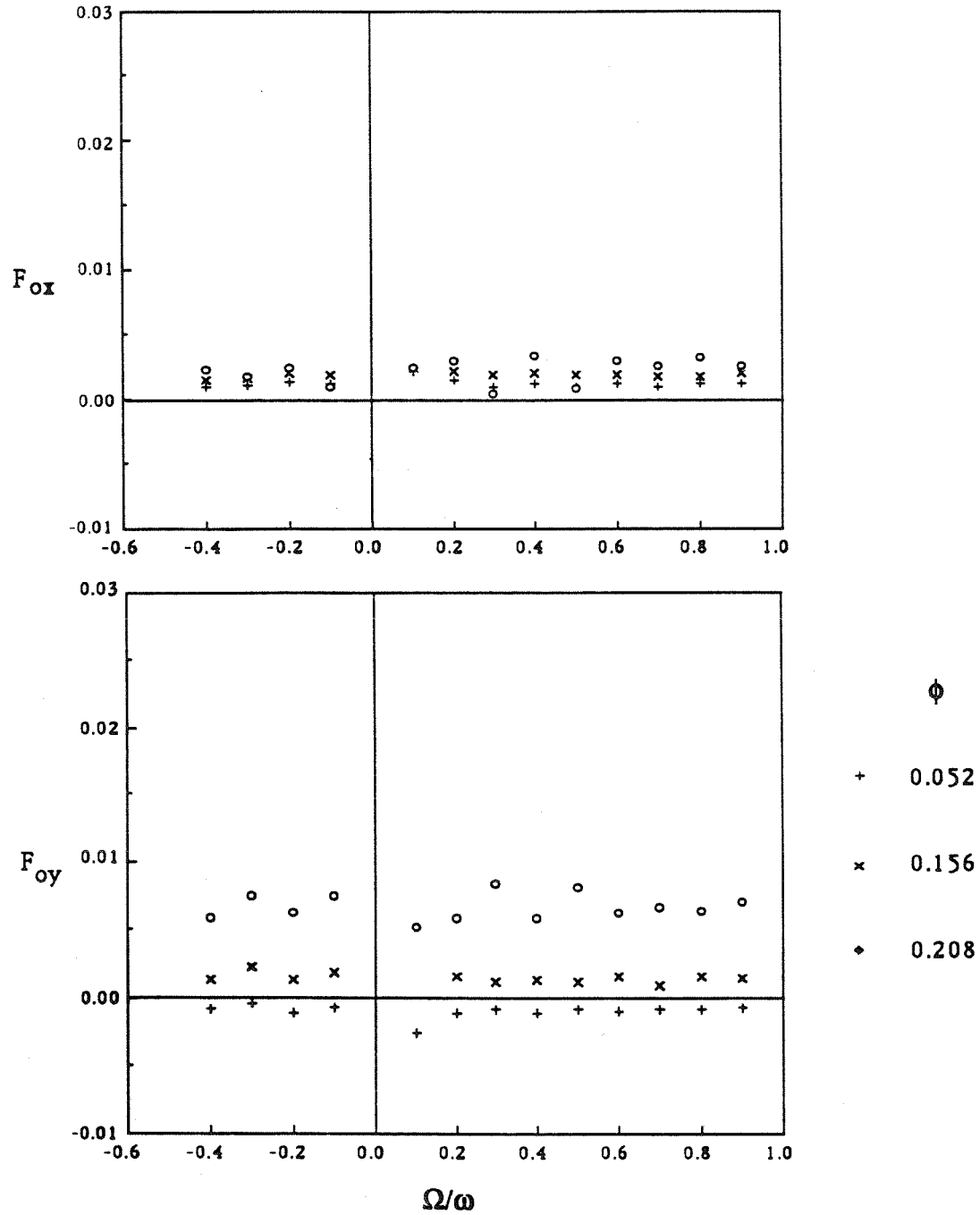

Figure 3.9 Dimensionless steady forces at 500 RPM, an eccentricity ε = 0.118 cm, a clearance H = 0.424 cm, offset d = 0 and various flow rates as follows: 0.631 ℓ/sec, 1.892 ℓ/sec, 3.154 ℓ/sec.

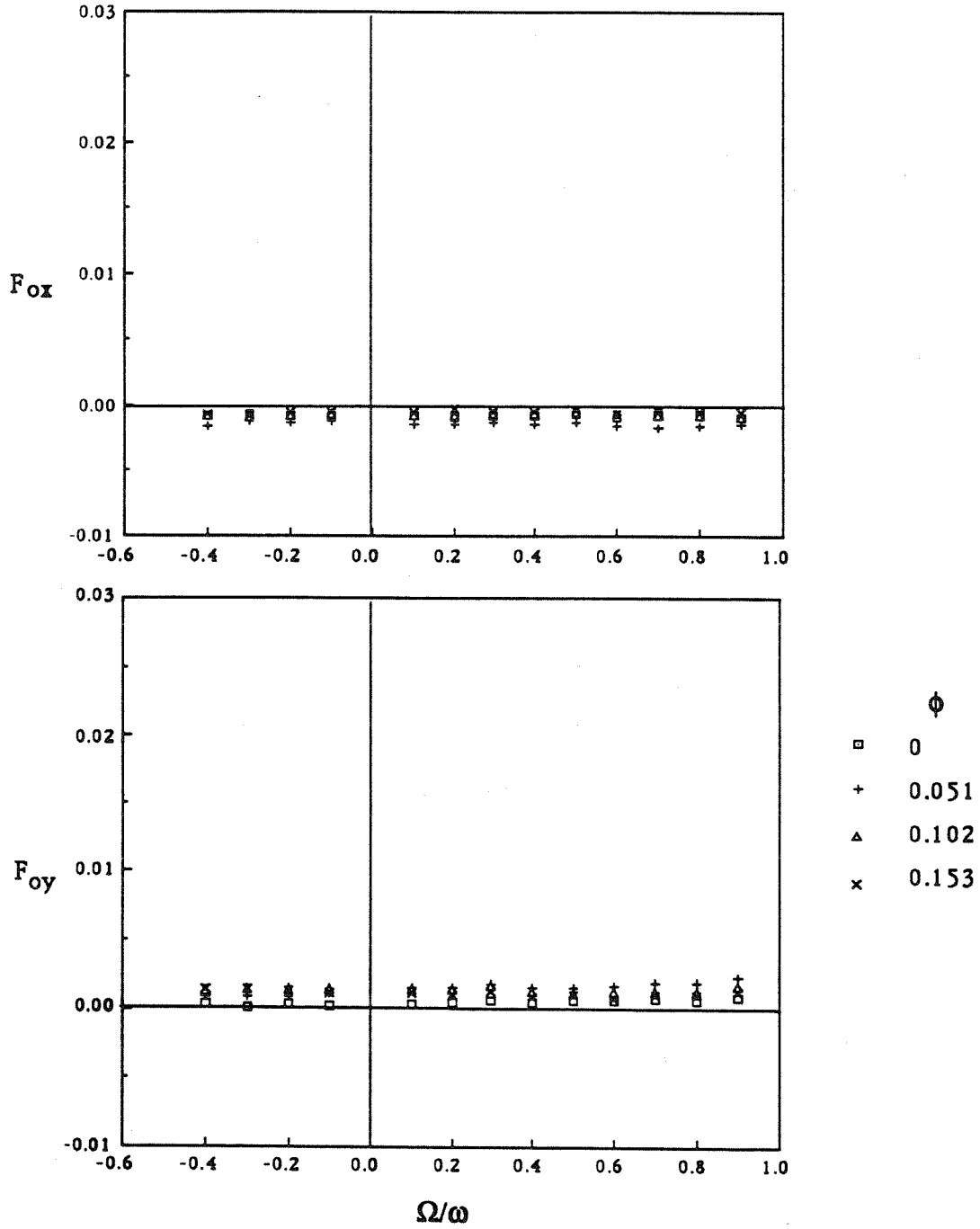

Figure 3.10 Dimensionless steady forces at 1000 RPM, an eccentricity ε = 0.118 cm, a clearance H = 0.212 cm, offset δ = 0 and various flow rates as follows: 0 ℓ/sec, 0.631 ℓ/sec, 1.262 ℓ/sec, 1.892 ℓ/sec.

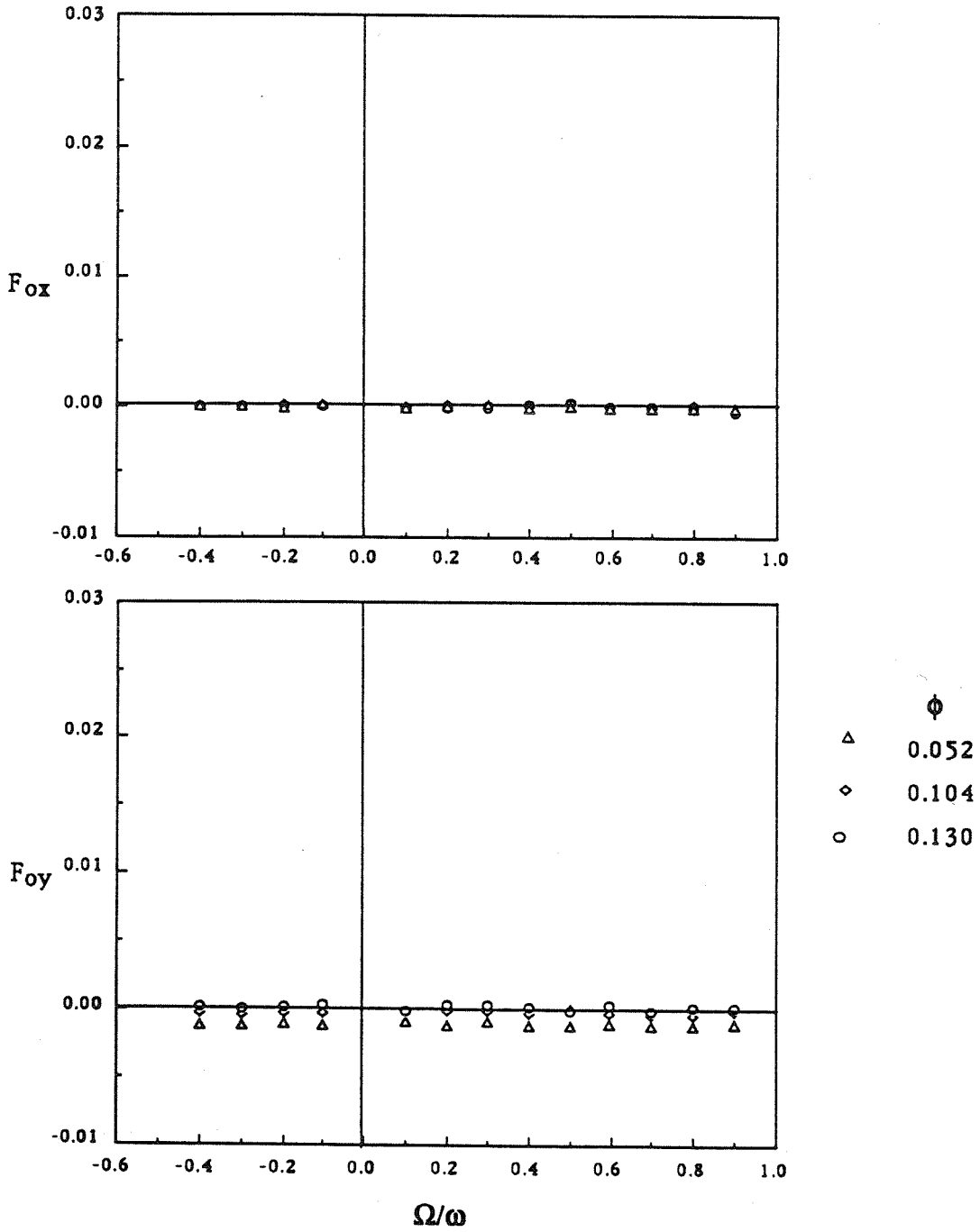

Figure 3.11 Dimensionless steady forces at 1000 RPM, an eccentricity ε = 0.118 cm, a clearance H = 0.424 cm, offset δ = 0 and various flow rates as follows: 1.262 ℓ/sec, 2.524 ℓ/sec, 3.154 ℓ/sec.

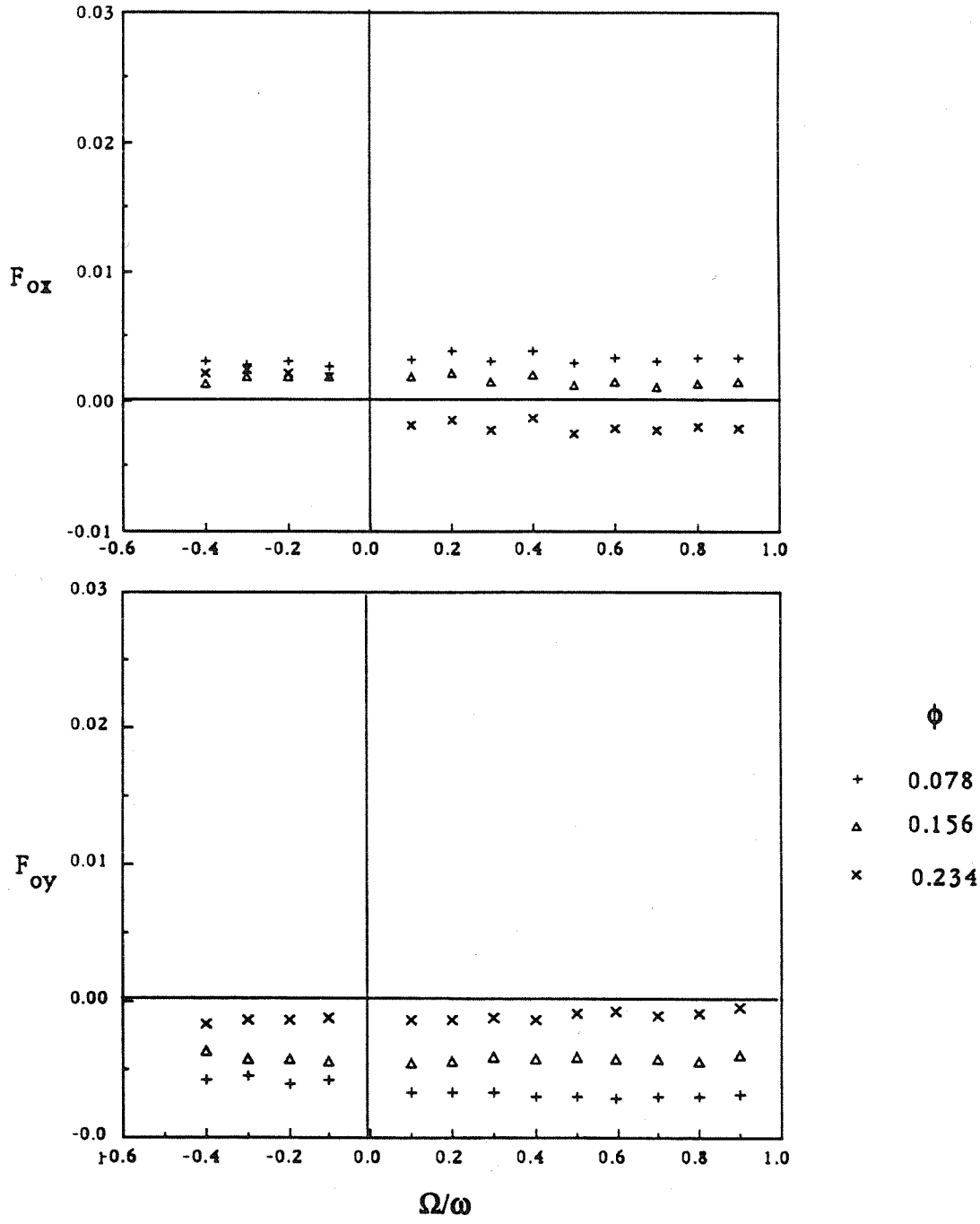

Figure 3.12 Dimensionless steady forces at 1000 RPM, an eccentricity ε = 0.118 cm, a clearance H = 0.140 cm, offset δ = 0 and various flow rates as follows: 0.631 ℓ/sec, 1.262 ℓ/sec, 1.892 ℓ/sec. The seal clearance is tightened to 0.0254cm.

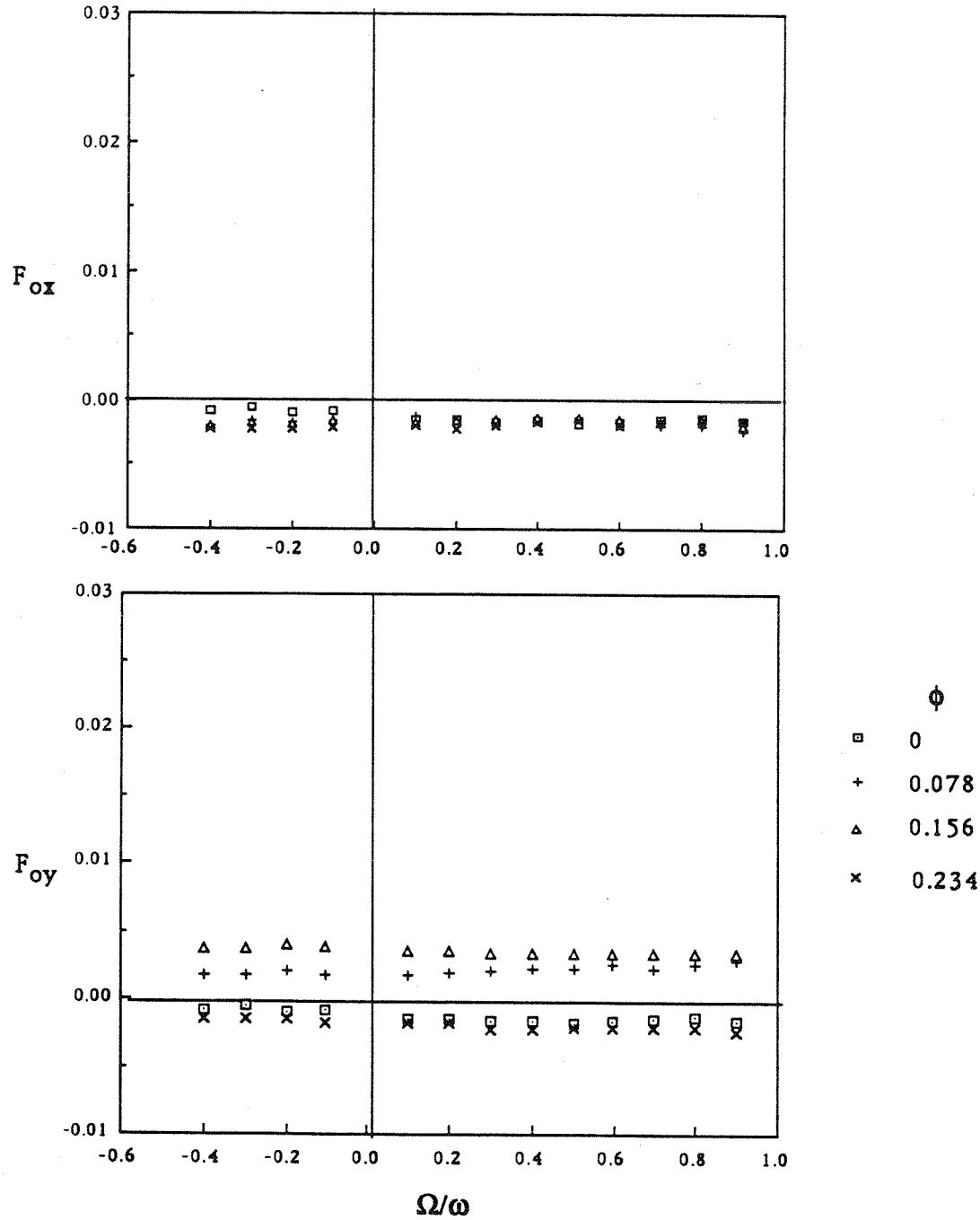

Figure 3.13 Dimensionless steady forces at 1000 RPM, an eccentricity ε = 0.118 cm, a clearance H = 0.140 cm, offset δ = 0 and various flow rates as follows: 0 ℓ/sec, 0.631 ℓ/sec, 1.262ℓ/sec, 1.892 ℓ/sec. The seal clearance is widened to 0.1016cm.

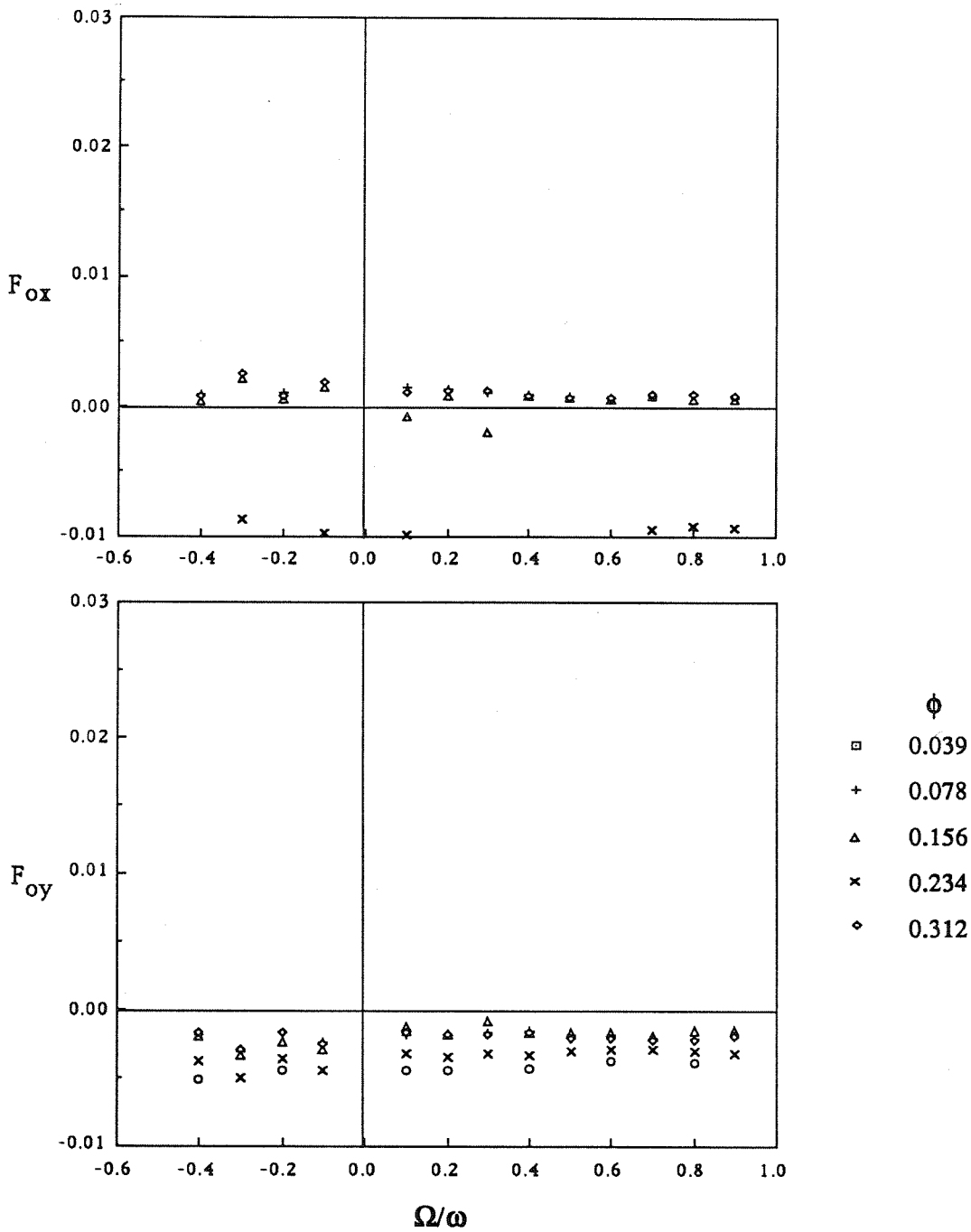

Figure 3.14 Dimensionless steady forces with inlet swirl at 1000 RPM, an eccentricity ε = 0.118 cm, a clearance H = 0.140 cm, offset δ = 0 and various flow rates (and inlet swirl ratios) as follows: 0.315 ℓ/sec (Γ=0.5), 0.631 ℓ/sec (Γ=1.0), 1.262 ℓ/sec (Γ=2.0), 1.892 ℓ/sec (Γ=3.0).

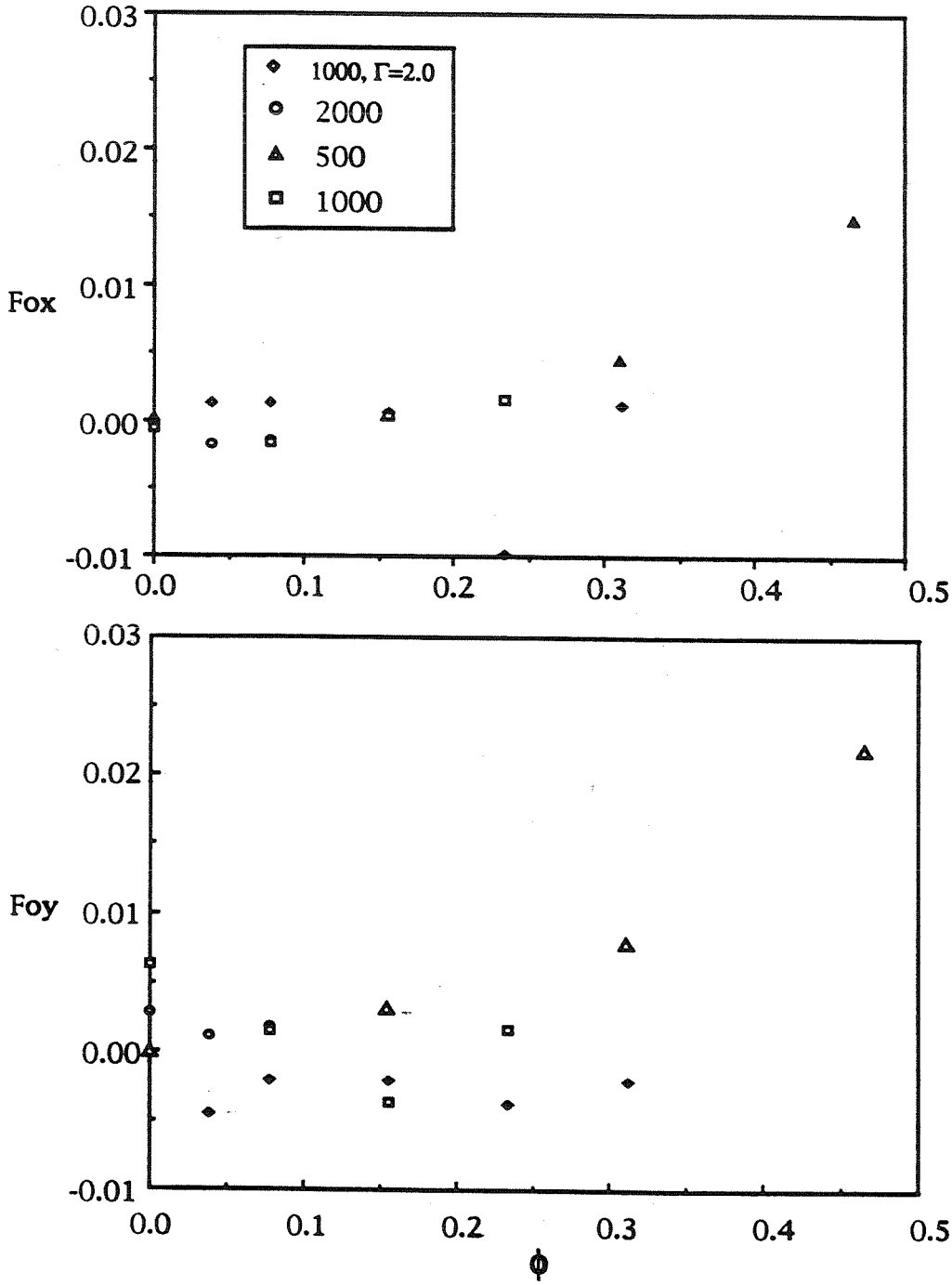

Figure 3.15 Dimensionless steady forces as a function of the flow coefficient at 1000 RPM, an eccentricity ε = 0.118 cm, a clearance H = 0.140 cm, offset δ = O and a seal clearance of 0.051 cm.

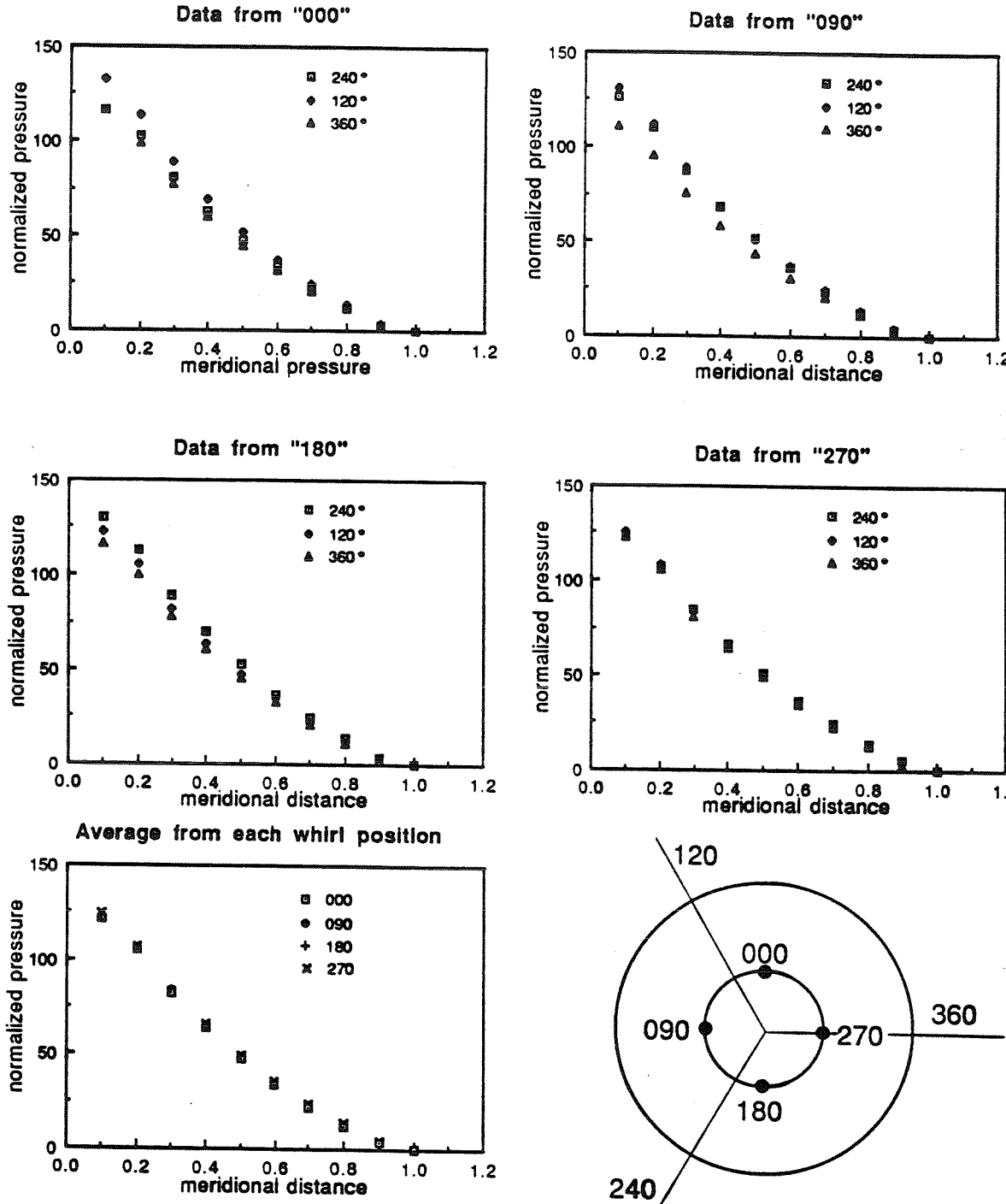

Figure 3.16 Pressure distribution along the shroud for different whirl positions at 1000 RPM, a flow of 10 GPM, an eccentricity $\varepsilon = 0.0254$ cm, a clearance H = 0.140 cm, offset δ = O and a seal clearance of 0.051 cm. The measurements are from each set of pressure taps along the meridional direction and are 120° apart.

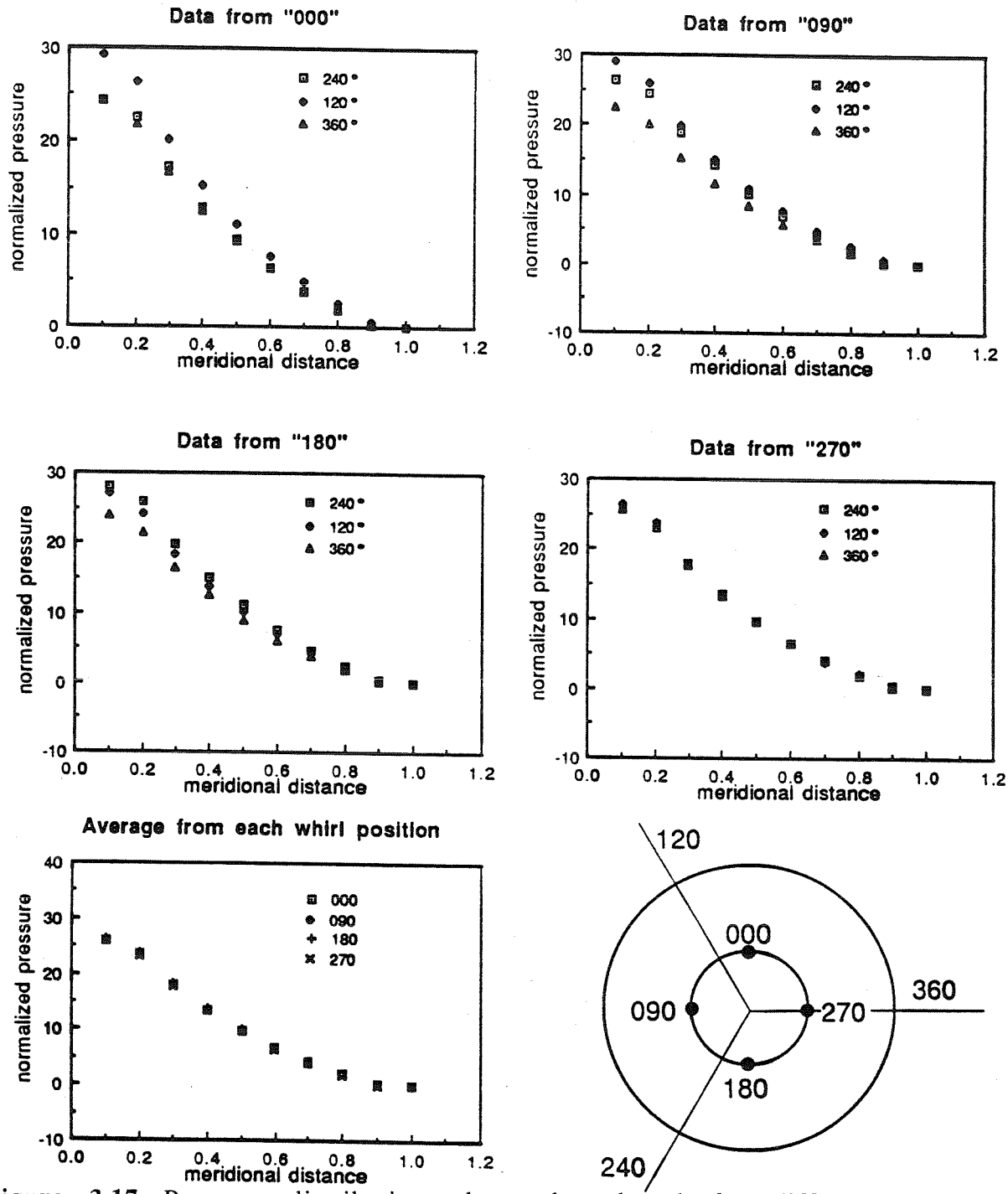

Figure 3.17 Pressure distribution along the shroud for different whirl positions at 1000 RPM, a flow of 20 GPM, an eccentricity $\varepsilon = 0.0254$ cm, a clearance H = 0.140 cm, offset δ = O and a seal clearance of 0.051 cm. The measurements are from each set of pressure taps along the meridional direction and are 120° apart.

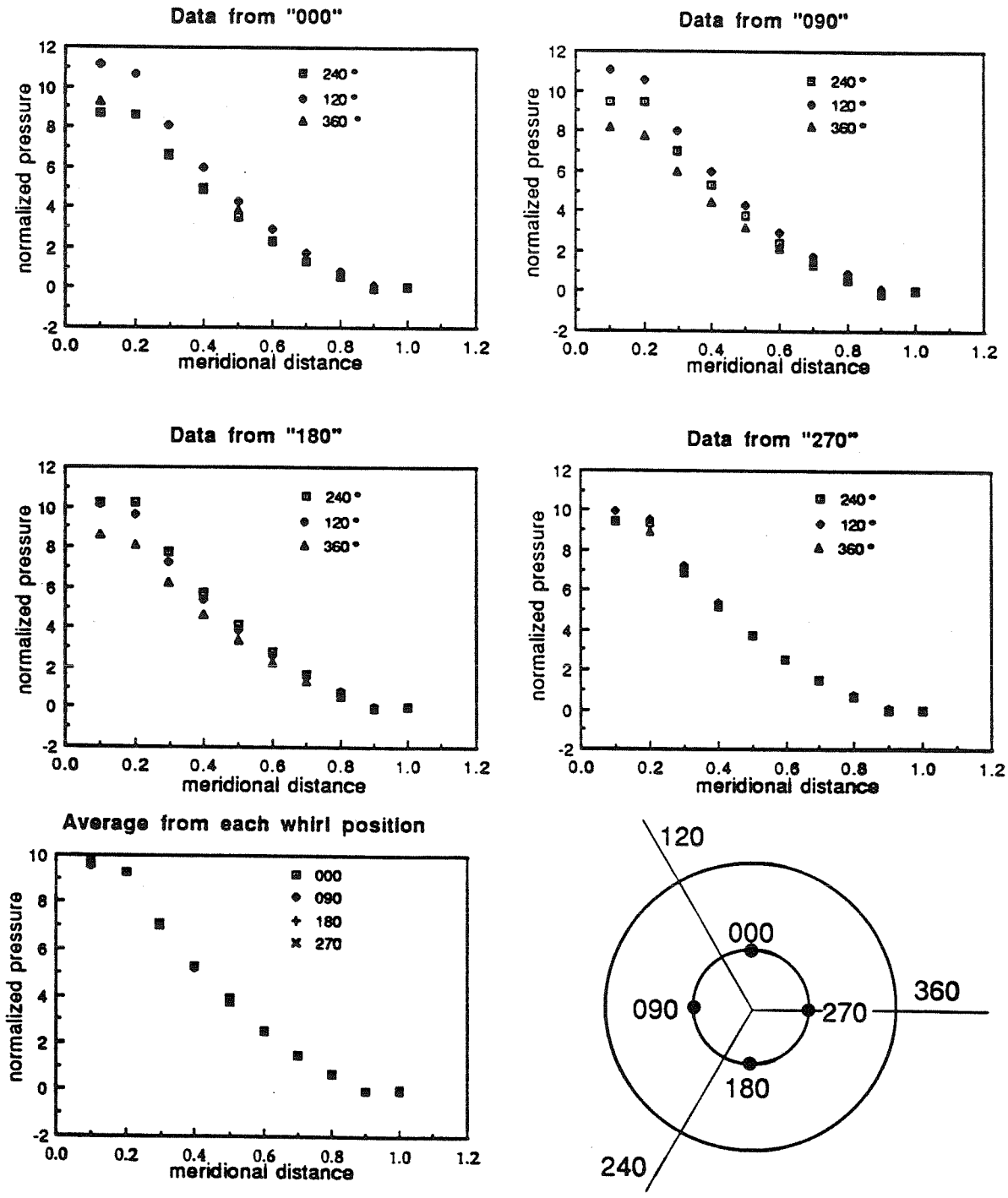

Figure 3.18 Pressure distribution along the shroud for different whirl positions at 1000 RPM, a flow of 30 GPM, an eccentricity $\varepsilon = 0.0254$ cm, a clearance H = 0.140 cm, offset δ = O and a seal clearance of 0.051 cm. The measurements are from each set of pressure taps along the meridional direction and are 120° apart.

CHAPTER 4

EXPERIMENTAL RESULTS FOR ROTORDYNAMIC FORCES

4.1 Force measurements with whirl

In this chapter, the rotordynamic results from the force balance measurements will be described. Recall that the normal force is in the direction normal to the whirl orbit and the tangential force is in the direction of eccentric motion. The unsteady forces F_n and F_t will be presented as functions of the whirl ratio or ratio of whirl frequency, Ω to rotating frequency, ω. Other dimensionless parameters are the flow coefficient, ϕ (= $Q/2\pi\omega R_2{}^2H$, where Q is the leakage flow rate); the shroud clearance ratio, H/R_2; the eccentricity ratio, ε/R_2; the Reynolds number based on the leakage velocity $Q/2\pi R_2\nu$; and the Reynolds number based on tip speed $\omega R_2{}^2/\nu$, where ν is the kinematic viscosity of the liquid.

4.2 General effects

The results are presented for different rotating speeds of 500, 1000, 2000 RPM, for different leakage flow rates (zero to 50 GPM), three different clearances, H, and two eccentricities, ε. The data is first presented for inlet swirl velocity ratios which are close to zero. Subsequent tests explore the effect of this parameter by installation of an inlet guide vane.

Note that the general form and magnitude of the data shown in figures 4.1 through 4.13 is very similar to that obtained for impellers by Jery (1986) and Adkins (1986) and to that from Childs' model in the absence of the "resonance." The parabolic shape of the normal force may be attributed to the added mass of the fluid. From the experiments performed, the tangential force is positive for small positive whirl ratios and thus destabilizing.

Figure 4.1 shows the components of the generalized hydrodynamic force matrix that result when the impeller whirls in an eccentric orbit of 0.0254cm, at 1000 RPM, and a clearance of 0.140 cm. Figures 4.2 and 4.3 are for the same

conditions as figure 4.1 except that the rotor speeds are 500 RPM and 2000 RPM respectively. Earlier, Jery (1986) showed that the nondimensionalized unsteady forces were independent of the rotor speed. Clearly, this comparison must be made by examining like flow coefficients. The trends with flow coefficient will be investigated further in chapter 5. However, it is already evident from these three figures that the features of these results are very similar.

Since the data of figures 4.1 and 4.4 were obtained under conditions which were the same except for the magnitude of the eccentricity, ε, it is reassuring to note the similarity between the two sets of data. Evidently these experiments lie within the linear regime of small eccentricities (note that the assumption of linearity was implicit in equation 1.1). Figures 4.5 and 4.6 are for the same conditions as figure 4.4 except that the rotor speeds are 500 RPM and 2000 RPM respectively. Thus, figure 4.5 and figure 4.2 also, only differ in the magnitude of the eccentricity. In a similar way, figure 4.6 and figure 4.3 only differ in the magnitude of the eccentricity. Consequently, it was possible to validify that the experiments were conducted in the linear regime of eccentricity for the three rotor speeds. Another reason for this apparent duplication of data is that this allows a wider range of flow coefficients to be investigated further in chapter 5.

Nguyen and Nelson (1988) developed a solution procedure for annular seals with what they term eccentricity of the seal. In the present research, this is termed the offset δ of the rotor, though it can also be viewed as an eccentricity at zero whirl frequency. They compared the results to the experimental data of Falco et al. (1984). The most important results of this study were that for small offsets ($\delta/H<0.3$), no effect was discerned on the rotordynamic coefficients. At larger offsets, the cross-coupled stiffness, k, and direct damping, C, increased with offset. The ratio of these two, k/C, is called the whirl ratio which provides a measure of the stabilizing effect on the rotor. In the present research there was zero offset; however, earlier work of Zhuang (1989) investigated the effect of an offset of the rotor which purely rotates about its own center (no whirl). In that work, the hydrodynamic forces were also found to increase nonlinearly with eccentricity. Two explanations for this apparent discrepancy can be given. Firstly, the clearance ratio, H/R was much larger than that used

in the present work where the experiments were shown to be in the linear regime of eccentricity. In addition, the forces for the larger clearance are smaller, so the variation with eccentricity is within the range of scatter.

It should also be noted that the forces are strong functions of both the leakage flow rate and the clearance, H. In the case represented by figure 4.7 the combination of small eccentricity and large clearance led to forces whose magnitudes were rather small and hence the larger scatter in the data presented in that figure. This is true for figure 4.8 where a small rotor speed and large clearance lead to small forces. Data was taken for this case so that a greater range of flow rates could be investigated in chapter 5.

In the figures which have been presented thus far, the effect of flow rate on the normal force is clearer than its effect on the tangential force. Clearly the Bernoulli effect (described in chapter 1) on the normal force increases with increasing flow at both positive and negative whirl ratios. It would also appear that the positive tangential forces at small positive whirl ratios are smallest at the highest flow rate and therefore increasing the flow is marginally stabilizing. The effect of increasing shroud clearance can be seen by comparing figures 4.4, 4.9, 4.10. The data of figure 4.9 was taken under the same conditions as the data of figure 4.4, namely 1000 RPM and an eccentricity of 0.118cm, but at a larger clearance of 0.212 cm. Figure 4.10 is for an even larger clearance of 0.424 cm. Thus, the effect of the clearance is much larger and it seems that all the forces are roughly inversely proportional to the clearance, H. Qualitatively, this can be explained as follows. For the same eccentricity and two different clearances, the smaller clearance generates larger perturbations in the flow which accentuate the acceleration in the fluid and increase the pressure differences.

From the point of view of rotordynamics, the unsteady tangential force F_t is usually of greater importance than the normal force, F_n. A tangential force in the direction of whirl motion will encourage the motion and is therefore destabilizing. There exists such a region for subsynchronous whirl, where Ft is positive at small positive whirl ratios. For negative whirl ratios, the force is positive and therefore stabilizing. It should be noted that the F_t is complicated and changes sign more than once for the no flow case. This is particularly

noticeable in figures 4.7 and 4.8, however it should also be noted that these experiments were taken under conditions which produced small forces and therefore large scatter. Similar behavior has been observed by Jery et al. (1985) on a centrifugal pump. The nondimensional force coefficients presented by Childs (1986) also show unexpected negative troughs in the radial force coefficients and positive peaks in the tangential force coefficients, which Childs describes as "resonance" of the leakage flow.

It is interesting to compare the magnitudes of the forces with previous results obtained for a real centrifugal impeller in the same facility. The data for Franz et al. (1989) on a Byron Jackson centrifugal pump was obtained with an eccentricity of 1.25 mm which is significantly larger than the present value of 0.254mm. Thus, it is appropriate to compare the "stiffnesses" F_n^*/ε and F_t^*/ε. At zero whirl ratio the present data for the clearances of 1.40 mm (and 4.24mm), yields values of 2.8 KN/m (and 0.46 KN/m) and 7.6 KN/m (and 1.88 KN/m) respectively compared to 6.8 KN/m and 2.28 KN/m for the data of Franz et al. (1989). Though the geometries of the leakage pathways are quite different this still suggests that the contribution of the shroud leakage flow to the rotordynamic forces may be substantial.

Adkins and Brennen (1988) attempted to separately evaluate the rotordynamic forces on the discharge and on the shroud of a centrifugal pump. Chamieh et al. (1985) had earlier measured the total rotordynamic force on a particular impeller/volute combination and obtained values of 6.0 KN/m and 2.7 KN/m for F_n^*/ε and F_t^*/ε at zero whirl ratio. Adkins and Brennen (1988) substantially increased the size of the gap external to the shroud for this impeller/volute combination and obtained altered values of 4.8 KN/m and 0.9 KN/m for F_n^*/ε and F_t^*/ε. This reduction implied a significant contribution from the shroud forces. Although the difference between the two leakage flow measurements is of the same order of magnitude as the present results, the geometries of the leakage flows are quite different.

4.3 Seal clearance effects

It is important to account for the effect of changing seal clearance such as would occur as a result of wear. To model these losses, an adjustable seal ring

was used (figure 2.2). The measurements presented thus far in figures 4.1 through 4.10 were for a face seal clearance of 0.051 cm. The effect of changing seal clearance is presented in figures 4.11 and figure 4.12, obtained with seal clearances of 0.1016cm and 0.0254cm respectively. Except for the seal clearance these measurements are taken under the same conditions as the measurement of figure 4.4. The smaller seal clearance exhibits a larger normal force and the tangential force is smaller, which therefore decreases the range of destabilization. In other words, the range of positive whirl ratios for which the tangential force is positive is decreased. While the results of Jery et al. (1985) on a centrifugal pump did not show any influence of the seal clearance, it should be noted that in that experiment there were several contributions. It is therefore reasonable to assume that the effect of the seal was perhaps small compared with the other effects.

4.4 Inlet swirl effects

In this section, the effects of inlet swirl velocity will be examined. In the absence of an inlet swirl vane, the swirl added to the leakage path by the incoming jet from the inlet pipe to the large cast iron test-section will be estimated as follows. The angular velocity with which the incoming jet sets the bulk of the fluid in motion is obtained purely from considerations of the location of the incoming jet with respect to the position of the shroud and was found to be at most one tenth that of the shaft speed for a shaft speed of 1000RPM and a leakage flow of 10 GPM. This ratio, the ratio of the tangential velocity of the incoming fluid to the rotor velocity, is of course the inlet swirl ratio and is clearly not a substantial quantity. Since one of the goals of this research was to investigate the effect of swirl on the results, an inlet guide vane was placed to add swirl to the inlet of the leakage path. The geometry of this vane is described in section 2.2.

Figure 4.13 shows data taken for a wide range of swirl conditions. This set can be compared with the data obtained for figure 4.4. Note that increasing the flow coefficient in figure 4.13 also increases the swirl ratio.

Figure 4.14 compares data without swirl at a flow coefficient of $\phi = 0.078$ to data with swirl ($\Gamma = 1.0$). Figure 4.15 shows the data at a higher flow coefficient

of $\phi = 0.156$ and since the same inlet guide vane was used, the swirl ratio in this set is higher ($\Gamma=2.0$). From both figure 4.14 and 4.15, it can be seen that the effect of swirl is to increase the tangential force and hence to increase the range of whirl ratios for which there is a potentially destabilizing force. Swirl also seems to increase the normal force at positive whirl. Figure 4.13 shows the tangential force decreasing as the flow coefficient increases. However, it should be noted that the flow coefficient is coupled to the swirl; therefore the swirl increases with the flow coefficient. For the normal force, an increase occurs with increased flow coefficient and hence swirl. So for the tangential force, the effects of flow and swirl seem to act in competition, while for the normal force the two effects act in competition at least for positive whirl ratios. Clearly it would be interesting to examine the case where flow is increasing and the swirl is fixed. This would require construction of additional inlet guides.

Figure 4.16 shows the same effect as 4.14, while figure 4.17 is similar to figure 4.15. The latter figures are taken at a lower eccentricity. If there is whirl induced resonance, then definite peaks are expected. However, none of the figures demonstrated this effect.

In the following section, the Reynolds number effect is investigated by looking at the results as a function of the flow coefficient. Figures 4.18 and 4.19 begin this process by looking at different experimental conditions for the same flow coefficient. In the earlier work of Zhuang (1989), the normal and tangential forces were seen to decrease slightly as the Reynolds number $Re_\omega = \omega R_2^2/\nu$ increased. Those experiments were performed for no flow conditions. In both examples presented in figures 4.18 and 4.19, wherein the flow coefficient is kept constant, the results do not change substantially as Re_ω increases. In figure 4.18, the higher Reynolds number case does show higher forces for both the tangential and normal force. However, for the higher flow coefficient (figure 4.19), no clear conclusion can be made regarding the tangential force. The results of Jery (1986) on a centrifugal pump were not affected by the Reynolds number. However, the clearance between the front shroud of the impeller and the casing in that experiment was large. In the present experiment, since the clearance is small, viscous effects are expected to occur.

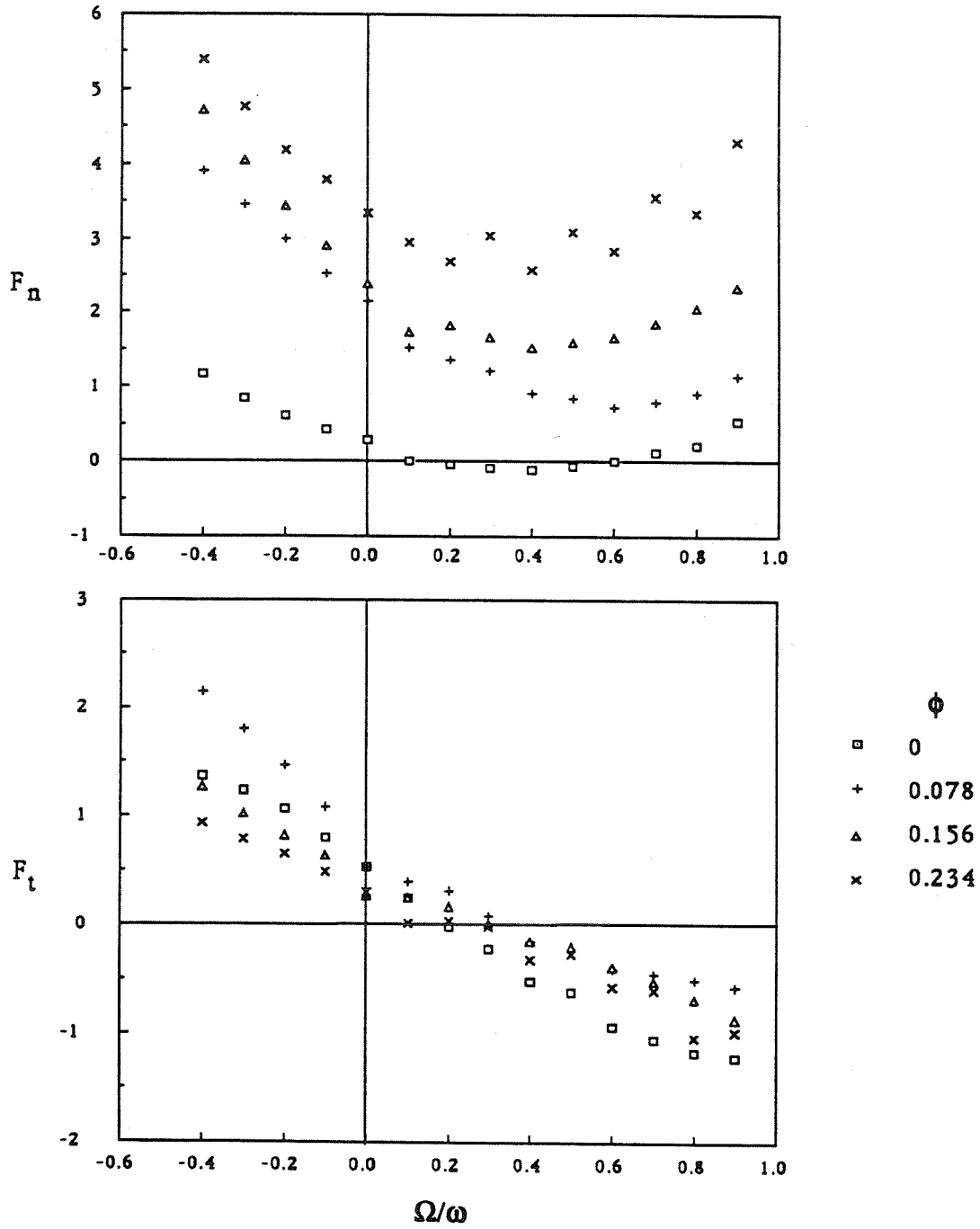

Figure 4.1 Dimensionless normal and tangential forces at 1000 RPM, an eccentricity ε = 0.0254 cm, a clearance H = 0.140 cm, offset δ = 0 and various flow rates as follows: 0 ℓ/sec, 0.631 ℓ/sec, 1.262 ℓ/sec, 1.892 ℓ/sec.

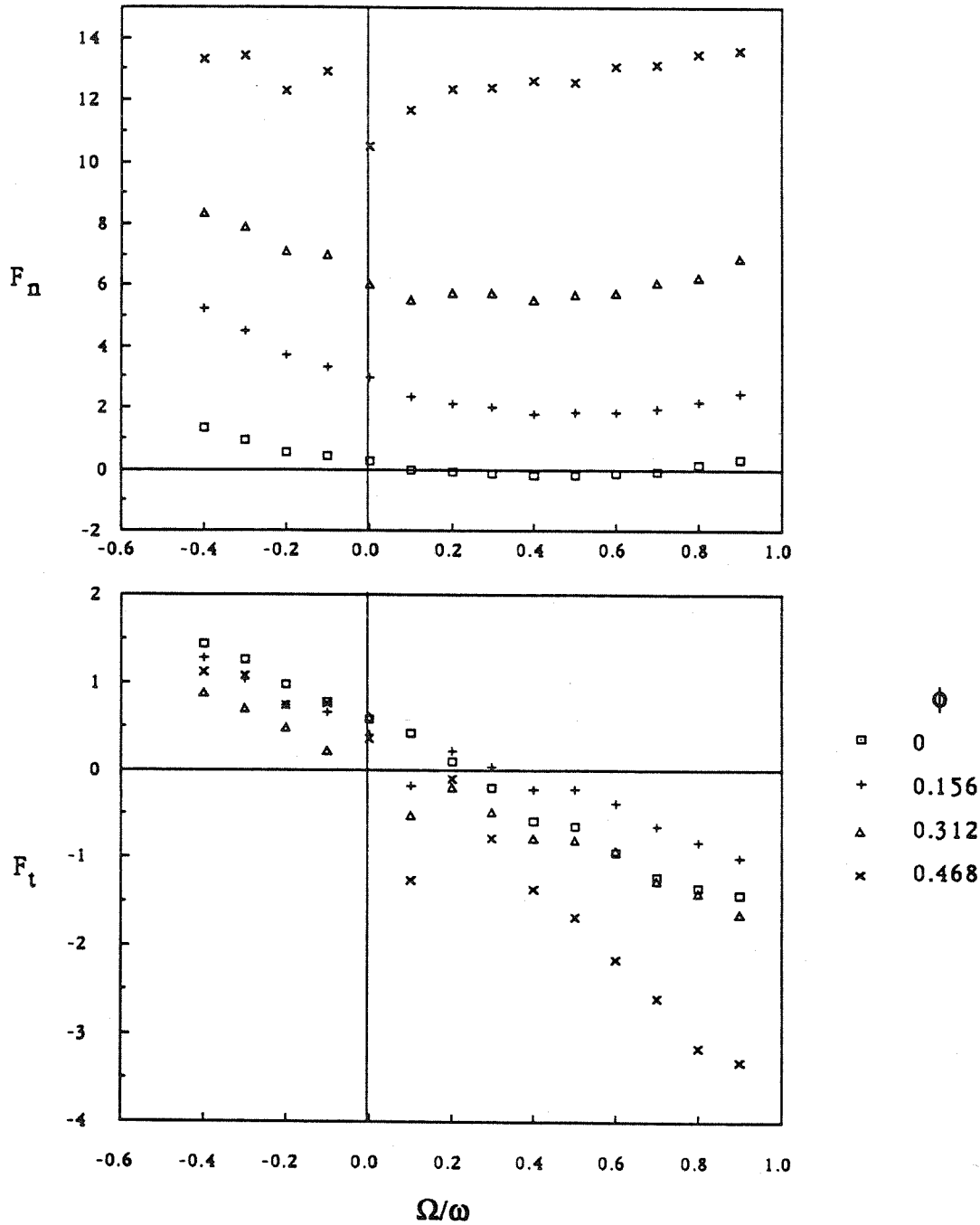

Figure 4.2 Dimensionless normal and tangential forces at 500 RPM, an eccentricity ε = 0.0254 cm, a clearance H = 0.140 cm, offset δ = 0 and various flow rates as follows: 0 ℓ/sec, 0.631 ℓ/sec, 1.262 ℓ/sec, 1.892 ℓ/sec.

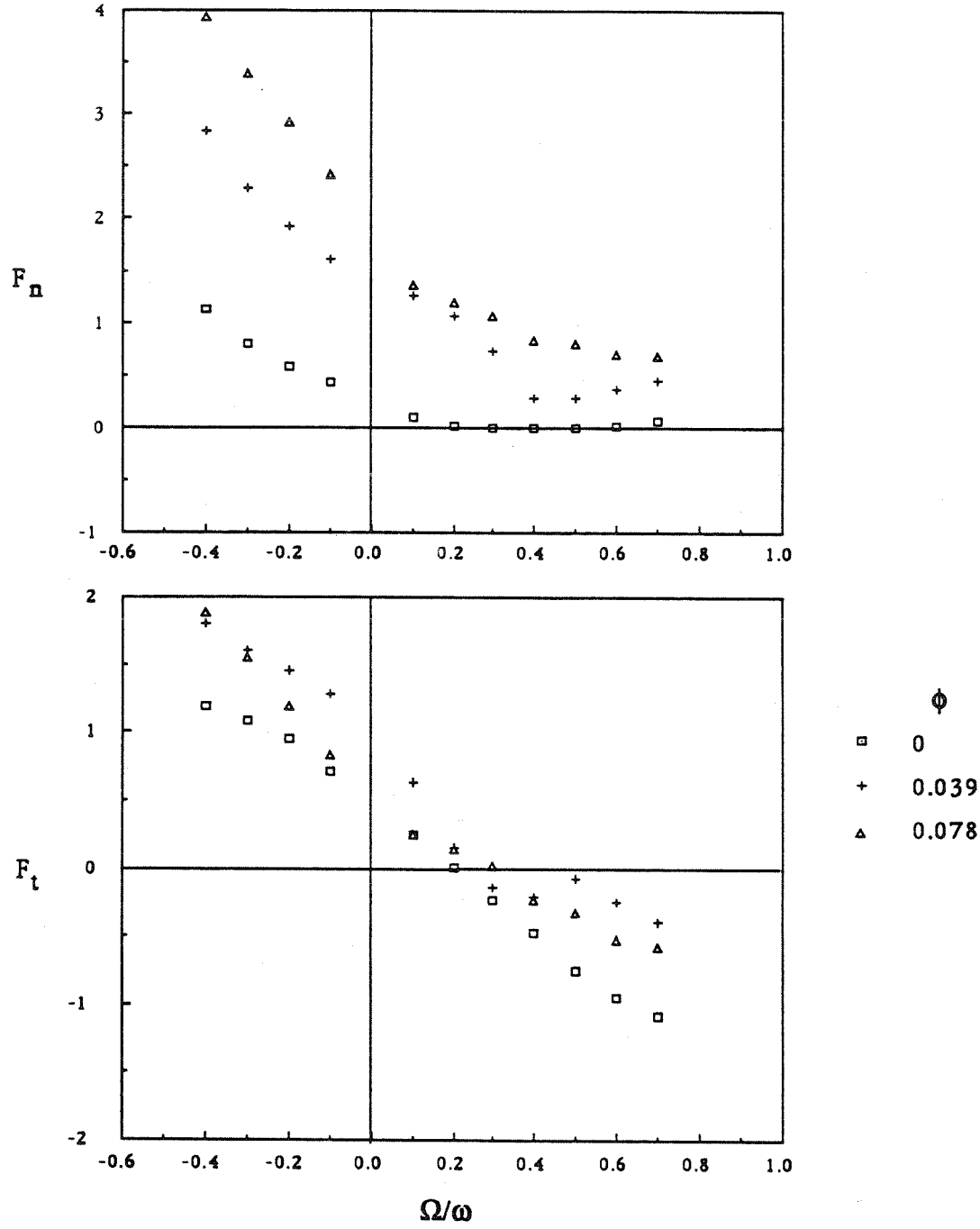

Figure 4.3 Dimensionless normal and tangential forces at 2000 RPM, an eccentricity ε = 0.0254 cm, a clearance H = 0.140 cm, offset δ = 0 and various flow rates as follows: 0 ℓ/sec, 0.631 ℓ/sec, 1.262 ℓ/sec.

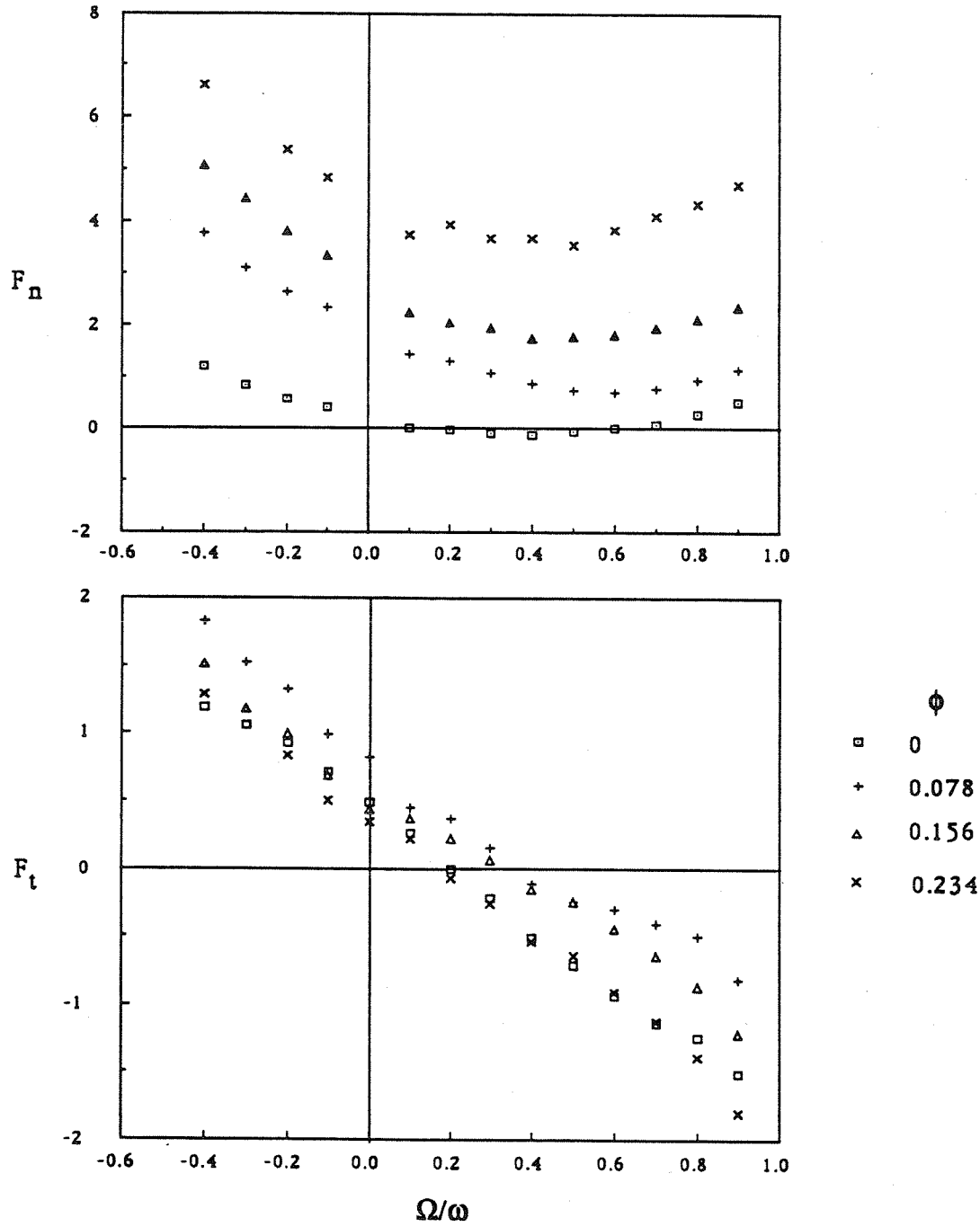

Figure 4.4 Dimensionless normal and tangential forces at 1000 RPM, an eccentricity ε = 0.118 cm, a clearance H = 0.140 cm, offset δ = 0 and various flow rates as follows: 0 ℓ/sec, 0.631 ℓ/sec, 1.262 ℓ/sec, 1.892 ℓ/sec.

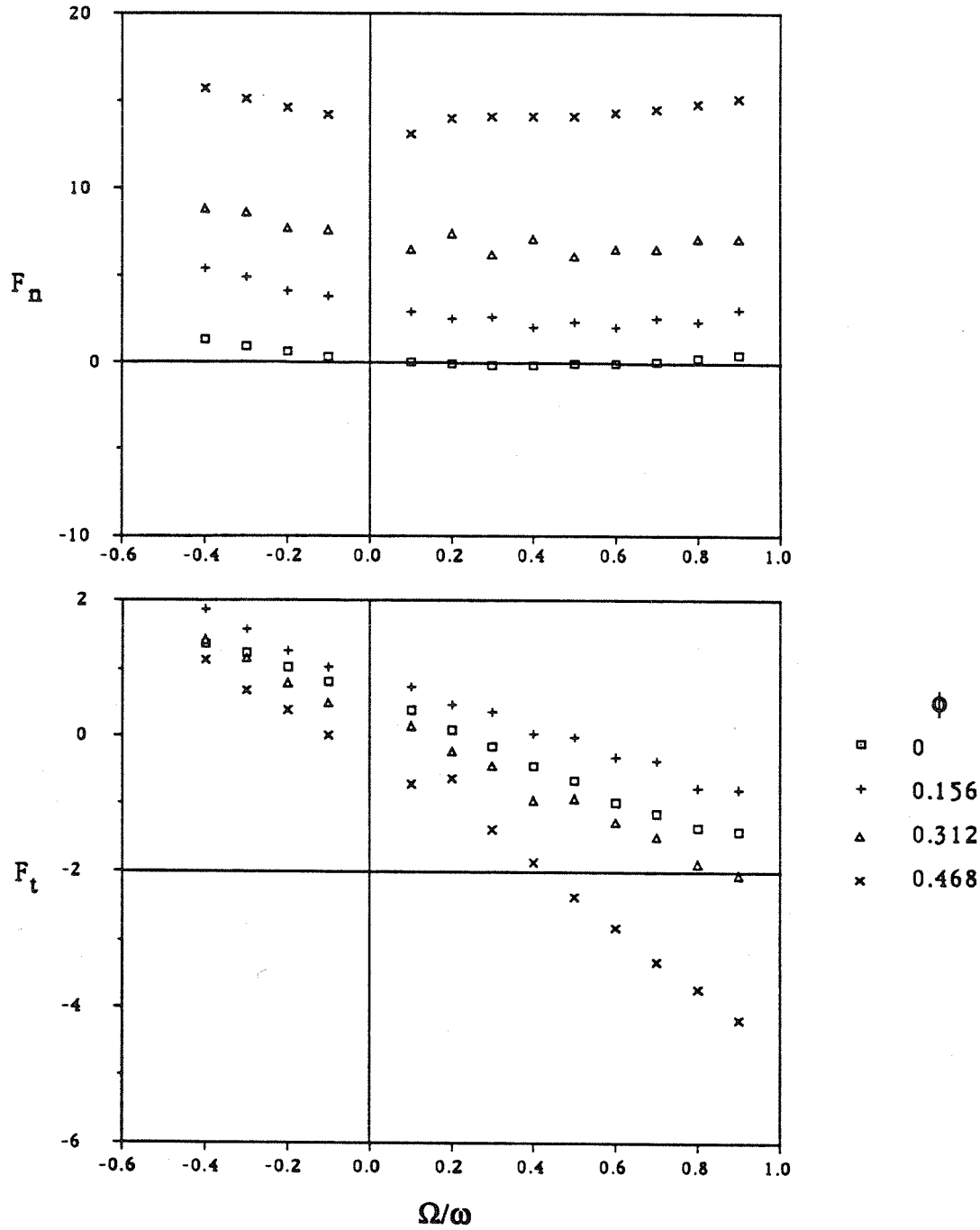

Figure 4.5 Dimensionless normal and tangential forces at 500 RPM, an eccentricity ε = 0.118 cm, a clearance H = 0.140 cm, offset δ = 0 and various flow rates as follows: 0 ℓ/sec, 0.631 ℓ/sec, 1.262 ℓ/sec, 1.892 ℓ/sec.

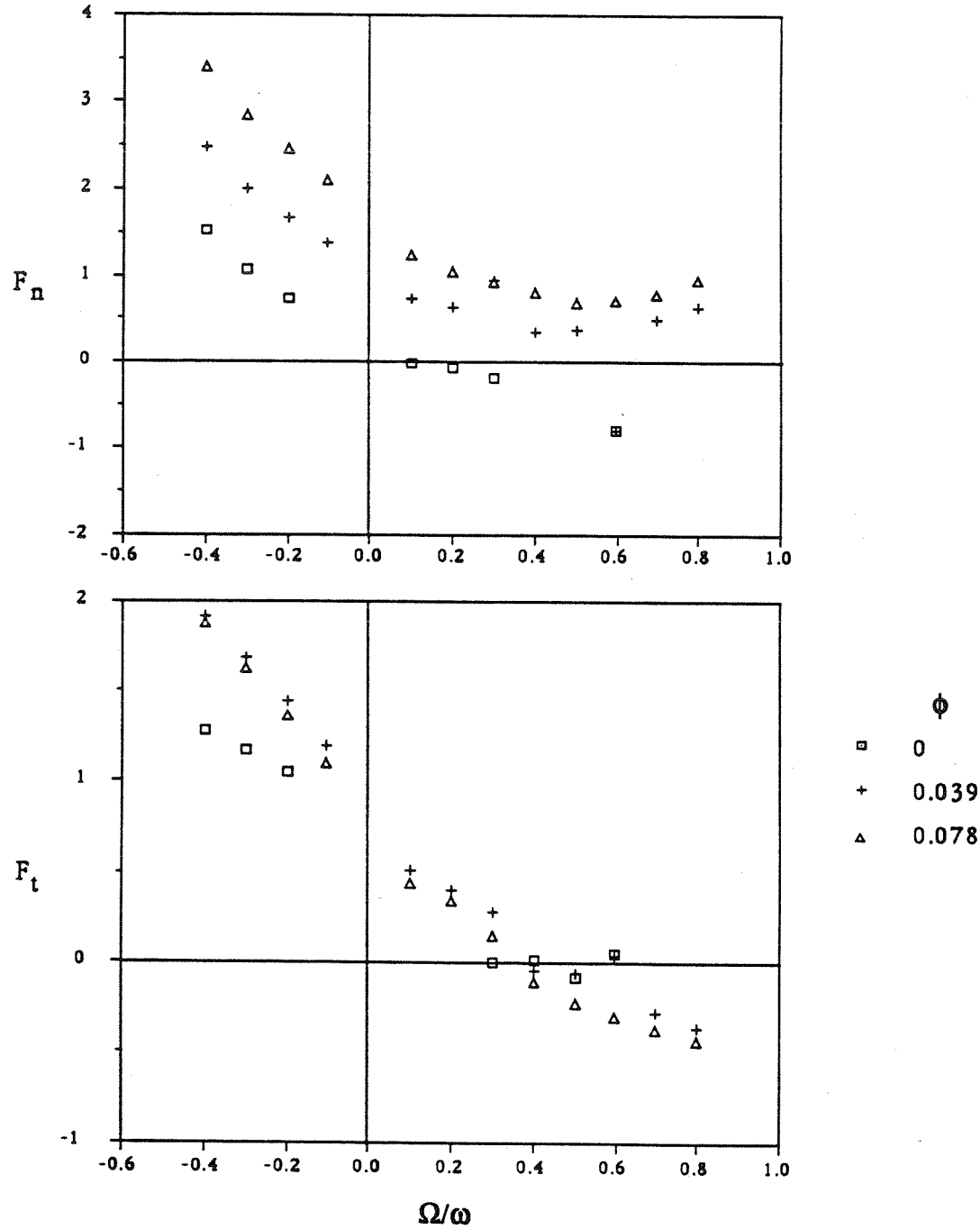

Figure 4.6 Dimensionless normal and tangential forces at 2000 RPM, an eccentricity ε = 0.118 cm, a clearance H = 0.140 cm, offset δ = 0 and various flow rates as follows: 0 ℓ/sec, 0.631 ℓ/sec, 1.262 ℓ/sec.

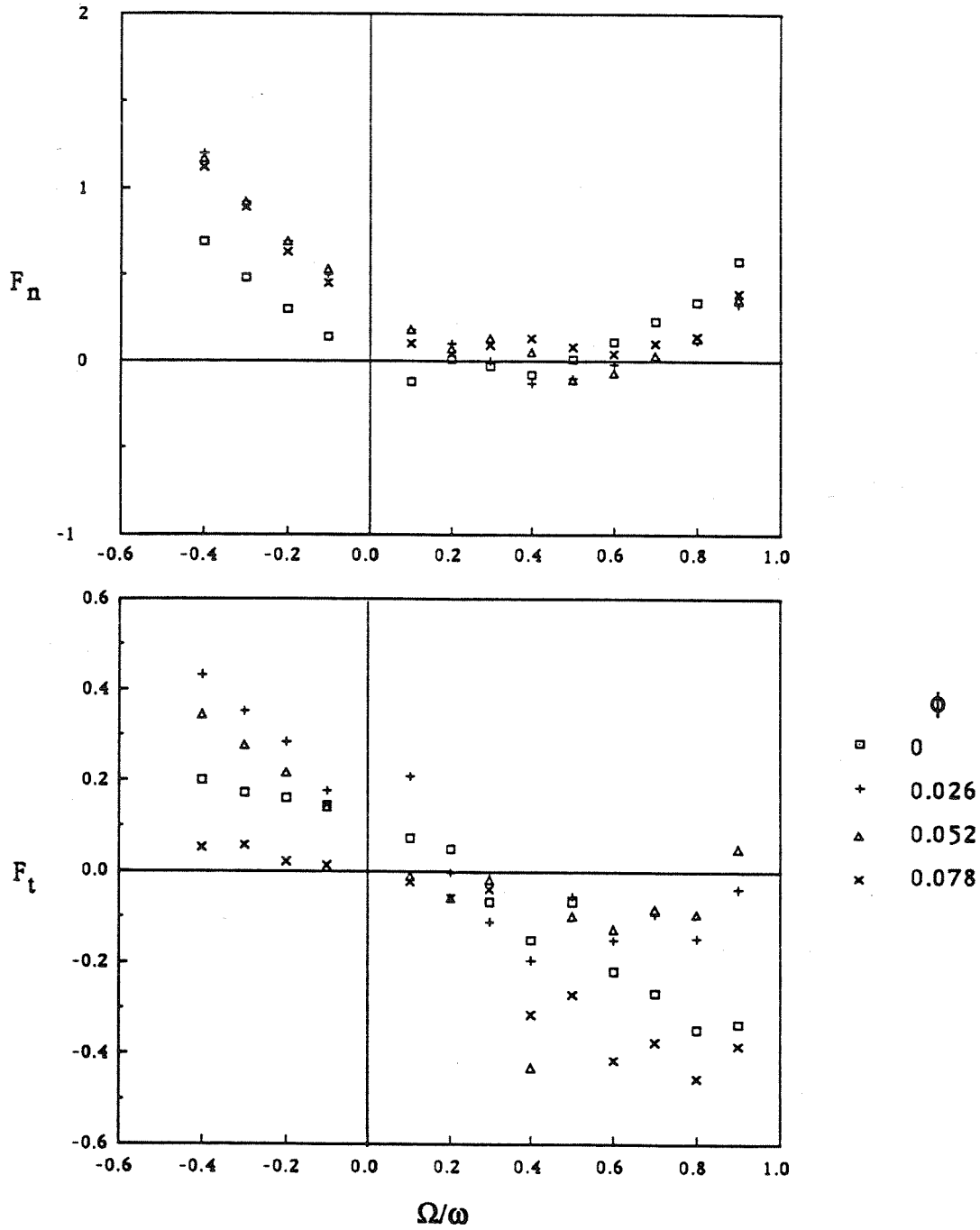

Figure 4.7. Dimensionless normal and tangential forces at 1000 RPM, an eccentricity ε = 0.0254 cm, a clearance H = 0.424 cm, offset δ = 0 and various flow rates as follows: 0 ℓ/sec, 0.631 ℓ/sec, 1.262 ℓ/sec, 1.892 ℓ/sec.

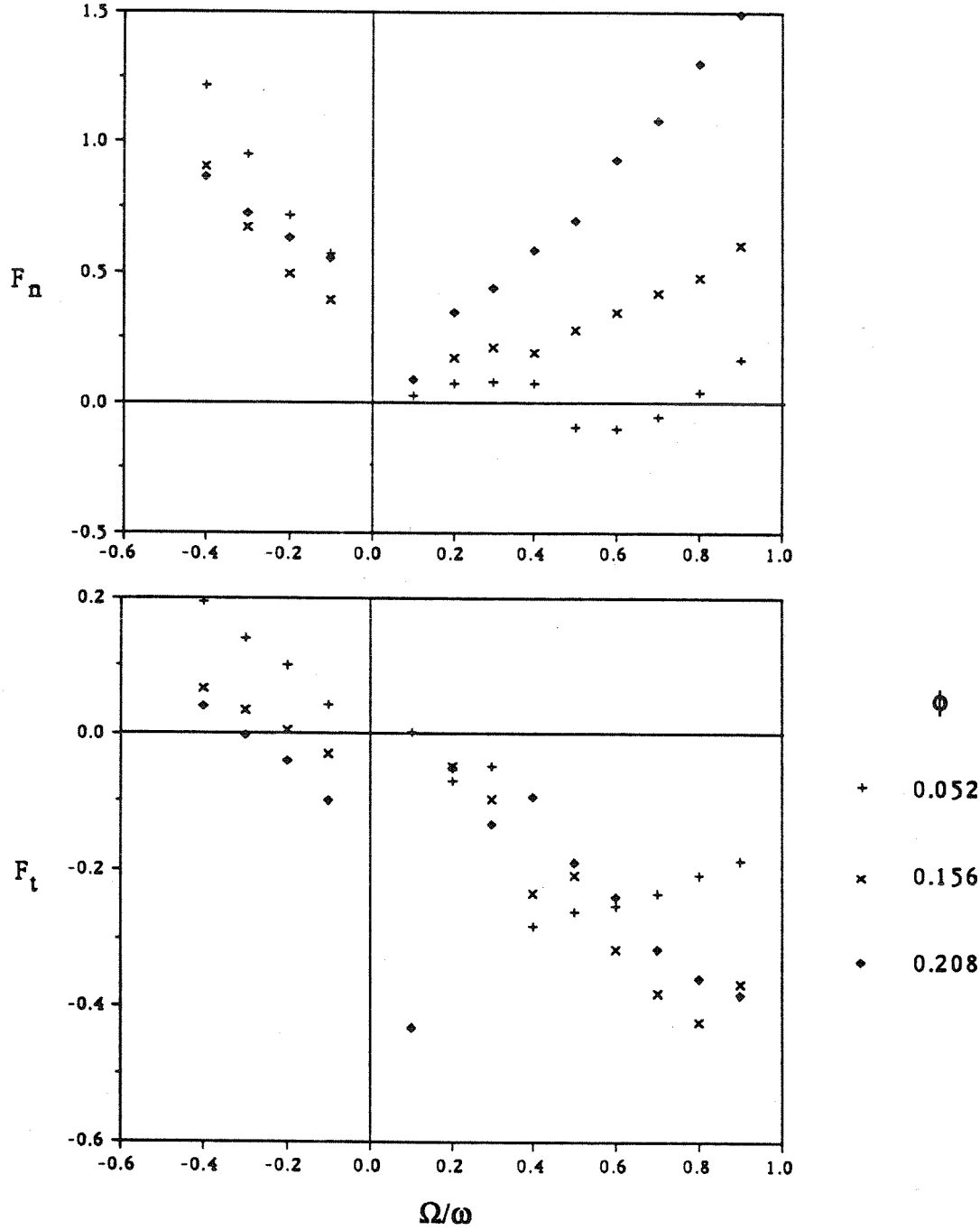

Figure 4.8 Dimensionless normal and tangential forces at 500 RPM, an eccentricity ε = 0.118 cm, a clearance H = 0.424 cm, offset δ = 0 and various flow rates as follows: 0.631 ℓ/sec, 1.892 ℓ/sec, 3.154 ℓ/sec.

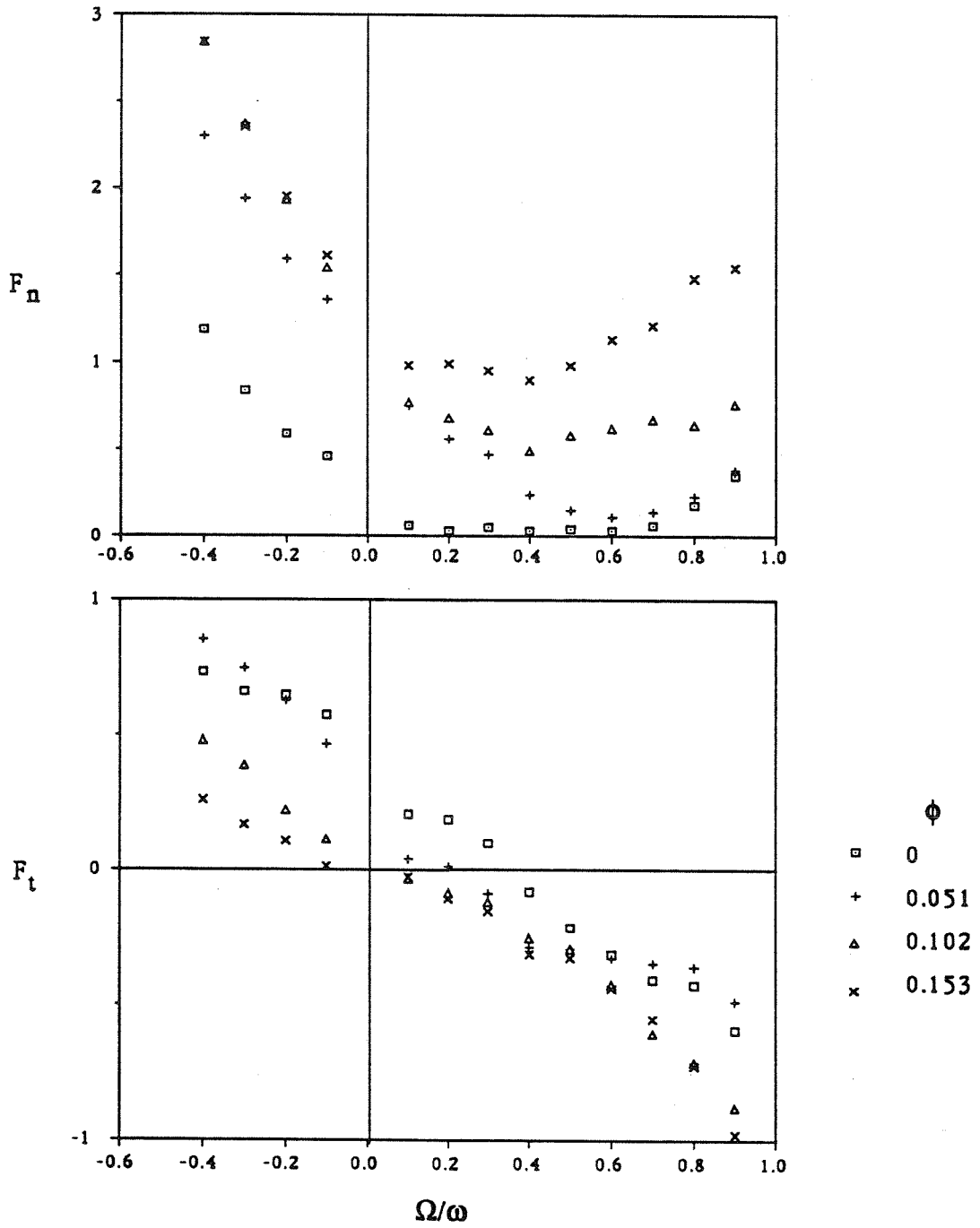

Figure 4.9 Dimensionless normal and tangential forces at 1000 RPM, an eccentricity ε = 0.118 cm, a clearance H = 0.212 cm, offset δ = 0 and various flow rates as follows: 0 ℓ/sec, 0.631ℓ/sec, 1.262ℓ/sec, 1.892 ℓ/sec.

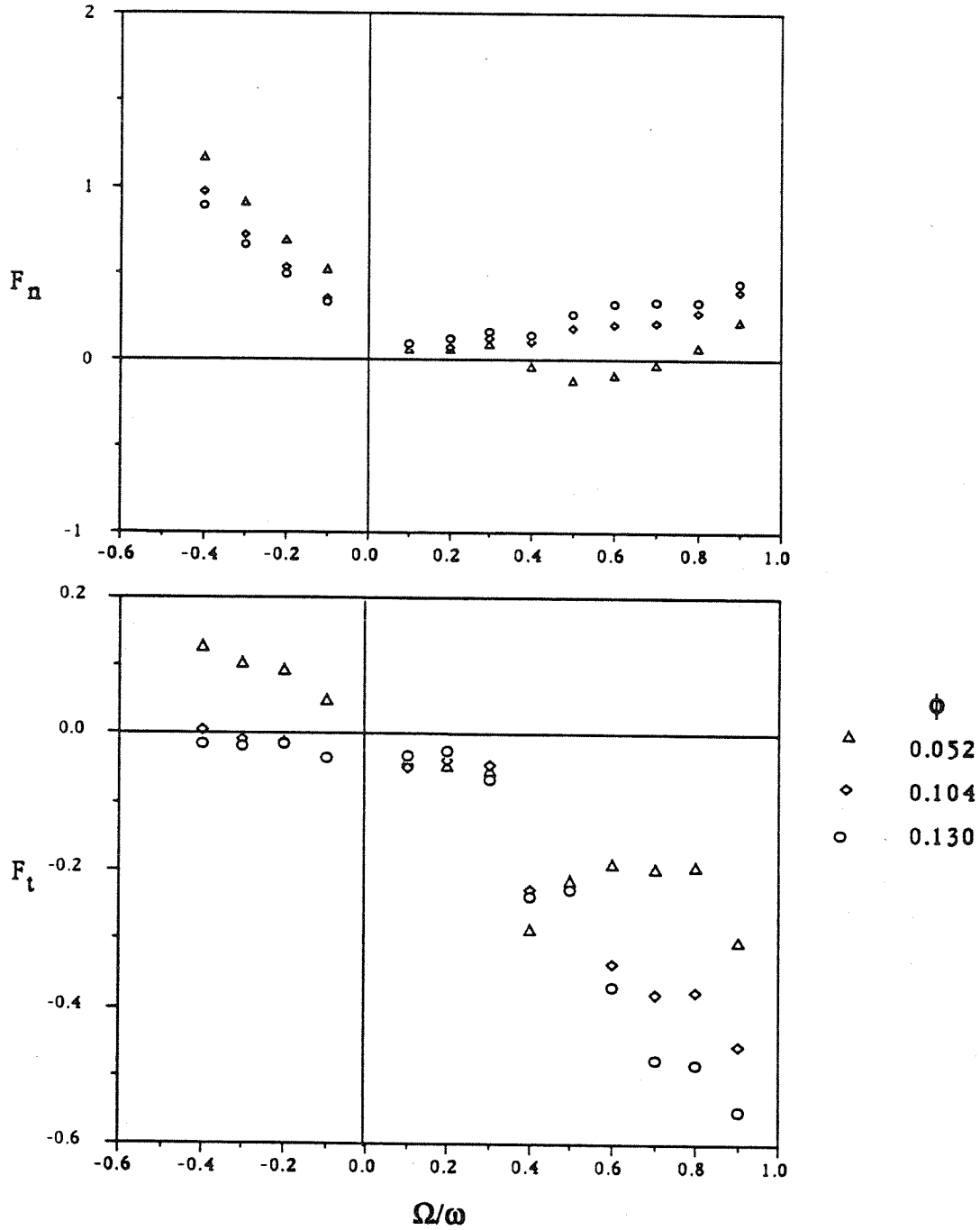

Figure 4.10 Dimensionless normal and tangential forces at 1000 RPM, an eccentricity ε = 0.118 cm, a clearance H = 0.424 cm, offset δ = 0 and various flow rates as follows: 1.262 ℓ/sec, 2.524 ℓ/sec, 3.154 ℓ/sec.

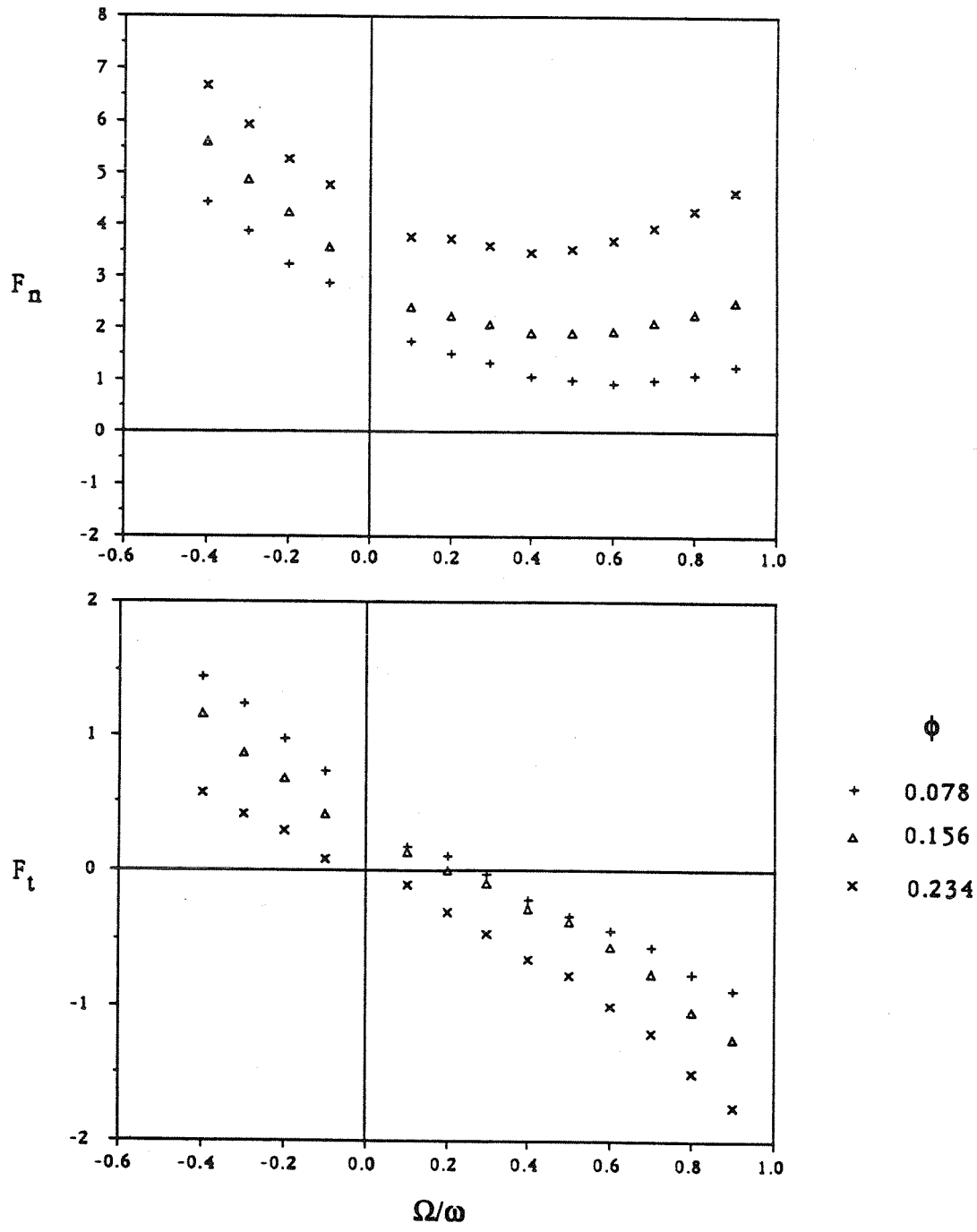

Figure 4.11 Dimensionless normal and tangential forces at 1000 rpm, an eccentricity ε = 0.118 cm, a clearance H = 0.140 cm, offset δ = 0 and various flow rates as follows: 0.631 ℓ/sec, 1.262 ℓ/sec, 1.892 ℓ/sec. The seal clearance is tightened to 0.0254cm.

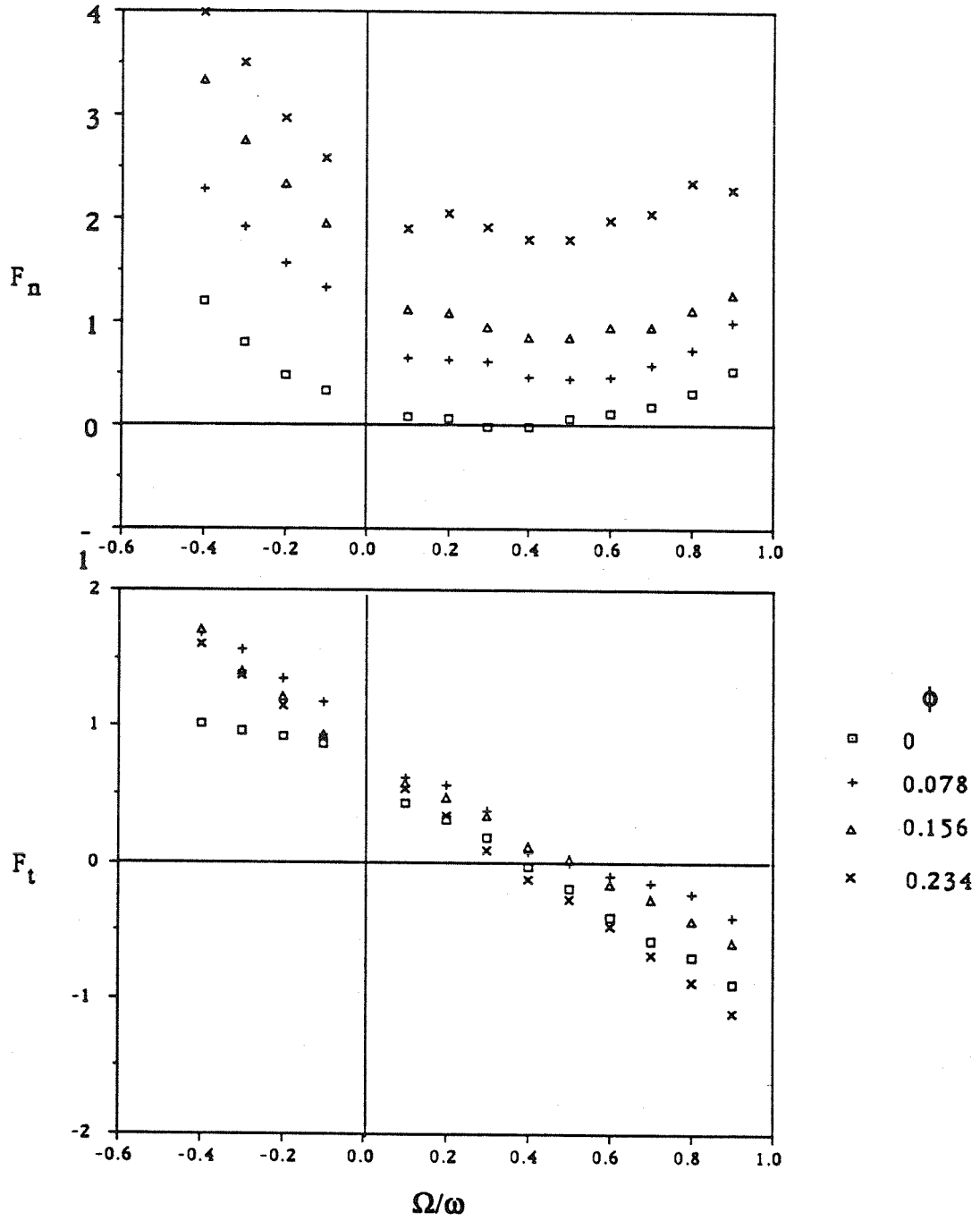

Figure 4.12 Dimensionless normal and tangential forces at 1000 rpm, an eccentricity ε = 0.118 cm, a clearance H = 0.140 cm, offset δ = 0 and various flow rates as follows: 0 ℓ/sec, 0.631 ℓ/sec, 1.262 ℓ/sec , 1.892ℓ/sec. The seal clearance is widened to 0.1016cm.

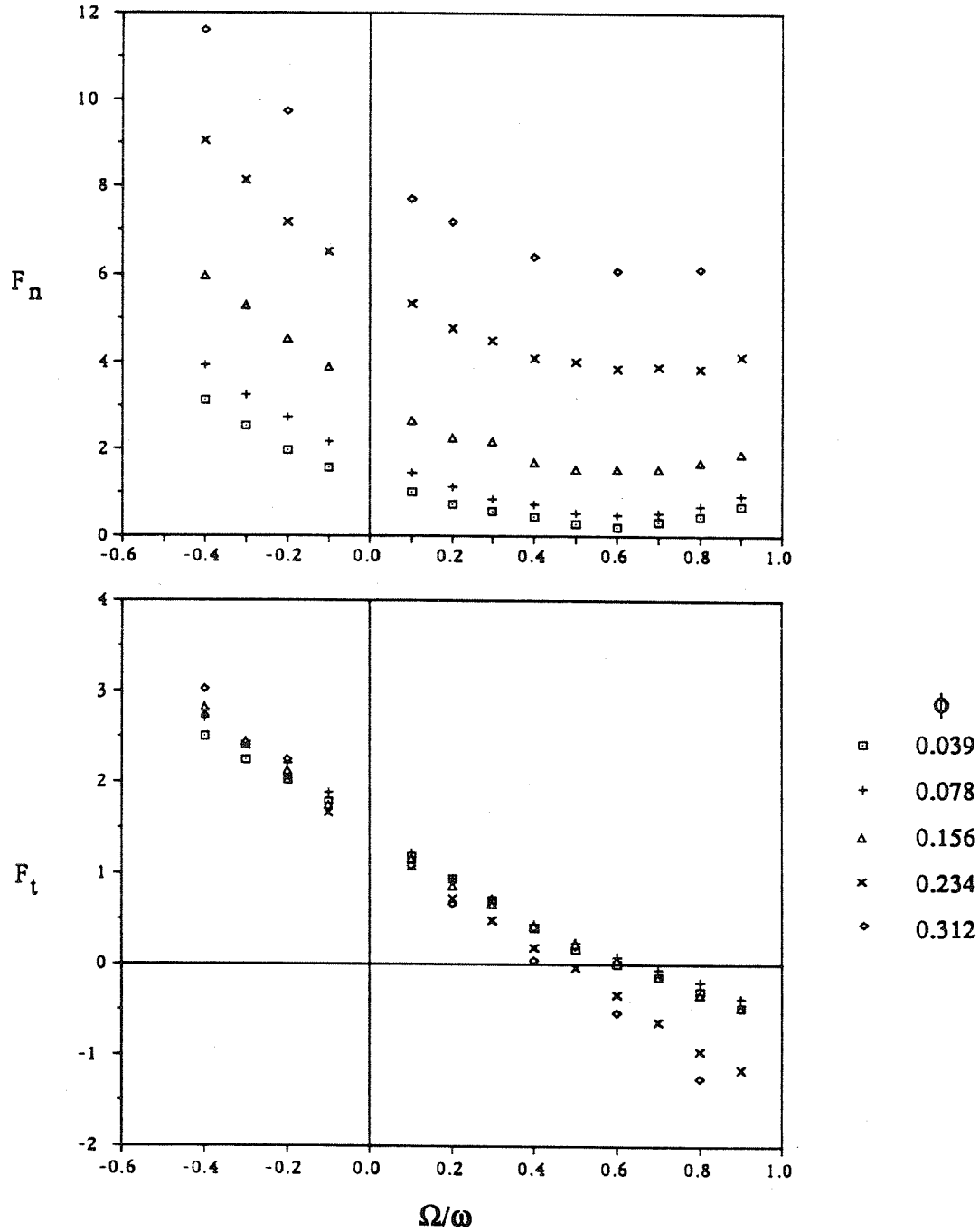

Figure 4.13 Dimensionless normal and tangential forces with inlet swirl at 1000 RPM, an eccentricity ε = 0.118 cm, a clearance H = 0.140 cm, offset δ = 0 and various flow rates (and inlet swirl ratios) as follows: 0.315 ℓ/sec (Γ=0.5), 0.631ℓ/sec (Γ=1.0), 1.262 ℓ/sec (Γ=2.0), 1.892 ℓ/sec (Γ=3.0).

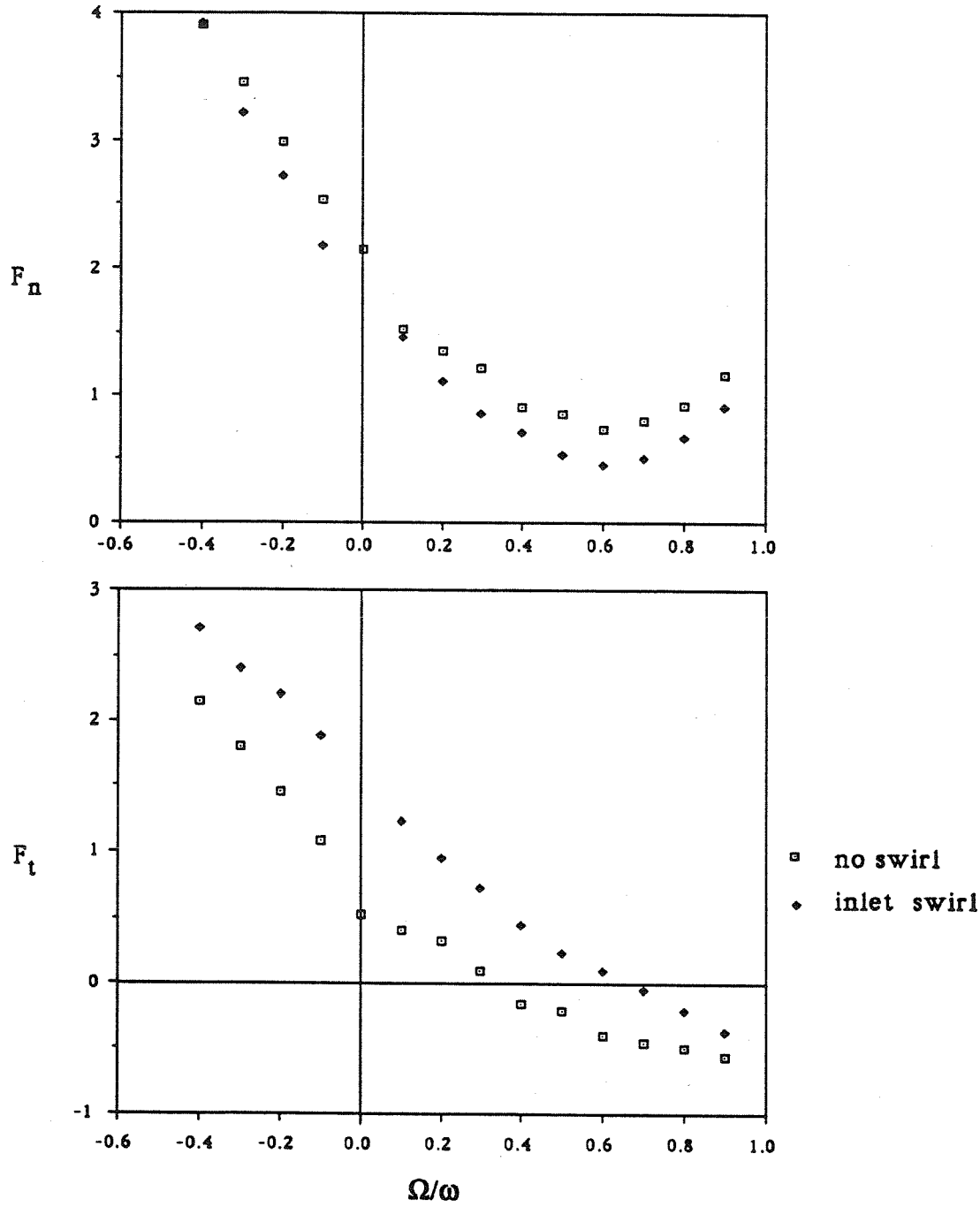

Figure 4.14 Comparison of the dimensionless normal and tangential forces with and without inlet swirl at 1000 RPM, an eccentricity ε = 0.118 cm, a clearance H = 0.140 cm, offset δ = 0 and a flow rate of 0.631 ℓ/sec. The inlet swirl is Γ=1.0

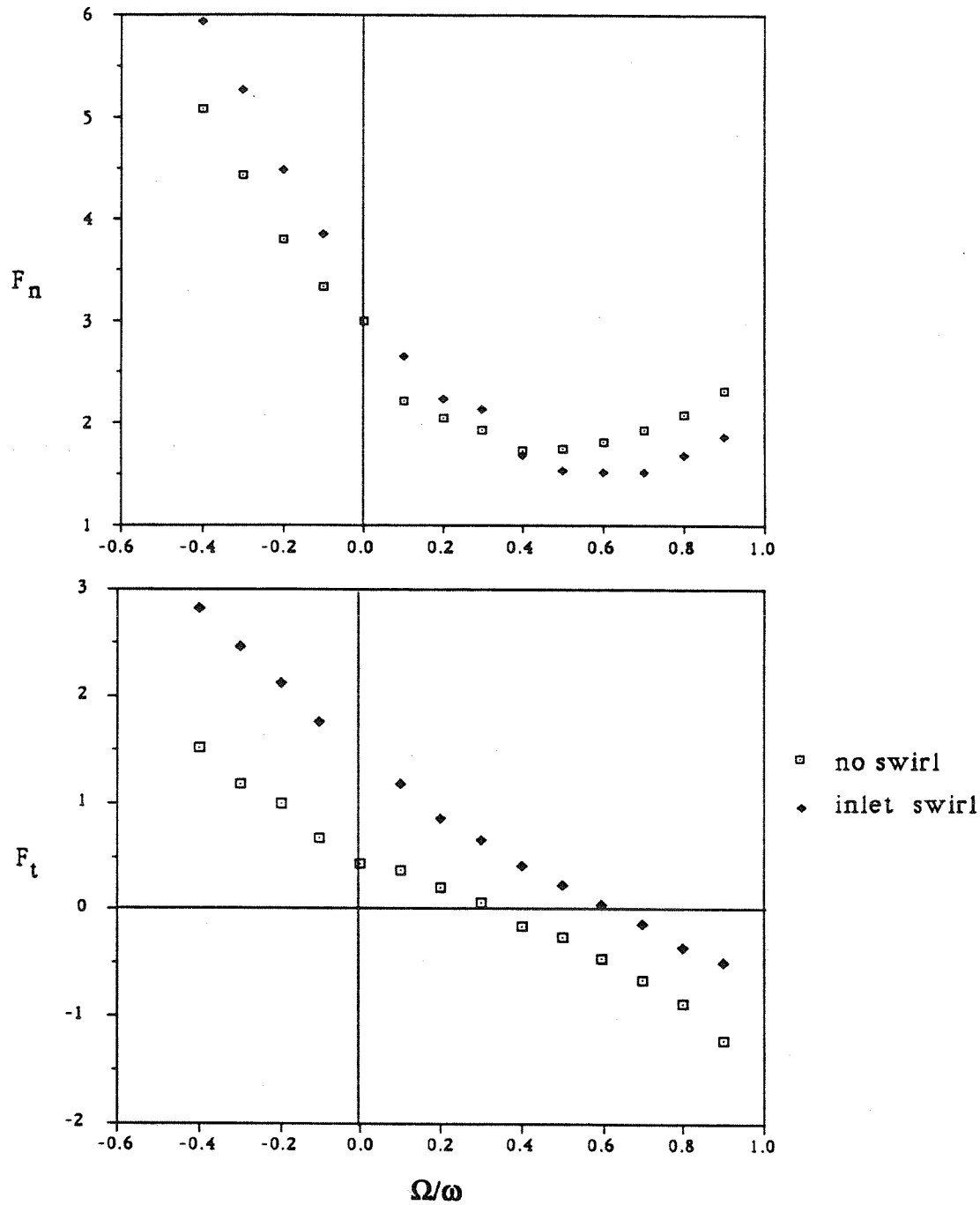

Figure 4.15 Comparison of the dimensionless normal and tangential forces with and without inlet swirl at 1000 RPM, an eccentricity ε = 0.118 cm, a clearance H = 0.140 cm, offset δ = 0 and a flow rate of 1.262 ℓ/sec. The inlet swirl is Γ=2.0

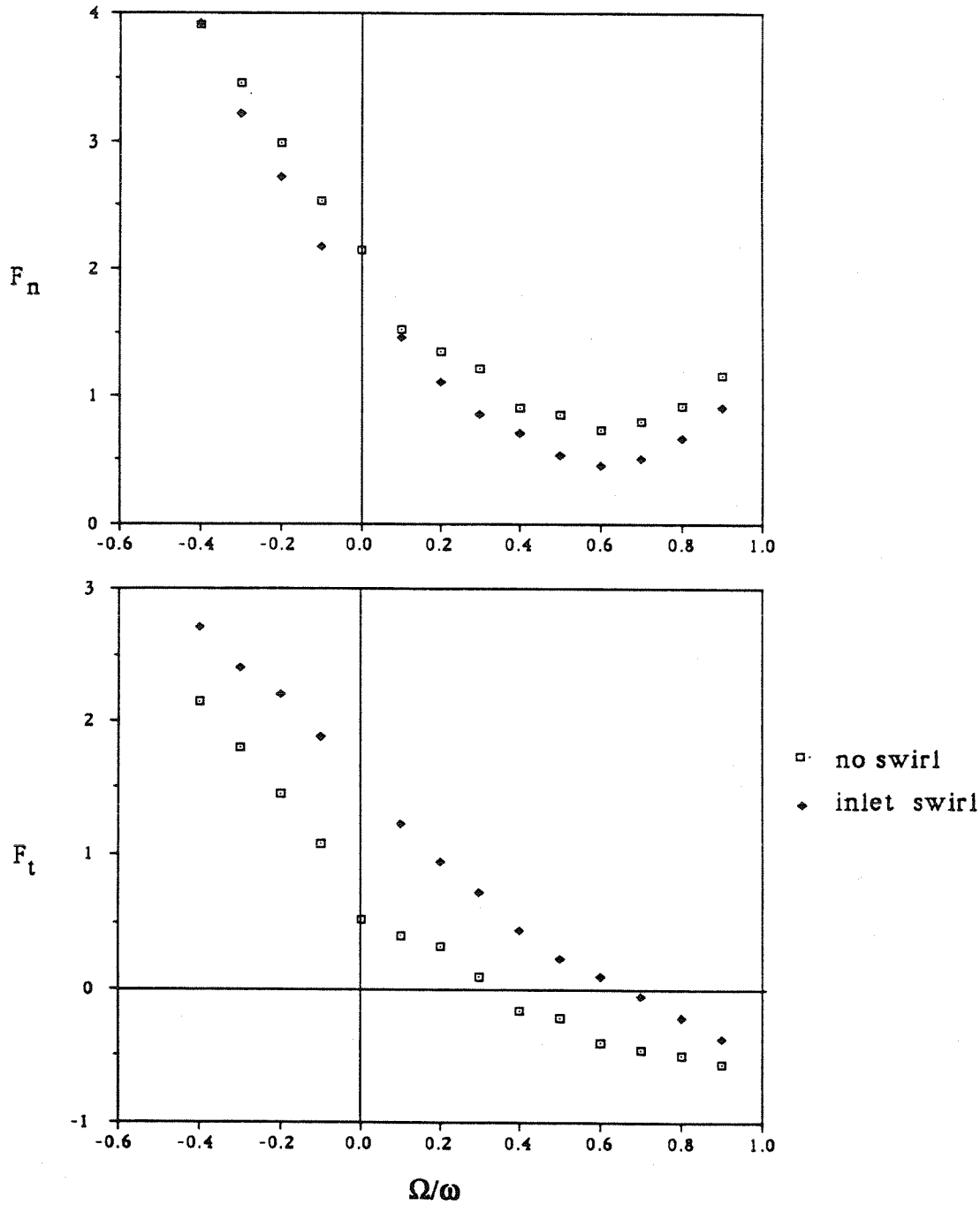

Figure 4.16 Comparison of the dimensionless normal and tangential forces with (eccentricity ε = 0.118 cm) and without (eccentricity ε = 0.0254 cm) inlet swirl at 1000 RPM, a clearance H = 0.140 cm, offset δ = 0 and a flow rate of 0.631 ℓ/sec. The inlet swirl is Γ=1.0

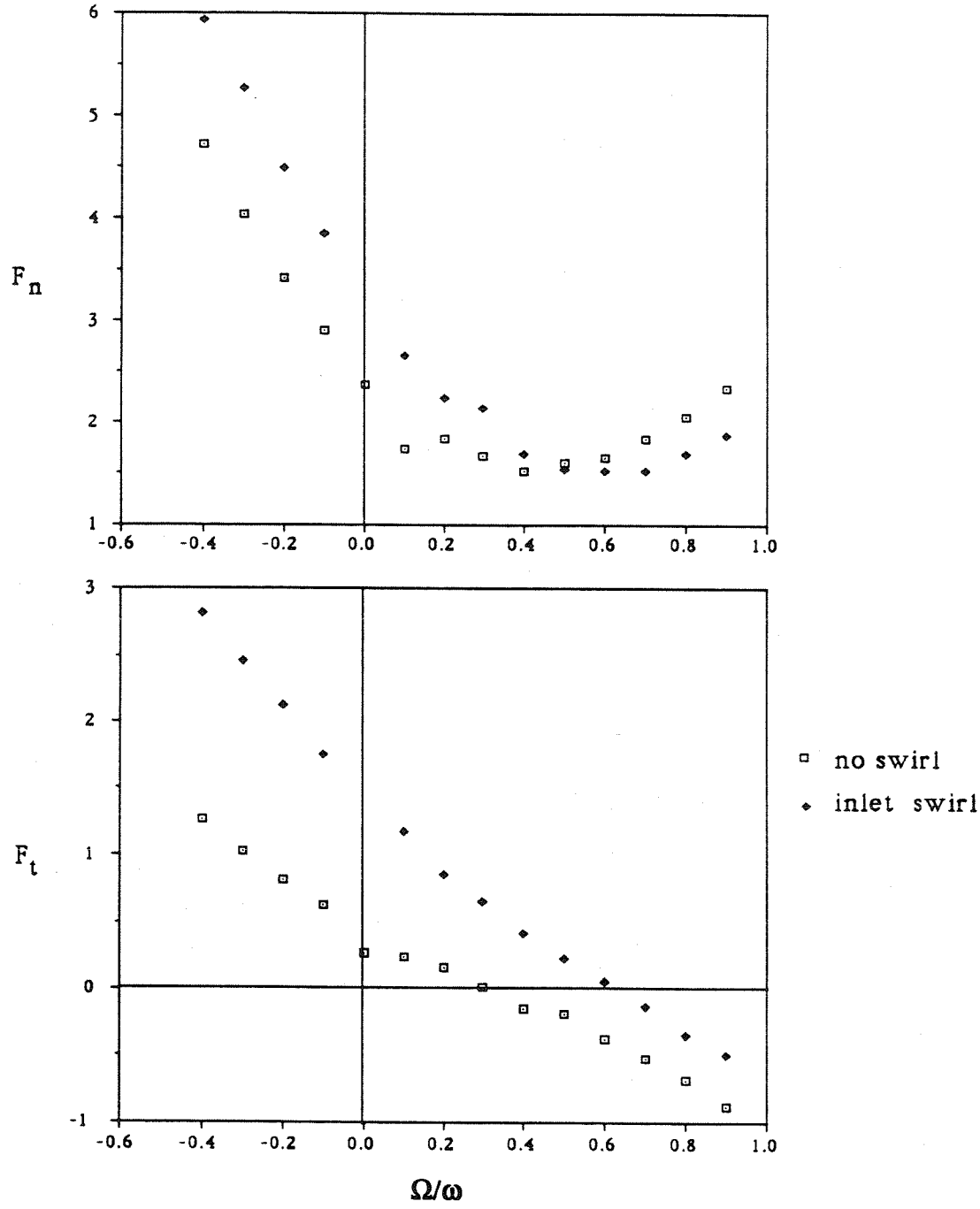

Figure 4.17 Comparison of the dimensionless normal and tangential forces with (eccentricity ε = 0.118 cm) and without (eccentricity ε = 0.0254 cm) inlet swirl at 1000 RPM, a clearance H = 0.140 cm, offset δ = 0 and a flow rate of 1.262 ℓ/sec. The inlet swirl is Γ=2.0

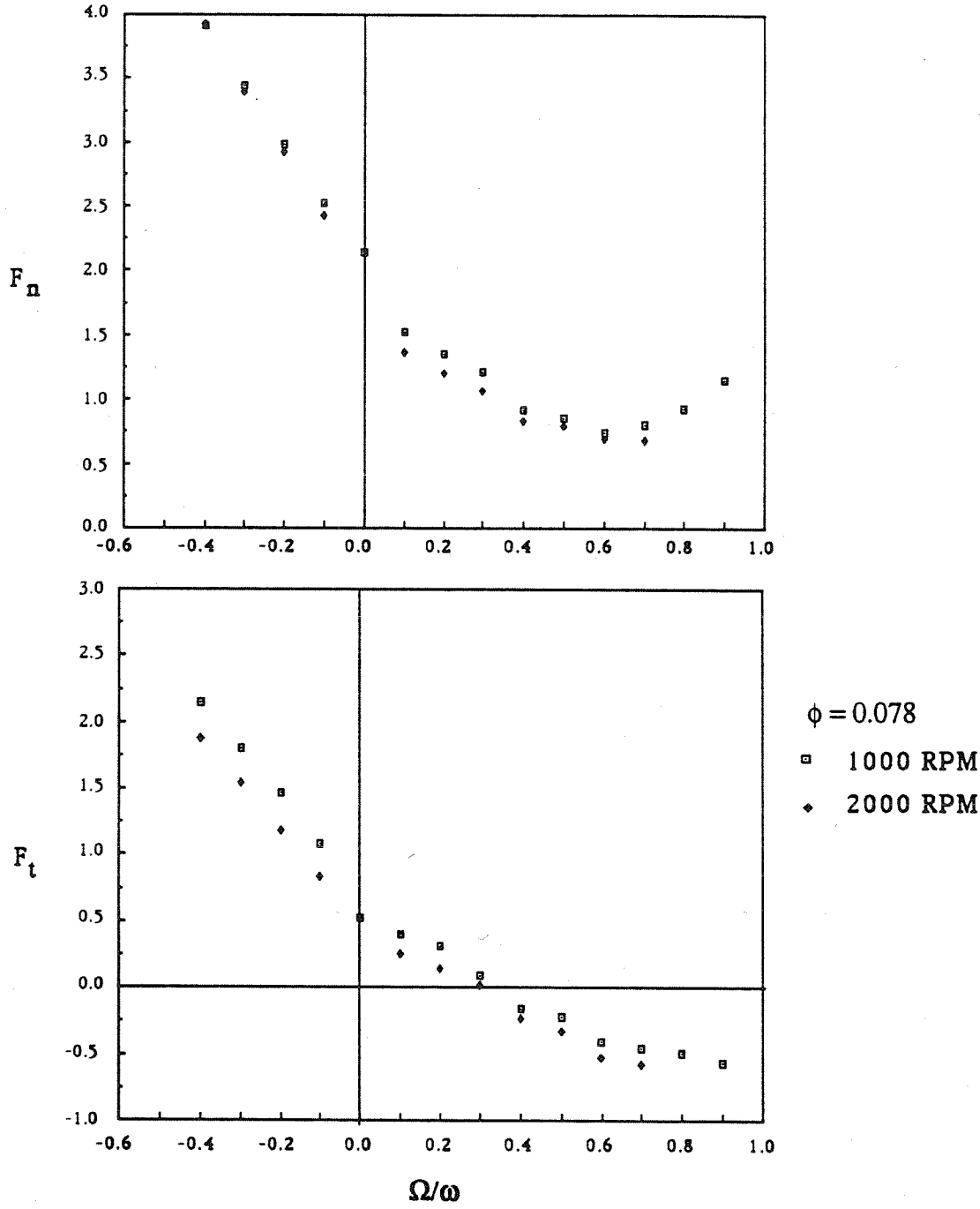

Figure 4.18 Dimensionless normal and tangential forces for two different experimental conditions with the same flow coefficient at an eccentricity ε = 0.0254 cm, a clearance, H = 0.140 cm, offset, δ = 0 and flow rates as follows: 0.631 ℓ/sec at 1000 RPM, and 1.262 ℓ/sec at 2000RPM.

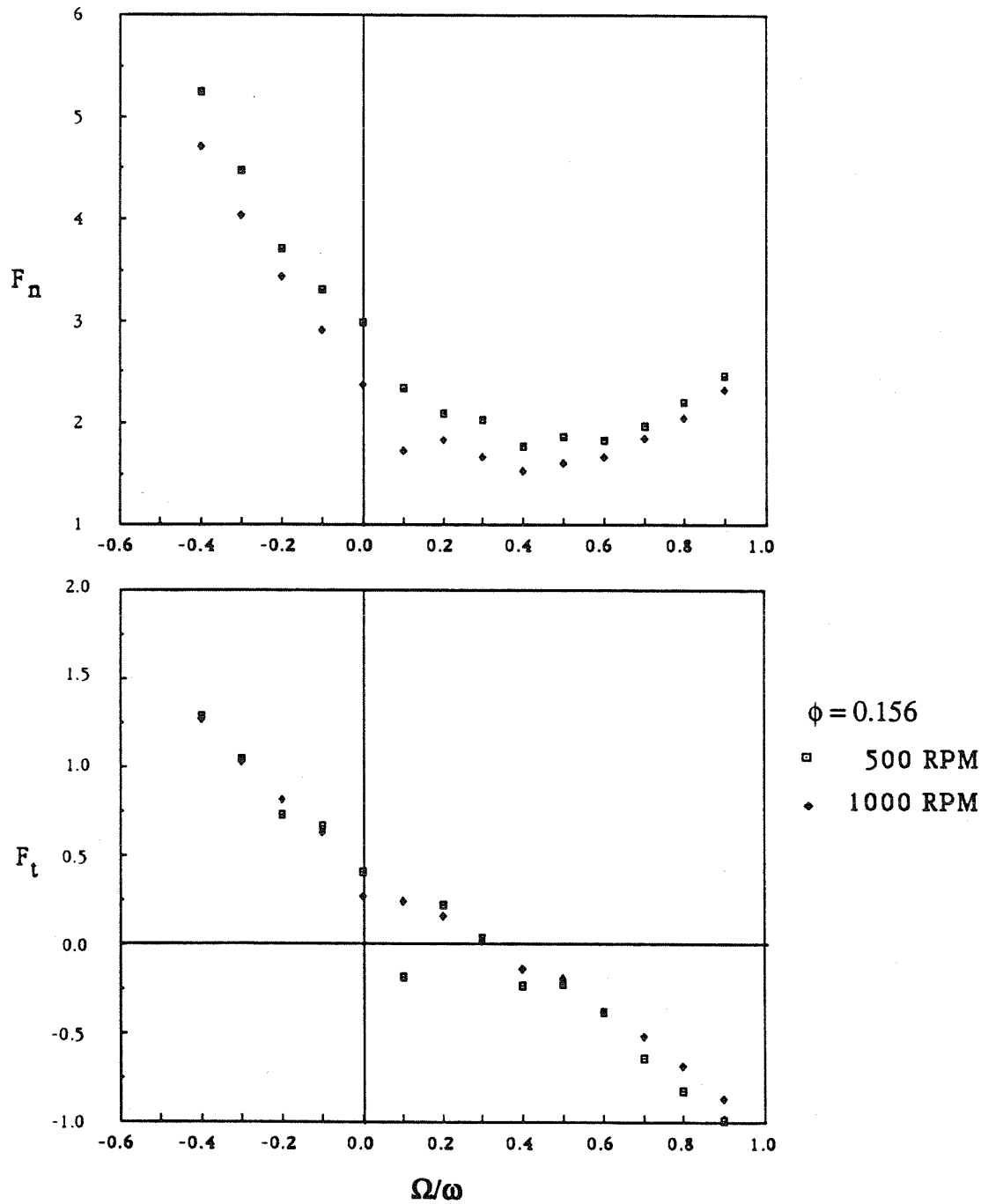

Figure 4.19 Dimensionless normal and tangential forces for two different experimental conditions with the same flow coefficient at an eccentricity ε = 0.0254 cm, a clearance, H = 0.140 cm, offset, δ = 0 and flow rates as follows: 0.631 ℓ/sec at 500 RPM, and 1.262 ℓ/sec at 1000RPM.

CHAPTER 5

ROTORDYNAMIC COEFFICIENTS

As was mentioned in the introduction, it is standard practice to express the matrix elements of [A] in powers of Ω/ω. Though the functional dependence of F_n on the whirl ratio is not necessarily quadratic, nor is F_t linear, it is nevertheless of value to the rotordynamicists to fit the data of the figures from chapter 4 to the following expressions:

$$F_n = M\left(\frac{\Omega}{\omega}\right)^2 - c\left(\frac{\Omega}{\omega}\right) - K \tag{5.1}$$

$$F_t = - C\left(\frac{\Omega}{\omega}\right) + k \tag{5.2}$$

where M, C, c, K, k are the dimensionless direct added mass (M), direct damping (C), cross-coupled damping (c), direct stiffness (K) and cross-coupled stiffness (k). The cross-coupled added mass (m) has been omitted for simplicity, since it is not a significant term. From a stability point of view, the tangential force is most interesting; a positive cross-coupled stiffness is destabilizing because it drives the forward orbital motion of the rotor. Positive direct damping and negative cross-coupled stiffness are stabilizing because they oppose orbital motion. Another important parameter is the ratio k/C as it indicates the region of stability. At whirl ratios above this, the tangential force will act in the direction opposite to the whirl motion and is therefore stabilizing. Table 5.1 lists these rotordynamic coefficients which are obtained by curve fitting the data of figures 4.1 through 4.13.

5.1 Experiments without inlet swirl

The data of Table 5.1 is presented in graphical form in figure 5.1 for a wide range of conditions where the dimensionless rotordynamic coefficients are plotted against the flow coefficient, ϕ. Various effects such as speed, eccentricity, seal clearance and swirl will be examined separately but they are shown together in figure 5.1 in order that the global effect on each coefficient with increasing leakage flow can be seen. A large negative stiffness results in a positive normal force which would tend to increase the radius of the orbital motion; increasing the leakage flow increases this force. On the other hand, a

positive cross-coupled stiffness is destabilizing because it drives the forward orbital motion of the rotor so as to encourage whirl but the leakage flow is stabilizing in that the tangential force decreases with leakage flow. Direct damping decreases slightly with flow and would therefore be less stabilizing since the tangential force increases. Below a flow coefficient of 0.7, direct damping is negative so it would seem to encourage whirl. At higher flow rates, direct damping begins to increase, which would decrease the tangential force. However, these flow rates are larger leakage flow rates than would occur in real pumps. The cross-coupled damping decreases slightly and the added mass term increases with flow, thus contributing to a larger normal force. In other words, inertial motion would discourage orbital motion of the impeller but drive the impeller in the direction of displacement. It is interesting to note that at higher flow rates, the trend of the added mass also changes. A convenient measure of the stability is the ratio of cross-coupled stiffness to direct damping, which would estimate the whirl ratio at which the force would no longer be destabilizing.

The results in figure 5.2 and 5.3 were obtained for a range of shaft speeds from 500 RPM to 2000 RPM and are seen to be independent of speed. Figure 5.2 was obtained with an eccentricity of 0.0254cm and a clearance of 0.140 cm, while figure 5.3 was obtained with the same clearance but a higher eccentricity of 0.118cm. All the other quantities were kept the same, so that the only variable left to be examined is speed. The similarity of the results obtained for the two eccentricities can be clearly seen.

Figures 5.4, 5.5 and 5.6 isolate the effect of eccentricity at different speeds: 1000, 2000, and 500 RPM respectively. Each graph shows two sets of data (two different eccentricities) at a given shaft speed and a clearance of 0.140 cm. Even when the shroud clearance is of the same order of magnitude as the eccentricity, the results are still in the linear regime. This set of three graphs shows that the magnitude of the eccentricity has no effect on the normalized rotordynamic coefficients.

The effect on the rotordynamic coefficients of the clearance between the rotating shroud and the stationary casing is next investigated in figure 5.7. The results are shown for 1000 RPM and three clearances: 0.140, 0.212, and

0.424 cm. At the largest clearance, the results are shown for both eccentricities and it can be seen that there is a wider range of scatter in the data. At the other two clearances, the results are shown at the larger eccentricity. The stiffness acts to increase the normal force as the clearance is decreased, which would drive the motion into a larger orbit. The cross-coupled stiffness increases so that the tangential force becomes more destabilizing. The direct damping increases as the clearance decreases, so it acts in competition with k. Rotordynamically speaking, a smaller force is generated with a larger clearance and is clearly demonstrated in figure 5.7.

The effect of increasing the seal clearance is examined in figure 5.8. In practice such a change could occur as a result of wear. The direct stiffness increases and the direct damping decreases, which is in competition with the effect of the cross-coupled damping, so as to decrease the normal force. The tangential force increases as a result of an increase in the cross-coupled stiffness, but the effect of the direct damping is not clear. So it would seem that wear of the seal is rotordynamically destabilizing. The effect of wear on the cross-coupled stiffness presented by Scharrer et al. (1991) is in agreement with the above results, however the direct stiffness decreases with wear in contrast with the above results.

The added masses listed in Table 5.1 could be compared with theoretical values derived as follows. The potential flow added mass for a fluid-filled annulus between two circular cylinders (inner and outer radii denoted by a, b respectively) is $\rho \pi L a^2 b^2/(b^2 - a^2)$ where L is the axial length (Brennen [1976]); this assumes no axial velocities which could relieve the pressures caused by acceleration of the inner cylinder. If this expression is integrated over the length of the leakage annulus shown in figure 2.3, it leads to an added mass given by

$$M = 0.160 \frac{R_2}{H} \tag{5.3}$$

or 3.53 for H = 0.424 cm and 0.71 for H = 0.140 cm. The fact that the actual values are about 40% of these may reflect the relief allowed by non-zero axial velocity. It is however interesting to note that the above result correctly models the functional dependence on H exhibited by the experimental data.

5.2 Experiments with prescribed inlet swirl

The inlet circumferential velocity was controlled by using the inlet guide vane, which is described in chapter 2. The device allowed known swirl to be added to the inlet flow. In other words, the leakage flow now has a tangential velocity component at the inlet. Figure 5.9 compares results obtained with the inlet guide vane in place, with data obtained without it and therefore no pre rotation of the inlet fluid. However, the inlet circumferential velocity could not be varied arbitrarily as it depends on the flow rate and given guide depth. Thus as the flow increases, the swirl increases as well, since only one device was used in these tests. Neither the direct stiffness nor the direct damping change substantially with the addition of swirl. However, the cross-coupled damping and hence the magnitude of the normal force increase with the addition of swirl. The cross-coupled stiffness and therefore the tangential force also increase. So the addition of swirl to the flow is destabilizing. The test results of Childs et al. (1990a,b) also demonstrated the favorable influence that a swirl brake has in reducing the seal destabilizing forces. Benckert and Wachter (1980) originally showed that a swirl brake, which reduces the inlet tangential velocity, would also reduce the cross-coupled stiffness. In earlier experiments on smooth seals by Childs et al. (1988), the direct damping was shown to be relatively insensitive to changes in inlet swirl, while the cross-coupled stiffness was shown to increase with swirl. The only result which is different is for the direct stiffness smooth seals, which shows a slight increase with swirl.

5.3 Rotordynamic stability

A convenient measure of the stability is the ratio of the cross-coupled coefficient, k to the direct damping coefficient, C. This provides an estimate of the whirl ratio at which the force would no longer be destabilizing. For circular synchronous orbits, it provides a ratio between the destabilizing force due to k and the stabilizing force due to C. Thus, reducing k/C improves the stability of the rotor system.

The role of the whirl ratio, k/C, was illustrated by Crandall (1982), who took the Sommerfeld bearing model and applied a dynamic analysis to the whirling

stability of an unloaded bearing. For a journal rotating with velocity Ω, the equilibrium position will be a displacement δ at right angles to the load. The solution for a journal whirling with velocity Ω about a circle of radius ε centered on the equilibrium position which is offset a distance δ from the bearing center, varies as follows. For $\delta/H < 0.5$, the neutral stability point $(\Omega/\omega)_{crit}$ is 0.5. As δ/H approaches 1.0, $(\Omega/\omega)_{crit}$ approaches 1/3. The heuristic proposal of Crandall (1982) agrees with the above stability analysis for $\delta/H < 0.5$, but $(\Omega/\omega)_{crit}$ is predicted smaller for δ/H approaching 1. While the present experiment involves a different geometry from the bearing model, the whirl ratio, k/C is of the same order of magnitude.

The results of Childs et al. (1988) show the influence of the inlet tangential velocity on the whirl ratio. The results for the smooth seal are more applicable for comparison than those of the labyrinth and honeycomb seals. In the former, as the circumferential velocity ratio increases from negative to positive, the whirl ratio increases correspondingly. It is interesting to see that when the swirl is small, a change in swirl (0 to 0.3) dramatically affects the whirl ratio (0 to 1.) However, when the swirl changes from 0.3 to 0.8, then the whirl frequency does not change substantially (1. to 1.1). For negative swirl (0 to -0.8), the whirl ratio also does not change as rapidly (0 to -0.3).

In the present experiments, it was shown earlier that the rotordynamic coefficients did not change with RPM. So it is not surprising that the whirl ratio is also independent of RPM. This is shown in figures 5.10 and 5.11 for the two eccentricities. In these figures no swirl is added to the inlet. However, the inlet tangential velocity of the bulk flow will clearly decrease as the flow increases. As the flow increases, the whirl ratio decreases. This trend agrees with Childs et al. (1988) wherein the whirl ratio decreases as the swirl decreases. Figure 5.12 shows that as the clearance is decreased for a given flow, the whirl ratio increases. The results of Hawkins and Childs (1988) also show that small clearance seals are more stable than the larger clearance seals. The effect of opening up the seal clearance is illustrated in figure 5.13. Here the larger seal clearance decreases the whirl ratio.

The whirl ratio from the results of Bolleter et al. (1989) gives surprisingly different results from the present research. For the total impeller, the ratio is

1.4; for the contribution from the seal alone the ratio is 0.85 and for the difference between these contributions, the ratio is 2.26. From the above discussion, it can be seen that the range for the results of the present experiments is smaller (-0.12 to 0.45). The discrepancies can be traced to the cross-coupled stiffness and the direct damping, which are both a lot larger in Bolleter et al. (1989) than in the present experiments.

Table 5.1. Dimensionless direct and cross-coupled stiffness, damping and added mass as functions of the flow coefficient.

		Direct Stiffness K	Cross-Coupled Stiffness k	Direct Damping C	Cross-Coupled Damping c	Direct Added Mass M
RPM = 1000 H = 0.140 cm ε = 0.0254 cm Seal = 0.0508 cm						
Flow =	0 ℓ/sec	-0.19	0.51	2.18	1.60	2.15
	0.631 ℓ/sec	-1.99	095	2.10	3.85	3.15
	1.262 ℓ/sec	-2.46	0.52	1.55	4.00	4.46
	1.892 ℓ/sec	-3.33	0.33	1.49	3.33	4.71
RPM = 1000 H = 0.424 cm ε = 0.0254 cm Seal = 0.0508 cm						
Flow =	0 ℓ/sec	-0.048	0.071	0.45	0.91	1.66
	0.631 ℓ/sec	-0.299	0.167	0.43	1.60	1.75
	1.262 ℓ/sec	-0.330	0.093	0.32	1.50	1.61
	1.892 ℓ/sec	-0.312	-0.053	0.43	1.35	1.55
RPM = 1000 H = 0.140 cm ε = 0.118 cm Seal = 0.0508 cm						
Flow =	0 ℓ/sec	-0.17	0.42	2.17	1.64	2.20
	0.631 ℓ/sec	-1.81	0.85	1.95	3.59	3.10
	1.262 ℓ/sec	-2.77	0.62	1.90	4.20	4.19
	1.892 ℓ/sec	-4.36	0.39	2.25	3.79	4.72
RPM = 1000 H = 0.213 cm ε = 0.118 cm Seal = 0.0508 cm						
Flow =	0 ℓ/sec	-0.277	0.371	1.071	1.445	1.694
	0.631 ℓ/sec	-0.987	0.327	1.057	2.589	2.043
	1.262 ℓ/sec	-1.218	0.087	0.958	2.881	2.779
	1.892 ℓ/sec	-1.354	-0.015	0.824	2.369	3.043
RPM = 1000 H = 0.424 cm ε = 0.118 cm Seal = 0.0508 cm						
Flow =	1.267 ℓ/sec	-0.305	0.006	0.328	1.555	1.586
	2.524 ℓ/sec	-0.274	-0.069	0.371	1.060	1.367
	3.155 ℓ/sec	-0.281	-0.079	0.440	0.857	1.236

		Direct Stiffness K	Cross-Coupled Stiffness k	Direct Damping C	Cross-Coupled Damping c	Direct Added Mass M
RPM = 2000 H = 0.140 cm ε = 0.0254 cm Seal = 0.0508 cm						
Flow =	0 ℓ/sec	-0.250	0.430	2.220	1.470	1.680
	0.631 ℓ/sec	-1.360	0.890	2.180	2.800	1.890
	1.262 ℓ/sec	-1.900	0.740	2.240	3950	3.200
RPM = 2000 H = 0.140 cm ε = 0.118 cm Seal = 0.0508 cm						
Flow =	0.631 ℓ/sec	-1.053	0.998	1.975	2.686	2.210
	1.262 ℓ/sec	-1.618	0.891	2.024	3.328	3.033
RPM = 500 H = 0.140 cm ε = 0.0254 cm Seal = 0.0508 cm						
Flow =	0 ℓ/sec	-0.180	0.530	2.350	1.840	2.190
	0.631 ℓ/sec	-2.830	0.470	1.610	4.210	4.260
	1.262 ℓ/sec	-6.220	0.120	1.920	3.650	4.790
	1.892 ℓ/sec	-12.160	0.028	3.650	1.260	3.660
RPM = 500 H = 0.424 cm ε = 0.118 cm Seal = 0.0508 cm						
Flow =	0.631 ℓ/sec	-0.305	0.006	0.328	1.555	1.586
	1.892 ℓ/sec	-0.274	0.069	0.371	1.060	1.367
	3.155 ℓ/sec	-0.281	0.079	0.440	0.857	1.236
RPM = 500 H = 0.140 cm ε = 0.118 cm Seal = 0.0508 cm						
Flow =	0 ℓ/sec	-0.148	0.520	2.350	1.796	2.331
	0.631 ℓ/sec	-3.231	0.920	1.610	4.020	3.909
	1.262 ℓ/sec	-7.190	0.301	1.920	2.930	3.115
	1.892 ℓ/sec	-14.072	0.361	3.650	2.037	3.738

		Direct Stiffness K	Cross-Coupled Stiffness k	Direct Damping C	Cross-Coupled Damping c	Direct Added Mass M
RPM = 1000 H = 0.140 cm ε = 0.118 cm Seal = 0.1016 cm						
Flow =	0 ℓ/sec	-0.220	0.564	1.559	1.398	1.944
	0.631 ℓ/sec	-0.987	0.950	1.671	2.316	2.352
	1.262 ℓ/sec	-1.569	0.864	1.604	3.077	3.132
	1.892 ℓ/sec	-0.236	0.773	2.053	2.657	3.097
RPM = 1000 H = 0.140 cm ε = 0.118 cm Seal = 0.0254 cm						
Flow =	0.631 ℓ/sec	-2.248	0.586	1.758	4.257	3.521
	1.262 ℓ/sec	-3.021	0.372	1.696	4.672	4.660
	1.892 ℓ/sec	-4.229	-0.031	1.707	3.963	4.876
PRESCRIBED INLET SWIRL RPM = 1000 H = 0.140 cm ε = 0.118 cm Seal = 0.0508 cm						
Flow =	0.315 ℓ/sec	-1.239	1.482	2.364	3.364	2.991
	0.631 ℓ/sec	-1.752	1.567	2.447	4.034	3.343
	1.262 ℓ/sec	-3.204	1.585	2.530	5.373	4.294
	1.893 ℓ/sec	-5.831	1.439	3.002	6.153	4.679
	2.524 ℓ/sec	-8.267	1.510	3.548	6.491	4.689

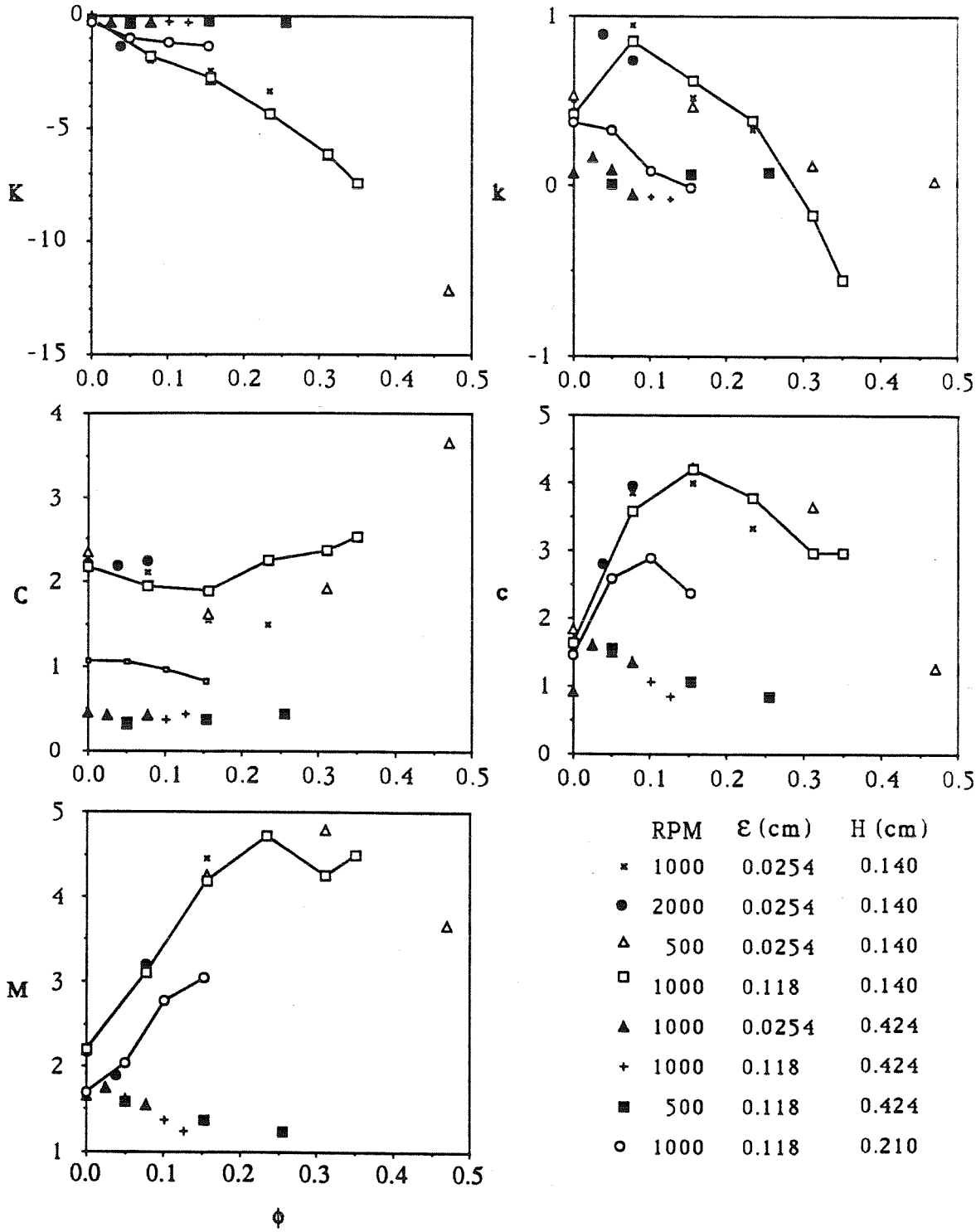

Figure 5.1 Dimensionless direct and cross-coupled stiffness, damping and added mass as functions of the flow coefficient.

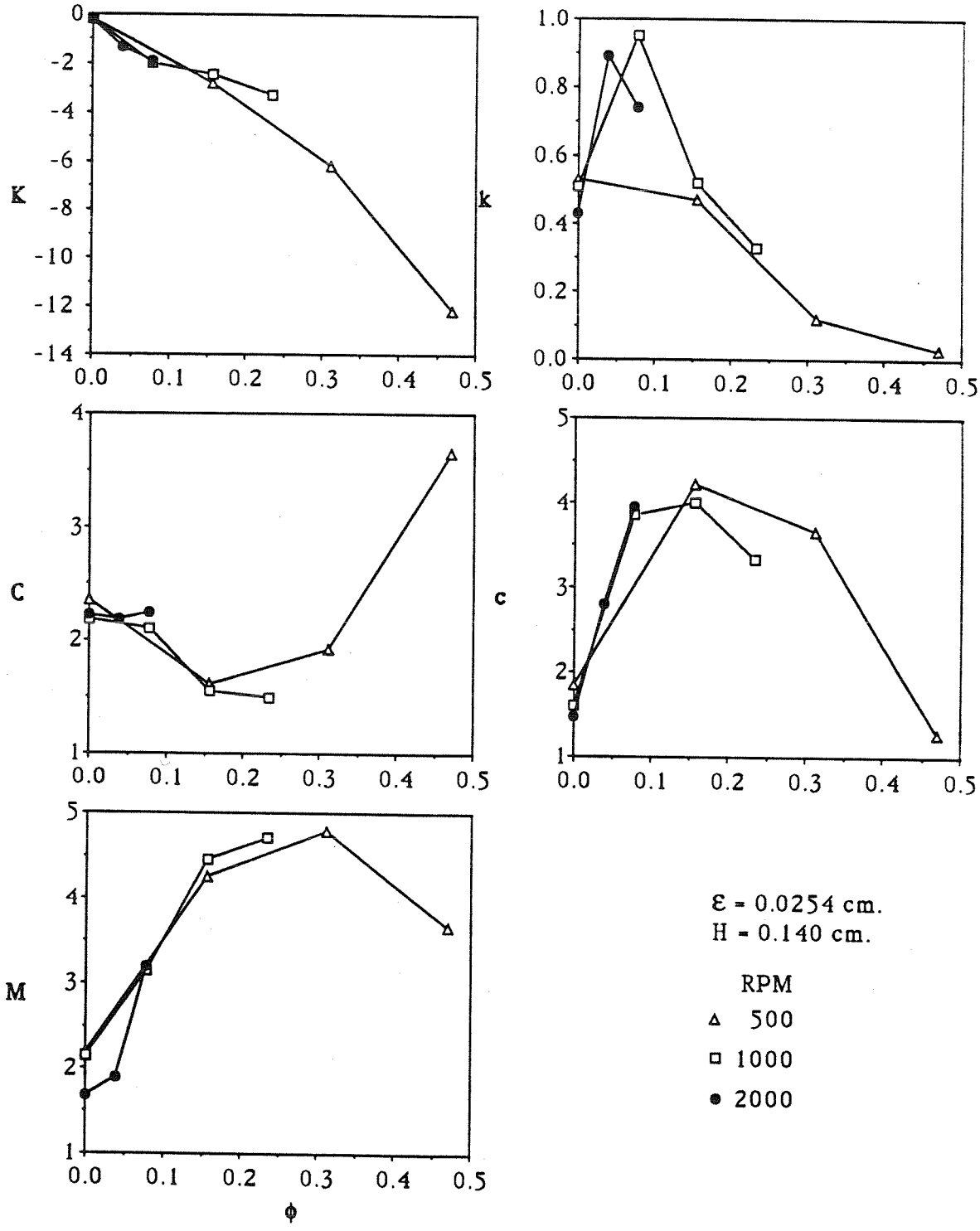

Figure 5.2 Rotordynamic coefficients for different shaft speeds as a function of flow coefficient for an eccentricity of 0.0254 cm.

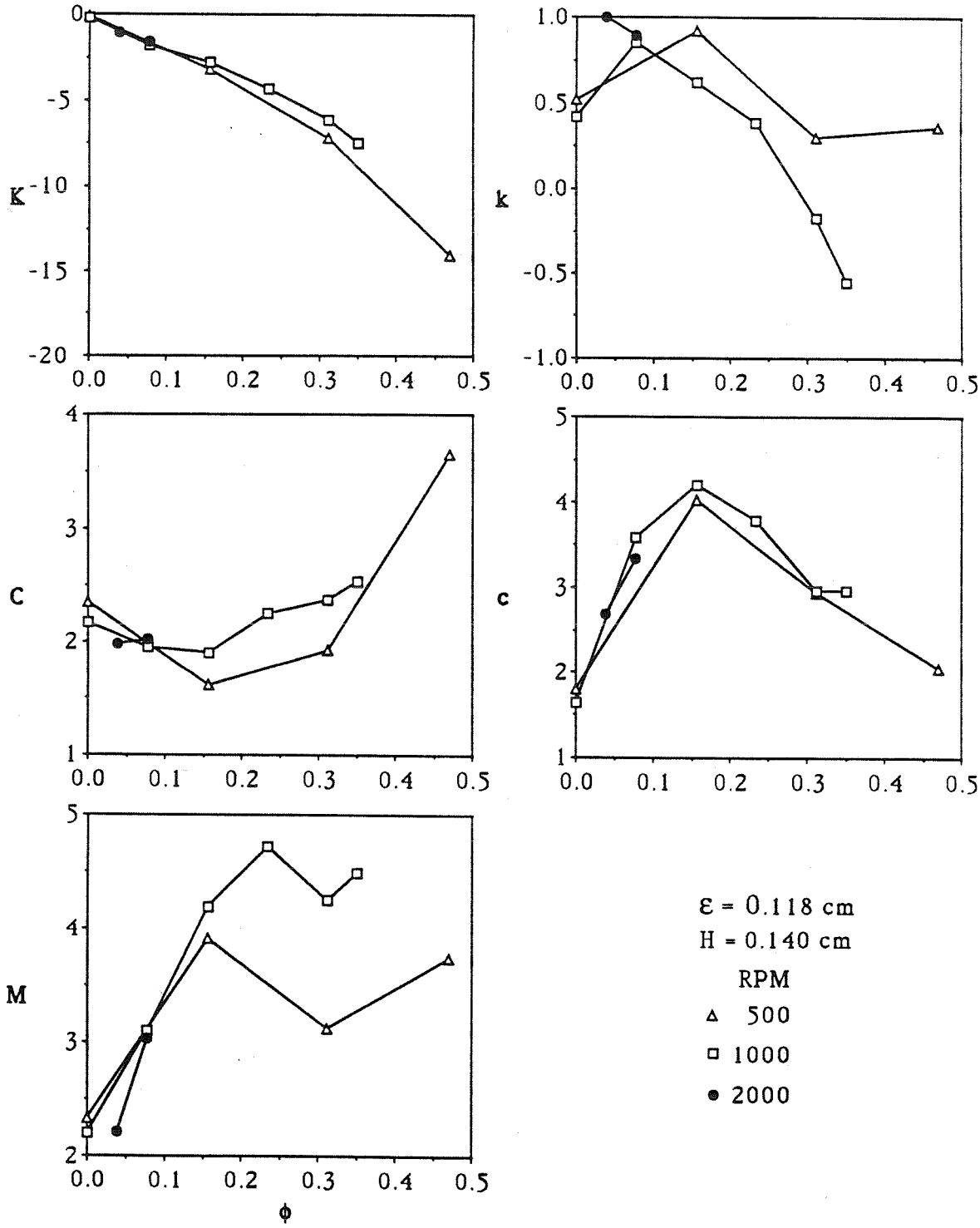

Figure 5.3 Rotordynamic coefficients for different shaft speeds as a function of flow coefficient for an eccentricity of 0.118 cm.

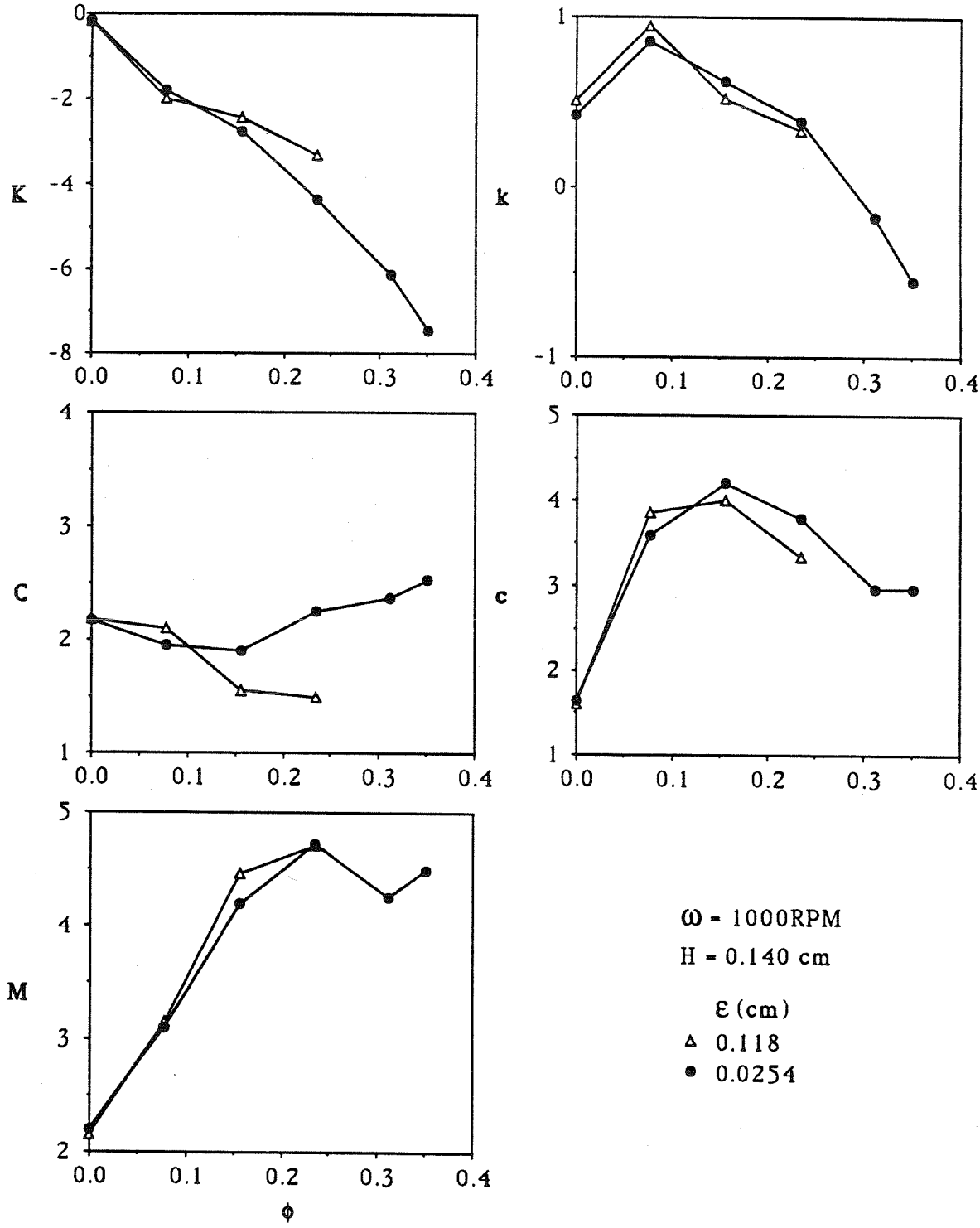

Figure 5.4 Rotordynamic coefficients showing the effect of eccentricity as a function of flow coefficient for 1000 RPM.

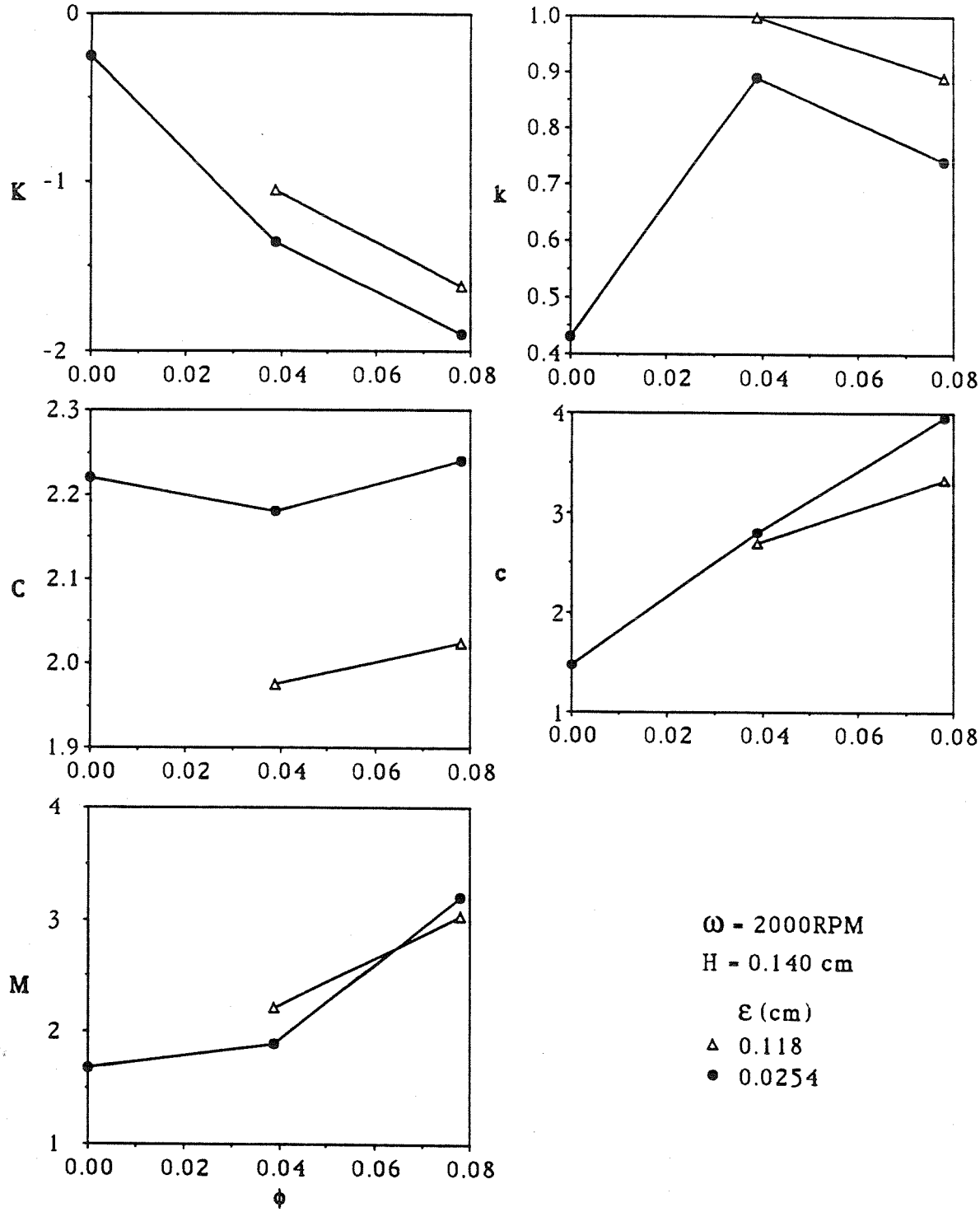

Figure 5.5 Rotordynamic coefficients showing the effect of eccentricity as a function of flow coefficient for 2000 RPM.

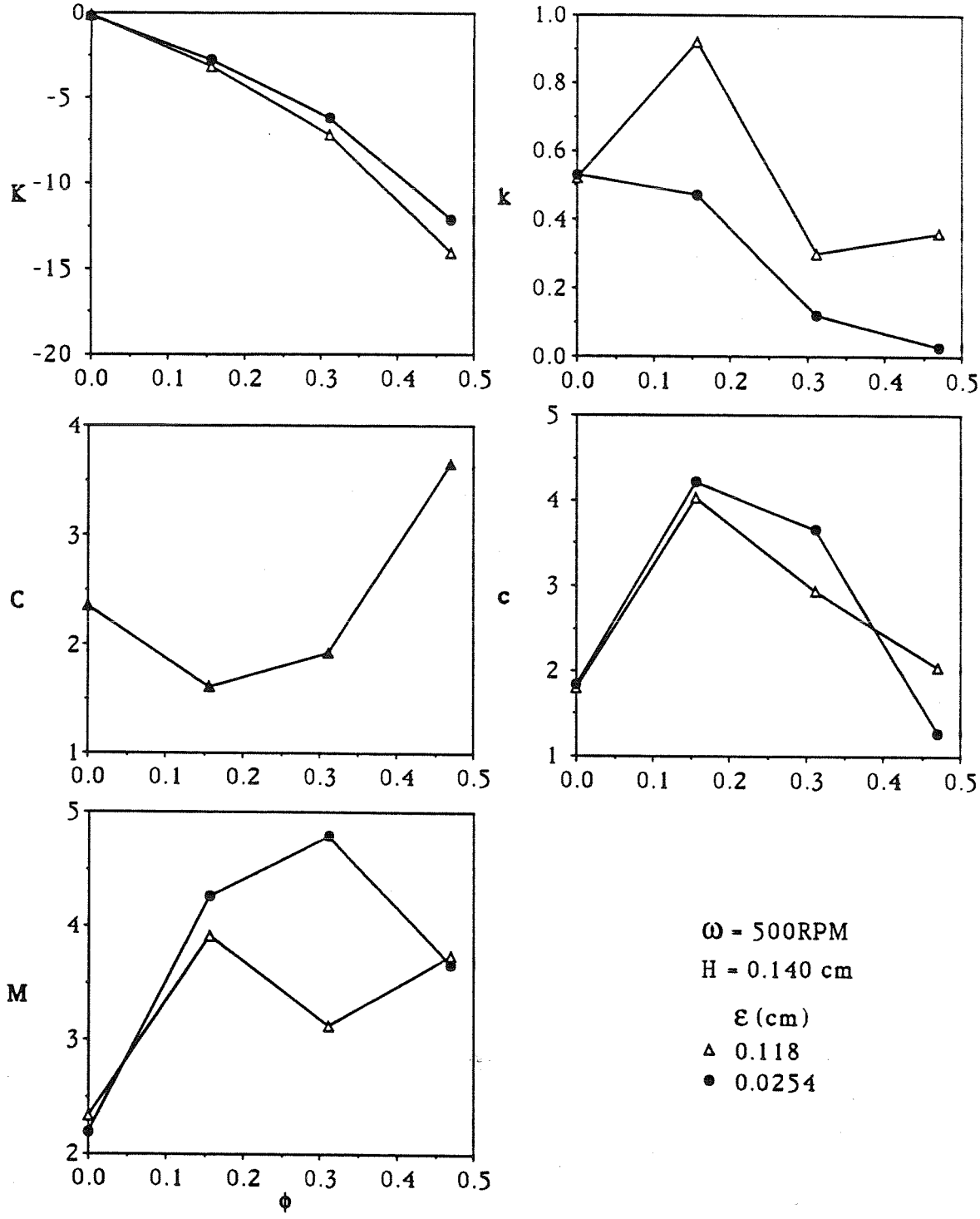

Figure 5.6 Rotordynamic coefficients showing the effect of eccentricity as a function of flow coefficient for 500 RPM.

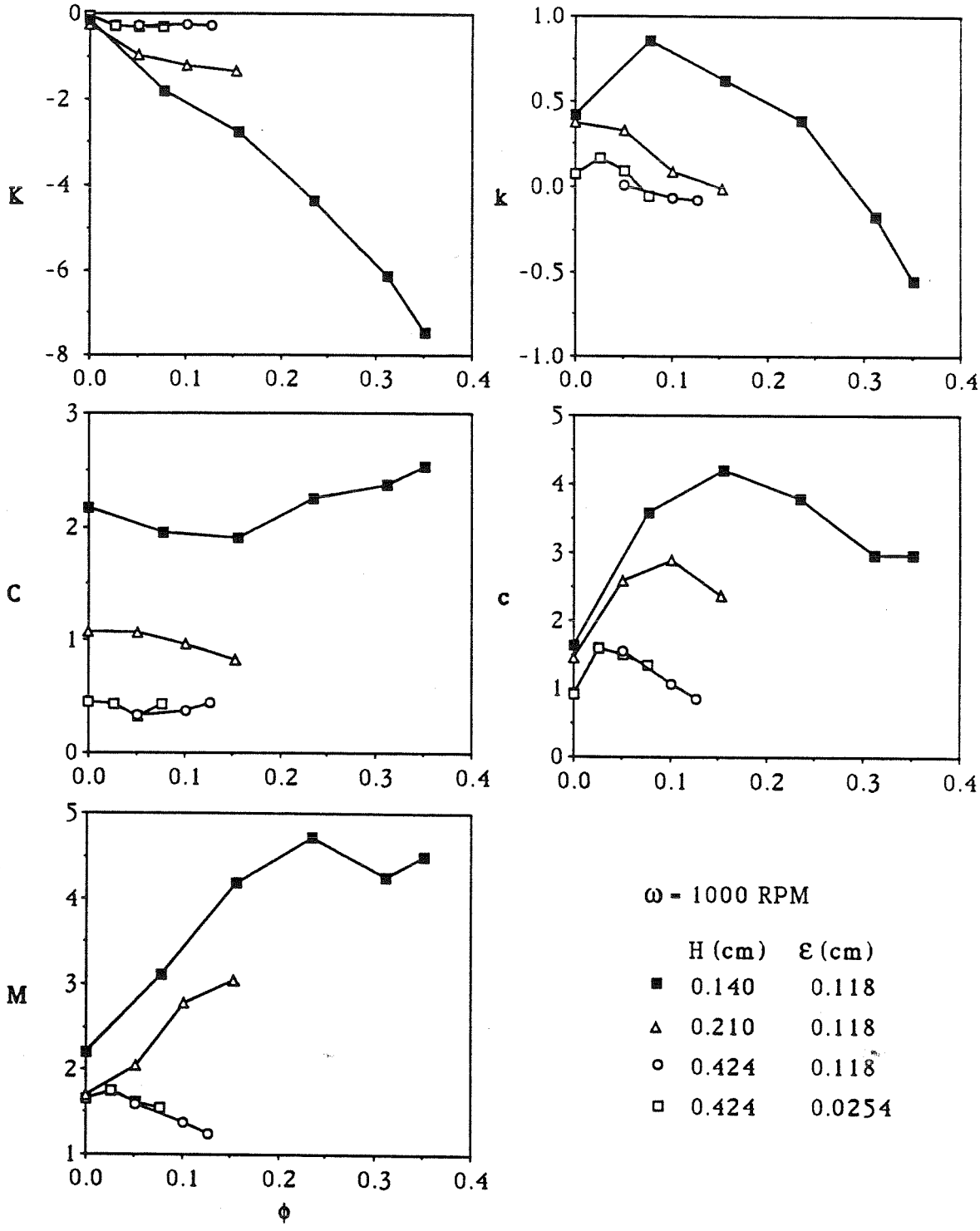

Figure 5.7 Rotordynamic coefficients showing the effect of shroud clearance as a function of flow coefficient for 1000 RPM and an eccentricity of 0.118 cm.

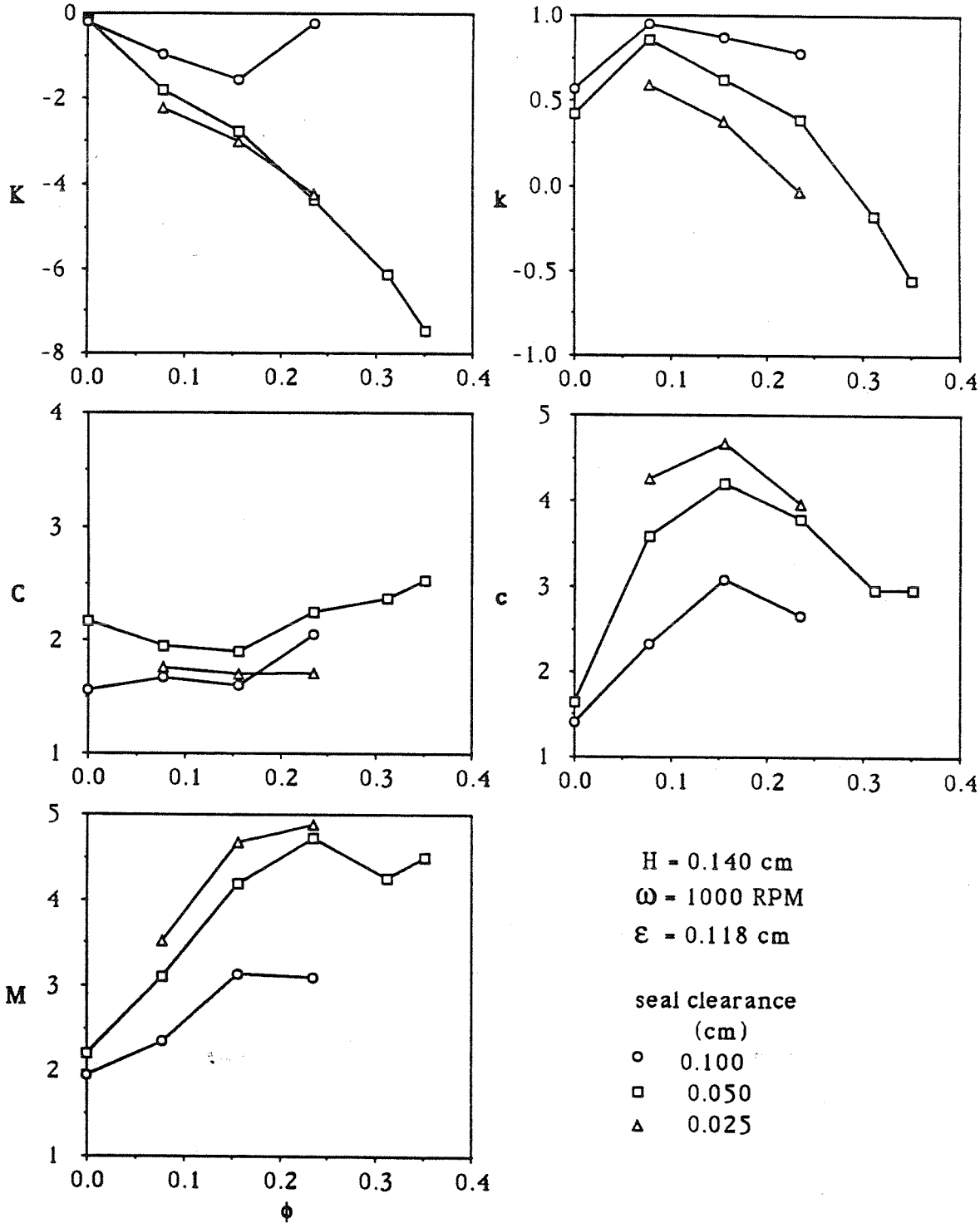

Figure 5.8 Rotordynamic coefficients showing the effect of seal clearance as a function of flow coefficient for 1000 RPM and an eccentricity of 0.118 cm.

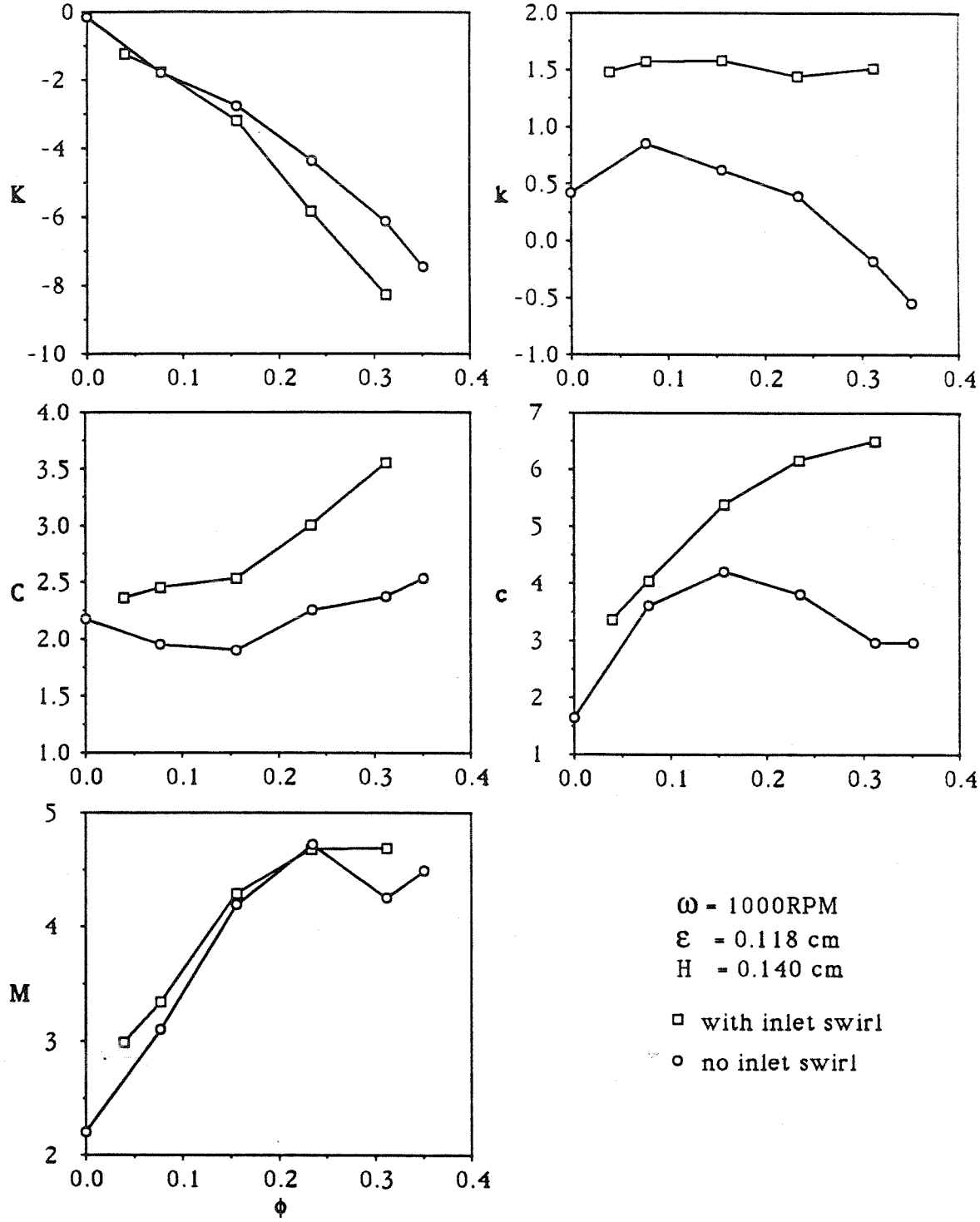

Figure 5.9 Rotordynamic coefficients showing the effect of inlet swirl as a function of flow coefficient for 1000 RPM and for an eccentricity of 0.118 cm.

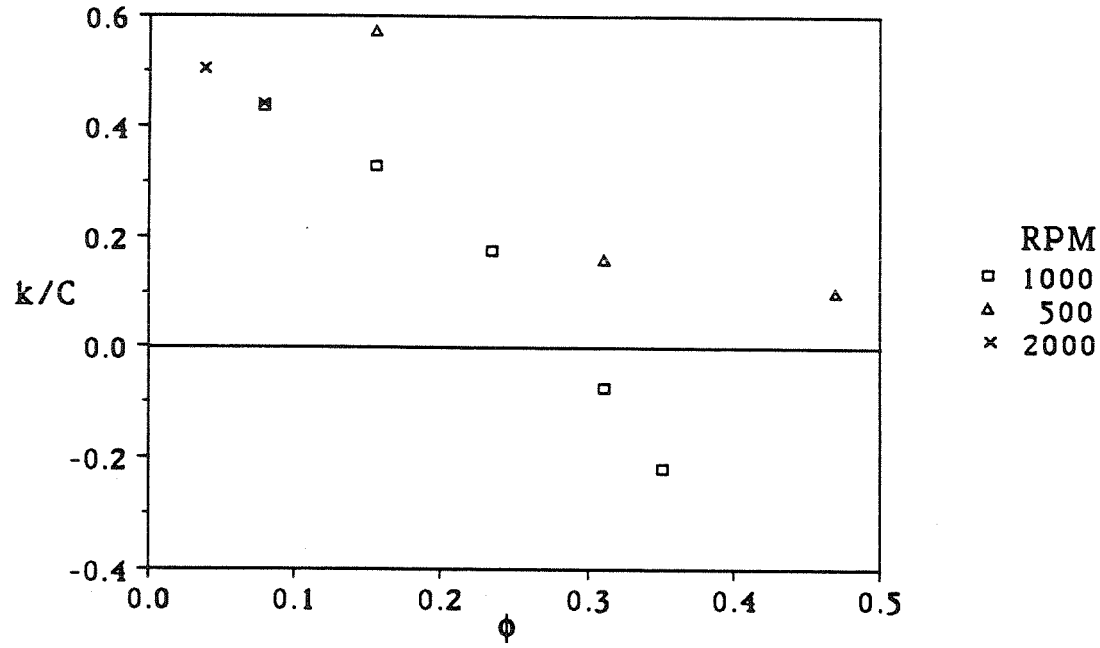

Figure 5.10 Whirl Ratio for an eccentricity ε = 0.118 cm, a clearance H = 0.140 cm, offset δ = 0 and various speeds as a function of flow coefficient.

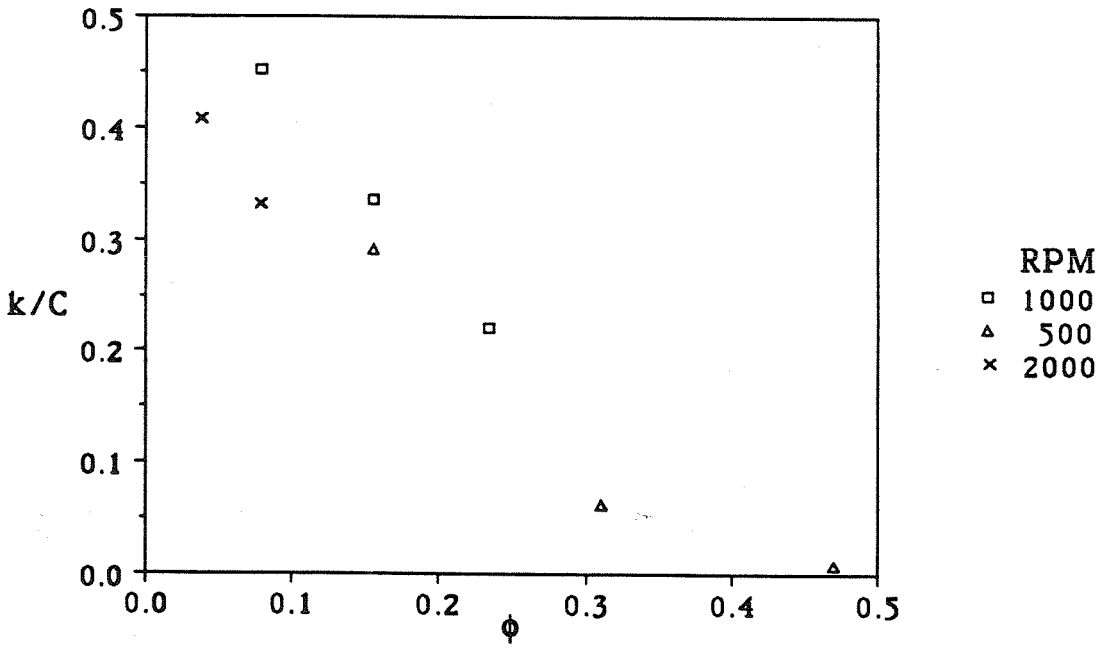

Figure 5.11 Whirl Ratio for an eccentricity ε = 0.0254 cm, a clearance H = 0.140 cm, offset δ = 0 and various speeds as a function of flow coefficient.

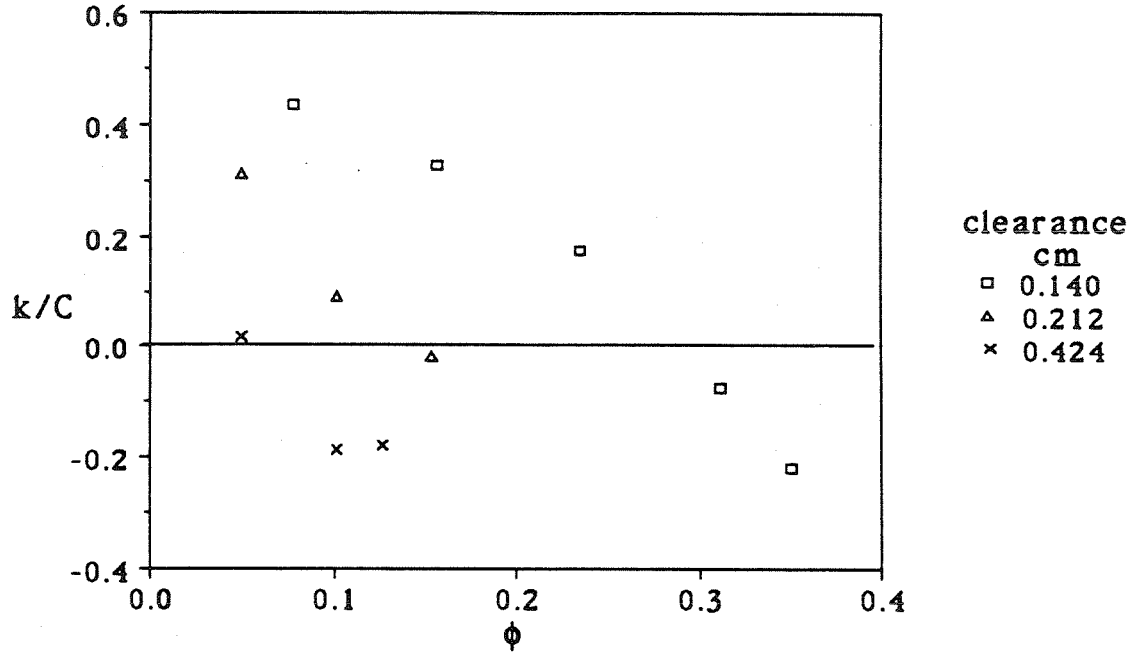

Figure 5.12 Whirl Ratio for an eccentricity ε = 0.118 cm, 1000 RPM, offset δ = 0 and various clearances as a function of flow coefficient.

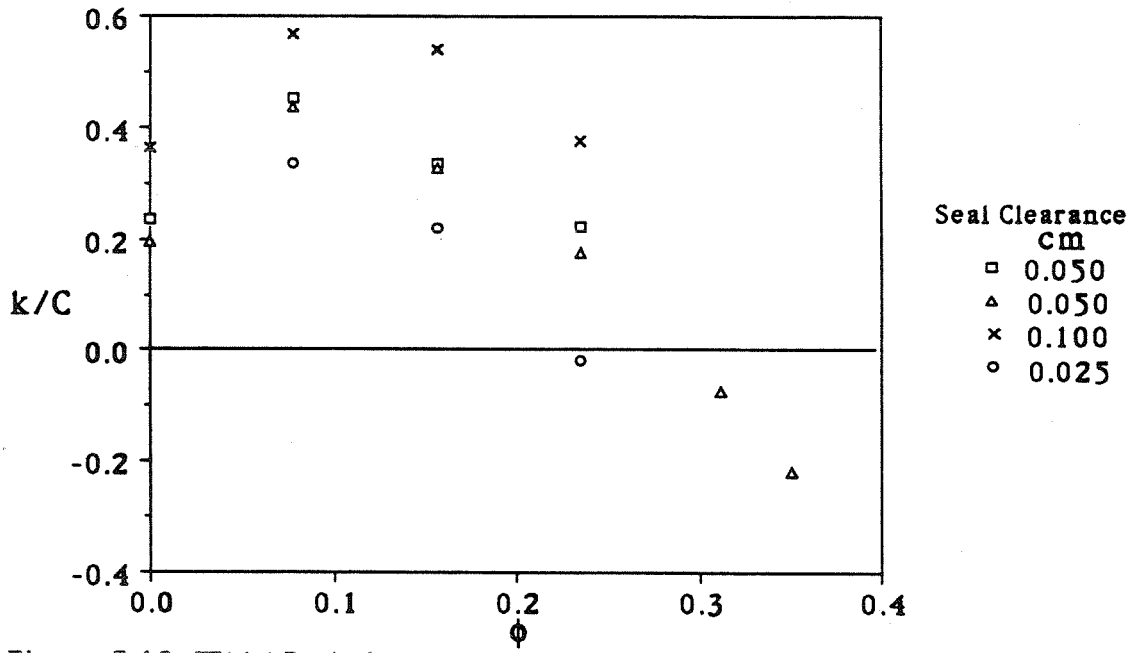

Figure 5.13 Whirl Ratio for an eccentricity ε = 0.118 cm, 1000 RPM, clearance H=0.140 cm, offset δ = 0 and various seal clearances as a function of flow coefficient.

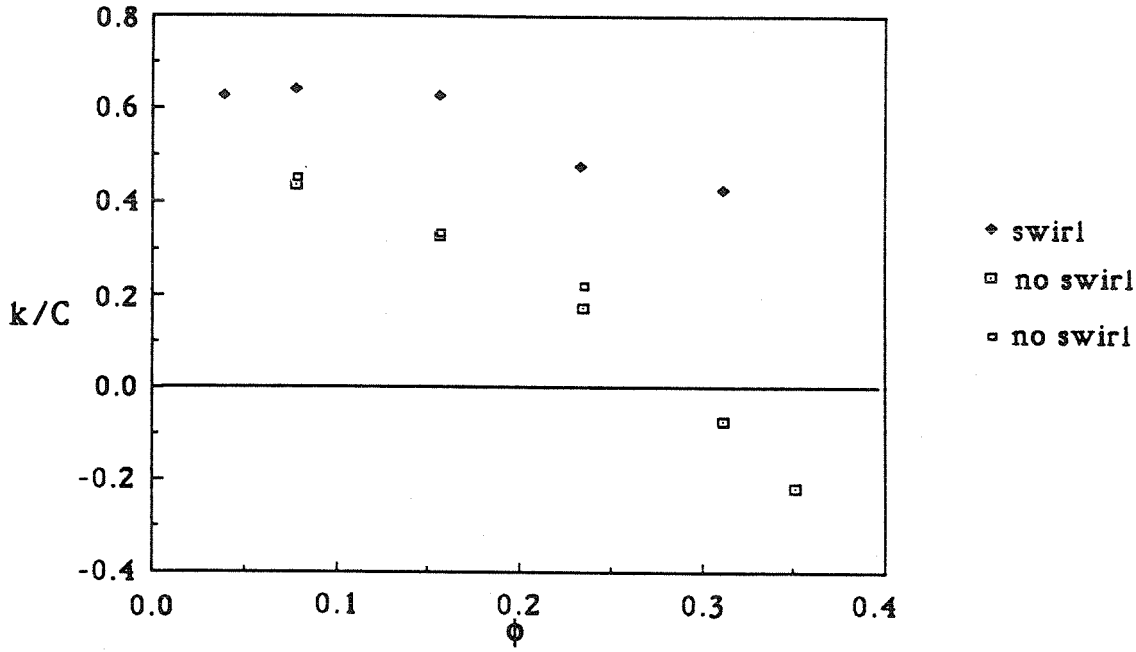

Figure 5.14 Whirl Ratio with and without the inlet swirl vane for an eccentricity ε = 0.118 cm, 1000 RPM, clearance H=0.140 cm, offset δ = 0 as a function of flow coefficient.

CHAPTER 6

THEORETICAL MODEL

6.1 Description of a theoretical model

This section describes a theoretical model for flow between a whirling shroud and a static casing. A numerical simulation was done by applying Childs (1989) theory to the present experimental conditions. Several modifications have been incorporated in the present work and convergent results have been achieved. It should be noted that the results are sensitive to inlet conditions, so appropriate boundary conditions are needed. The way in which the inlet conditions change the results and the sensitivity of the results to the geometry will be discussed.

The prediction by Childs (1989) of the rotordynamic forces uses a bulk flow model for the leakage flow between the impeller shroud and the pump housing based on the meridional momentum, circumferential momentum and continuity equations. The bulk flow model neglects any variation in dependent variables across the fluid. Figure 6.1 is an illustration of the parameters for the theoretical problem. The clearance or leakage path is assumed to be circumferentially symmetric in the undisplaced position. The bulk-flow velocity and pressure components, (U_S, U_θ, P) are calculated as a function of the coordinates, (R, θ, S) and time, (t). The velocities are normalized by the inlet rotor tip speed and the lengths are normalized by the length of the shroud, as follows:

$$u_S = \frac{U_S}{\omega R_2}$$

$$u_\theta = \frac{U_\theta}{\omega R_2}$$

$$p = \frac{P}{(\omega R_2)^2}$$

$$s = \frac{S}{L}$$

$$h = \frac{H}{L}$$

$$r = \frac{R}{L} \qquad (6.1)$$

The governing equations are solved by a perturbation expansion which includes only terms which are linear in the eccentricity ratio, ε and neglects terms which are quadratic or of higher order. Because of the eccentricity, the shaft rotation generates a rotating pressure field. Changes in the velocity and pressure, (u_s, u_θ, p) that are due to changes in the clearance, $h(s,\theta,t)$ are represented by the following expansions.

$$h = h^0 + \varepsilon h^1$$

$$u_s = u_s^0 + \varepsilon u_s^1$$

$$u_\theta = u_\theta^0 + \varepsilon u_\theta^1$$

$$p = p^0 + \varepsilon p^1 \qquad (6.2)$$

The geometry is described by the axial location z(s), the radial location r(s), and the clearance h(s) as functions of the meridional coordinate, s. In the numerical procedure, the first derivatives of these functions are calculated using forward differences and the last node point is assumed to have the same derivative as the previous node.

Substitution of the expanded variables given by equation (6.2) into the governing equations yields a set of zeroth and first order equations. The zeroth order equations describe the flow through the centered impeller and are solved for (u_s^0, u_θ^0, p^0) as described in the next section. The solution of the first order equations for $u_s^1(s)$, $u_\theta^1(s)$, $p^1(s)$ is described in section 6.

6.2 Zeroth order solutions

The continuity equation can be solved exactly for $u_s^0(s)$, since r(s) and $h^0(s)$ are known and is given by:

$$u_s^0(s) = u_s^0(0)\frac{r(0)}{r(s)}\frac{h^0(0)}{h^0(s)} \tag{6.3}$$

Since it is needed in later calculations, the derivative for the axial flow velocity is also calculated at each node, using

$$\frac{du_s^0}{ds} = -u_s^0\left(\frac{1}{r}\frac{dr}{ds} + \frac{1}{h^0}\frac{dh^0}{ds}\right) \tag{6.4}$$

The meridional momentum and circumferential momentum equations which are used to solve for the velocity $u_\theta^0(s)$, and the pressure $p^0(s)$ are as follows:

$$\frac{dp^0}{ds} = \frac{(u_\theta^0)^2}{r}\frac{dr}{ds} - \left(\frac{\lambda_r+\lambda_s}{2} - \frac{1}{h^0}\frac{dh^0}{ds} - \frac{1}{r}\frac{dr}{ds}\right)(u_s^0)^2 \tag{6.5}$$

$$\frac{du_\theta^0}{ds} = -\frac{u_\theta^0}{r}\frac{dr}{ds} - \frac{[\lambda_r\,(u_\theta^0 - \frac{L}{R_2}r) + \lambda_s u_\theta^0]}{2} \tag{6.6}$$

where the wall shear stresses on the fluid are modeled following Hirs' (1972) approach. The turbulent flow is treated by considering only the bulk-flow relative to a surface or wall and the corresponding shear stress at that surface or wall. The theory is characterized by an empirical power law function which relates the wall shear stress and the Reynolds number, which is defined in terms of the bulk flow velocity relative to the wall at which the shear stress is exerted. This definition is expressed nondimensionally as a friction factor at the stator and the rotor as follows:

$$\lambda_S = ns\,\frac{L}{H^0}\,Re^{ms}\,[1+(u_\theta^0/u_s^0)^2]^{\frac{ms+1}{2}}$$

$$\lambda_r = nr\,\frac{L}{H^0}\,Re^{mr}\,[1+[(u_\theta^0 - \frac{L}{R_2}r)/u_s^0]^2]^{\frac{mr+1}{2}}$$

$$Re = \frac{2\,H\,U_s}{\nu} \tag{6.7}$$

The subscripts r and s refer to parameters relating to the different stresses due to the rotor and stator respectively. The parameters (ns,ms) and (nr,mr) are empirical coefficients which account for different surface roughness on the stator and rotor respectively. As in Childs (1989), both walls were assumed smooth; for the present calculation, the following values were assumed:

$$nr=ns=0.079$$

and

$$mr=ms=-0.25.$$

These values are similar to those obtained by Yamada (1960) from measurements of the flow between rotating cylinders. It should be noted that these parameters depend weakly on the roughness of the surface, inertia effects, type of flow (flow under influence of pressure gradient or due to sliding of a surface or combination of flows).

Childs's model has been programmed so that predictions of the rotordynamic coefficients can be compared with experimental results. A fourth order Runge-Kutta scheme is used to numerically integrate the ordinary differential equations (6.5) and (6.6) from s=0 to s=1. The integration requires two initial conditions to solve for $u_{\theta 0}(s)$ and $p_0(s)$.

The nondimensional tangential velocity $u_\theta{}^0(0)$ describes the amount of swirl that the flow in the volute at the exit of the impeller would deliver to the leakage path. Most of the physical experiments in this research had zero inlet swirl and as already mentioned, no "resonances". It will be shown in the next chapter that to model the average flow in the path between the stationary casing and the rotating shroud, only one value for the inlet swirl does not display "resonances". It will also be shown that for the present calculations this ratio will depend on parameters such as the shroud clearance and the flowrate.

6.3 Description of loss coefficients

The analytical model incorporates various loss coefficients which will be

discussed in this section. The losses at the inlet are accounted for by an inlet loss coefficient ξ. Therefore the zeroth order pressure, $p^0(0)$, is expressed nondimensionally as:

$$p^0(0) = p_s - \frac{1}{2}(1+\xi)\,(u_s{}^0)^2(0) \tag{6.8}$$

where the supply pressure, ps for the leakage flow along the impeller face is just the discharge pressure of the impeller.

In many pumps, a wear ring seal at the leakage flow exit provides a restriction so losses are incurred by the flow as it passes through the seal. Here this is modeled by the exit loss coefficient Cde. When this is used in the zeroth order solution, the mass flow rate can be related to the pressure drop across the complete leakage flow. Thus, Childs defines the exit loss coefficient in terms of nondimensional variables as:

$$C_{de} = \frac{p(L) - p_e}{\frac{1}{2} u_s{}^2\,(L)} \tag{6.9}$$

where the pressure at the exit of the leakage flow, Pe, is just the inlet pressure to the impeller.

Since the losses can have a substantial effect on the radial and tangential forces, it is important to consider appropriate values for Cde. If there were no exit losses, the Bernoulli's equation would yield:

$$p_e = p(L) + \frac{1}{2} u_s{}^2(L) \tag{6.10}$$

which would give Cde = -1. In practice the exit pressure recovery is not complete and the exit pressure is somewhat lower than given by Bernoulli's equation. At the other extreme, if the jet dynamic head is completely lost then the exit pressure would just be the pressure in the annulus at the exit of the leakage path; hence C_{de} would be zero.

Another estimate of the losses for the wear-ring seal can be obtained by modeling the flow using the exact geometry of the seal, as shown in figure 6.4. Further assumptions need to be made along the leakage path, in the vicinity of

the seal. If there are no entrance losses to the seal, Bernoulli's equation can be applied between station 1 at the end of the leakage path, and station 2 at the entrance to the seal:

$$p_1 + \frac{1}{2} u_1^2 = p_2 + \frac{1}{2} u_2^2 \tag{6.11}$$

and continuity gives

$$u_2 = u_2 \frac{A}{A_s} \tag{6.12}$$

where the leakage area, $A=2\pi RH$, where R is the radius at the inlet to the seal, H is the leakage path clearance and the seal area , $A_s=2\pi R_s H_s$, where R_s is the radius of the seal, H_s is the seal clearance.

If frictional losses along the seal can be ignored, Bernoulli's equation can be applied between station 2 and station 3.

$$p_2 + \frac{1}{2} u_2^2 = p_3 + \frac{1}{2} u_3^2 \tag{6.13}$$

and from continuity along the seal:

$$u_3 = u_2 = u_1 \frac{A}{A_s} \tag{6.14}$$

Combining the above equations leads to a relation between station 1 and station 3 in figure 6.4.

In the region of the seal exit, two extreme cases will be considered. If the velocity head at the seal exit is recovered then Bernoulli's equation can be applied.

$$p_e = p_3 + \frac{1}{2} u_3^2 \tag{6.15}$$

On the other hand if the jet dynamic head is completely lost at the exit so that $p_e=p_3$, and finally the equation can be written as

$$p_1 - p_e = \frac{1}{2}\left(\left(\frac{A}{A_s}\right)^2 - 1\right) u_1^2 \qquad (6.16)$$

Comparison of the above equation with equation 6.9 leads to an estimate of C_{de} which models the losses incurred as a result of the seal.

$$Cde = \left(\left(\frac{A}{A_s}\right)^2 - 1\right) \qquad (6.17)$$

Applying the present experimental configuration to the above equation, with R=44 mm and R_s=35 mm, results in the following table of values of C_{de} for different shroud clearances, H and seal clearances, H_s.

Table 6.1 Values for Cde for different H and H_s.

	H		
	0.1397 cm	0.2134 cm	0.4242 cm
0.025 cm	47	111	449
H_s 0.050 cm	11	27	109
0.100 cm	2	6	27

It is interesting to observe the range of coefficients in the above table. By comparison, the Sulzer geometry used in the calculations made by Childs, (R=118 mm, R_s=118-0.36 mm, H=5.8 mm, H_s=0.36 mm) would result in a value of C_{de}=259.

It can be seen from the foregoing analysis that the various geometry configurations will give rise to a wide range of values for C_{de}, the exit loss coefficient. If it were possible to model the geometry of the seal exactly, then the exit loss coefficient would be less important, since it would emerge from the calculation. This point will be made in the chapter which discusses the numerical results.

6.4 Pressure distribution

As part of the experimental procedure, some of the data included pressure distributions obtained experimentally from the water manometers. (See section 3.3). So it would seem reasonable to compare them to the numerically generated pressure distributions. Two such comparisons are shown in figures 6.2 and 6.3 for two different flow coefficients. The meridional distance is normalized by the shroud length and begins at the leakage inlet. The pressures are normalized by the dynamic head at the leakage inlet and are expressed relative to the leakage inlet pressure. The numerical results are shown for three different inlet swirl values. For the experimental results, only distributions along the inclined part of the shroud are shown, as the pressure taps do not extend into the area surrounding the seal. The bumps in the numerical curves represent the pressure distribution along the seal, which has a smaller clearance than the shroud clearance. The three different experimental results are from the three sets of pressure taps which are arranged circumferentially 120° apart. The first thing to note is that the variation in pressure of the experimental results due to a different circumferential location is much smaller compared to the variation in the numerical results due to a different inlet swirl value. Clearly, the choice of inlet swirl is an important parameter in order to model the experiment. One of the motivations would be to check what value of inlet swirl results in the theoretical distribution being closest in magnitude to the experimental pressure distribution. For the higher flowrate shown in figure 6.3, it would appear that an inlet swirl of $\Gamma=0$ results in the magnitude of the numerical pressure distribution being closest to the experimental pressure distribution. This is not too surprising as the inlet swirl vane was not in place (the implication is that the inlet swirl is zero) for the experiments corresponding to the pressure distributions which are shown. In figure 6.3, the pressure drop predicted by an inlet swirl of zero is closer in magnitude to the experimental results. However, an inlet swirl of 0.5 predicts the distribution in pressure near the inlet of the leakage path. The numerical results are based on a bulk-flow model. Thus, it would seem reasonable to take as the flow velocity, the average of the velocity of the two shroud surfaces. This would be an inlet swirl of 0.5. (recall that the definitionof the swirl is the tangential velocity

normalized by the rotor velocity.) The only difference between the two figures is the flowrate. Thus it would seem that at higher flowrates, it is not correct to average the velocities of the surfaces at the inlet, as the flow dampens out the effect of swirl.

6.5 Perturbation analysis

Once a solution to the zeroth order equations has been obtained, the calculation proceeds to the solution of the first order equations. These equations are functions of all the variables (s,θ,t).

The θ dependency is eliminated by assuming a simple sinusoidal variation:

$$u_s^1 = u_s^1{}_c \cos\theta + u_s^1{}_s \sin\theta$$

$$u_\theta^1 = u_\theta^1{}_c \cos\theta + u_\theta^1{}_s \sin\theta$$

$$p^1 = p^1{}_c \cos\theta + p^1{}_s \sin\theta \qquad (6.18)$$

In other words, the higher order perturbations like $\sin n\theta$, $\cos n\theta$, $n>1$ are neglected. When the relations in (6.18) are substituted into the first order partial differential equations for u_s^1, u_θ^1 and p^1 and the coefficients of $\cos\theta$ and $\sin\theta$ are equated, six equations result. Alternatively, complex variables can be introduced to express the above variables as complex functions of (s,t).

$$\underline{u}_s^1 = u_s^1{}_c + j u_s^1{}_s$$

$$\underline{u}_\theta^1 = u_\theta^1{}_c + j u_\theta^1{}_s$$

$$\underline{p}^1 = p^1{}_c + j p^1{}_s \qquad (6.19)$$

Thus the equations result in three complex differential equations for $\underline{u}_s^1(s,t)$, $\underline{u}_\theta^1(s,t)$, and $\underline{p}^1(s,t)$. The time dependency, t is eliminated from the differential equations, by assuming a harmonic perturbation in time, as follows:

$$\underline{u}_s^1(s,\tau) = \bar{u}_s^1(s)\, e^{i\Omega t}$$

$$\underline{u}_\theta^1(s,\tau) = \bar{u}_\theta^1(s)\, e^{i\Omega t}$$

$$\underline{p}^1(s,\tau) = \bar{p}^1(s)\, e^{i\Omega t} \qquad (6.20)$$

So the partial differential equations are now reduced to three complex ordinary differential equations for $\bar{u}_s{}^1(s)$, $\bar{u}_\theta{}^1(s)$, and $\bar{p}^1(s)$ as follows.

$$\frac{d}{ds}\begin{pmatrix}\bar{u}_s{}^1\\ \bar{u}_\theta{}^1\\ \bar{p}^1\end{pmatrix}+[A]\begin{pmatrix}\bar{u}_s{}^1\\ \bar{u}_\theta{}^1\\ \bar{p}^1\end{pmatrix}=\begin{pmatrix}g_1\\ g_2\\ g_3\end{pmatrix} \tag{6.21}$$

$$[A]=\begin{pmatrix}\frac{1}{r}\frac{dr}{ds}+\frac{1}{h^0}\frac{dh^0}{ds} & -j\frac{\omega T}{r} & 0\\ \frac{A_{3\theta}}{u_s{}^0} & \frac{A_{2\theta}+j\Gamma T}{u_s{}^0} & -j\frac{1}{ru_s{}^0}\\ A_{3s}-u_s{}^0\left(\frac{1}{r}\frac{dr}{ds}+\frac{1}{h^0}\frac{dh^0}{ds}\right)+j\Gamma T & A_{2s}+j\omega T u_s{}^0 & 0\end{pmatrix} \tag{6.22}$$

$$\begin{pmatrix}g_1\\ g_2\\ g_3\end{pmatrix}=\frac{H_2}{L}\begin{pmatrix}\zeta+j\frac{\Gamma T}{h^0}\frac{dz}{ds}\\ -\frac{A_{1\theta}}{u_s{}^0}\frac{dz}{ds}\\ -A_{1s}\frac{dz}{ds}-u_s{}^0\zeta-ju_s{}^0\frac{\Gamma T}{h^0}\frac{dz}{ds}\end{pmatrix} \tag{6.23}$$

where,

$$\Gamma=\Omega-\omega\frac{u_\theta{}^0}{r}\frac{R_2}{L}$$

$$\zeta=\frac{u_s{}^0}{h^0}\left(\frac{d^2z}{ds^2}-\frac{1}{h^0}\frac{dh^0}{ds}\frac{dz}{ds}\right) \tag{6.24}$$

and the rest of the variables are explained in appendix C.

6.6 First order solutions

The solution of the first order equations requires three boundary conditions. The following conditions were assumed.

1) The entrance perturbation velocity is zero.

$$\bar{u}_\theta{}^1(0) = 0 \tag{6.25}$$

2) The expression for the entrance loss coefficient results in the following relation between $\bar{p}^1(0)$ and $\bar{u}_s{}^1(0)$.

$$\bar{p}^1(0) = -(1+\xi)\,\bar{u}_s{}^1(0) \tag{6.26}$$

3) The expression for the exit loss coefficient results in the following relation between $\bar{p}^1(1)$ and $\bar{u}_s{}^1(1)$.

$$\bar{p}^1(1) = Cde\; u_s{}^0(1)\bar{u}_s{}^1(1) \tag{6.27}$$

There is no indication that these boundary conditions are physically reasonable assumptions. They all follow from the original boundary conditions which assume a constant relation for these unsteady flows. This may not be true in practice, as there may be oscillations in the flow before it enters the leakage path. It is suggested that in particular, the value of the first boundary condition be varied to see its effect on the rotordynamic forces. The other two boundary conditions result from assumptions about the loss at the inlet and the exit of the leakage flows, so the same comments apply as noted for the first boundary condition. In all cases, the actual losses in the unsteady flow may well be complex and frequency dependent.

Note that two of the above conditions apply at the entrance, s=0 and one at the exit, s=1. The problem is converted to an initial value problem in the following way. The exit condition is ignored temporarily and is replaced by an assumed initial condition imposed on $\bar{u}_s{}^1(0)$. From the second boundary condition $\bar{p}^1(0)$ can then be calculated and hence all three perturbation variables are defined at s=0. The differential equations are then integrated to s=1 using a fourth order Runge-Kutta scheme. At this point, the exit value, $\bar{p}^1(1)$, must be checked against the prescribed boundary condition. A new or

improved value for $\bar{u}_s{}^1(0)$ is then evaluated using Newton's method as follows. Suppose the initial guess for $\bar{u}_s{}^1(0)$ is α; then the improved value α^*, is obtained from

$$\alpha^* = \alpha - \frac{f(\alpha)}{f'(\alpha)} \tag{6.28}$$

where $f(\alpha)$ is the function to be minimized, in this case the boundary condition at the exit.

$$f(\alpha)=\bar{p}^1(1) - Cde\, u_s{}^0(1)\bar{u}_s{}^1(1) \tag{6.29}$$

The derivative $\frac{df(\alpha)}{d\alpha}$ is not known explicitly. Therefore the following approximation was used:

$$\alpha=(a_1,a_2) \tag{6.30}$$

$$\Delta a_1=0.01a_1 \tag{6.31}$$

$$\Delta a_2=0.01a_2 \tag{6.32}$$

$$\frac{df(\alpha)}{d\alpha} = \left(\frac{f(a_1+\Delta a_1,a_2)-f(a_1,a_2)}{\Delta a_1} + j\, \frac{f(a_1,a_2+\Delta a_2)-f(a_1,a_2)}{\Delta a_2} \right) \tag{6.33}$$

When the function was minimized to the desired accuracy, the first order velocity and pressure profiles were then calculated. For later purposes, the real and imaginary components of $\bar{u}_s{}^1, \bar{u}_\theta{}^1, \bar{p}^1$ are defined as follows:

$$\begin{pmatrix} \bar{u}_s{}^1 \\ \bar{u}_\theta{}^1 \\ \bar{p}^1 \end{pmatrix} = \begin{pmatrix} f_{1c}+j\, f_{1s} \\ f_{2c}+j\, f_{2s} \\ f_{3c}+j\, f_{3s} \end{pmatrix} \tag{6.34}$$

Finally, the normal and tangential forces were calculated by integrating the first order profiles for each whirl ratio. The resulting nondimensional normal and tangential forces are:

$$F_n = \frac{R_2}{H_2}\left(\frac{Us_2}{\omega R_2}\right)^2 \int_0^1 [f_{3c}\frac{dz}{ds} + f_{1c}\frac{dr}{ds}B_{s1} - f_{1s}B_{\theta 1}]$$

$$+ [f_{2c}\frac{dr}{ds}B_{s2} - f_{2s}B_{\theta 2} - \frac{dz}{ds}\frac{dr}{ds}B_{s3}]$$

$$F_t = \frac{R_2}{H_2}\left(\frac{Us_2}{\omega R_2}\right)^2 \int_0^1 [f_{3s}\frac{dz}{ds} + f_{1s}\frac{dr}{ds}B_{s1} - f_{1c}B_{\theta 1}]$$

$$+ [f_{2s}\frac{dr}{ds}B_{s2} - f_{2c}B_{\theta 2} - \frac{dz}{ds}\frac{dr}{ds}B_{\theta 3}] \qquad (6.35)$$

where the new coefficients, B_{s1}, $B_{\theta 1}$, etc. are defined in appendix C.

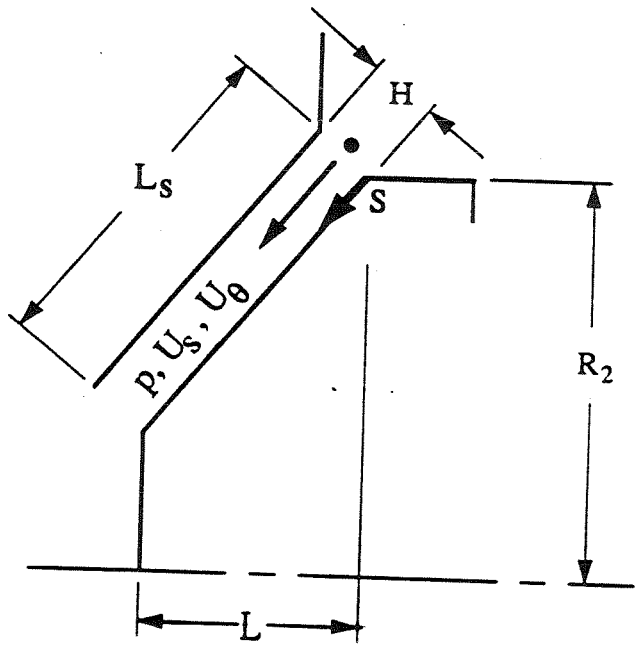

Figure 6.1 Illustration of the variables for the numerical calculation.

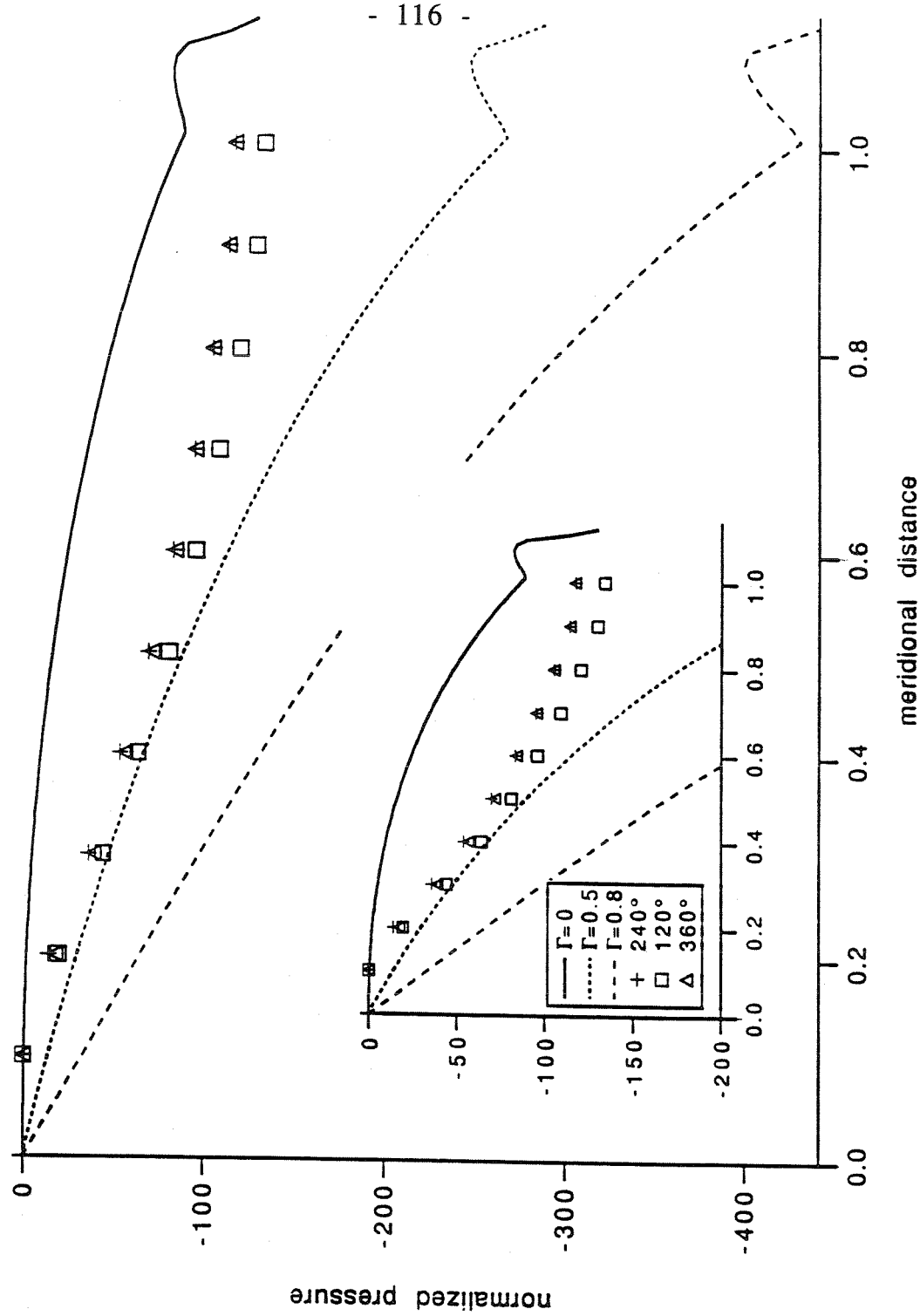

Figure 6.2 Numerical predictions of the pressure distribution along the shroud for different inlet swirl ratios, compared with the experimental observation for 1000RPM, a clearance of 0.0424cm, and a flow of 10 GPM.

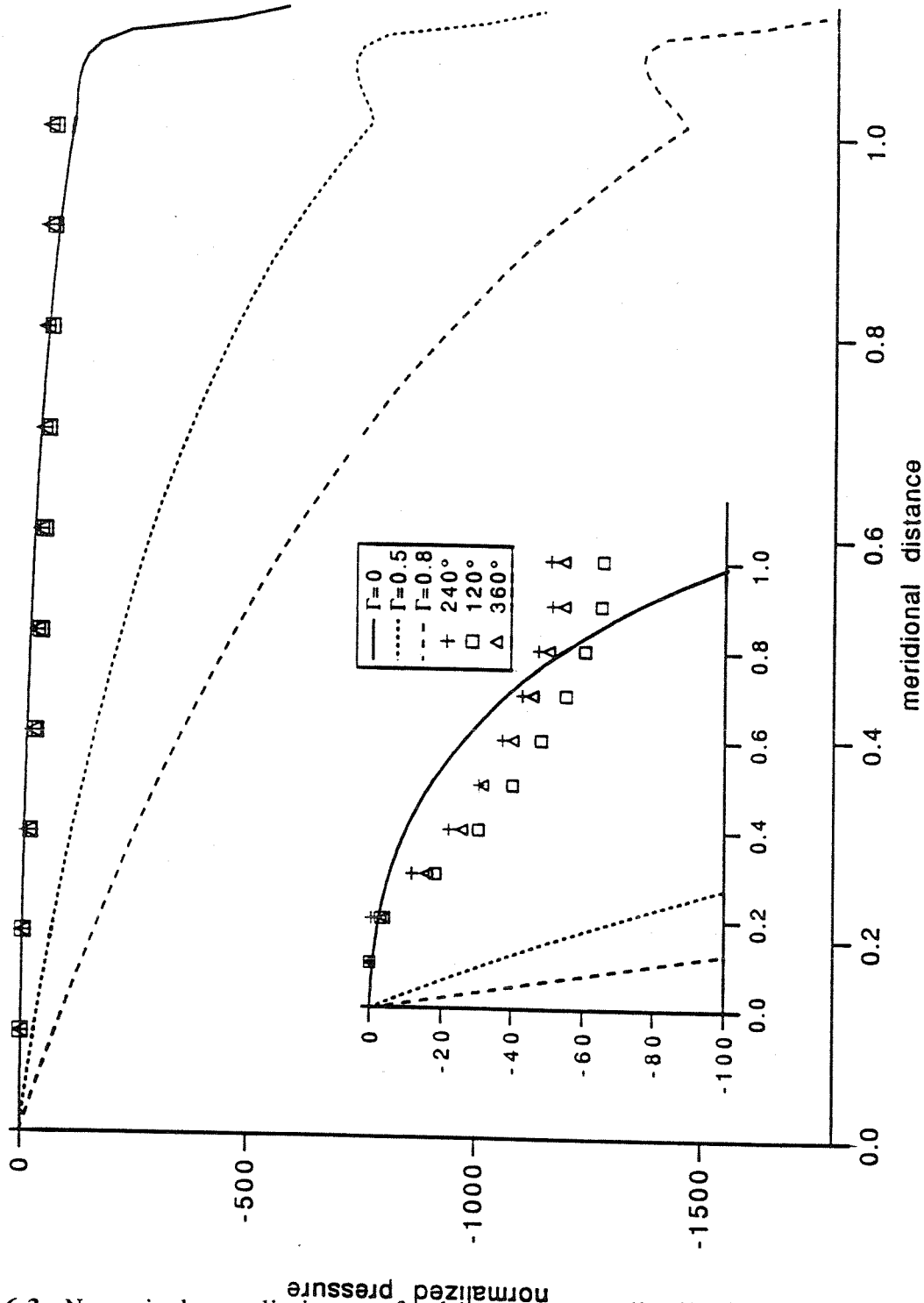

Figure 6.3 Numerical predictions of the pressure distribution along the shroud for different inlet swirl ratios, compared with the experimental observation for 1000RPM, a clearance of 0.0424cm, and a flow of 30 GPM.

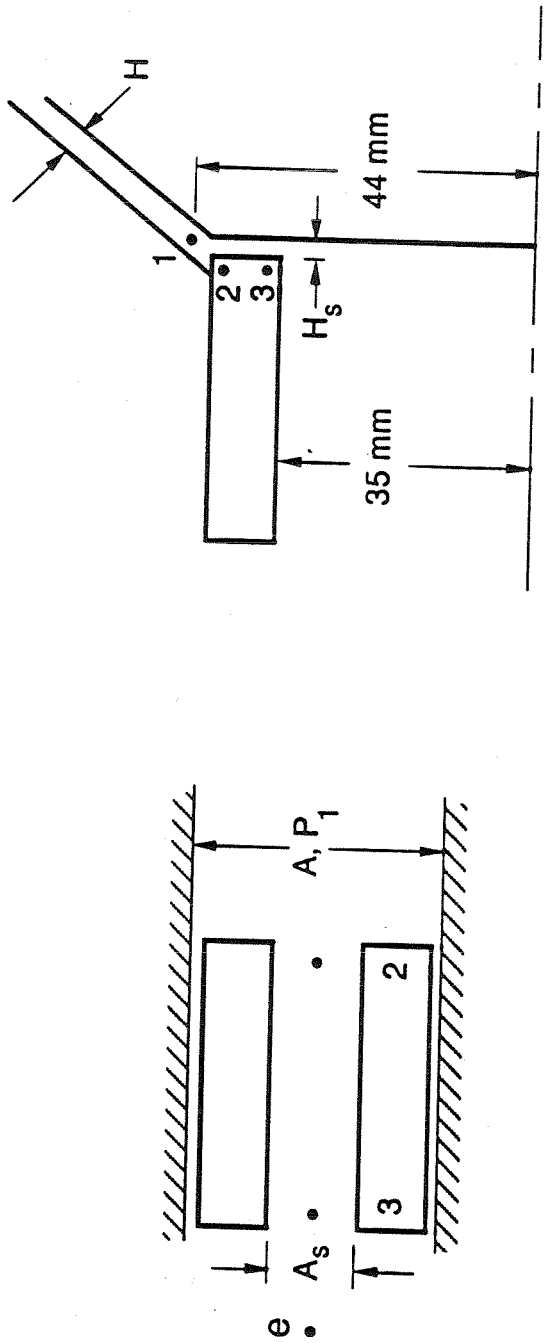

Figure 6.4 Close-up of seal geometry.

CHAPTER 7

NUMERICAL RESULTS

7.1 Validation of numerical procedure.

The theory of the previous section was implemented in a numerical procedure and the results of that effort are presented in this section (a listing of the program is given in appendix F). The solutions were tested for convergence by running the program with different numbers of nodes (coordinates). When the program was run with either 100 or 200 nodes, the results for the forces were indistinguishable. This is acceptable since the first order part of the calculation in fact uses half as many nodes as for the zeroth order calculation. (This implies that 50 and 100 coordinates are used for the force calculation.) With convergence established, the effect of other variables pertinent to the physical model were explored. Various initial conditions such as the definition of the geometry of the leakage flow path, C_{de}, and ξ are thought to affect the results. The effect of these parameters on the numerical results will be discussed in this chapter.

7.2 Analytical solution for turbulent annular seals

A check on the validity of the program was made by comparing the numerical results to the analytic expressions derived for the dynamic coefficients of annular seals by Childs (1983b). An annular seal would correspond to a leakage flow in which the rotating shroud was cylindrical and the clearance was constant along its length. The "short-bearing" solution for an annular seal assumes that the first order tangential velocity, u^1_θ can be neglected and yields the following results for the rotordynamic coefficients when the inlet swirl ratio is 0.5.

$$K = \phi^2 \frac{R}{2\lambda_1 L}\left\{\mu_0 - \mu_2 \left(\frac{L}{2\phi R}\right)^2\right\}$$

$$C = 2k = \frac{\phi\mu_1}{2\lambda_1}$$

$$M = = c = \frac{\mu_2 L}{2\lambda_1 R} \qquad (7.1)$$

where the constants are defined as follows:

ξ = inlet pressure loss coefficient = 0.1 from Yamada (1962)

$$\phi = \frac{U_s}{\omega R}$$

$$Re = \frac{2HU_s}{\nu}$$

m= -0.25 from Yamada (1962)

n = 0.079 from Yamada (1962)

$$\lambda_1 = n\, Re^m \left\{1 + \frac{1}{4\phi^2}\right\}^{(m+1)/2}$$

$$\lambda_2 = \frac{L}{H}\lambda_1$$

$$\mu_0 = \frac{5}{2}\lambda_2{}^2\, \mu_5$$

$$\mu_1 = 2\,\lambda_2\, \{\mu_5 + \lambda_2 \mu_4\, (\mu_5 + \frac{1}{6})/2\}$$

$$\mu_2 = \lambda_2\, (\mu_5 + \frac{1}{6})$$

$$\mu_4 = (1+7\phi^2)/(1+4\phi^2)$$

$$\mu_5 = (1+\xi)/2\ (1+\xi+\mu_4\lambda_2)$$

In the above analysis, the following dimensionless parameters have an

important effect on the reults: L/R, H/R, ϕ. The results of the preceding analysis will be compared with the numerical results for the following parameters, which are taken from the example given in Childs (1983a):

ω=3600 RPM

ρ=1000 kg/m^3

ΔP= 3.44 x 10^6 Pa

H/R=0.025

R=0.0762 m

H=1.905 x 10^{-4} m

Tables 7.1 Specific parameters for different length ratios

L/R	0.2	0.5	1.0
L (m)	0.01524	0.03048	0.06096
ϕ	1.536	1.009	0.679

Tables 7.2a-c compares the following three solutions in nondimensional form.

a) Finite length seal solutions from Childs (1983a).

b) Finite length seal solutions of the present numerical analysis.

c) Short seal solutions from Childs (1983b), using the equations listed above.

	a	b	c
L/R =0.2			
K	235.6	237.83	248.84
k	53.28	70.64	64.53
C	106.6	143.82	129.06
c	5.75	2.39	10.93
M	5.75	2.43	10.93
L/R =0.5			
K	111.70	114.60	134.06
k	130.00	135.79	158.34
C	260.00	273.17	316.68
c	33.59	29.34	49.52
M	33.62	29.41	49.52
L/R =1.0			
K	24.7	29.07	39.71
k	238.0	234.00	363.21
C	477.4	470.50	729.6
c	102.5	96.89	165.38
M	102.6	96.86	165.47

The agreement between the results in columns (a) and (b) of table 7.2 is encouraging as this shows that the program used in the present discussion obtains similar results to that obtained by Childs (1983a). The differences shown in column (c) are discussed further by Childs (1983b), but briefly they result from neglecting the first order tangential velocity in the analysis. For the seal model, it is clear that the results are not sensitive to the first order tangential velocity. However, it is expected that the rotating shroud in the present experiment will be sensitive to this velocity, as the centrifugal acceleration terms become important in the inclined leakage path.

7.3 Exit flow models.

In the experiments, both the inlet pressure and the exit pressure are known quantities from the pressure gages upstream and downstream of the shroud respectively. Therefore, an attempt to reproduce the experimental conditions numerically can be made by computing the pressure distribution along the leakage path, starting with the measured inlet pressure. Specifically, the downstream pressure tap is the pressure downstream of the seal exit. Thus, for a given set of experimental conditions, an estimate of the exit loss coefficient, C_{de} could be obtained by comparing the pressure computed at the end of the seal and the measured exit pressure.

As described in section 6.3, the exit seal could be analytically modeled in two different ways. Table 7.3 lists the coordinates, that were used to describe the detailed geometry of the seal in the case in which the shroud clearance was 0.140 cm and the face seal clearance was 0.050 cm (referred to later as "detailed geometry"). For the method in which the seal is approximated by the exit loss coefficient exclusively, only the first two coordinates are used (referred to later as "partial geometry").

Table 7.3 Geometry of the leakage flow path (dimensions in m)

S	Z	R	H
0	0.024	0.094	0.0014
0.0645	0.070	0.048	0.0014
0.0665	0.071	0.047	0.0005
0.0755	0.071	0.038	0.0005

The effect of these two approximations of the seal is shown in figure 7.1. The curves were obtained by imposing the same pressure drop in both cases and resulted in two different estimates of C_{de}. When the detailed geometry is used, the expected loss coefficient should be close to zero. Computing the loss coefficient yields C_{de}=-0.3. This negative loss coefficient implies that the theoretical pressure distribution decreases below the measured exit pressure by 3 psi. This unreasonable result can be explained by inaccuracies of the order of 1 psi in each of the pressure gages. For F_n inclusion of the seal geometry (C_{de}=-0.3) increases the stiffness of the system, as the curve is

shifted down when compared with the data set obtained with the partial geometry in which the seal is modeled by the exit loss coefficient exclusively (C_{de}=10). It is encouraging to note that this number is the same order of magnitude (C_{de}=11), as that obtained by calculation by assuming that the jet dynamic head is completely lost at the exit (details of this model were discussed earlier in chapter 6). The effect on Ft of including the detailed seal geometry in the calculation, is to increase the damping.

In figure 7.2, the results which arise from the two different geometrical models of the seal are shown for a larger clearance. The magnitude of C_{de} obtained through computation for the partial geometry is 109, which compares remarkably well to the theoretical estimate (described earlier) of 109 for this case. The value for C_{de} is calculated to be -0.2, when the detailed geometry is used. As observed in figure 7.1, the effects which are obtained by using the two different geometries of damping on the tangential force and stiffness on the normal force can also be observed in figure 7.2, although to a different degree. Note, also that the magnitude of the force is much smaller for the larger clearance. This point will be discussed later.

The differences observed in figure 7.2 for F_n and F_t might be attributed to the different geometrical descriptions for the two cases. However, each case also uses a different loss coefficient. Therefore figure 7.3 shows the effect of C_{de}, by imposing the large C_{de} obtained for the partial geometry case on the detailed geometry case. The results show that a large change in C_{de} results in a small change in the rotordynamic forces.

The effect of the geometry on F_n and F_t is explored further in Figure 7.4 by imposing the same value of C_{de} obtained for the geometry without the seal also on the geometry which includes the seal. Note that this would result in the two cases having different total pressure drops. The curves obtained for the two different geometries are similar in shape for F_n and F_t, however, inclusion of the seal amplifies the instabilities or "peaks". Thus, judging from the results presented in figure 7.4 and figure 7.3, the results are more sensitive to the geometry than to the value of the loss-coefficient. Clearly, the effect of C_{de} on the magnitude of the forces is negligible.

7.4 General observations from the numerical results

In figure 7.4, the relationship between the shroud clearance and the magnitude of the rotordynamic forces is shown. Note that the forces seem to be inversely proportional to the clearance. The two dotted curves are for different values of C_{de} obtained with the small shroud clearance. Notice that at the smaller clearance, the curves are relatively smooth, possibly because the flow is constrained to reach equilibrium more rapidly after entering the leakage flow passage.

In the discussion which follows, the entire seal geometry will be used to calculate the forces. The conditions that are examined are chosen to match those of the present experiment where possible. The total pressure drop, C_d, is obtained from the pressure gages at the inlet and exit of the leakage path. This in turn allows the loss coefficient, C_{de} to be calculated as mentioned above. The inlet loss-coefficient has a negligible effect on the forces, nevertheless the same loss coefficient of 0.1 that was used by Childs (1983) was used for the following numerical results.

In figure 7.6, the effect of inlet swirl or tangential velocity ratio is examined for the larger shroud clearance. The curves with incoming swirl values different from 0.5 show "resonances" or "peaks", which might be attributed to the fact that the incoming flow is not matched to the flow in the gap region.

In figure 7.7, the effect of clearance is examined again for conditions similar to those obtained for in figure 7.5 but with a swirl ratio of 0.5. The inverse relationship between the shroud clearance and the magnitude of the rotordynamic forces is also observed when the inlet flow has swirl. At this ratio of swirl velocity, both clearances result in smooth curves, possibly due to the fact that the inlet flow matches the average flow in the leakage path.

Variation with the inlet swirl velocity is shown in figure 7.8 for the smaller clearance. Note that at inlet swirl ratios different from 0.5, the curves show "resonances". In figure 7.9, the same results are shown for a lower flow rate. The "resonance" is more pronounced for the curve with no inlet swirl.

This may be caused by the fact that at the lower flow rates, the damping of the swirl velocity is reduced.

Figures 7.10, 7.11, 7.12 examine the effect of flow for different swirl ratios. For all the ratios shown, the normal force exhibits a decrease with flow except in the neighborhood of the "resonances". This is contrary to experimental observations, where flow is seen to increase the normal force. The effect of flow on the tangential force for no swirl (figure 7.10) is similar to experimental results. In both cases, the flow is stabilizing thereby decreasing the tangential force. For swirl ratios of 0.5 (figure 7.11) and 0.8 (figure 7.12), the effect is the same as in the experiments except near the "resonances". There is definitely an inconsistency between experimental and numerical results on what the effect of the leakage flow has on the forces.

The conditions which are obtained in figure 7.11, for a swirl ratio of 0.5 are presented in figures 7.13 and 7.14 for different seal clearances. The results obtained in figure 7.13 are obtained with a tighter seal clearance than the reults obtained in figure 7.11. As in figure 7.11, the trends with flow on the rotordynamic forces are also inconsistent with the experimental results. It is interesting to note that the case with the tighter seal clearance yields curves which do not show the resonances of the previous figures. Results with a widened seal clearance are shown in figure 7.14

Figure 7.15 presents the effect of seal clearance for a flow rate of 10 GPM and figure 7.16 shows the same effect at 20 GPM. The two flow rates do not exhibit the same trend with the seal clearance. For the lower flowrate shown in figure 7.15, the tangential force varies inversely with the seal clearance. For positive whirl ratios, the normal force actually decreases with decreasing flow. At the larger flowrate shown in figure 7.16, the trends seem haphazard with seal clearance and certainly do not agree with figure 7.15. Therefore, it is not possible to predict a trend with seal clearance.

The effect of the swirl ratio is examined for a larger clearance in figures 7.17 at 30 GPM and 7.18 at 10 GPM. Together with figure 7.6 at 20 GPM, they make up a set. As was the case with the smaller clearance examined in figures 7.9 and 7.10, the swirl ratio at which peaks do not appear seems to be at 0.5. The

manifestation of the peaks is a strong function of the flow coefficient. What this means is that for the swirl ratios different from 0.5, at the lower flow rates, the peaks appear more pronounced. This fact can be observed in figures 7.19, 7.20, and 7.21 which present results for swirl ratios of 0, 0.5, and 0.8 respectively.

One method of solution of the problem would be to split it up into parts. From the initial figures 7.1 through 7.5, it would appear that the contribution from the seal portion is significant. So the perturbations from the flow along the seal could be calculated by using the exit parameters from the shroud exit. In this manner, discontinuities at the seal transition could be avoided and loss coefficients could be ignored. The effect of varying the seal clearance was shown in figures 7.13 through 7.16. It might be expected that as the seal clearance was opened up, the forces would approach those that were obtained with only the partial geometry description. Since this was not found, clearly something is missing from the model.

7.5 Assessment of numerical predictions by comparison with experimental results.

One of the major discrepancies between the experimental results and the numerical results was that no peaks were observed for the range of prescribed inlet swirl ratios for the experiments. The swirl velocity at the inlet in the experiment was not measured, so it is possible that the flow adjusted itself to the mean flow rather fast and in fact is not given as simply as by equation 2.1. Nevertheless, it should be noted that even at the largest inlet swirl ratio of 4.0, no "resonances" were obtained for the experiments.

Figure 7.22 shows experimental results obtained with an eccentricity of 0.0254 cm, flow of 20 GPM (ϕ= 0.052), 1000 RPM, clearance of 0.424 cm and no swirl. The numerical results are shown for three values of swirl, including no swirl. Although, there is a peak at 0.4 for F_t, the forces obtained experimentally are small at this large clearance and there is therefore scatter. The magnitudes of the two differently obtained results agree most when no swirl is an input. It is interesting to note that there is also a peak in the numerical results at this same whirl ratio, but is concave up. The F_n data is

smooth and most closely matched by $\Gamma = 0$ at higher positive whirl ratios. For negative whirl, all the swirl values give about the same results.

Figure 7.23 shows experimental results obtained with an eccentricity of 0.118 cm, a flow of 10 GPM ($\phi = 0.078$), a speed of 1000 RPM, a clearance of 0.140 cm and no inlet swirl. The numerical results are shown for three values of inlet swirl, including no swirl. Both the F_n and the F_t experimental curves ares smooth. For positive large whirl ratios, the solution obtained for the numerical results with $\Gamma = 0$ gives the best agreement in magnitude with the experimental results, but for large negative whirl, the results obtained with Γ=0.8 is closer to the experimental results in magnitude and for small whirl, agreement with $\Gamma = 0.5$ is closer in magnitude.

Figure 7.24 shows experimental results obtained with an eccentricity of 0.118 cm, a flow of 20 GPM ($\phi = 0.156$), a speed of 1000 RPM, a clearance of 0.140 cm and no inlet swirl. The numerical results are shown for three values of inlet swirl, including no swirl. Both the F_n and the F_t experimental curves ares smooth. As with the previous figures, agreement in magnitude is obtained with the numerical solution for $\Gamma = 0$. However, at whirl ratios of 0.5 and higher, the numerical solution for $\Gamma = 0.8$ presents a closer agreement in magnitude to the experimental results. It should be noted that it is with the whirl ratios of 0.5 that no peaks are obtained in the numerical results.

Figures 7.24 and 7.25 show experimental results obtained with an eccentricity of 0.118 cm, a range of flows, a speed of 1000 RPM, a clearance of 0.140 cm and no inlet swirl. The numerical results are shown for an inlet swirl of 0.5. Figures 7.24 is for a seal clearance of 0.0025 cm and 7.25 is for a seal clearance of 0.01cm. As mentioned in the previous section, the trend with flow coefficient is opposite for the numerical reults, compared with the experimental results. It is still encouraging to note that the magnitudes of the forces agree.

While agreement in magnitude is achieved for the zero swirl ratio case, it is the ratio of 0.5 which presents no peaks in the results. This is one of the problems with using the bulk flow model. Clearly, the flow enters the leakage flow inlet area with no swirl in the experimental apparatus, but the bulk flow

model expects the flow to average between the velocity at the stationary wall and the velocity at the rotating shroud immediately.

7.6 Summary

It would appear that the general trends in the magnitudes of the shroud forces are adequately predicted by the numerical model. In particular the inverse proportionality effect of the shroud clearance is predicted. However, as far as describing the particular trends for varying flow coefficient, seal clearance or inlet swirl, the numerical results do not agree with the experimental results. Childs suggested that the "resonance" effect of the leakage flow developed when the swirl velocity ratio at inlet exceeded 0.5. However, the present numerical simulation shows that "resonance" occurs bellow 0.5 as well. It would thus appear that the model is perhaps valid for only one value of inlet swirl, where the "resonance" does not occur.

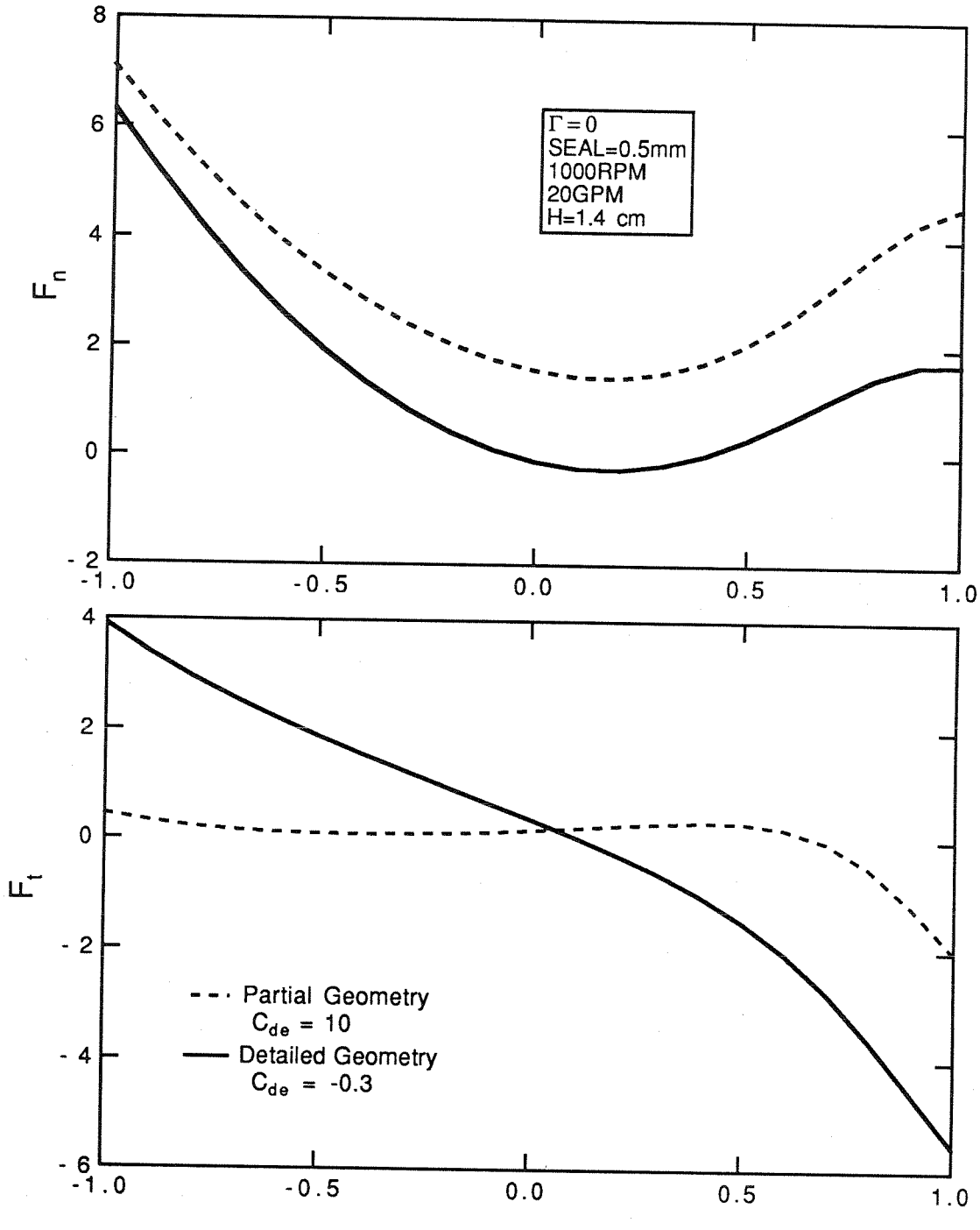

Figure 7.1 Numerical predictions of the normal and tangential forces, as a function of whirl ratio for the following conditions: inlet swirl, Γ=0, seal clearance = 0.5 mm, 1000 RPM, 20 GPM, and a clearance, H=1.4 cm. Results are shown for two models of the shroud geometry. The solid line is obtained with the detailed seal geometry included in the calculation, (C_{de}=-0.3). The dashed line is obtained with the partial geometry and the seal is approximated by the exit loss coefficient alone, (C_{de}=10).

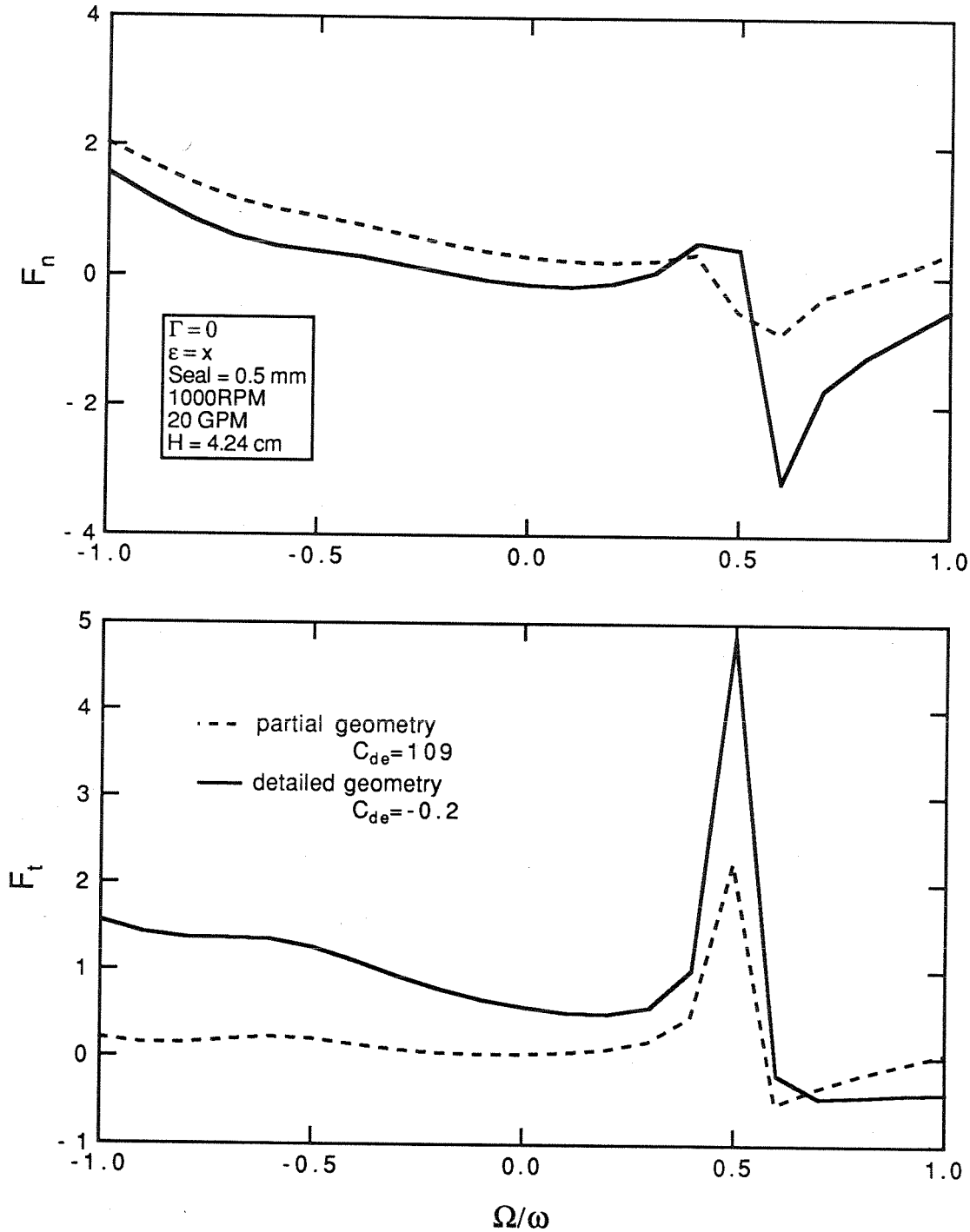

Figure 7.2 Numerical predictions of the normal and tangential forces, as a function of whirl ratio for the following conditions: inlet swirl, Γ=0, seal clearance = 0.5 mm, 1000 RPM, 20 GPM, and a clearance, H=4.24cm. Results are shown for two models of the shroud geometry. The solid line is obtained with the detailed seal geometry included in the calculation, (C_{de}=-0.2). The dashed line is obtained with the partial geometry and the seal is approximated by the exit loss coefficient alone, C_{de}=109.

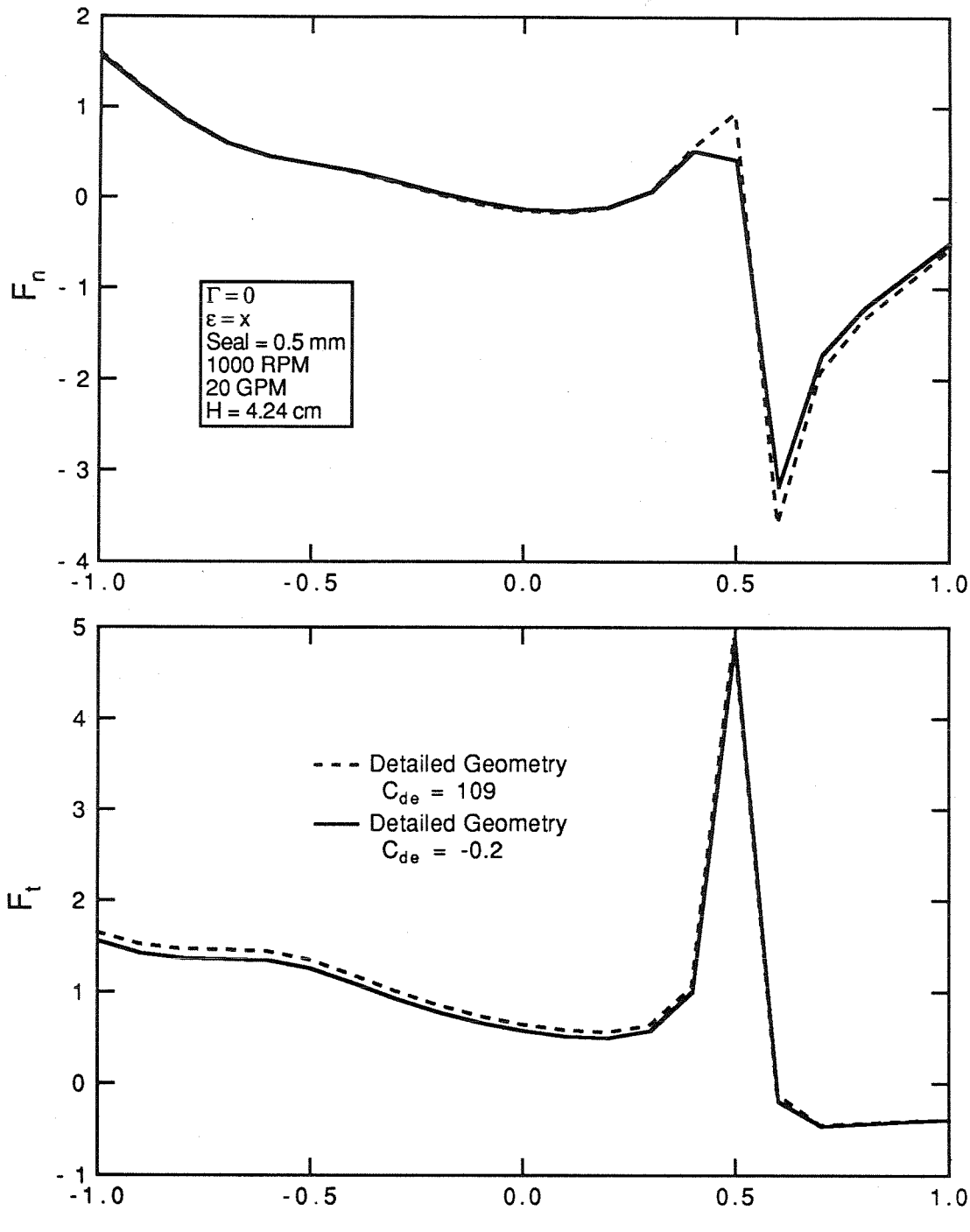

Figure 7.3 Numerical predictions of the normal and tangential forces, as a function of whirl ratio for the following conditions: inlet swirl, Γ=0, seal clearance = 0.5 mm, 1000 RPM, 20 GPM, H=4.24cm. Both curves show the results for the detailed seal geometry included in calculation. The solid line is with C_{de} from the calculation, C_{de}=-0.2. The dashed line uses the loss coefficient from the partial geometry in which the seal is approximated by the exit loss coefficient alone, C_{de}=109.

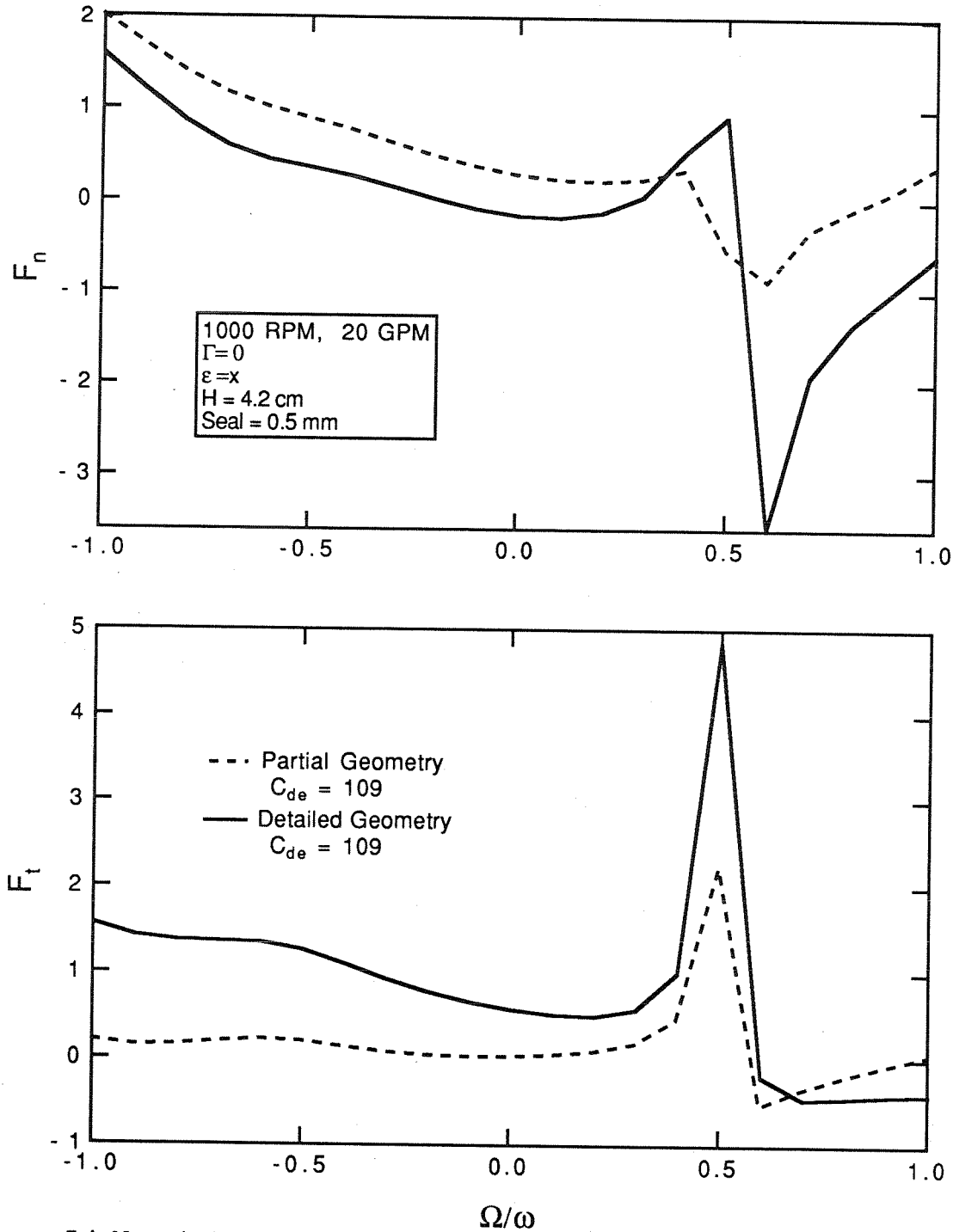

Figure 7.4 Numerical predictions of the normal and tangential forces, as a function of whirl ratio for the following conditions: inlet swirl, Γ=0, seal clearance = 0.5 mm, 1000 RPM, 20 GPM, H=4.24cm. The solid line is obtained with the detailed seal geometry included in the calculation, using C_{de} from the partial geometry without the seal, C_{de}=109. The dashed line is obtained with the partial geometry and the seal is approximated by the exit loss coefficient alone, C_{de}=109.

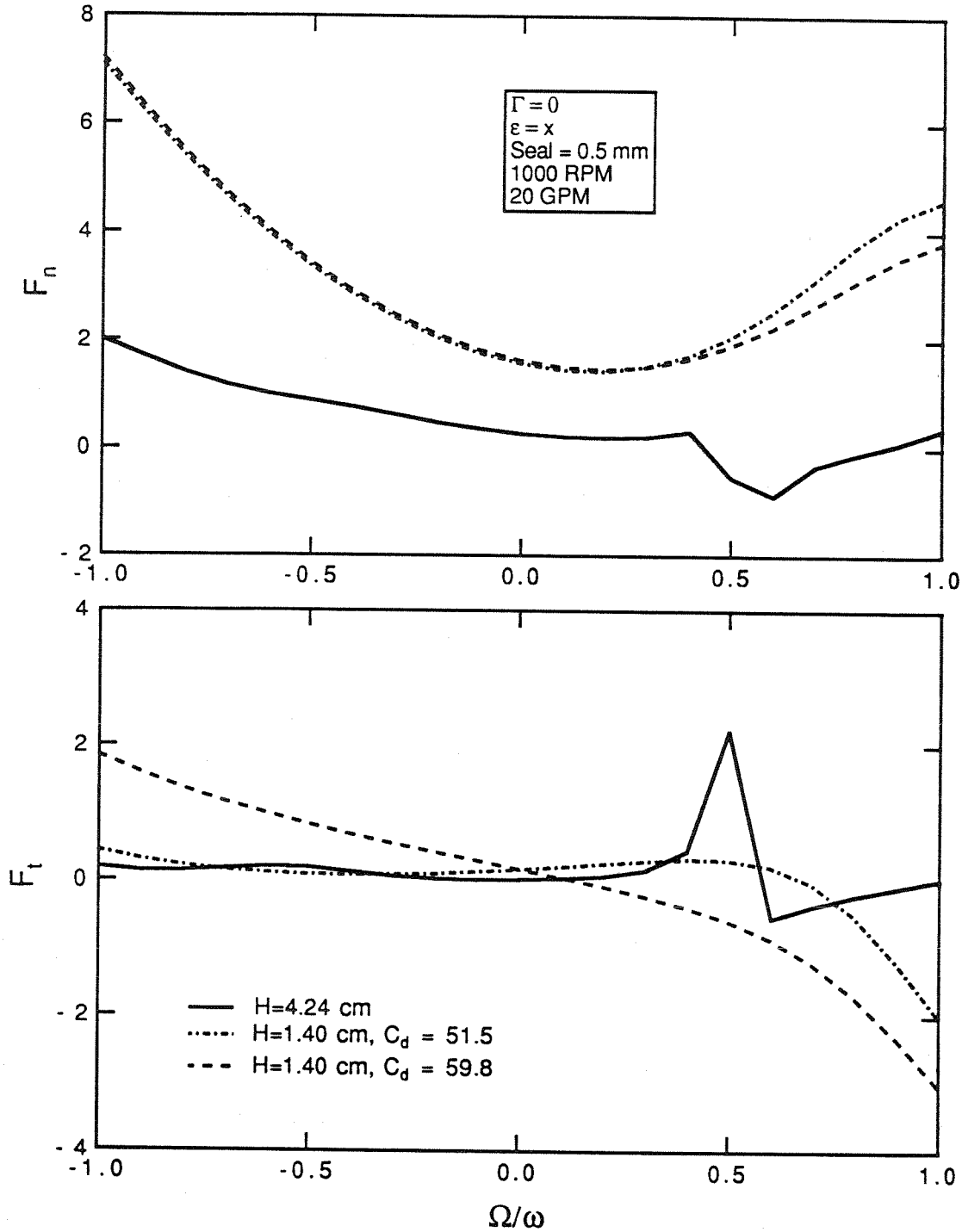

Figure 7.5 Numerical predictions of the normal and tangential forces, as a function of whirl ratio for the following conditions: inlet swirl, Γ=0, seal clearance= 0.5 mm, 1000 RPM, 20 GPM. All the curves are obtained with the seal approximated by the exit loss coefficient alone. The solid line is for the clearance, H=4.24 cm, C_{de}=109. The other curves are for the clearance, H=1.4 cm and two different total pressure drops.

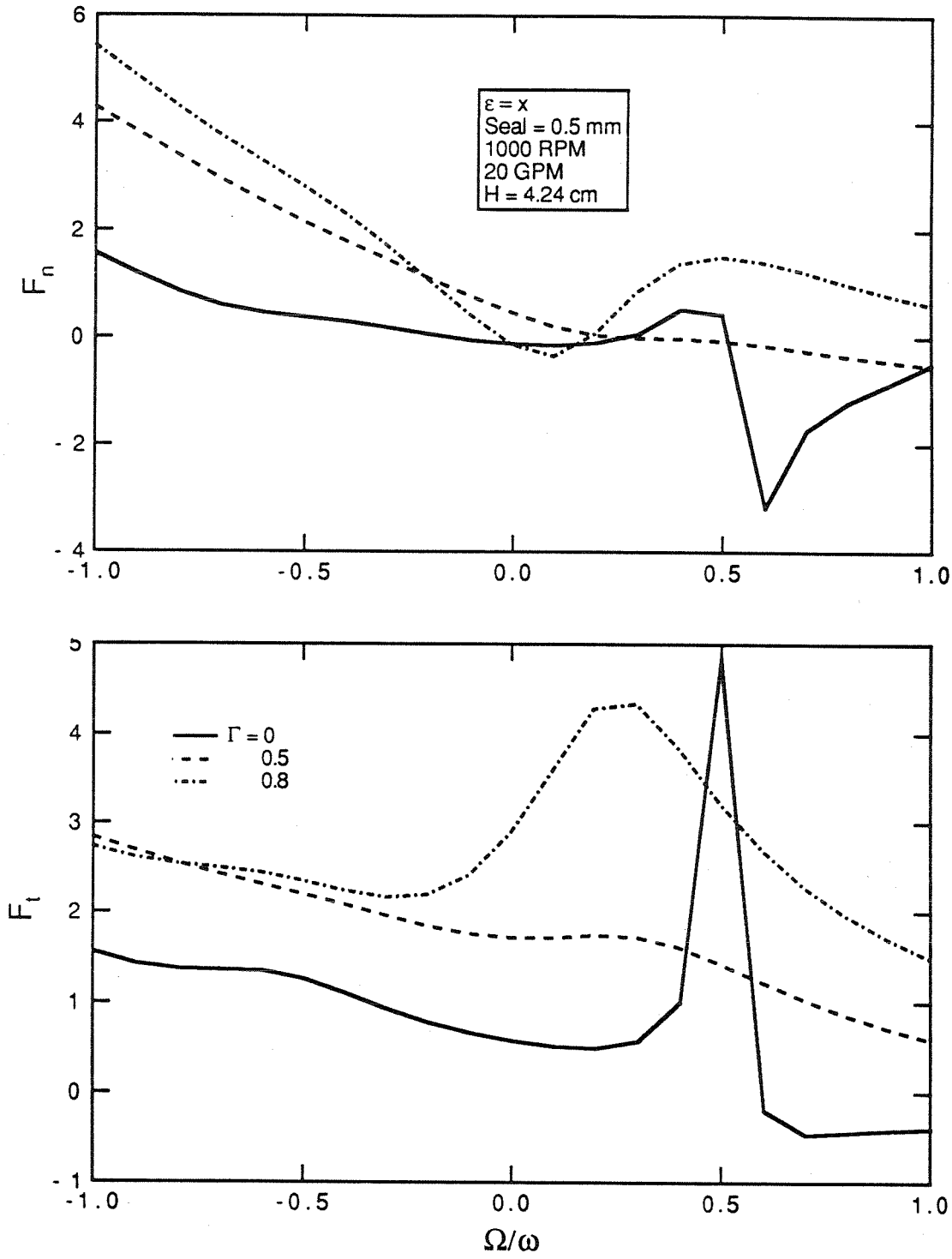

Figure 7.6 Numerical predictions of the normal and tangential forces, as a function of whirl ratio for the following conditions: seal clearance= 0.5 mm, 1000 RPM, 20 GPM, clearance, H=4.24cm and three different inlet swirl ratios, 0, 0.5, and 0.8.

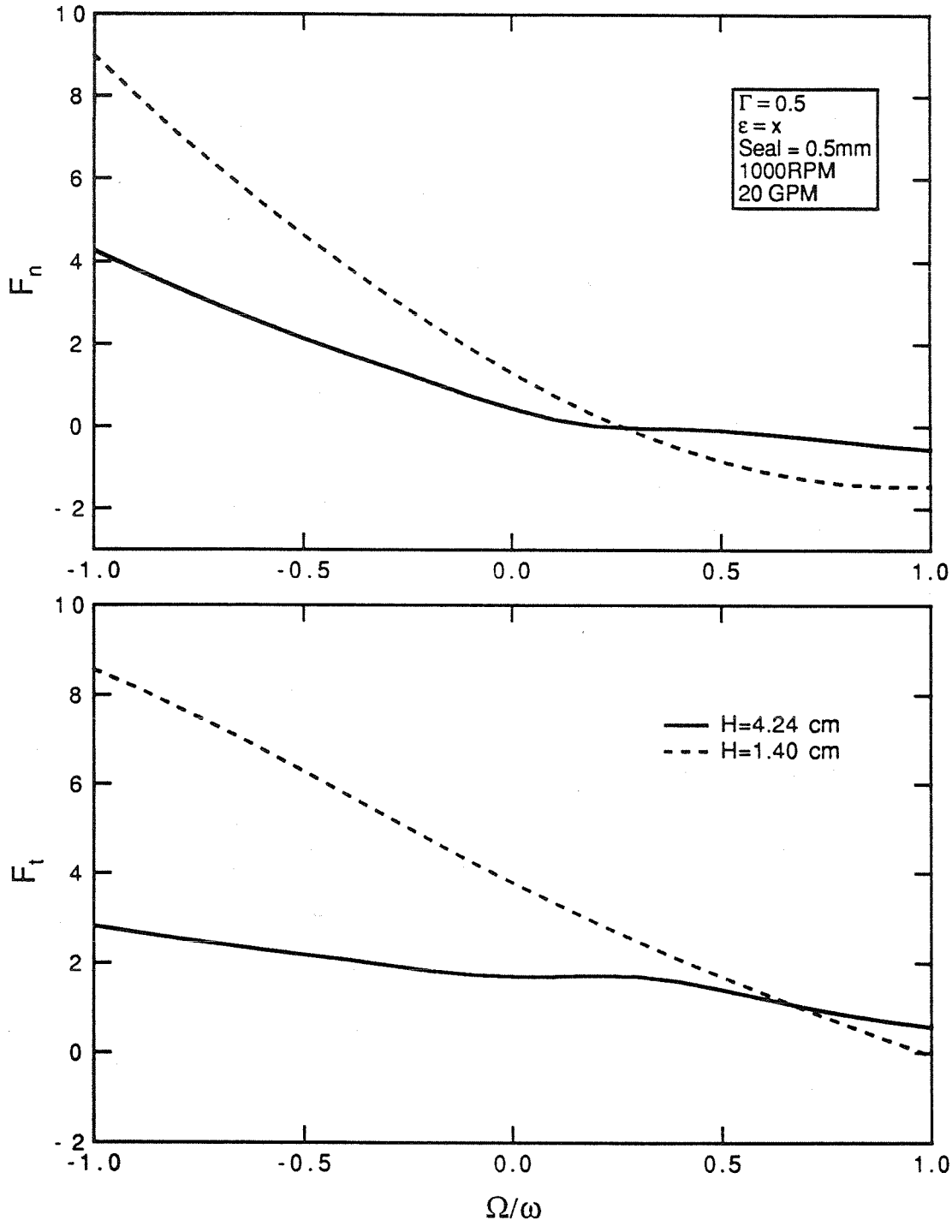

Figure 7.7 Numerical predictions of the normal and tangential forces, as a function of whirl ratio for the following conditions: Γ=0.5, seal clearance= 0.5 mm, 1000 RPM, 20 GPM. The solid line is for a clearance, H=4.24cm and the dotted line is for a clearance, H=1.4cm.

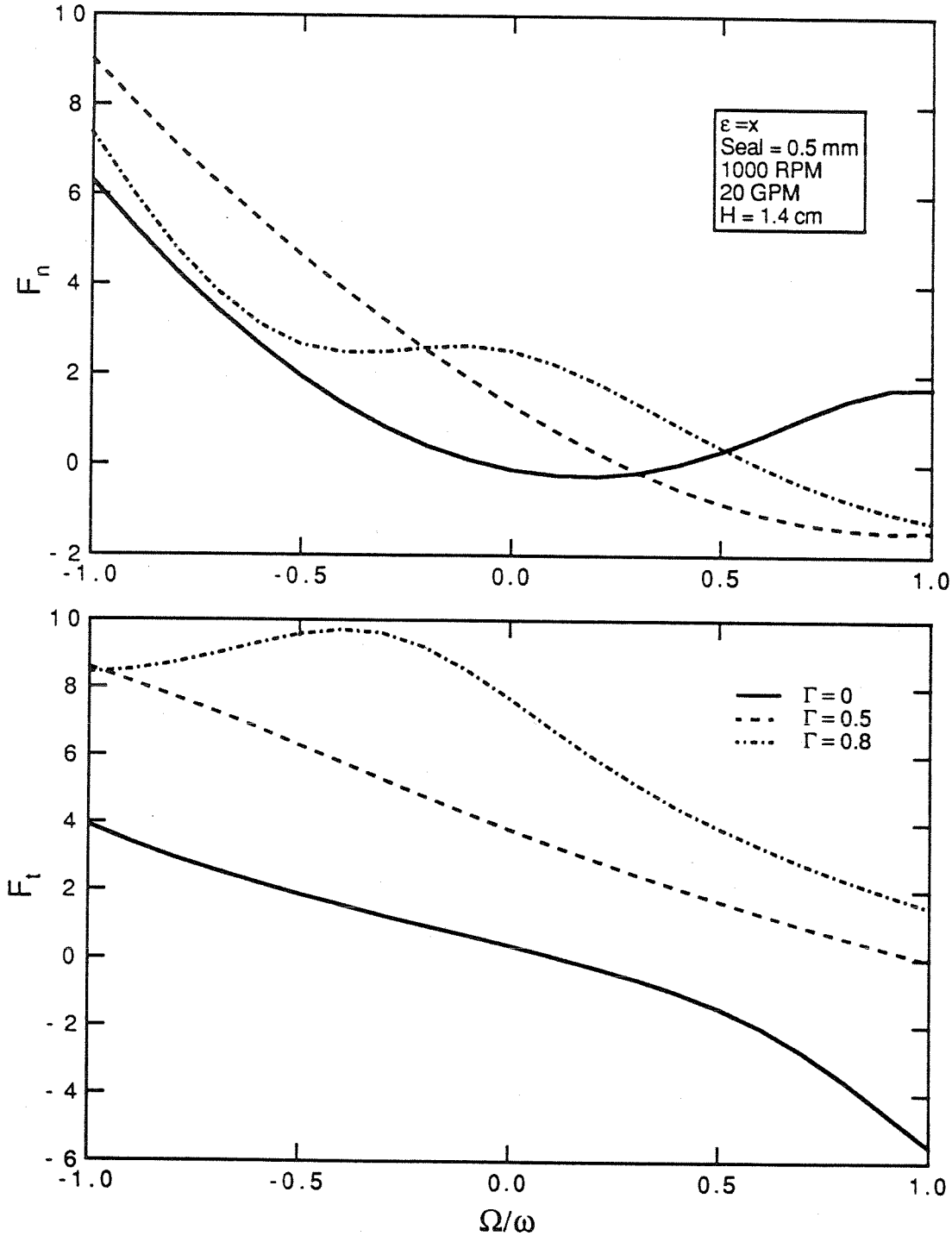

Figure 7.8 Numerical predictions of the normal and tangential forces, as a function of whirl ratio for the following conditions: seal clearance= 0.5 mm, 1000 RPM, 20 GPM H=1.4 cm and three different inlet swirl ratios, 0, 0.5, and 0.8.

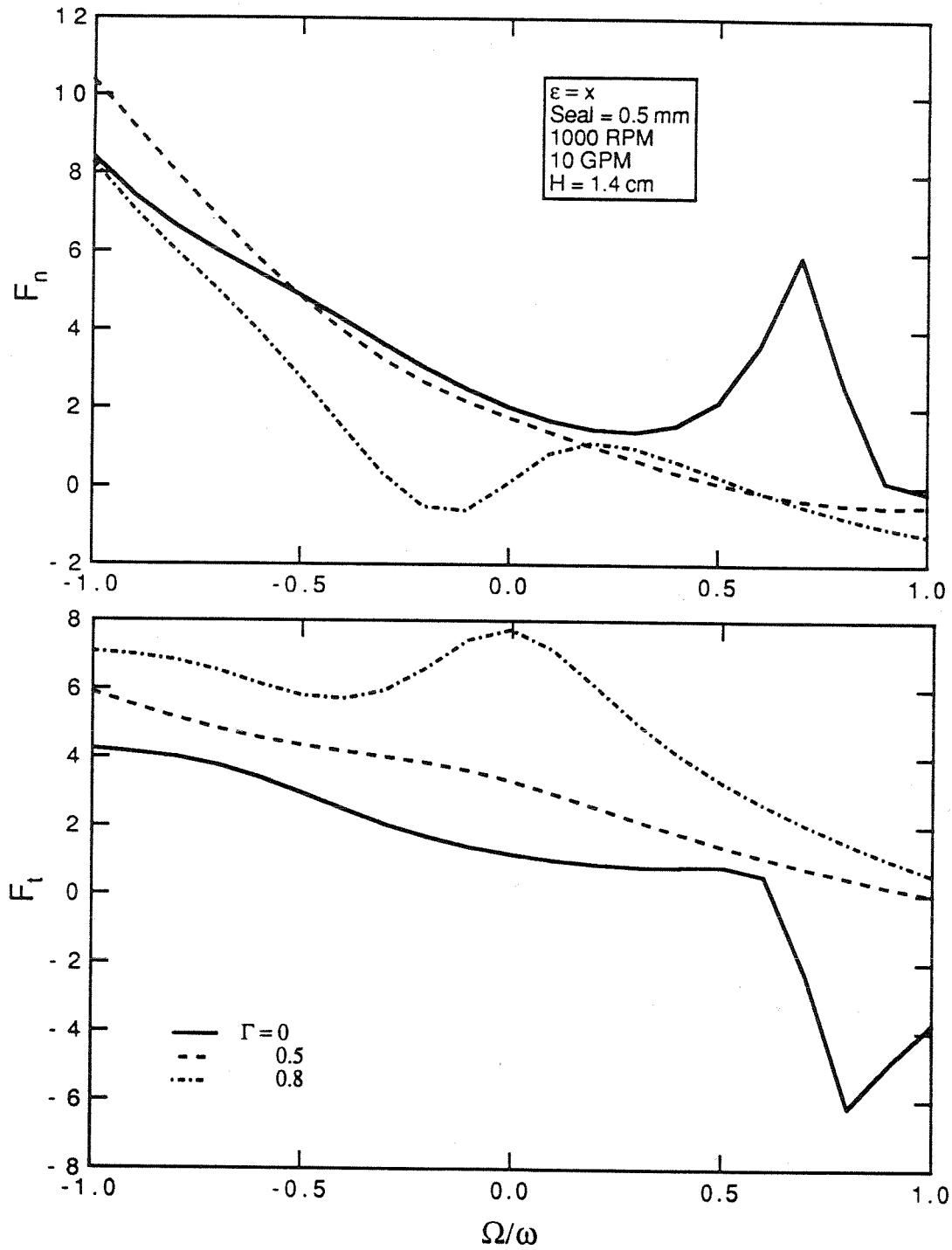

Figure 7.9 Numerical predictions of the normal and tangential forces, as a function of whirl ratio for the following conditions: seal clearance= 0.5 mm, 1000 RPM, 10 GPM H=1.4 cm and three different inlet swirl ratios, 0, 0.5, and 0.8.

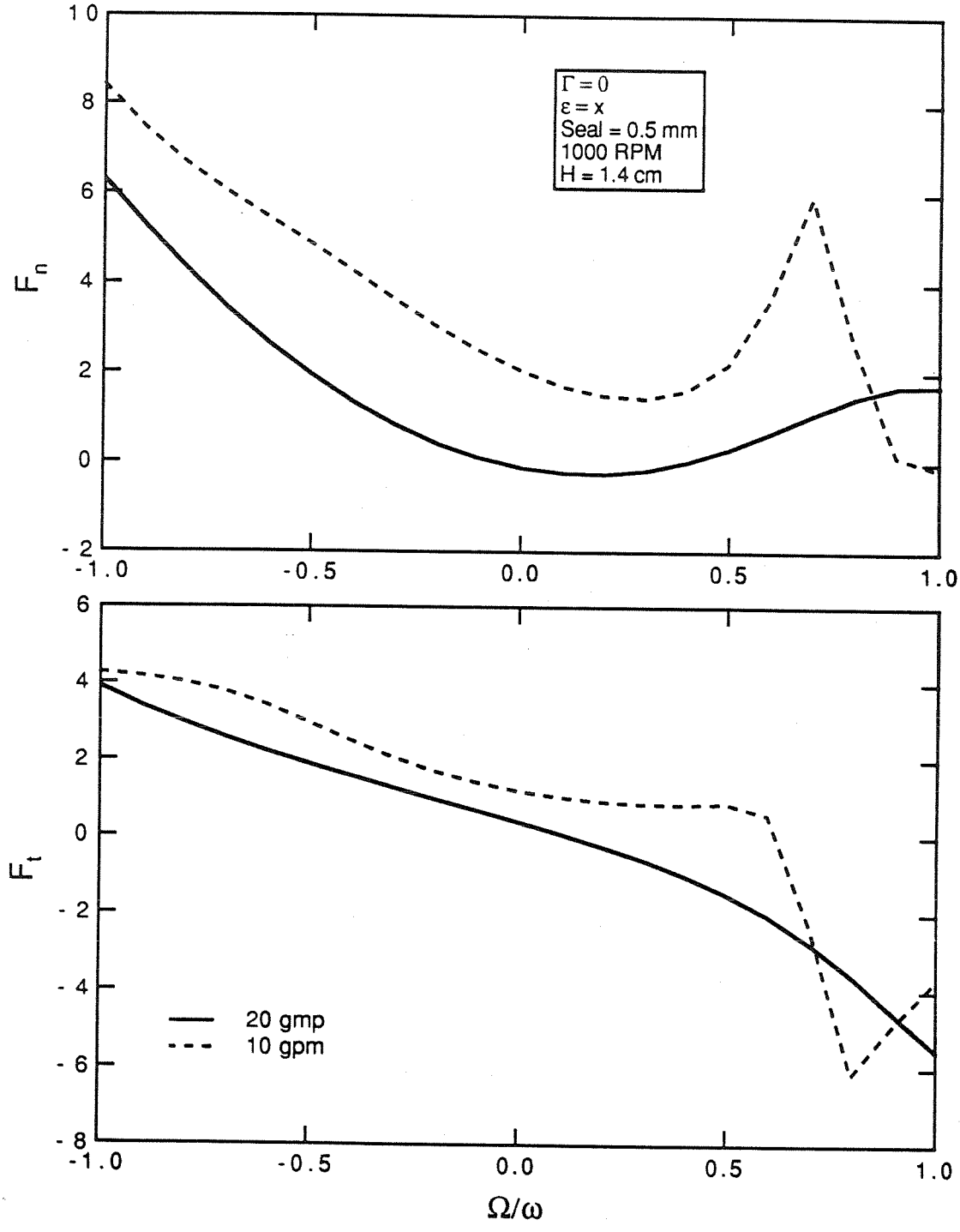

Figure 7.10 Numerical predictions of the normal and tangential forces, as a function of whirl ratio for the following conditions: Γ=0, seal clearance= 0.5 mm, 1000 RPM, H=1.4cm and different flowrates at 10 GPM and 20 GPM.

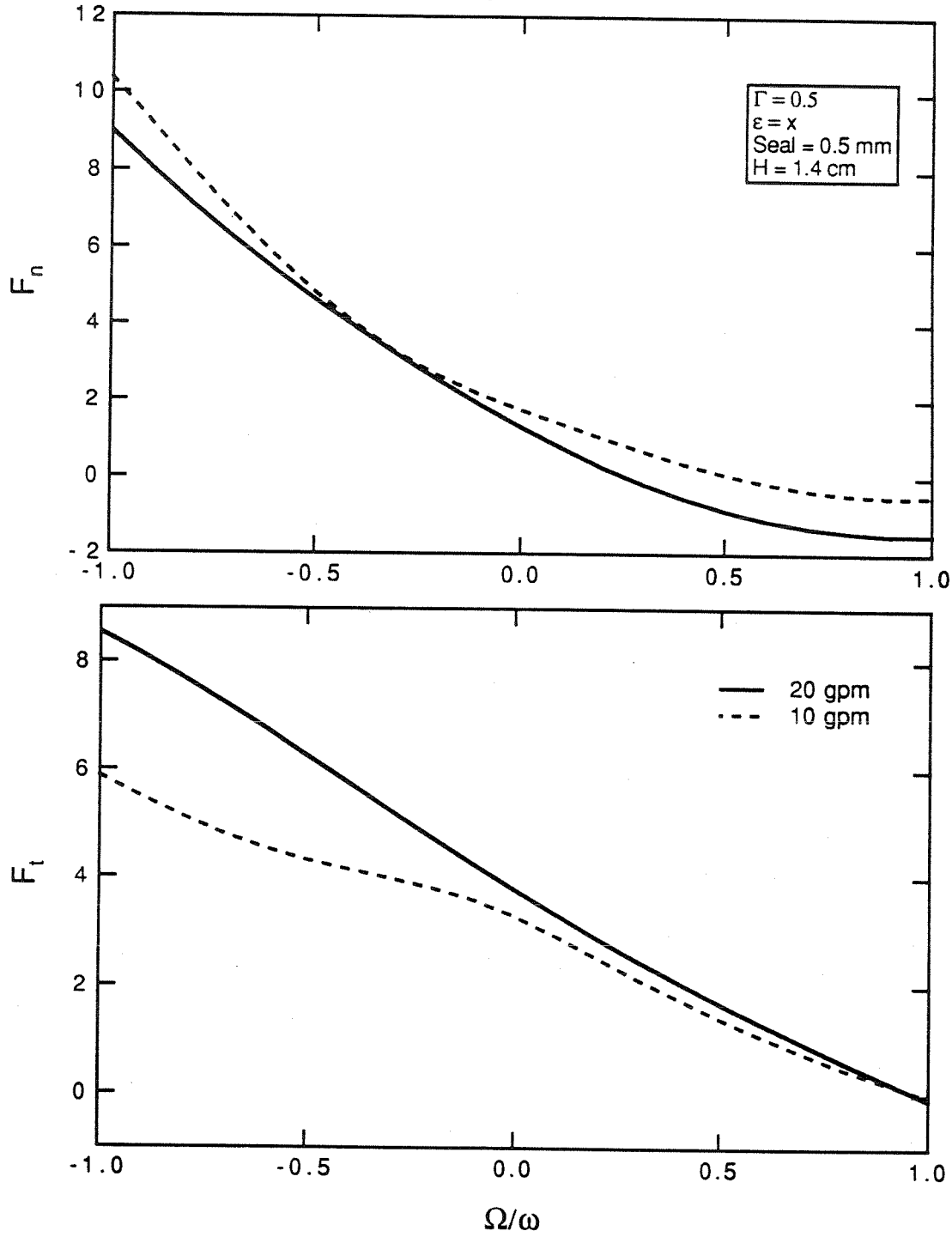

Figure 7.11 Numerical predictions of the normal and tangential forces, as a function of whirl ratio for the following conditions: Γ=0.5, seal clearance= 0.5 mm, 1000 RPM, H=1.4cm and different flowrates at 10 GPM and 20 GPM.

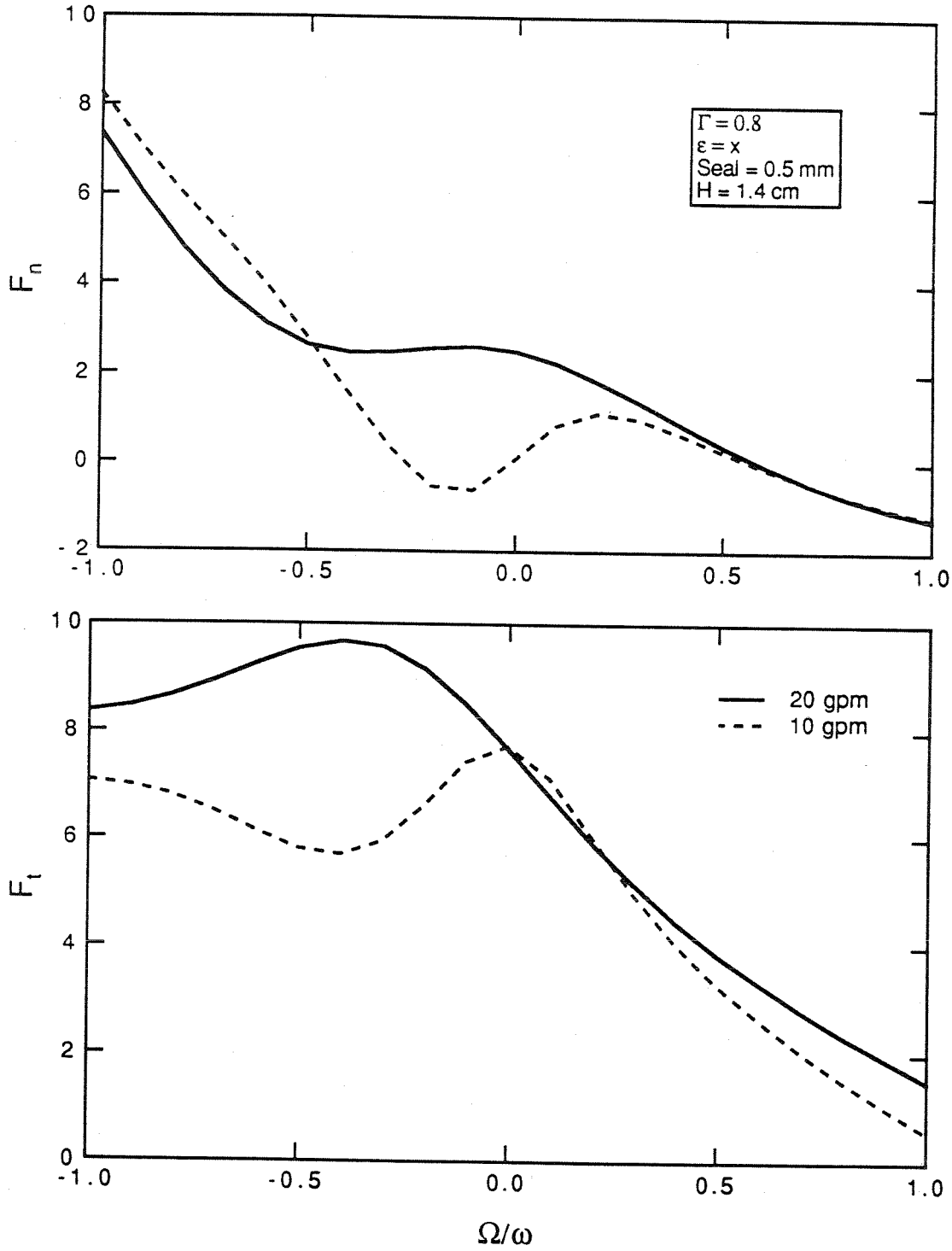

Figure 7.12 Numerical predictions of the normal and tangential forces, as a function of whirl ratio for the following conditions: Γ=0.8, seal clearance= 0.5 mm, 1000 RPM, H=1.4cm and different flowrates at 10 GPM and 20 GPM.

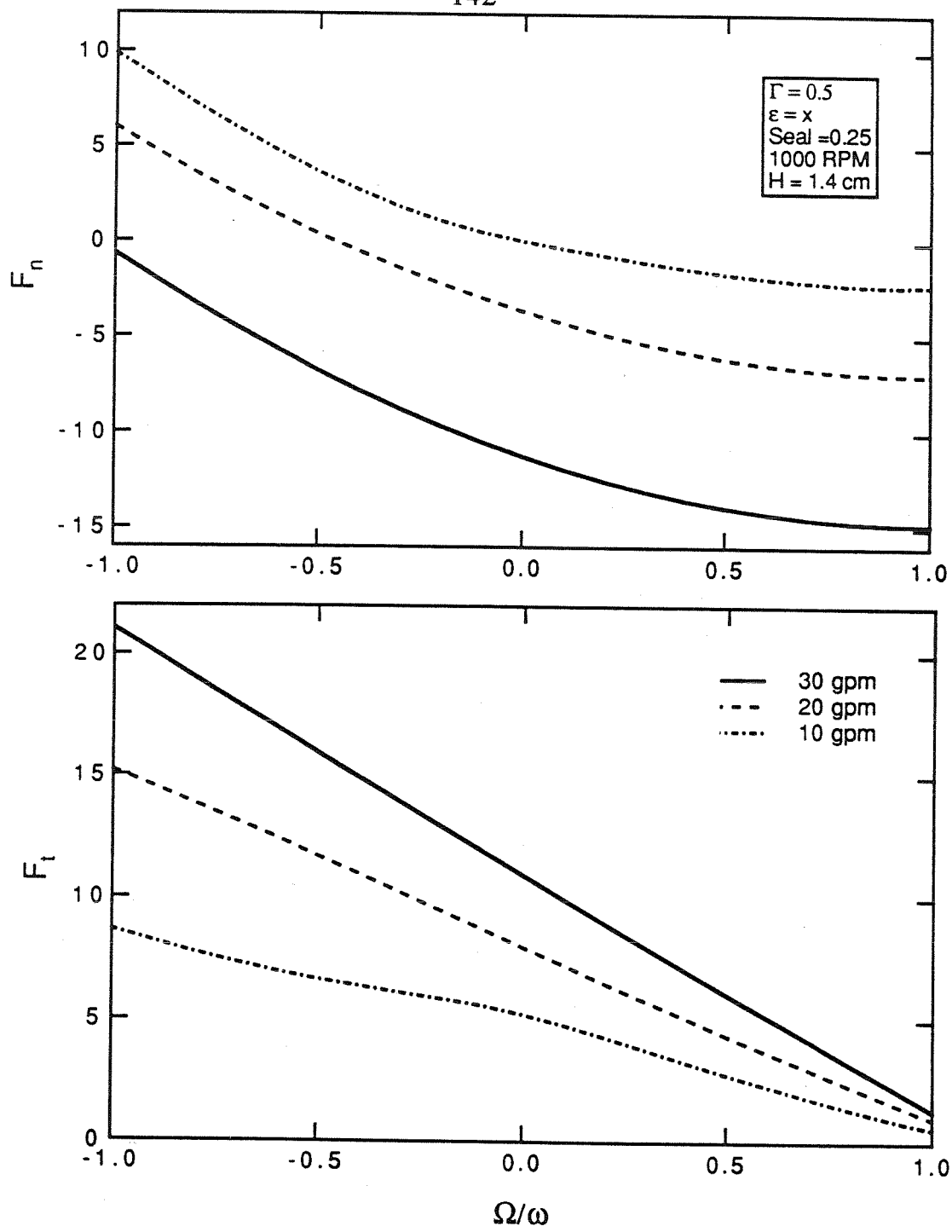

Figure 7.13 Numerical predictions of the normal and tangential forces, as a function of whirl ratio for the following conditions: Γ=0.5, seal clearance= 0.25 mm, 1000 RPM, H=1.4cm and different flowrates at 10, 20 and 30 GPM.

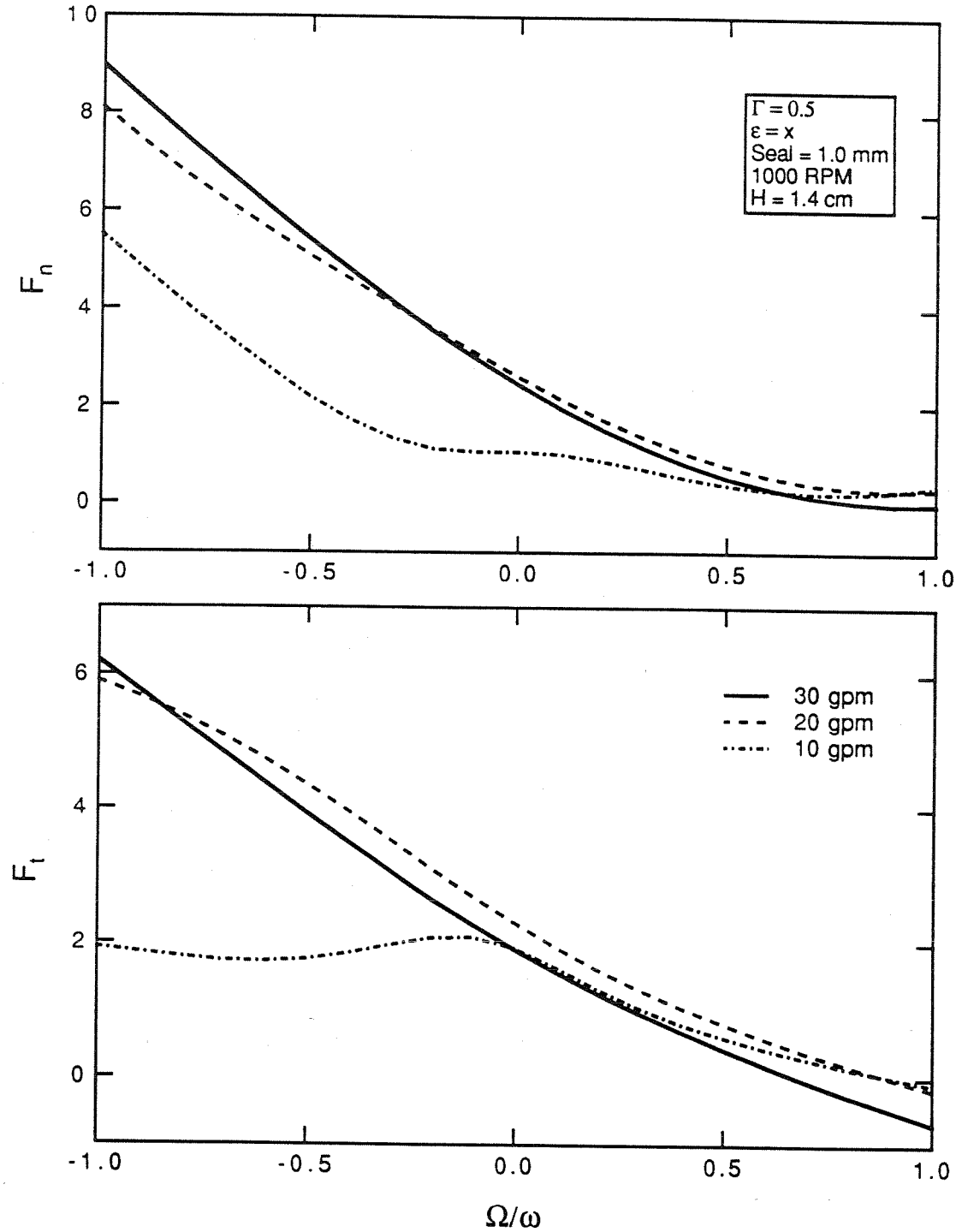

Figure 7.14 Numerical predictions of the normal and tangential forces, as a function of whirl ratio for the following conditions: Γ=0.5, seal clearance= 1.0 mm, 1000 RPM, H=1.4cm and different flowrates at 10, 20 and 30 GPM.

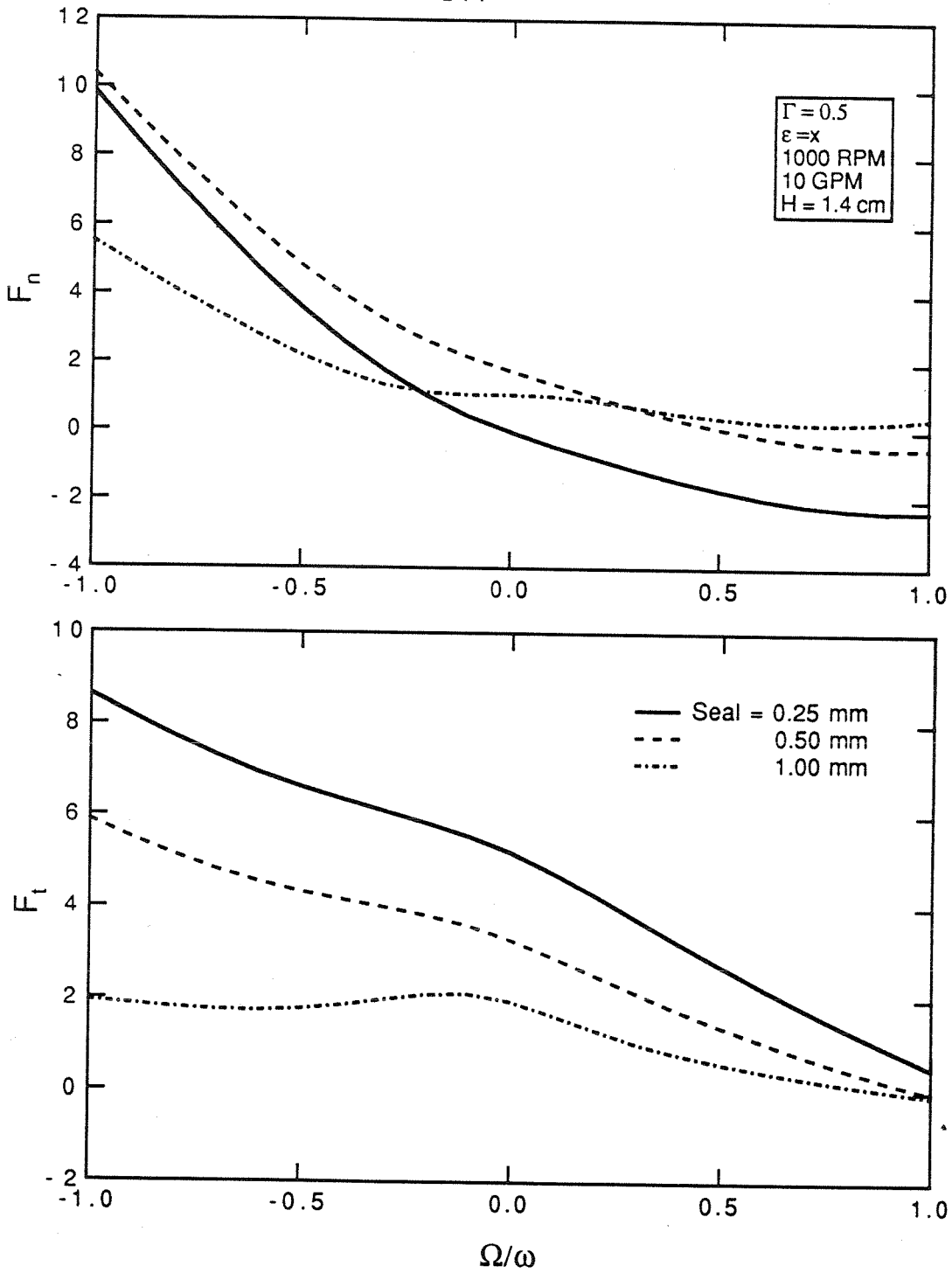

Figure 7.15 Numerical predictions of the normal and tangential forces, as a function of whirl ratio for the following conditions: Γ=0.5, 10 GPM, 1000 RPM, H=1.4 cm and three different seal clearances, 0.25, 0.50, and 1.00mm.

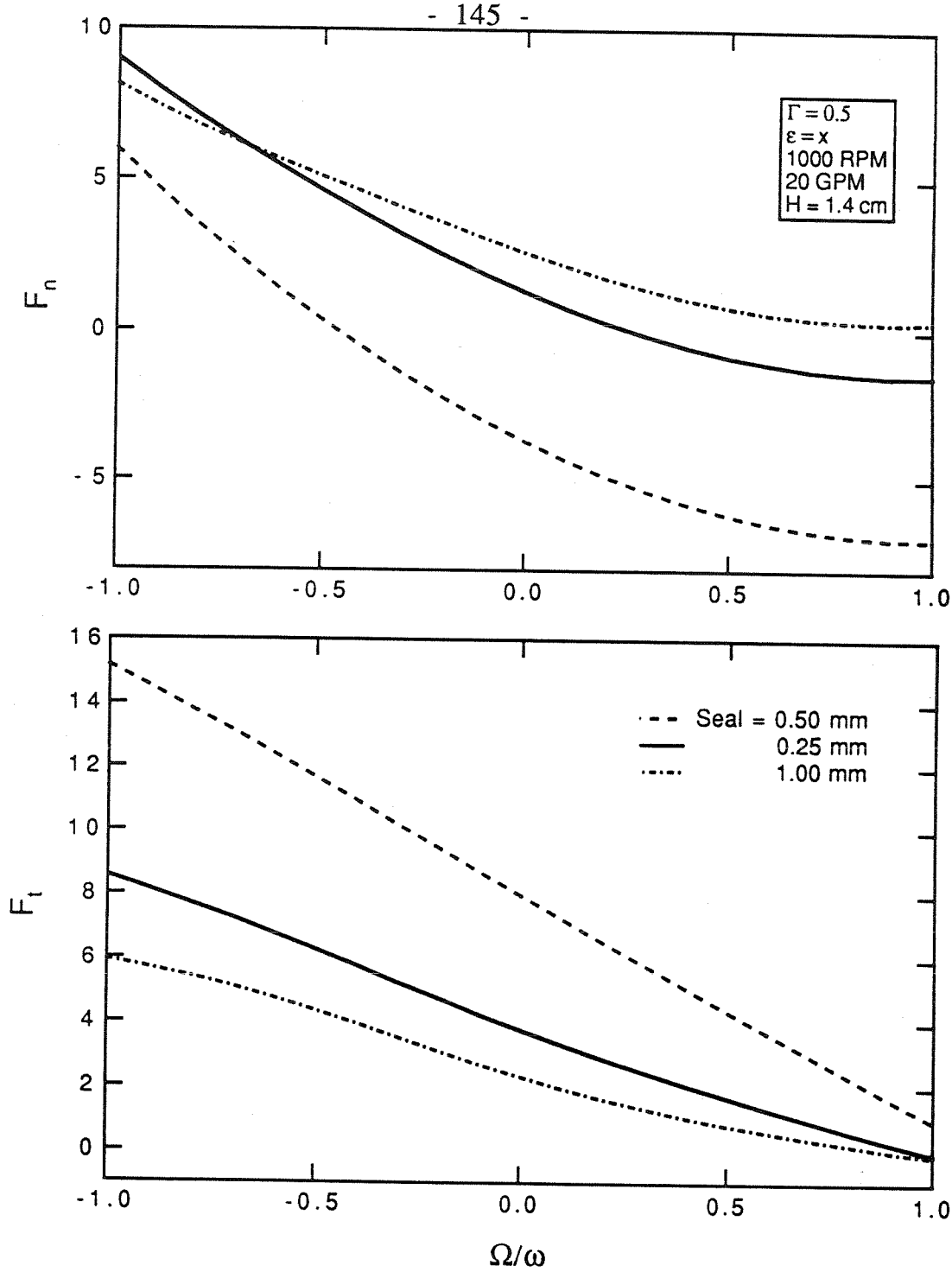

Figure 7.16 Numerical predictions of the normal and tangential forces, as a function of whirl ratio for the following conditions: Γ=0.5, 20 GPM, 1000 RPM, H=1.4 cm and three different seal clearances, 0.25, 0.50, and 1.00mm.

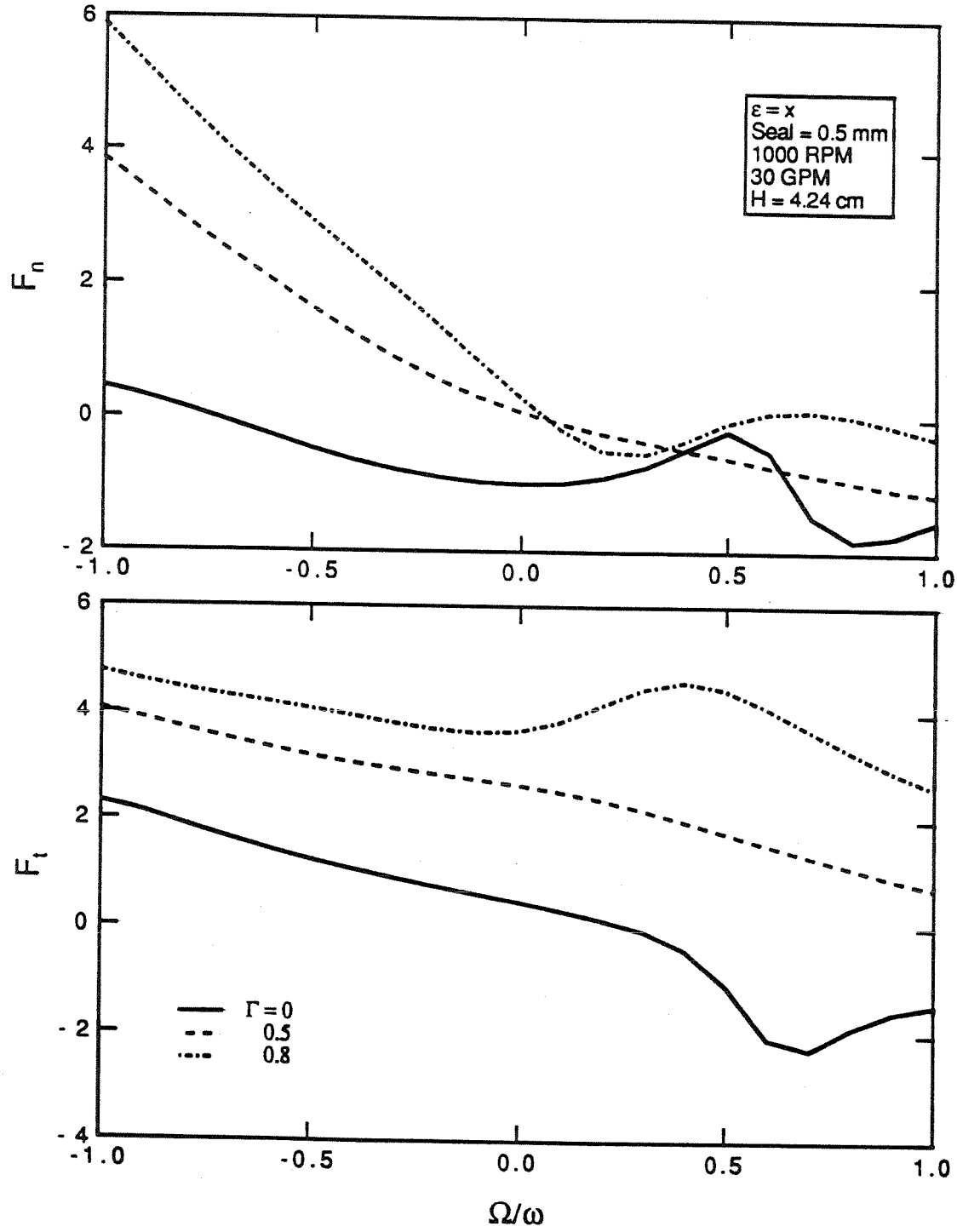

Figure 7.17 Numerical predictions of the normal and tangential forces, as a function of whirl ratio for the following conditions: seal clearance= 0.5 mm, 1000 RPM, 30 GPM H=4.24cm and three different inlet swirl ratios, Γ=0, 0.5, and 0.8.

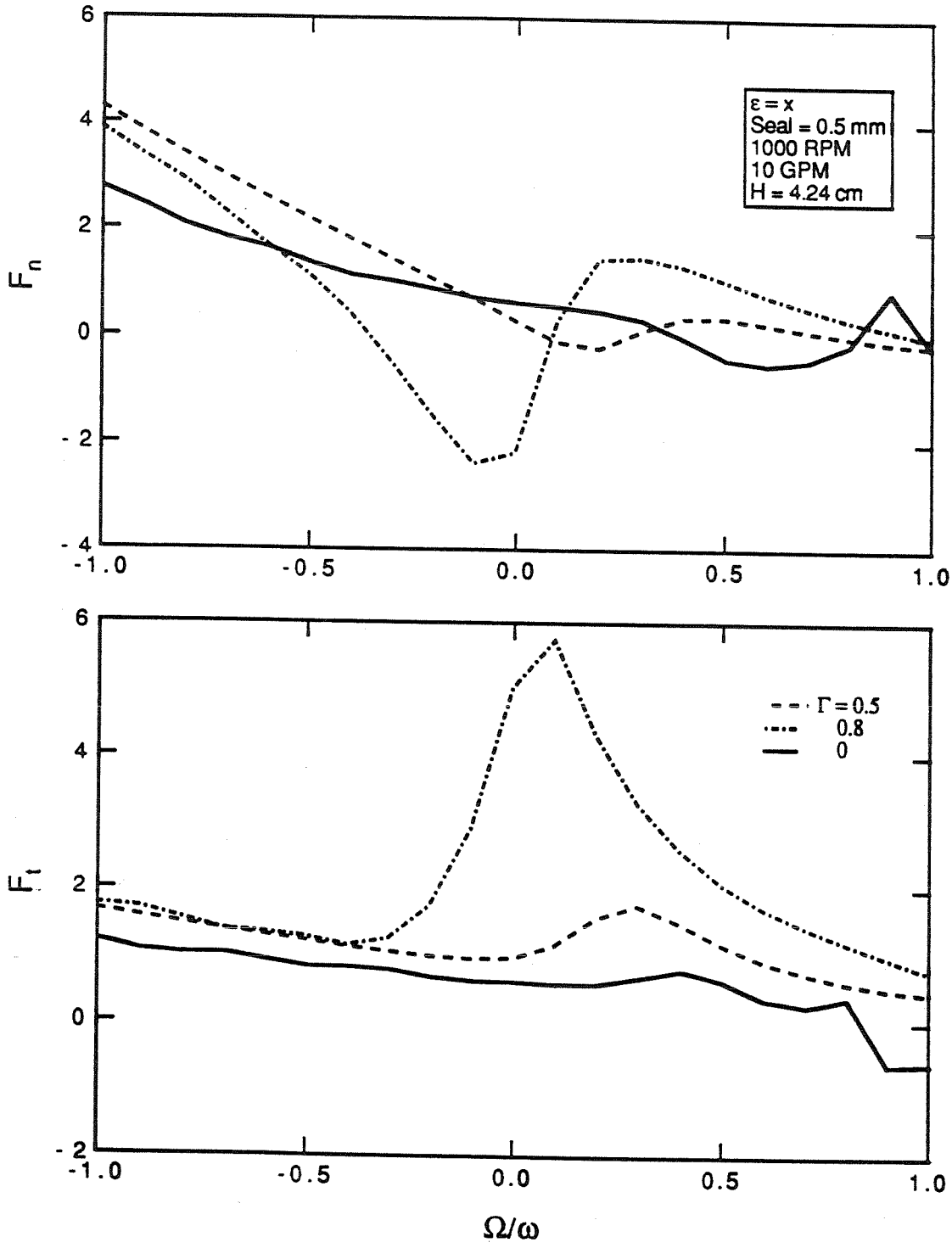

Figure 7.18 Numerical predictions of the normal and tangential forces, as a function of whirl ratio for the following conditions: seal clearance=0.5 mm, 1000 RPM, 10 GPM H=4.24cm and three different inlet swirl ratios, Γ=0, 0.5, and 0.8.

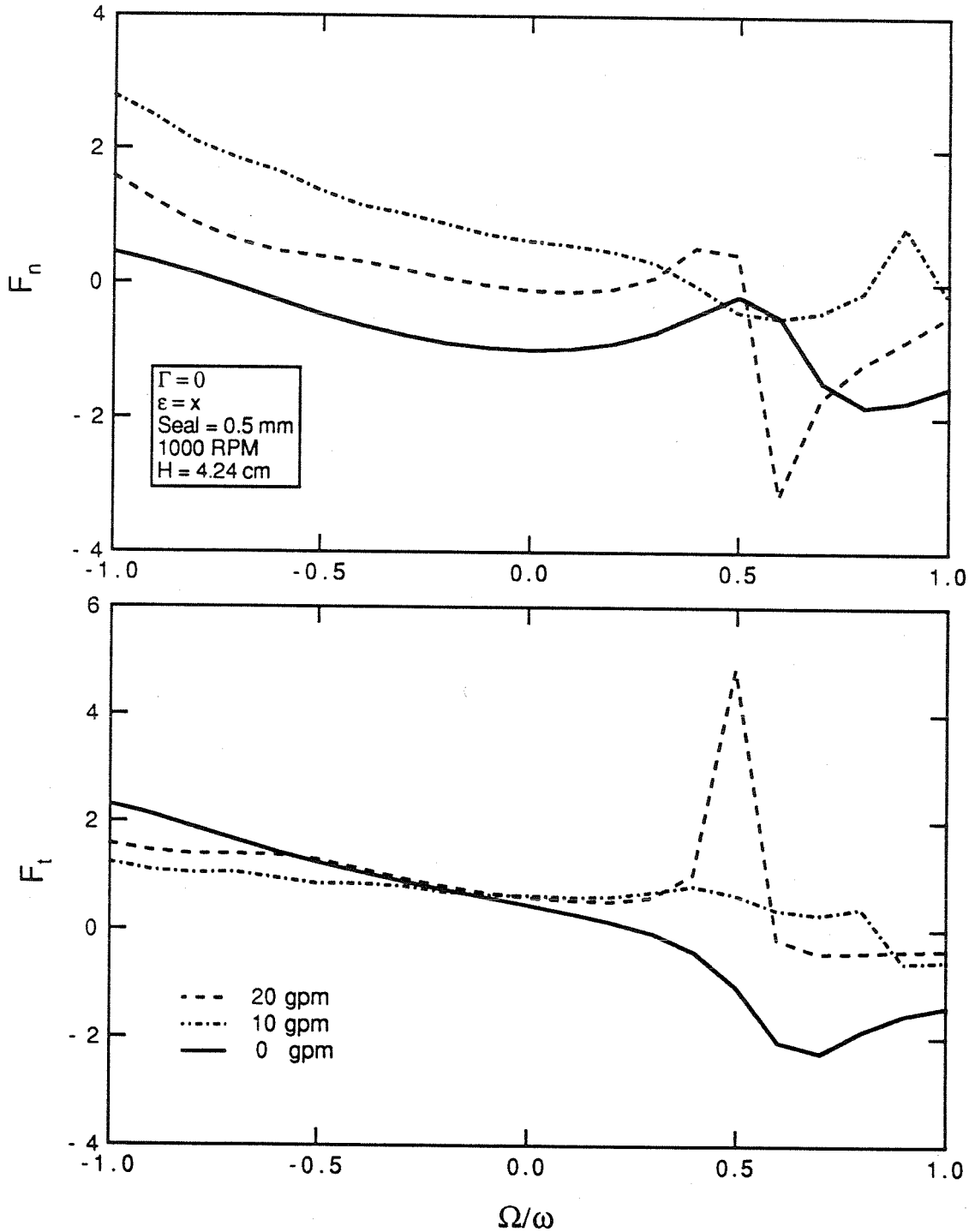

Figure 7.19 Numerical predictions of the normal and tangential forces, as a function of whirl ratio for the following conditions: Γ=0, seal clearance = 0.5 mm, 1000 RPM, H=4.24cm and three different flowrates, 10, 20, and 30 GPM.

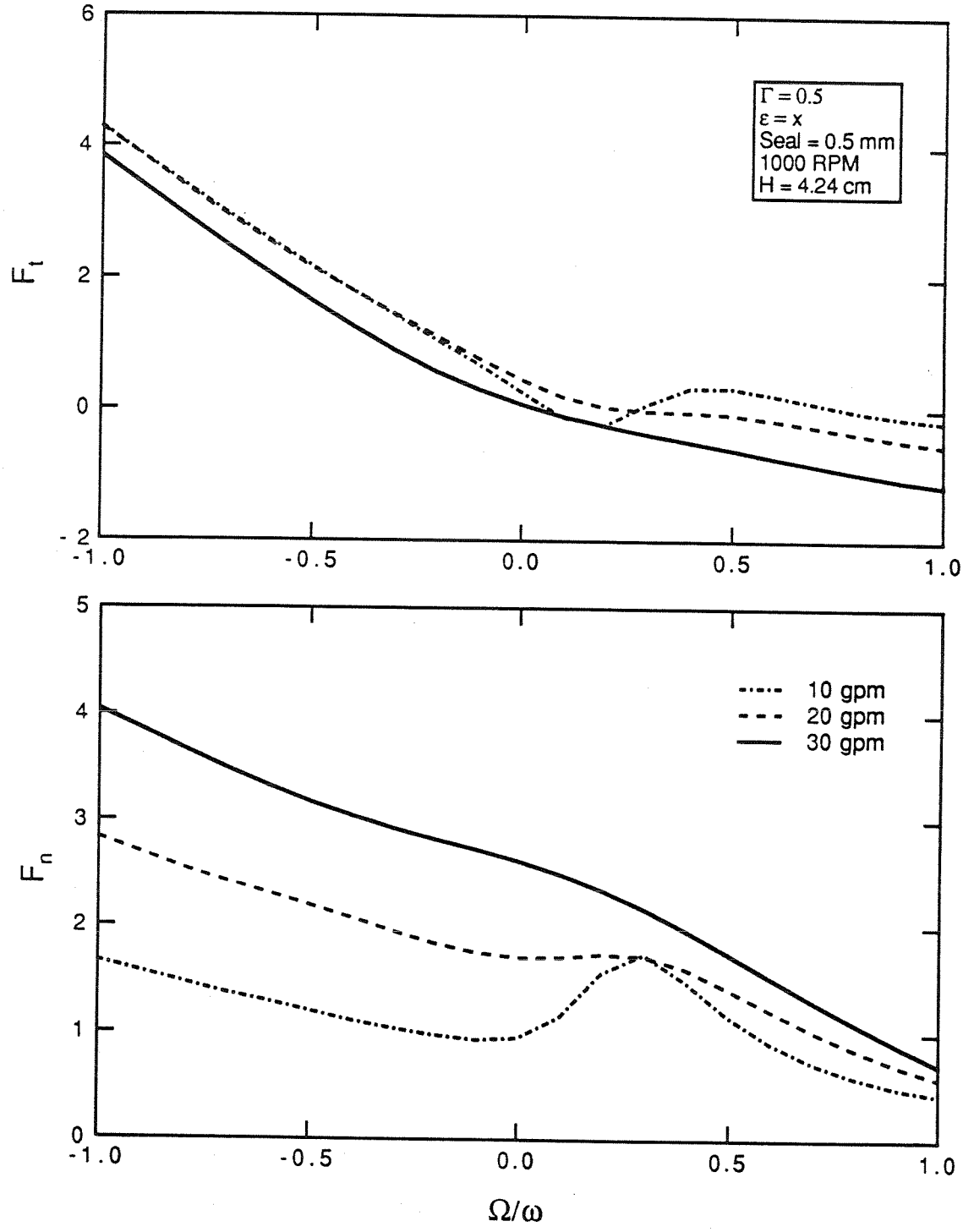

Figure 7.20 Numerical predictions of the normal and tangential forces, as a function of whirl ratio for the following conditions: Γ=0.5, seal clearance = 0.5 mm, 1000 RPM, H=4.24cm and three different flowrates, 10, 20, and 30 GPM.

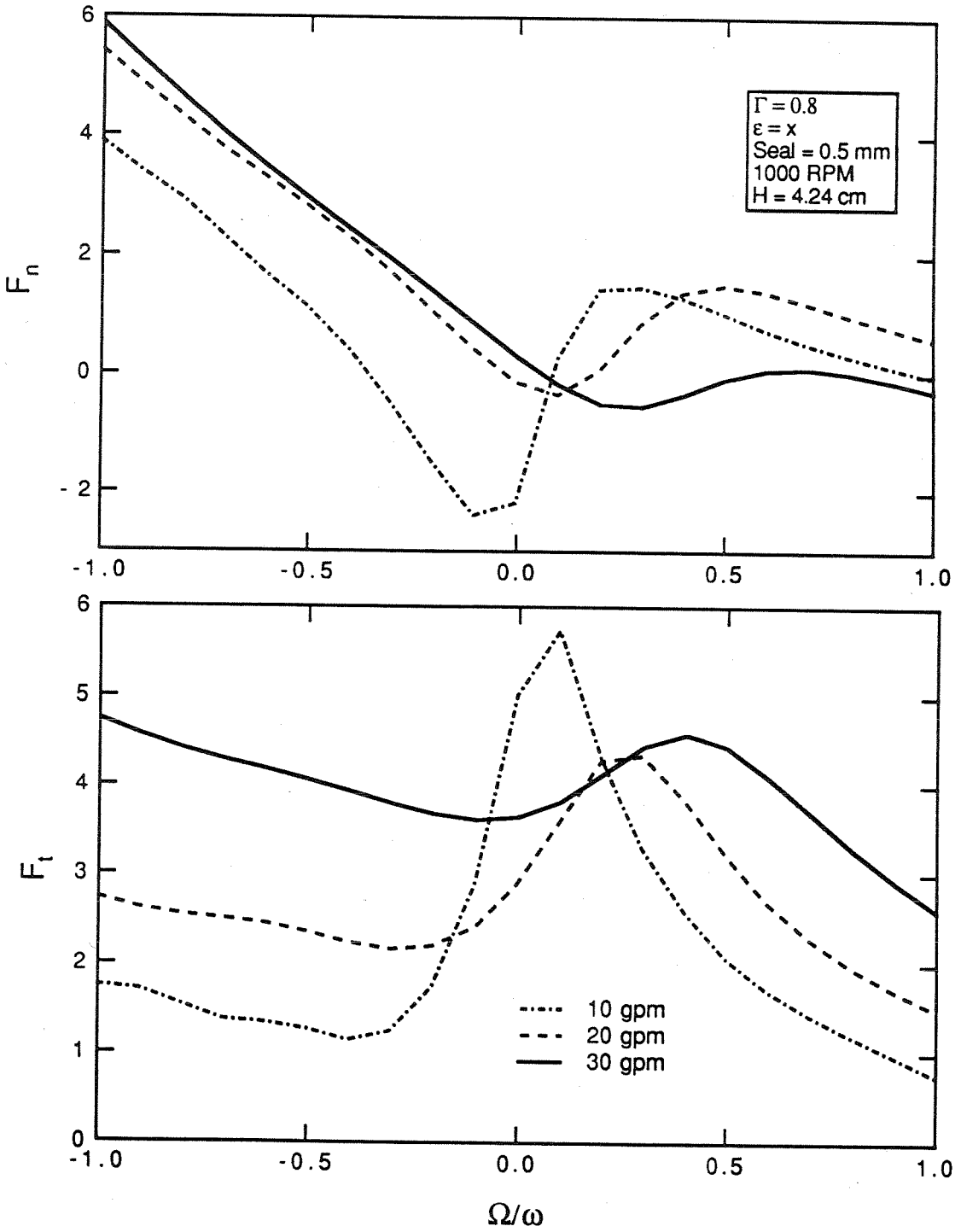

Figure 7.21 Numerical predictions of the normal and tangential forces, as a function of whirl ratio for the following conditions: Γ=0.8, seal clearance= 0.5 mm, 1000 RPM, H=4.24cm and three different flowrates, 10, 20, and 30 GPM.

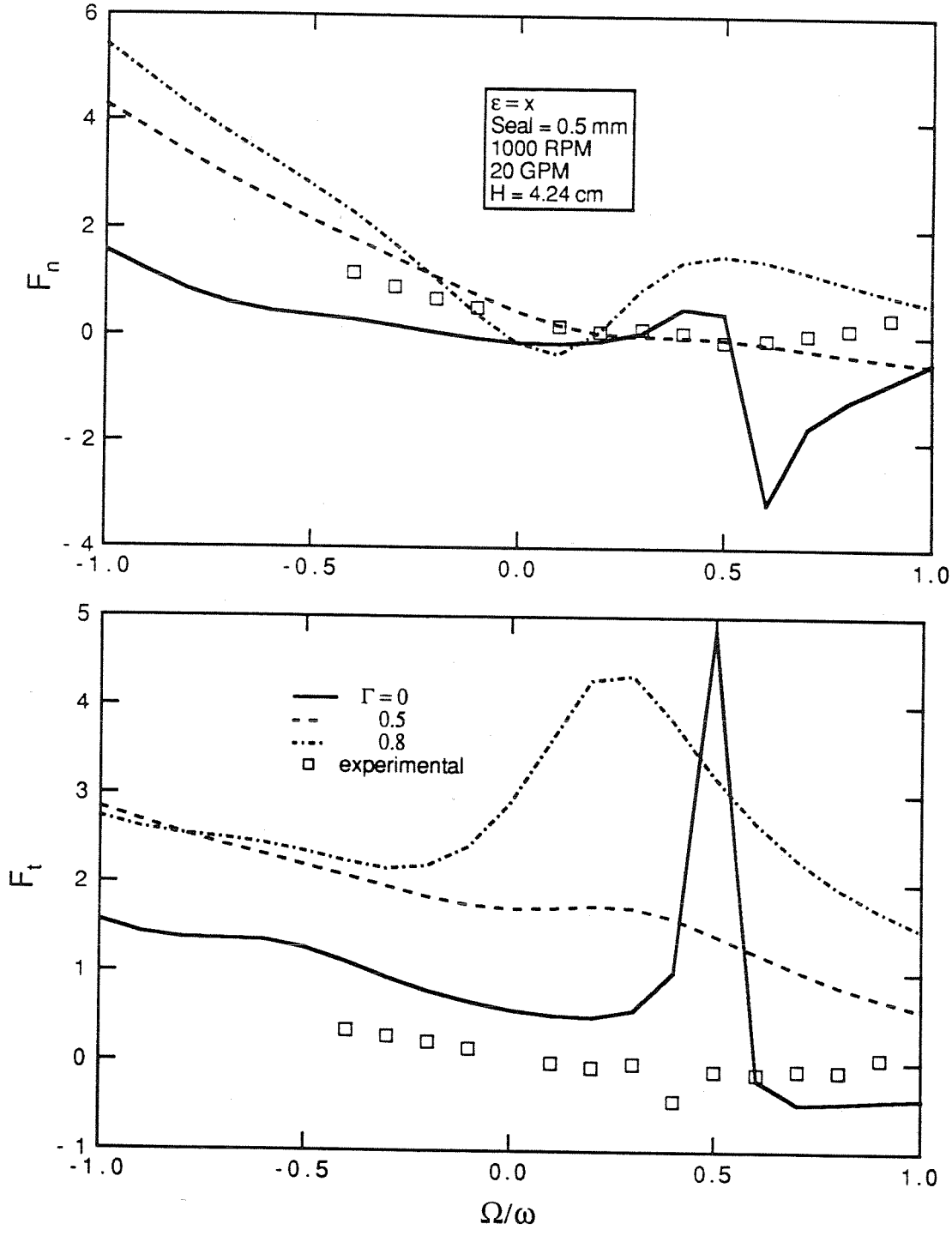

Figure 7.22 Comparison of the normal and tangential forces, as a function of whirl ratio from the numerical predictions for different inlet swirl ratios, Γ=0, 0.5, and 0.8 with the experimental results for the following conditions: seal clearance= 0.5 mm, 1000 RPM, a flow rate of 1.262 *ℓ*/sec, a clearance H=4.24cm and an eccentricity ε=0.0254 cm.

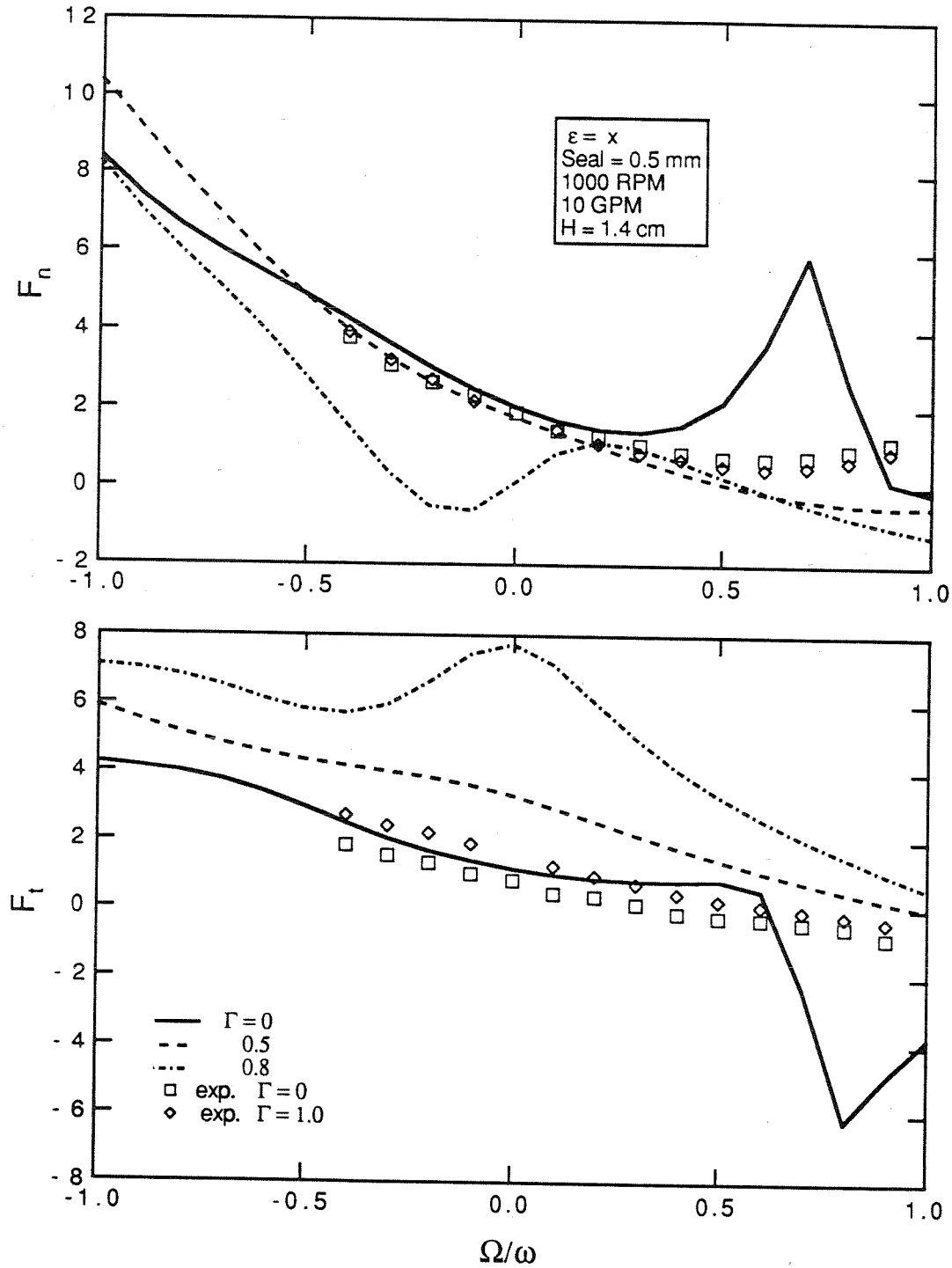

Figure 7.23 Comparison of the normal and tangential forces, as a function of whirl ratio from the numerical predictions for different inlet swirl ratios, Γ=0, 0.5, and 0.8 with the experimental results for the following conditions: seal clearance= 0.5 mm, 1000 RPM, a flow rate of 0.631 *ℓ*/sec, a clearance H=1.40cm and an eccentricity ε=0.118 cm.

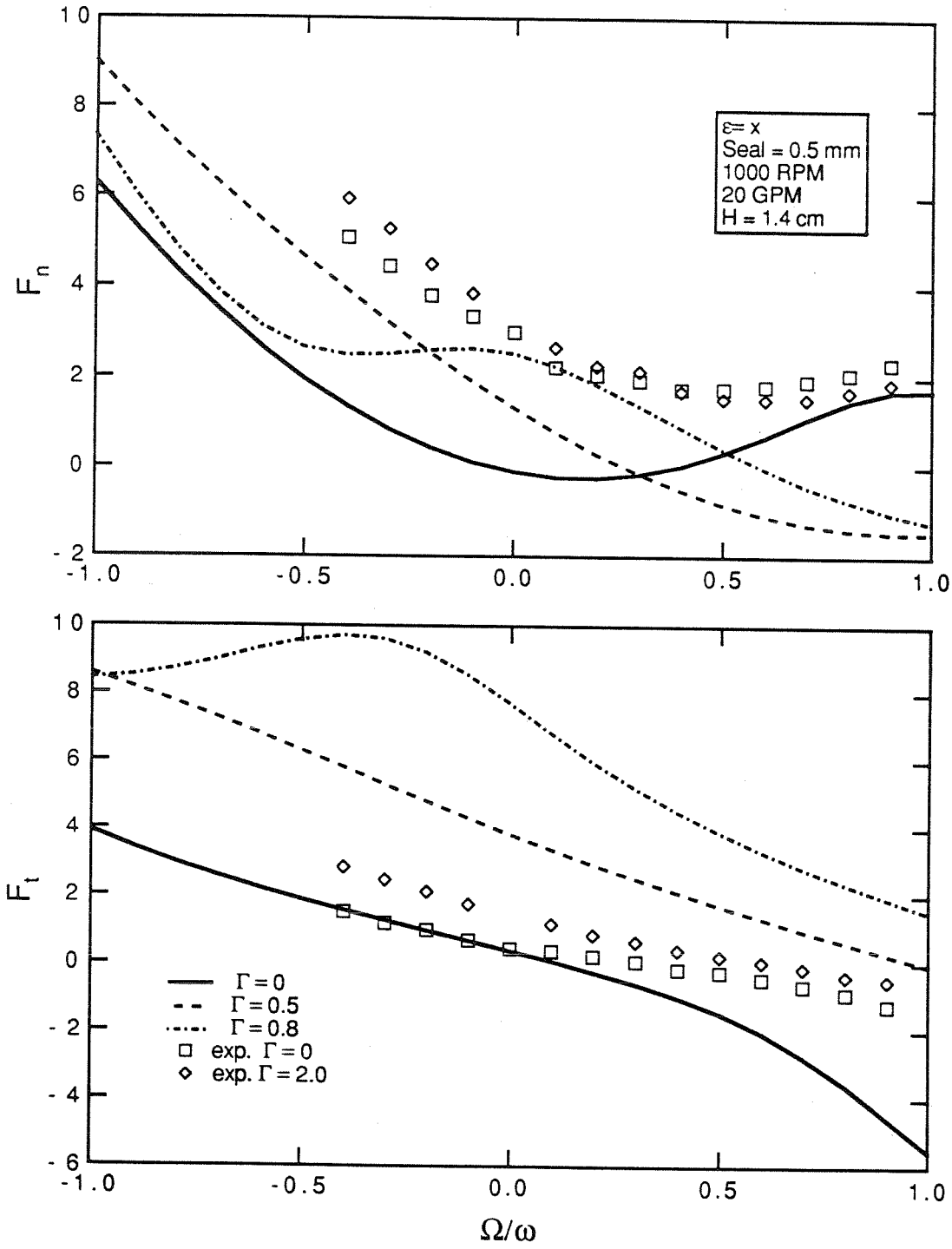

Figure 7.24 Comparison of the normal and tangential forces, as a function of whirl ratio from the numerical predictions for different inlet swirl ratios, Γ=0, 0.5, and 0.8 with the experimental results for the following conditions: seal clearance= 0.5 mm, 1000 RPM, a flow rate of 1.262 *ℓ*/sec, a clearance H=1.40cm and an eccentricity ε=0.118 cm.

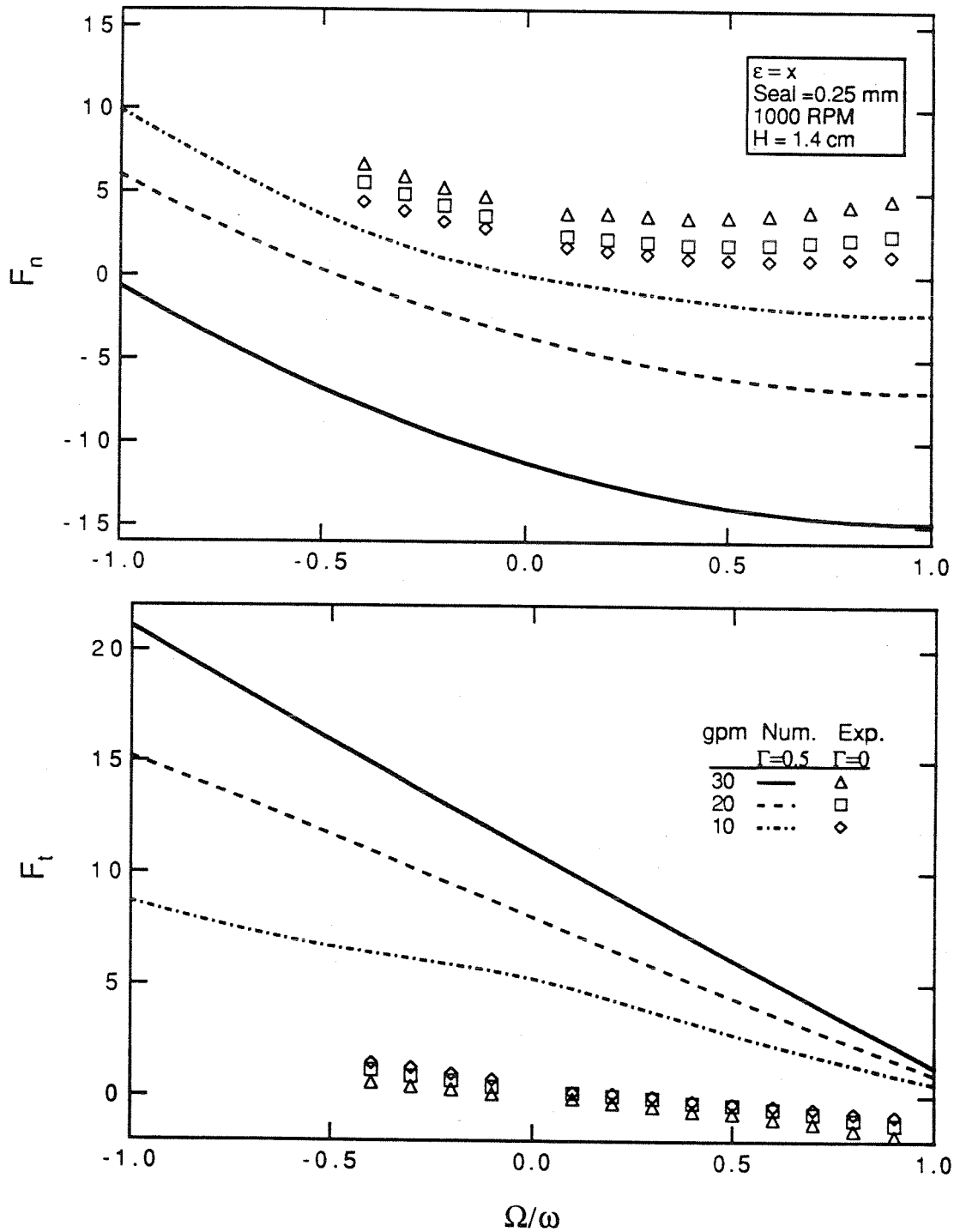

Figure 7.25 Comparison of the normal and tangential forces, as a function of whirl ratio from the numerical predictions for an inlet swirl ratio $\Gamma=0.5$ with the experimental results for the following conditions: different flow rates (0.631 *ℓ*/sec, 1.262 *ℓ*/sec, 1.892 *ℓ*/sec), a seal clearance= 0.25 mm, 1000 RPM, a clearance H=4.24cm and an eccentricity $\varepsilon=0.0254$ cm.

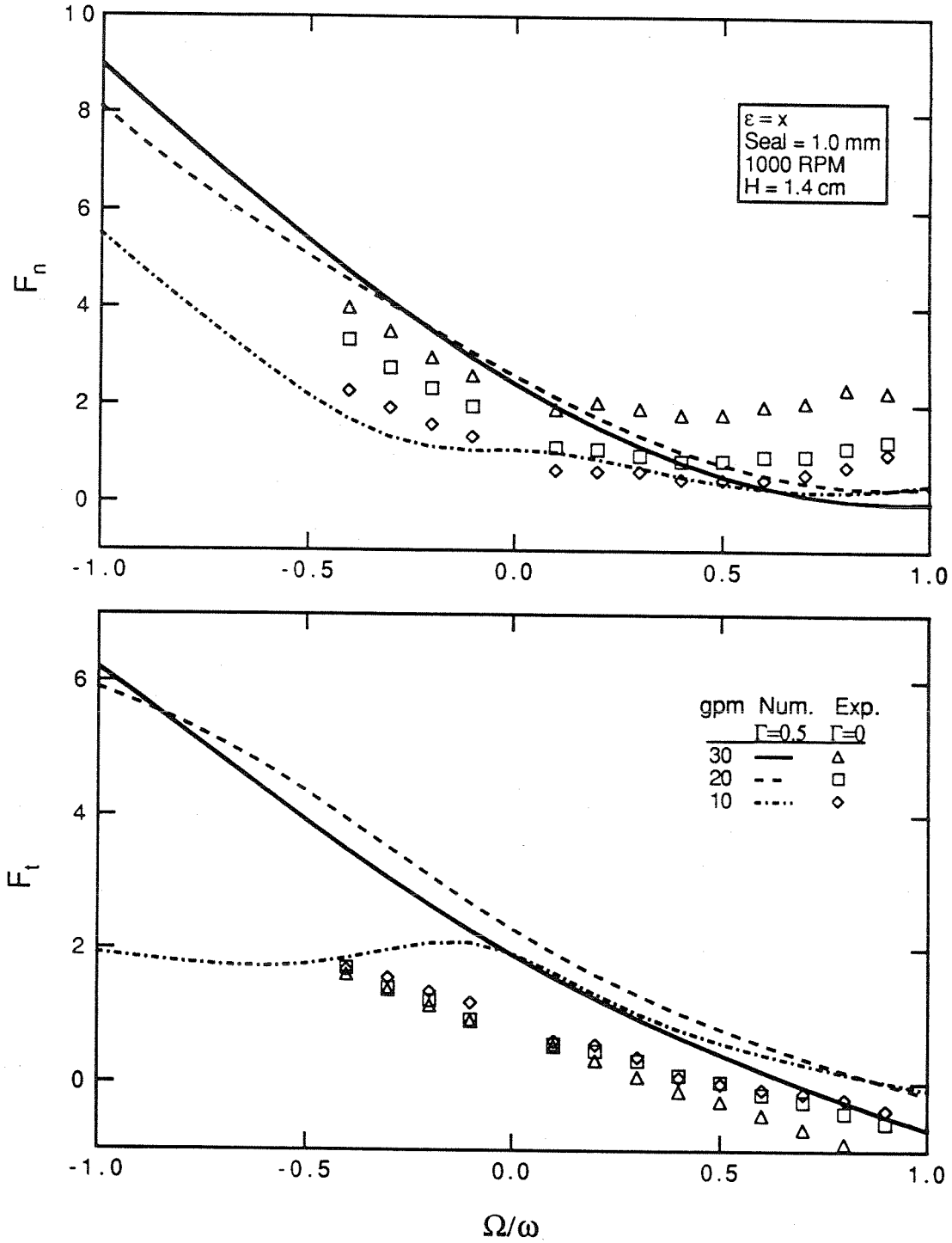

Figure 7.26 Comparison of the normal and tangential forces, as a function of whirl ratio from the numerical predictions for an inlet swirl ratio $\Gamma=0.5$ with the experimental results for the following conditions: different flow rates (0.631 *ℓ*/sec, 1.262 *ℓ*/sec, 1.892 *ℓ*/sec), a seal clearance= 1.0 mm, 1000 RPM, a clearance H=4.24cm and an eccentricity $\varepsilon=0.118$ cm.

CHAPTER 8

CONCLUSIONS

Measurements of the steady and unsteady fluid forces that are due to the discharge-to-suction leakage flows around pump impellers were made using a rotating dynamometer on which the shroud was directly mounted. The objective was to study the behavior of the hydrodynamically-induced force-matrix [A] for different operating conditions. A review of the existing experimental and analytical results shows that the discharge-to-suction leakage flows in centrifugal pumps can contribute substantially to the fluid-induced rotordynamic forces for that turbomachine. While the geometry of the impeller shroud/pump casing annulus varies considerably in previous studies [Chamieh et al. (1985), Jery et al. (1985), Adkins et al. (1988)] the indications are that the contributions from the leakage flow can be of the same order as those acting on the impeller discharge. This motivated the current experimental study of leakage flows between the shroud and the stationary casing of a centrifugal pump and their rotordynamic effects.

Experimental results for simulated leakage flows of rather simple geometry are presented for different whirl frequencies, eccentricities, clearances and flow rates. As with previous results for impellers, the forces scaled with the square of the rotor speed. The functional dependence on whirl frequency to rotating frequency ratio (termed the whirl ratio) is very similar to that measured in experiments and to that predicted in the theoretical work of Childs. Two sets of results taken at different eccentricities yield quite similar nondimensional rotordynamic forces indicating that the experiments probably lie within the linear regime. The dimensionless forces are found to be functions not only of the whirl ratio but also of the flow rate and of the clearance. A region of forward whirl for which the average tangential force is destabilizing, was found. This region decreased with the flow coefficient. While the dependence on flow rate is not simple, it would appear that the dimensionless rotordynamic forces are roughly inversely proportional to the clearance. The change with the discharge resistance was slightly more

complicated. Reverse whirl was found to be fairly stable.

The effect of swirl is to increase the tangential force thereby also increasing the range of whirl ratios for which there is a potentially destabilizing force. Thus reducing the swirl to the flow would be stabilizing. As for the normal force, swirl seems to decrease the force at positive whirl. The effects of swirl are in contrast to the effects of increasing the leakage flow, which causes a decrease in the normal force and an increase in the tangential force. Clearly it would be interesting to examine the case where flow is increased while the swirl remains fixed. This would however, require the construction of additional inlet guides.

The experimental results which included the addition of swirl to the inlet flow agreed surprisingly well with the magnitudes of the results that were predicted by a numerical model based on the analysis of Childs (1989). The shroud clearance effect on the rotordynamic forces was found to be the same in both methods. However, for the other parameters such as the seal clearance or the flow coefficient, the two methods did not agree with each other in predicting a trend. Finally, the experiments showed none of the "resonances" predicted by the bulk flow models proposed by Childs.

REFERENCES

Adkins, D.E. 1986. Analyses of Hydrodynamic Forces on Centrifugal Pump Impellers. Ph.D. Thesis, California Institute of Technology, Pasadena, Calif.

Adkins, D.R., and Brennen, C.E. 1988. Analyses of Hydrodynamic Radial Forces on Centrifugal Pump Impellers. ASME J. Fluids Eng., Vol. 110, No. 1, pp. 20-28.

Alford, J.S. 1965. Protecting Turbomachinery from Self-Excited Rotor Whirl. J. Eng. for Power, October 1965, pp. 333-344

Andrews, K.A. 1988. Orifice Coefficients for an Asymmetrical Flow in a Slot. E200.26, Division of Engineering and Applied Science, California Institute of Technology.

Arndt, N.K.E. and Franz, R.J. 1986. Observations of Hydrodynamic Forces on Several Inducers including the SSME LPOTP. Division of Engineering and Applied Science, California Institute of Technology, Pasadena, CA, Report No. 249.3.

Arndt, N.K.E. 1988. Experimental Investigation of Rotor-stator Interaction in Diffuser Pumps. Ph.D. Thesis, California Institute of Technology, Pasadena, Calif.

Benckert, H. and Wachter, J. 1980. Flow Induced Spring Coefficients of Labyrinth Seals for Application in Rotor Dynamics. Workshop on Rotordynamic Instability Problems in High Performance Turbomachinery, pp. 189-212.

Black, H.F. 1969. Effects of Hydraulic Froces in Annular Pressure Seals on the Vibrations of Centrifugal Pump Rotors. J. Mech. Eng. Science, Vol. 11, No. 2, pp. 206-213.

Bolleter, U., Wyss, A., Welte, I. and Sturchler, R. 1985. Measurements of Hydrodynamic Interaction Matrices of Boiler Feed Pump Impellers. ASME Paper No. 85-DET-148. See also Bolleter et al. 1987.

Bolleter, U., Wyss, A., Welte, I., Stürchler, R. 1987. Measurement of Hydrodynamic Interaction Matrices of Boiler Feed Pump Impellers. ASME J. Vibration, Acoustics, Stress, and Reliability in Design, Vol. 109, pp. 144-151.

Bolleter, U., Leibundgut, E., Sturchler, R. 1989. Hydraulic Interaction and Excitation Forces of High Head Pump Impeller. Pumping Machinery- 1989, Vol. 81, 3rd Joint ASCE/ASME Mechanics Conference, UCSD, July 9-12, 1989, pp. 187-193.

Brennen, C. 1976. On the Flow in an Annulus Surrounding a Whirling Cylinder. J. Fluid Mech., Vol. 75, pp. 173-191.

Brennen, C.E., Acosta, A.J. and Caughey, T.K. 1986. Impeller Fluid Forces. NASA Proc. Advanced Earth-to-Orbit Propulsion Tech. Conf., Huntsville, AL, NASA Conf. Publ. 2436, pp. 270-295.

Chamieh, D.S. 1983. Forces on a Whirling Centrifugal Pump-Impeller. Ph.D. Thesis, Division of Engineering and Applied Science, California Institute of Technology, Pasadena, CA.

Chamieh, D.S., Acosta, A.J., Brennen, C.E., Caughey, T.K. 1985. Experimental Measurements of Hydrodynamic Radial Forces and Stiffness Matrices for a Centrifugal Pump-Impeller. ASME Journal of Fluids Engineering, Vol. 107, No.3, pp. 307-315.

Childs, D. W. 1983a. Dynamic Analysis of Turbulent Annular Seals Based on Hirs' Lubrication Equation. Transactions of the ASME: Journal of Lubrication Technology, Vol. 105. ASME/ASLE Joint Lubrication Conference, Washington, D.C., October 5-7, 1982, Paper No. 82-Lub-41, pp. 429-436.)

Childs, D. W. 1983b. Finite-Length Solutions for Rotordynamic Coefficients of Turbulent Annular Seals. Transactions of the ASME: Journal of Lubrication Technology, Vol. 105, July 1983,ASME/ASLE Joint Lubrication Conference, Washington, D.C., October 5-7, 1982, Paper No. 82-Lub-42, pp. 437-445.

Childs, D.W. 1986. Force and Moment Rotordynamic Coefficients for Pump-Impeller Shroud Surfaces. Proceedings of Advanced Earth-to-Orbit Propulsion Technology Conference, Hunstville, AL, May 1986, NASA Conf Publ. 2436, pp. 296-326.

Childs, D. W. 1987. Fluid Structure Interaction Forces at Pump-Impeller-Shroud Surfaces for Rotordynamic Calculations. Rotating Machinery Dynamics, Vol 2, ASME, pp. 581-594.

Childs, D. W. 1989. Fluid Structure Interaction Forces at Pump-Impeller-Shroud Surfaces for Rotordynamic Calculations. ASME J. Vibration, Acoustics, Stress, and Reliability in Design, Vol. 111, pp. 216-225.

Childs, D.W., Elrod, D., Hale, K. 1988. Annular Honeycomb Seals: Test Results for Leakage and Rotordynamic Coefficients; Comparisons to Labyrinth and Smooth Configurations. 3rd Conference on Advanced Earth-to-Orbit Propulsion Technology, Huntsville, Alabama, May, 1988, pp. 79-94.

Childs, D. W., Ramsey, C. 1990a. Seal-Rotordynamic-Coefficient Test Results for a Model SSME ATD-HPFTP Turbine Interstage Seal With and Without Swirl Brake. Joint ASME/STLE Tribology Conference, Toronto, Canada, October 7-10, Paper No. 90-Trib-12.

Childs, D. W., Baskharone, E., Ramsey, C. 1990b. Test Results for Rotordynamic Coefficients of the SSME HPOTP Turbine Interstage Seal with Two Swirl Brakes. Joint ASME/STLE Tribology Conference, Toronto, Canada, October 7-10, Paper No. 90-Trib-45.

Crandall, Stephen H. 1982. Heuristic Explanation of Journal Bearing Instability. Rotordynamic Instability Problems of High Performance Turbomachinery. NASA Conference Publication 2250, pp. 274-283.

Domm, U. and Hergt, P. 1970. Radial Forces on Impeller of Volute Casing Pumps. Flow Research on Blading, editor L.S. Dzung, Elsevier Publ. Co., Netherlands, pp. 305-321.

Falco, M., Mimmi, G., Pizzigoni, B., Marenco, G., Negri, G. 1984. Plain Seal Behavior - Experimental and Analytical Results. IMechE C303/84.

Franz, R.J. and Arndt, N.K.E. 1986. Measurements of Hydrodynamic Forces on a Two-Dimensional Impeller and a Modified Centrifugal Pump. Division of Engineering and Applied Science, California Institute of Technology, Pasadena, CA, Report No. 249.4.

Franz, R. 1989. Experimental Investigation of the Effect of Cavitation on the Rotordynamic Forces on a Whirling Centrifugal Pump Impeller. Ph.D. Thesis, California Institute of Technology, Pasadena, Calif.

Franz, R., Acosta, A.J., Brennen, C.E., Caughey, T.K. 1989. The Rotordynamic Forces on a Centrifugal Pump Impeller in the Presence of Cavitation. Proceedings of 3rd Joint ASCE/ASME Mechanics Conference, UCSD, July 1989, Pumping Machinery, Vol. 81, pp. 205-212.

Guinzburg, A., Brennen, C.E., Acosta, A.J. and Caughey, T.K. 1990. Rotordynamic Forces Generated by Discharge-to-suction Leakage Flows in Centrifugal Pumps. NASA CP-3092.

Guinzburg, A., Brennen, C.E., Acosta, A.J. and Caughey, T.K. 1990. Measurements of the Rotordynamic Shroud Forces for Centrifugal Pumps. ASME Turbomachinery Forum, Toronto, Canada, June 1990.

Guinzburg, A., Brennen, C.E., Acosta, A.J., Caughey, T.K. 1992a. The Effect of Swirl on the Rotordynamic Shroud Forces in a Centrifugal Pump. To be presented at the 1992 ASME TURBO EXPO, Cologne.

Guinzburg, A., Brennen, C.E., Acosta, A.J., Caughey, T.K. 1992b. The Rotordynamic Characteristics of Leakage Flows in Centrifugal Pumps. To be presented at the 1992 NFDC, Los Angeles.

Hawkins, L. and Childs D.W. 1988. Experimental Results for Labyrinth Gas Seals with Honeycomb stators: Comparisons to Smooth-Stator Seals and Theoretical Predictions. 3rd Conference on Advanced Earth-to-Orbit Propulsion Technology, Huntsville, Alabama, May, 1988, pp. 94-111.

Hergt, P. and Krieger, P. 1969-70. Radial forces in centrifugal pumps with guide vanes. Proc. Inst. Mech. Eng., Vol. 184, Part 3N, pp. 101-107.

Hirs, G.G. 1972. A Bulk-Flow Theory for Turbulence in Lubricant Films, Transactions of the ASME: Journal of Lubrication Technology. International Lubrication Conference, New York, NY, October 9-12, 1972, Paper No. 72-Lub-12, pp. 137-146.

Iversen, H.W., Rolling, R.E., and Carlson, J.J. 1960. Volute Pressure Distribution, Radial Force on the Impeller and Volute Mixing Losses of a Radial Flow Centrifugal Pump. ASME Journal of Engineering for Power, Vol. 82, No. 2, pp. 136-144.

Jery, B. 1986. Experimental Study of Unsteady Hydrodynamic Force Matrices on Whirling Centrifugal Pump Impellers. Ph.D Thesis, California Institute of Technology.

Jery, B., Acosta, A.J., Brennen, C.E., and Caughey, T.K. 1985. Forces on Centrifugal Pump Impellers. Second International Pump Symposium, Houston, Texas, April 29-May 2, 1985.

Lomakin, A. 1958. Calculation of Critical Speed and Securing of the Dynamic Stability of the Rotor Hydraulic High Pressure Machines With Reference to Forces Arising in Seal Gaps. Energomashinostroenie, Vol 4. (in Russian)

Nguyen, D.T., Nelson, C.C. 1988. Effects of Eccentricity in Annular Pressure Seals on Rotordynamic Coefficients and Rotordynamics. 3rd Conference on Advanced Earth-to-Orbit Propulsion Technology, Huntsville, Alabama, May, 1988, pp. 52-65.

Pinkus, 0., Sternlicht, B. 1961. Theory of Hydrodynamic Lubrication. McGrawhill

Scharrer, J.K., Hecht, R.F., Hibbs Jr.,R.I. 1991. The Effects of Wear on the Rotordynamic Coefficients of a Hydrostatic Journal Bearing. ASME J. Tribology, Vol. 113, pp. 210-213.

Sherzer, A.F. 1924. Determination of Internal Leakage in Centrifugal Pumps. Engineering News-Record, Vol. 92, No. 25, pp. 1056-1058.

Stafford, J. A. T., Ferguson, T. B., Hirst, E. S. and Asquith, R. W.1975. An Experimental Investigation Observing Some Unsteady Flows Induced by a Rotating Disc. Proc. of the 5th Conference on Fluid Machinery, 2, 1071-1079, Budapest.

Thompson, W.E. 1978. Fluid Dynamic Excitation of Centrifugal Compressor Rotor Vibrations. ASME J. Fluids Eng., Vol. 100, pp. 73-78.

Yamada, Y. 1960. Resistance of a Flow through an Annulus with an Inner Rotating Cylinder, Bulletin of JSME, Vol. 5, No. 18, pp. 302-310.

Vance, J.M. 1988. Rotordynamics of Turbomachinery. John Wiley & Sons, Inc.

Vance, J.M., Laudadio, F.J. 1982. Experiment Measurement of Alford's Force in Axial-Flow Turbomachinery, Rotordynamic Instability Problems of High Performance Turbomachinery, NASA Conference Publication 2250, pp. 260-273.

Zhuang, F. 1989. Experimental Investigation of the Hydrodynamic Forces on the Shroud of a Centrifugal Pump Impeller. E249.9, Division of Engineering and Applied Science, California Institute of Technology.

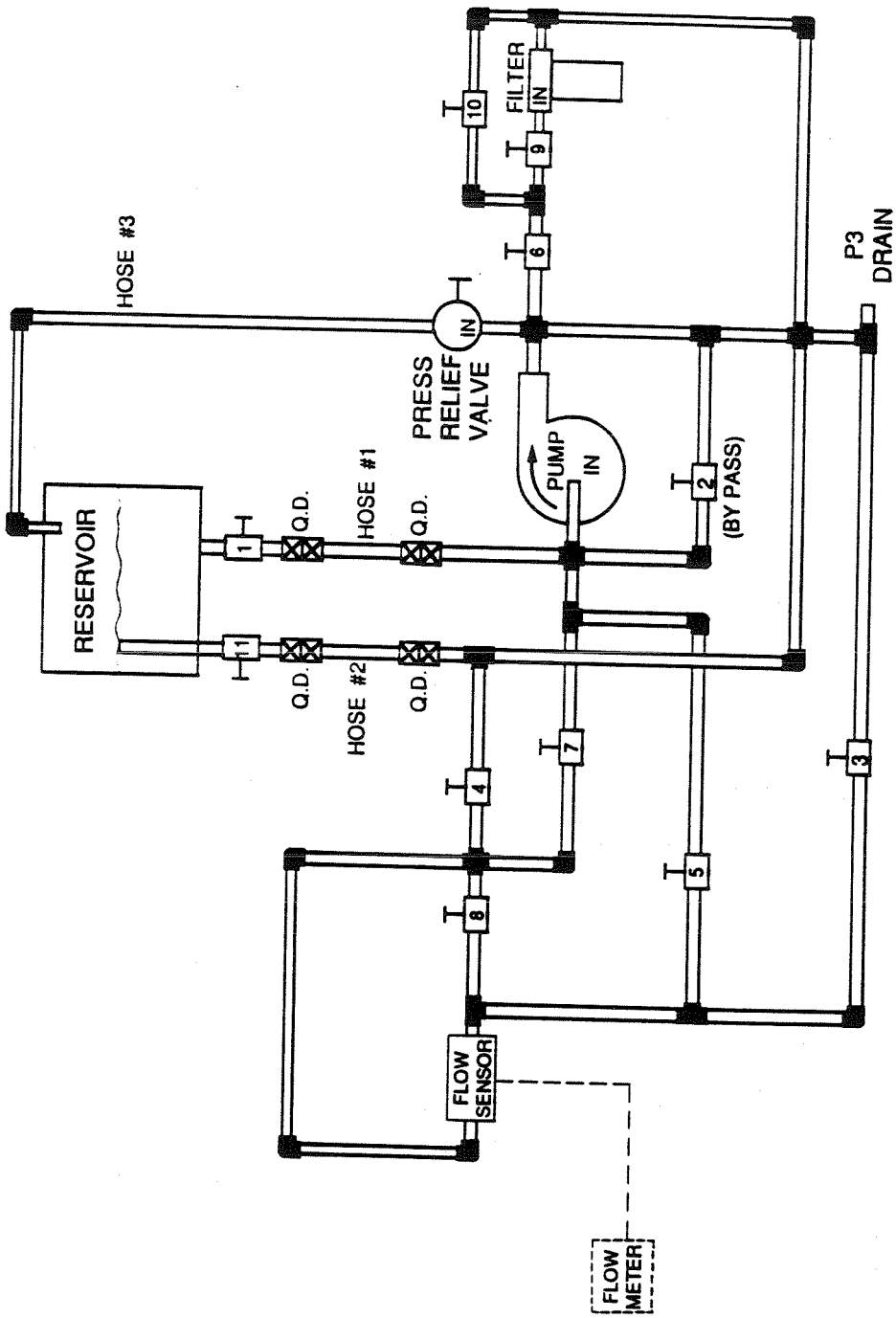

Figure A.1 Sketch of the pump used for the leakage flow.

APPENDIX A: Leakage flow estimate calculation and flow loop

A typical head coefficient for an impeller is on the order of 0.4 and the corresponding flow coefficient is 0.14:

$$\phi_t = U_c/\omega R_2 = 0.14$$

$$\text{where } U_c = Q_c / A \text{ , } A = \pi R_1^2$$

Atypical ratio of the leakage flow Q_L to the flow through the impeller Q_c, is about 7% and this gives a value of 10 GPM for the leakage flow.

APPENDIX B: Swirl ratio calculation

The following equations are defined:

$$\Gamma = U_\theta/\omega R_2$$

$$\phi = U_s/\omega R_2$$

Assuming that the fluid will be constrained to flow along the guide vane, the turning angle of the vane is related to the fluid velocities as follows:

$$\text{Tan } \alpha = U_R / U_T$$

$$U_R = \frac{H}{B} U_s$$

$$U_T = U_\theta$$

$$\Gamma = \frac{Q}{B} \frac{1}{2\pi R_2^2 \omega} \frac{1}{\tan \alpha}$$

$$\text{Tan } \alpha = \frac{Q}{B} \frac{1}{2\pi R_2^2 \omega} \frac{1}{\Gamma} = \frac{Q}{B} \frac{1}{\Gamma} \frac{1}{RPM} \times 0.427$$

To yield a wide range of swirl ratios, for low flow coefficients, the turning angle was chosen to be 2°, and the width of the vane , B was chosen to be 0.3175 cm.

APPENDIX C: Description of the first order parameters

Perturbation Coefficients

$$A_{1s}=[\lambda_s(1-ms)+\lambda_r(1-mr)]u_{so}^2/2h_o$$

$$A_{2s}=-\frac{2u_{\theta o}}{r}\frac{dr}{ds}+[\lambda_r(mr+1)\beta_o+\lambda_s(ms+1)\beta_1]u_{so}/2$$

$$A_{3s}=\frac{du_{so}}{ds}+\frac{[(2+mr)\lambda_r+(2+ms)\lambda_s]u_{so}}{2}-\frac{(1+mr)\lambda_r\beta_o(u_{\theta o}-r)+(1+ms)\lambda_s\beta_1 u_{\theta o}}{2}$$

$$2A_{1\theta}=u_{so}[(1-mr)(u_{\theta o}-r)\lambda_r+(1-ms)u_{\theta o}\lambda_s]/h_o$$

$$2A_{2\theta}=u_{so}(\lambda_r+\lambda_s)+\lambda_r(mr+1)(u_{\theta o}-r)\beta_o+\lambda_s(ms+1)u_{\theta o}\beta_1+2\frac{u_{so}}{r}\frac{dr}{ds}$$

$$2A_{3\theta}=\lambda_r(u_{\theta o}-r)[mr-(1+mr)\beta_o(u_{\theta o}-r)/u_{so}]+\lambda_s u_{\theta o}[ms-(1+ms)\beta_1 u_{\theta o}/u_{so}]$$

$$\beta_o=(u_{\theta o}-r)/u_{so}\{1+[(u_{\theta o}-r)/u_{so}]^2\}$$

$$\beta_1=u_{\theta o}/u_{so}[1+(u_{\theta o}/u_{so})^2]$$

$\tau_{r\theta}$ Perturbation Coefficients

$$B_{\theta 1}=\frac{H}{L}\lambda_r(1+mr)(u_{\theta o}-r)[1-\beta_o(u_{\theta o}-r)/u_{so}]/2$$

$$B_{\theta 2}=\frac{H}{L}\lambda_r[u_{so}+(1+mr)(u_{\theta o}-r)\beta_o]/2$$

$$B_{\theta 3}=\frac{H}{L}\lambda_r mr(u_{\theta o}-r)u_{so}/2h_o$$

τ_{rs} Perturbation Coefficients

$$B_{s1}=\frac{H}{L}\lambda_r[(2+mr)u_{so}-(1+mr)\beta_o(u_{\theta o}-r)]/2$$

$$B_{s2}=\frac{H}{R}\lambda_r(1+mr)\beta_o u_{so}/2$$

$$B_{s3}=\frac{H}{L}\lambda_r mr u_{so}^2/2h_o$$

APPENDIX D: Matrix of test runs

Name	ε (cm)	H (cm)	RPM	ℓ/sec	H_S (cm)	Γ
0B0OC	0.0254	0.424	1000	0	0.050	0
0B0AC				0.631		
0B0BC				1.262		
0B0CC				1.892		
0B00A		0.140		0		
0B0AA				0.631		
0B0BA				1.262		
0B0CA				1.892		
0G00A			2000	0		
0G0AA				0.631		
0G0BA				1.262		
0F00A			500	0		
0F0AA				0.631		
0F0BA				1.262		
0F0CA				1.892		
1B10A	0.118	0.140	1000	0		
1B1AA				0.631		
1B1BA				1.262		
1B1CA				1.892		
1B1GA				2.524		
1B1HA				3.154		

Name	ε (cm)	H (cm)	RPM	ℓ/sec	H_S (cm)	Γ
1G10A	0.118	0.140	2000	0	0.050	0.
1G1AA				0.631		
1G1BA				1.262		
1F10A			500	0		
1F1AA				0.631		
1F1BA				1.262		
1F1CA				1.892		
1B10B		0.212	1000	0.		
1B1AB				0.631		
1B1BB				1.262		
1B1CB				1.892		
1B1BC		0.424		1.262		
1B1GC				2.524		
1B1HC				3.155		
1F1AC			500	0.631		
1F1CC				1.892		
1F1HC				3.154		
2B20A		0.140		0.	0.100	
2B2AA				0.631		
2B2BA				1.262		
2B2CA				1.892		
3B3AA				0.631	0.0250	
3B3BA				1.262		
3B3CA				1.892		

Name	ε (cm)	H (cm)	RPM	ℓ/sec	H_S (cm)	Γ
TBTFA				0.315	0.0500	0.5
TBTAA				0.631		1.0
TBTBA				1.262		2.0
TBTCA				1.892		3.0
TBTGA				2.524		4.0

APPENDIX E: Nondimensional quantities

$$\varphi = Q/2\pi R^2 H\omega = \frac{Q}{H\ RPM} \times 0.427$$

Table of φ for 10 GPM

	RPM		
H(cm)	500	1000	2000
0.140	0.155	0.078	0.039
0.212	0.101	0.051	0.025
0.424	0.051	0.026	0.013

Table of φ for 1000 RPM

	GPM		
H(cm)	10	20	30
0.140	0.078	0.156	0.234
0.212	0.051	0.102	0.153
0.424	0.026	0.052	0.078

Table of $Re_\omega = \omega R_2^2/\nu$

RPM	500	1000	2000
Re_ω	462 000	925 000	1 851 000

Table of $Re_\phi = \frac{2\ H\ U_s}{\nu}$

GPM	10	20	30
Re_ϕ	2136	4272	6408

APPENDIX F: Program listing

```
      program bet
c     this program models the equations in the paper by Childs.


      implicit none

      integer nmax
      parameter (nmax=500)              !number of points

c if more than 21 whirl points will be used then the number of files opened
c must be changed

      integer i,j,k,intf,icount
      integer nwhirl,nw                 !number of increments for whirl
      integer nc,nn                     !number of coordinates
                                        !number of increments for geometry
      integer nwc                       !counter to print whirl output
      integer iwcount,iunit             !counter to open or not files
      real wcount

      real flag,wflag
      real alpha,b,cde,cd,ci,ds,hh,gpm,pi,ps,pe,q,ri,vi,xsi
      real eps,q0,bigt
      real rpm,bomeg,someg,f

      real s0,r0,h0,zi
      real dh0ds,drds,dzds
      real d2rds,d2zds
      real us0,ut0,p0
      real nu,ro

      real rmag,ang
      real f1c,f2c,f3c
      real f1s,f2s,f3s
      real rline1,rline2,rline
      real r1,r2,r3,r4
      real tline1,tline2,tline
      real t1,t2,t3,t4
      real frsum,frsum1,frsum2,frsum3,frsum4
      real ftsum,ftsum1,ftsum2,ftsum3,ftsum4
      real norm                                 !normalisation as exp

      real l,ls
      real ns,nr,ms,mr
      real nsone,nrone,msone,mrone
      real ra0(nmax),las(nmax),lar(nmax),beta0(nmax),beta1(nmax)
      real bt1(nmax),bt2(nmax),bt3(nmax),bs1(nmax),bs2(nmax),bs3(nmax)

      real s(nmax),r(nmax),h(nmax),z(nmax)
```

```
      real rd(nmax),rdd(nmax),hd(nmax),zd(nmax),zdd(nmax)
      real cs(nmax),cr(nmax),ch(nmax),cz(nmax)
      real crd(nmax),crdd(nmax),chd(nmax),czd(nmax),czdd(nmax)

      real frq(nmax),ftq(nmax)
      real fn(nmax),ft(nmax)
      real frqint(4,nmax),ftqint(4,nmax)
      real y(3,nmax),ydot(3,nmax)
      real z0(3),zdot(3)                !y(1)=us0,y(2)=ut0,y(3)=p0,ydot=dy/ds
      real fc(3,nmax),fs(3,nmax)
      real pus0(nmax),put0(nmax),pp0(nmax),pus0d(nmax),put0d(nmax),pp0d(nmax)
c                       !dummy variables to pass in sub-prog.

      complex y1(3,nmax),y1dot(3,nmax)
      complex z1(3),z1dot(3)            !y1(1)=ut1,y1(2)=p1,y1(3)=us1,y1dot=dy1/ds
      complex dumy1(3,nmax),dumy1dot(3,nmax),dumz1(3),dumz1dot(3)
      complex dum,dum1,dum2,fdum1,fdum2,pfdum
      complex xj
      complex g(3),aa(3,3)
      real bet0,bet1
      real ut1,sr,ss,zz
      real alt,a2t,a3t,als,a2s,a3s
      real gamma,f1,f2,f3,g0

      character filea*10, fileb*10, filec*10, char*1, boq*1,filch*4
      character cdeq*1

c the following is on the  assumption of only 21 whirl points

      character filed(21)*10, filee(21)*10, filef(21)*10, fileg(21)*10
      character fileh(21)*10, filei(21)*10, filej(21)*10
      character filek*10, filel*10
      character filem(21)*10, filen(21)*10, fileo(21)*10
      character filep(21)*10, fileq(21)*10, filer(21)*10
      character dumf(21)*10,anum(21)*2

      common b,vi
      common /step/ds
      common /geom/ z,zd,zdd,r,rd,rdd,h,hd
      common /pass/ pus0,put0,pp0,pus0d,put0d,pp0d
      common /all/ alpha,l,ls,ri,ci,bigt,eps,q0
      common /freq/bomeg,someg,f        !f=bomeg/someg,bomeg=whirlfreq,
c                                       !              someg=rotorfreq
      common /fric/ ns,nr,ms,mr
      common /frione/ nsone,nrone,msone,mrone
      common /xnu/ nu

      read (*,1) filch
    1 format(a4)
      read (*,2) char
    2 format(a1)
      read (*,2) cdeq

      anum(1)='01'
      anum(2)='02'
      anum(3)='03'
      anum(4)='04'
      anum(5)='05'
      anum(6)='06'
      anum(7)='07'
      anum(8)='08'
      anum(9)='09'
```

```
      anum(10)='10'
      anum(11)='11'
      anum(12)='12'
      anum(13)='13'
      anum(14)='14'
      anum(15)='15'
      anum(16)='16'
      anum(17)='17'
      anum(18)='18'
      anum(19)='19'
      anum(20)='20'
      anum(21)='21'

      print *,'enter the number of impeller coordinates'
              accept *, nc

      print *,'enter the number of increments for the geometry data'
              accept *, nn

      print *,'enter the number of increments for whirl'
      print *,'must be a multiple of 20'
      print *,'20,40 etc'
              accept *, nw

      nwhirl=nw+1
      nwc=nw/20.

     open (unit=2,file=char//'zero.out',type='new')
              write(2,*)'number of increments =',nn
              write(2,*)'whirl increments =',nw


     open (unit=5,file=char//'coord.out',type='new')
     call open (char//'rcoord.out',15)
     call open (char//'zcoord.out',25)
     call open (char//'hcoord.out',35)
              write(5,*)'number of coordinates =',nc
              write(5,*)'number of increments =',nn

c     list of symbols used in this program

      print *,'enter angle in deg'
              accept *, alpha
              write(2,*)'angle =',alpha
      alpha=alpha*acos(-1.)/180.       !angle of the cone

      print *,'read v, q or b'
      read (*,2)boq
      if(boq.eq.'q')goto 127
      if(boq.eq.'b')goto 327

      print *,'enter inlet veloc, vi'
              accept *,vi
              write(2,*)'vi= ',vi
      go to 227

 327  continue
      print *,'enter the helical ratio, b'
              accept *,b               !helical ratio
              write(2,*)'b= ',b
      go to 227
```

```
127   continue
      print *,'flowrate in gpm'
            accept *,q                !volumetric flowrate
            write(2,*)'q=',q,'GPM'
            q=q*3.85e-3/60.
227   continue

      print *,'calculate(c) or give(g) cde'
            write(2,*)'cdeq=',cdeq

      print *,'enter cde'
            accept *, cde             !leakage path discharge coefficient
            write(2,*)'cde=',cde

      print *,'enter cd'
      print *,'if to be calculated, enter 0'
            accept *, cd
            write(2,*)'cd=',cd

      print *,'enter ci in meters'
            accept *,ci               !inlet leakage depth=4.24e-3m (0.167in)
            write(2,*)'ci=',ci

      ds=1./nn                        !path variable increment,s

      print *,'enter epsilon, eps'
            accept *,eps
            write(2,*)'eps=',eps

      print *,'enter leakage depth, h'
            accept *,hh
            write(2,*)'h=',hh

c     i                               !loop variable
c     las,lar                         !shroud, housing friction factors

      print *,'enter l'
            accept *,l
            write(2,*)'l=',l

      print *,'enter ls'
            accept *,ls
            write(2,*)'ls=',ls

      print *,'enter coefficient,ms'
            accept *,ms               !empirical coefficients for the surface
            write(2,*)'ms=',ms
      print *,'enter coefficient,mr'
            accept *,mr               !roughness
            write(2,*)'mr=',mr
      print *,'enter coefficient,ns'
            accept*,ns
            write(2,*)'ns=',ns
      print *,'enter coefficient,nr'
            accept*,nr
            write(2,*)'nr=',nr

      print *,'enter coefficient,msone'
            accept *,msone            !empirical coefficients for the surface
            write(2,*)'msoneone=',msone
      print *,'enter coefficient,mrone'
            accept *,mrone            !roughness
```

```
        write(2,*)'mrone=',mrone
print *,'enter coefficient,nsone'
        accept*,nsone
        write(2,*)'nsone=',nsone
print *,'enter coefficient,nrone'
        accept*,nrone
        write(2,*)'nrone=',nrone

print *,'enter nu, viscosity'
        accept*,nu
        write(2,*)'nu=',nu

pi=acos(-1.)

print *,'enter supply pressure for the leakage flow in Pa, ps'
        accept*,ps
        write(2,*)'ps=',ps
print *,'enter exit pressure for the leakage flow in Pa, pe'
        accept*,pe
        write(2,*)'pe=',pe

print *,'enter coefficient,q0'
        accept *,q0              !constant for the displ.
        write(2,*)'q0=',q0
print *,'enter inlet radius'     !inlet leakage radius in m
        accept*,ri
        write(2,*)'ri=',ri

print *,'enter density,ro'
        accept*,ro
        write(2,*)'ro=',ro

print *,'enter rpm'
        accept *,rpm             !speed of the shaft
        write(2,*)'rpm=',rpm
someg=rpm*pi/30.
xj=(0.,1.)

print *,'enter xsi'
        accept *,xsi             !inlet loss coefficient
        write(2,*)'xsi=',xsi

c       initial conditions and geometry of the problem

      if(boq.eq.'b')goto 27
      if(boq.eq.'v')goto 57
      vi=q/(2*ri*pi*ci)          !q is given
      b=vi/(someg*ri)
      write (2,*)'vi=',vi
      write(2,*)'b=',b
      goto 72
   57 continue                   !vi is given
      b=vi/(someg*ri)
      write(2,*)'b=',b
      go to 72
   27 continue
      vi=someg*ri*b              ! b is given
      write (2,*)'vi=',vi
      q=2*pi*ri*ci*vi
      write (2,*)'q=',q
   72 continue
      bigt=ls/vi                 !characteristic time thru impeller
```

```
      print *,'enter u-theta(0)'
            accept *, y(2,1)
      y(3,1)=ps/ro/vi**2-(1.+xsi)/2.

      if(cd.ne.0)goto 929
      cd=2*(ps-pe)/ro/vi**2
      write (2,*)'cd=',cd
929   continue

     open (unit=1,file=filch//'.dat',type='old')
      do 999 i=1,nc
     read (1,*)cs(i),cz(i),cr(i),ch(i)
999   continue
      close (unit=1)

      do 998 i=1,nc-1
      czd(i)=(cz(i+1)-cz(i))/(cs(i+1)-cs(i))
      czdd(i)=0.
      crd(i)=(cr(i+1)-cr(i))/(cs(i+1)-cs(i))
      crdd(i)=0.
      chd(i)=(ch(i+1)-ch(i))/(cs(i+1)-cs(i))
 998  continue
      czd(nc)=czd(nc-1)
      crd(nc)=crd(nc-1)
      chd(nc)=chd(nc-1)

      do 997 i=1,nc
      cs(i)=cs(i)/ls
      cz(i)=cz(i)/l
      cr(i)=cr(i)/ri
      ch(i)=ch(i)/ci
      czd(i)=czd(i)*ls/l
      czdd(i)=0.
      crd(i)=crd(i)*ls/ri
      crdd(i)=0.
      chd(i)=chd(i)*ls/ci
997   continue

      s(1)=cs(1)
      z(1)=cz(1)
      r(1)=cr(1)
      h(1)=ch(1)

      icount=1                          !loop 1,nc

      do 911 i=1,nn*2

      s(i+1)=ds*(i)/2.

      zd(i)=czd(icount)
      zdd(i)=czdd(icount)
      rd(i)=crd(icount)
      rdd(i)=crdd(icount)
      hd(i)=chd(icount)

      if(cs(icount+1).le.s(i+1))icount=icount+1

      z(i+1)=cz(icount)+czd(icount)*(s(i+1)-cs(icount))
      r(i+1)=cr(icount)+crd(icount)*(s(i+1)-cs(icount))
      h(i+1)=ch(icount)+chd(icount)*(s(i+1)-cs(icount))

      write(5,*)i,icount,s(i),z(i),zd(i),r(i),rd(i),h(i),hd(i)
```

```
        call xyout(15,s(i),r(i))
        call xyout(25,s(i),z(i))
        call xyout(35,s(i),h(i))
 911    continue
        zd(2*nn+1)=czd(nc)
        zdd(2*nn+1)=czdd(nc)
        rd(2*nn+1)=crd(nc)
        rdd(2*nn+1)=crdd(nc)
        hd(2*nn+1)=chd(nc)
        write(5,*)i,icount,s(i),z(i),zd(i),r(i),rd(i),h(i),hd(i)
        call xyout(15,s(i),r(i))
        call xyout(25,s(i),z(i))
        call xyout(35,s(i),h(i))
        close (unit=5)
        call close (15)
        call close (25)
        call close (35)

       call open (char//'us0.plt',1)
       call open (char//'ut0.plt',3)
       call open (char//'p0.plt',4)

        write(2,511)
 511    format(1x,/,t4,'s',t15,'y(1)',t26,'y(2)',t37,'y(3)',t48,'ydot(1)'
     1  t59,'ydot(2)',t70,'ydot(3)',/,t15,'u-s',t26,'u-theta',t37,'p')

c       start iteration s=0: the inlet of the impeller flow.
c       zeroth order solutions

c       NOTE THERE ARE TWICE AS MANY GEOMETRY POINTS AS VEL,PRESS POINTS

        do 10 i=1,nn
        y(1,i)=1./(r(2*i-1)*h(2*i-1))
               do 111 k=1,3
               z0(k)=y(k,i)
 111           continue
       s0=s(2*i-1)
       call deriv0(s0,z0,zdot)
               do 222 k=1,3
               ydot(k,i)=zdot(k)
 222           continue
  33   write(2,510)s(2*i-1),y(1,i),y(2,i),y(3,i),ydot(1,i),ydot(2,i)
     c ,ydot(3,i)
510     format(1x,7e11.4)
        call xyout(1,s(2*i-1),y(1,i))
        call xyout(3,s(2*i-1),y(2,i))
        call xyout(4,s(2*i-1),y(3,i))

        call rk4(z0,zdot,3,s0,ds,z0,deriv0)
               do 333 k=1,3
               y(k,i+1)=z0(k)
 333           continue

       us0=y(1,i)
       ut0=y(2,i)

       ra0(i)=2*h(2*i-1)*ci*y(1,i)*vi/nu

       las(i)=ns*ra0(i)**msone*(1.+(y(2,i)/b/y(1,i))**2)**((msone+1.)/2.)
       lar(i)=(1.+((y(2,i)-r(2*i-1))/b/y(1,i))**2)**((mrone+1.)/2.)
       lar(i)=nrone*ra0(i)**mrone*lar(i)
```

```
      beta0(i)=(ut0-r(2*i-1))/((b**2*us0)*(1+((ut0-r(2*i-1))/(b*us0))**2))
      beta1(i)=ut0/b**2/(us0*(1+(ut0/b/us0)**2))

      bt1(i)=lar(i)*(1+mrone)
      bt1(i)=bt1(i)*(ut0-r(2*i-1))*(1-beta0(i)*(ut0-r(2*i-1))/us0)/(2.*b)
      bt2(i)=lar(i)*(us0+(1+mrone)*(ut0-r(2*i-1))*beta0(i))/(2.*b)
      bt3(i)=lar(i)*mrone*(ut0-r(i))*us0/(2*b*h(2*i-1))

      bs1(i)=lar(i)*((2.+mrone)*us0-(1.+mrone)*beta0(i)*(ut0-r(2*i-1)))/2.
      bs2(i)=lar(i)*(1.+mrone)*beta0(i)*us0/2.
      bs3(i)=lar(i)*mrone*us0**2/(2.*h(2*i-1))

10    continue
            do 1111 k=1,3
            z0(k)=y(k,i)
1111        continue
      s0=s(2*i-1)
      call deriv0(s0,z0,zdot)
            do 2222 k=1,3
            ydot(k,i)=zdot(k)
2222        continue
      write(2,510)s(2*i-1),y(1,i),y(2,i),y(3,i),ydot(1,i),ydot(2,i)
     c ,ydot(3,i)
      call xyout(1,s(2*i-1),y(1,i))
      call xyout(3,s(2*i-1),y(2,i))
      call xyout(4,s(2*i-1),y(3,i))
      if (cdeq.ne.'c')goto 17
      cde=(y(3,nn+1)*ro*vi**2-pe)/(ro*(y(1,nn+1)*vi)**2/2)
      write (2,*)cde
17    continue
      call close (1)
      close (unit=2)
      call close (3)
      call close (4)

      do 1009 i=1,nn+1
      pus0(i)=y(1,i)
      put0(i)=y(2,i)
      pp0(i)=y(3,i)
      pus0d(i)=ydot(1,i)
      put0d(i)=ydot(2,i)
      pp0d(i)=ydot(3,i)
1009  continue

c#############################################################################################
      do 458 i=1,21
      filed(i)=char//'one'//anum(i)//'.out'
c6    filee(i)=char//'usm'//anum(i)//'.plt'
c7    filef(i)=char//'utm'//anum(i)//'.plt'
c8    fileg(i)=char//'pm'//anum(i)//'.plt'

c10   fileh(i)=char//'usa'//anum(i)//'.plt'
c11   filei(i)=char//'uta'//anum(i)//'.plt'
c12   filej(i)=char//'pa'//anum(i)//'.plt'
      dumf(i)=char//'dumm'//anum(i)//'.out'

      filem(i)=char//'usr'//anum(i)//'.plt'
      filen(i)=char//'utr'//anum(i)//'.plt'
      fileo(i)=char//'pr'//anum(i)//'.plt'
      filep(i)=char//'usi'//anum(i)//'.plt'
      fileq(i)=char//'uti'//anum(i)//'.plt'
      filer(i)=char//'pi'//anum(i)//'.plt'
```

```
458   continue

      filek=char//'frq.plt'
      filel=char//'ftq.plt'

     open (unit=13,file=filek,type='new')
     open (unit=14,file=filel,type='new')
      filek=char//'fn.plt'
      filel=char//'ft.plt'

     open (unit=53,file=filek,type='new')
     open (unit=54,file=filel,type='new')

     call open (char//'frq1.plt',21)
     call open (char//'frq2.plt',22)
     call open (char//'frq3.plt',23)
     call open (char//'frq4.plt',24)
     call open (char//'ftq1.plt',25)
     call open (char//'ftq2.plt',26)
     call open (char//'ftq3.plt',27)
     call open (char//'ftq4.plt',28)

c     first order solutions
c     this involves solving a boundary value problem. convert to an intial
c     value problem by selecting an initial value and solving to satisfy the
c     given boundary value.

      icount=1

      do 81 intf=1,nwhirl,1          !begin loop for whirl ratio
      wcount=real (intf-1)/nwc
      iwcount=int (intf-1)/nwc
      iunit=iwcount+1
      if (wcount.eq. iwcount)wflag =1
      if (wflag.ne.1)goto 267
    open (unit=5,file=filed(iunit),type='new')
c6    open (unit=6,file=filee(iunit),type='new')
c7    open (unit=7,file=filef(iunit),type='new')
c8    open (unit=8,file=fileg(iunit),type='new')

c10    open (unit=10,file=fileh(iunit),type='new')
c11    open (unit=11,file=filei(iunit),type='new')
c12    open (unit=12,file=filej(iunit),type='new')

     open (unit=9,file=dumf(iunit),type='new')

     call open (filem(iunit),15)
     call open (filen(iunit),16)
     call open (fileo(iunit),17)
     call open (filep(iunit),18)
     call open (fileq(iunit),19)
     call open (filer(iunit),20)
267   continue
      f=((real(intf)-1.)*2./nw-1.)

c  THE FIRST ORDER EQ USE HALF AS MANY POINTS AS FOR ZEROTH: SO 1/4 OF GEOM
ccccccccccccccccccccccccccccccccccccccccccccccccccccccccccccccccccccccccc

c     given boundary conditions for the first order set of equations
      y1(2,1)=cmplx(0,0)                                          !1)

c     dummy initial conditions
```

```
      dum1=cmplx(1.,1.0000)                    !this is done before the whirl
c loop and the next whirl ratio uses the previous whirl's final value of dum1

 95   continue
      dum2=(xj)**(icount)*(.99-.05/(icount)**.5)*dum1

      y1(1,1)=dum1
c     y1(3,1)=-(1+xsi)*y(1,1)*y1(1,1)          !assume an extra b.c.
      y1(3,1)=-(1+xsi)*y1(1,1)                 !follows from b.c. 2)
                                               !follows from b.c. 2)
                                               !error in Child's paper

      dumy1(1,1)=dum2
      dumy1(3,1)=-(1+xsi)*y(1,1)*dumy1(1,1)

c     select dum such that:
c     fdum=y1(3,nn/2+1)-cde*y(1,nn+1)*y1(1,nn/2+1)=0 =f(dum)   !3)
c     use non-linear equation solver eg. Newton's method
c     next dum=dum-f(dum)/f'(dum)
c     Since f'(dum) is not known, will calculate:
c     df/ddum=(f(dum)-f(0.95*dum))/(.05*dum)

      do 101 i=1,nn/2
             do 91 k=1,3
             z0(k)=y(k,2*i-1)
             zdot(k)=ydot(k,2*i-1)
             z1(k)=y1(k,i)
             dumz1(k)=dumy1(k,i)
 91          continue
      s0=s(4*i-3)
      call deriv1(s0,z1,z1dot)
      s0=s(4*i-3)
      call deriv1(s0,dumz1,dumz1dot)
             do 92 k=1,3
             y1dot(k,i)=z1dot(k)
             dumy1dot(k,i)=dumz1dot(k)
 92          continue

      s0=s(4*i-3)
      call rk4im(z1,z1dot,3,s0,ds*2,z1,deriv1)
      s0=s(4*i-3)
      call rk4im(dumz1,dumz1dot,3,s0,ds*2,dumz1,deriv1)
             do 93 k=1,3
             y1(k,i+1)=z1(k)
             dumy1(k,i+1)=dumz1(k)
 93          continue
101   continue

      fdum1=y1(3,nn/2+1)-cde*y(1,nn+1)*y1(1,nn/2+1)
      fdum2=dumy1(3,nn/2+1)-cde*y(1,nn+1)*dumy1(1,nn/2+1)
      pfdum=(fdum1-fdum2)/(dum1-dum2)
      write(9,*)icount,dum1,fdum1,pfdum

      if((cabs(fdum1)/cabs(y1(3,nn/2+1))).lt.1.e-2)goto 512
      icount=icount+1
      if(icount.gt.100)goto 512
c     use a relaxation factor
      dum1=dum1-.9*fdum1/pfdum
      goto 95

512   continue
      if (wflag.ne.1)goto 219
      write (5,*) 'icount=',icount             !write,store final values
```

```
          write (5,*) 'dum=',dum1
          write (5,*) 'fdum=',fdum1
          write (5,*) 'f=',f,'intf=',intf
          do 399 i=1,nn/2+1
          write(5,510)s(4*i-3),y1(1,i),y1(2,i),y1(3,i),y1dot(1,i),y1dot(2,i),
     c    y1dot(3,i)
  399     continue
  219     continue
          icount=1
          flag=0
         do 397 i=1,nn/2+1
          do 16 k=1,3
          fc(k,i)=real(y1(k,i))/(q0/eps)
          fs(k,i)=aimag(y1(k,i))/(q0/eps)
    16    continue

          if (wflag.ne. 1)goto 699
          call xyout(15,s(4*i-3),fc(1,i))
          call xyout(16,s(4*i-3),fc(2,i))
          call xyout(17,s(4*i-3),fc(3,i))
          call xyout(18,s(4*i-3),fs(1,i))
          call xyout(19,s(4*i-3),fs(2,i))
          call xyout(20,s(4*i-3),fs(3,i))

          rmag=sqrt((real(y1(1,i)))**2+(aimag(y1(1,i)))**2)
c6        write(6,*)s(i),rmag                              !mag of y1(1,i)
          rmag=sqrt((real(y1(2,i)))**2+(aimag(y1(2,i)))**2)
c7        write(7,*)s(i),rmag                              !mag of y1(2,i)
          rmag=sqrt((real(y1(3,i)))**2+(aimag(y1(3,i)))**2)
c8        write(8,*)s(i),rmag                              !mag of y1(3,i)

          if(real(y1(1,i)).ne.0) goto 531
          if(aimag(y1(1,i)).ge.0) then
          ang=90
          else
          ang=-90
          endif
          goto 532
  531     ang=180./pi*atan(aimag(y1(1,i))/real(y1(1,i)))
  532     continue
c10       write(10,*)s(i),ang                              ! phase of y1(1,i)
          if(real(y1(2,i)).ne.0.) goto 541
          if (aimag(y1(2,i)).ge.0.) then
          ang=90
          else
          ang=-90
          endif
         goto 542
  541     ang=180./pi*atan(aimag(y1(2,i))/real(y1(2,i)))
  542     continue
c11       write(11,*)s(i),ang                              ! phase of y1(2,i)

          if(real(y1(3,i)).ne.0.) goto 551
          if(aimag(y1(3,i)).ge.0.) then
          ang=90
          else
          ang=-90
          endif
         goto 552
  551     ang=180./pi*atan(aimag(y1(3,i))/real(y1(3,i)))
  552     continue
c12       write(12,*)s(i),ang                              ! phase of y1(3,i)
```

```
699     continue
  397  continue
       if (wflag.ne.1)goto 266
       close (unit=5)
c6     close (unit=6)
c7     close (unit=7)
c8     close (unit=8)
       close (unit=9)
c10    close (unit=10)
c11    close (unit=11)
c12    close (unit=12)
       call close (15)
       call close (16)
       call close (17)
       call close (18)
       call close (19)
       call close (20)
       wflag=0
 266   continue
c      Rotordynamic coefficients for displacement peturbations
c      integrate using trap rule,well sort of
       frsum=0.
       frsum1=0.
       frsum2=0.
       frsum3=0.
       frsum4=0.

       ftsum=0.
       ftsum1=0.
       ftsum2=0.
       ftsum3=0.
       ftsum4=0.

       do 79 i=1,nn/2+1
       us0=y(1,2*i-1)
       ut0=y(2,2*i-1)

       s0=s(4*i-3)
       zi=z(4*i-3)
       dzds=zd(4*i-3)
       d2zds=zdd(4*i-3)
       r0=r(4*i-3)
       drds=rd(4*i-3)
       d2rds=rdd(4*i-3)
       h0=h(4*i-3)
       dh0ds=hd(4*i-3)

       r1=(fc(1,i)*ri/ls*drds*bs1(2*i-1)-fs(1,i)*bt1(2*i-1))*r(2*i-1)
       r2=(fc(2,i)*ri/ls*drds*bs2(i)-fs(2,i)*bt2(2*i-1))*r(2*i-1)
       r3=(fc(3,i)*l/ls*dzds)*r(2*i-1)
       r4=(-(l*ri/ls**2)*dzds*drds*bs3(2*i-1))*r(2*i-1)
       rline=r1+r2+r3+r4

       t1=(fs(1,i)*ri/ls*drds*bs1(2*i-1)+fc(1,i)*bt1(2*i-1))*r(2*i-1)
       t2=(fs(2,i)*ri/ls*drds*bs2(2*i-1)+fc(2,i)*bt2(2*i-1))*r(2*i-1)
       t3=(fs(3,i)*l/ls*dzds)*r(2*i-1)
       t4=(-(l/ls)*dzds*bs3(2*i-1))*r(2*i-1)
       tline=t1+t2+t3+t4
c
       if(i.eq.1.or.i.eq.(nn+1))goto 18
       rline=rline*2.
       r1=r1*2.
```

```
      r2=r2*2.
      r3=r3*2.
      r4=r4*2.
      tline=tline*2.
      t1=t1*2.
      t2=t2*2.
      t3=t3*2.
      t4=t4*2.
 18   continue
      frsum=frsum+rline
      frsum1=frsum1+r1
      frsum2=frsum2+r2
      frsum3=frsum3+r3
      frsum4=frsum4+r4

      ftsum=ftsum+tline
      ftsum1=ftsum1+t1
      ftsum2=ftsum2+t2
      ftsum3=ftsum3+t3
      ftsum4=ftsum4+t4

 79   continue                              !integrate
C     twice ds, because ds is step for zeroth
      frq(intf)=-pi/cd*ls/l*(2*ds)/2.*frsum
      frqint(1,intf)=-pi/cd*ls/l*(2*ds)/2.*frsum1
      frqint(2,intf)=-pi/cd*ls/l*(2*ds)/2.*frsum2
      frqint(3,intf)=-pi/cd*ls/l*(2*ds)/2.*frsum3
      frqint(4,intf)=-pi/cd*ls/l*(2*ds)/2.*frsum4

      ftq(intf)=-pi/cd*ls/l*(2*ds)/2.*ftsum
      ftqint(1,intf)=-pi/cd*ls/l*(2*ds)/2.*ftsum1
      ftqint(2,intf)=-pi/cd*ls/l*(2*ds)/2.*ftsum2
      ftqint(3,intf)=-pi/cd*ls/l*(2*ds)/2.*ftsum3
      ftqint(4,intf)=-pi/cd*ls/l*(2*ds)/2.*ftsum4

      write (13,348)f,frq(intf)
      call xyout(21,f,frqint(1,intf))
      call xyout(22,f,frqint(2,intf))
      call xyout(23,f,frqint(3,intf))
      call xyout(24,f,frqint(4,intf))

      write (14,348)f,ftq(intf)
      call xyout(25,f,ftqint(1,intf))
      call xyout(26,f,ftqint(2,intf))
      call xyout(27,f,ftqint(3,intf))
      call xyout(28,f,ftqint(4,intf))

      norm=(cd*q*q)/(4*pi**3*ri**3*someg**2*ci**3)
      fn(intf)=frq(intf)*norm
      ft(intf)=ftq(intf)*norm
      write (53,348)f,fn(intf)
      write (54,348)f,ft(intf)

348   format(1x,f5.2,1e13.4)


 81   continue                              !end loop for whirl ratio

      close (UNIT=9)
      close (UNIT=13)
      close (UNIT=14)
      close (UNIT=53)
```

```
      close (UNIT=54)
      call close (21)
      call close (22)
      call close (23)
      call close (24)
      call close (25)
      call close (26)
      call close (27)
      call close (28)
      call close (29)
      stop
      end


      subroutine sigma(sr,ss,s0)
      implicit none

      integer i
      real ds
      real alpha,b
      real ci
      real ri,vi

      real s0,r0,h0,zi
      real d2rds,d2zds
      real dh0ds,drds,dzds

      real nu,ra0,ro
      real ss,sr
      real bigt

      real l,ls,las,lar,ns,nr,ms,mr

      real y(3)
      real us0d,ut0d,p0d,dus0d,dut0d,dp0d
      real z(500),zd(500),zdd(500),r(500),rd(500),rdd(500),h(500),hd(500)

      common b,vi
      common /all/ alpha,l,ls,ri,ci
      common /fric/ ns,nr,ms,mr
      common /step/ds
      common /geom/ z,zd,zdd,r,rd,rdd,h,hd
      common /zeroth/ us0d,ut0d,p0d,dus0d,dut0d,dp0d

      common /xnu/ nu

      i=(s0/ds)*2.+1.
      zi=z(i)
      dzds=zd(i)
      d2zds=zdd(i)
      r0=r(i)
      drds=rd(i)
      d2rds=rdd(i)
      h0=h(i)
      dh0ds=hd(i)

      y(1)=us0d
      y(2)=ut0d
      y(3)=p0d

      ra0=2*h0*ci*y(1)*vi/nu
      las=ns*ra0**ms*(1+(y(2)/b/y(1))**2)**((ms+1.)/2.)
```

```
      lar=nr*ra0**mr*(1+((y(2)-r0)/b/y(1))**2)**((mr+1.)/2.)
      ss=(ls/h0/ci)*las
      sr=(ls/h0/ci)*lar
      return
      end


      subroutine deriv0(s,y,ydot)
      implicit none

      integer i
      real ds
      real b,alpha,ci,ri
      real s,r,h0,zi
      real dh0ds,drds,dzds
      real d2rds,d2zds

      real y(3),ydot(3)
      real ls,l
      real sr,ss

      real us0d,ut0d,p0d,dus0d,dut0d,dp0d
      real z(500),zd(500),zdd(500),rr(500),rd(500),rdd(500),h(500),hd(500)

      common /step/ds
      common /geom/ z,zd,zdd,rr,rd,rdd,h,hd
      common /zeroth/ us0d,ut0d,p0d,dus0d,dut0d,dp0d

      common b
      common /all/ alpha,l,ls,ri,ci

c     s is automatiy updated by the main program
      i=(s/ds)*2.+1.
      zi=z(i)
      dzds=zd(i)
      d2zds=zdd(i)
      r=rr(i)
      drds=rd(i)
      d2rds=rdd(i)
      h0=h(i)
      dh0ds=hd(i)

      us0d=Y(1)
      ut0d=Y(2)
      p0d=Y(3)

      call sigma(sr,ss,s)
c     ydot(1)=dus0/ds
      ydot(1)=-y(1)*(dh0ds/h0+drds/r)
c     ydot(2)=dut0/ds
      ydot(2)=-(y(2)/r*drds+(sr*(y(2)-r)+ss*y(2))/2.)
c     ydot(3)=dp/ds
      ydot(3)=drds/r*(y(2)/b)**2
      ydot(3)=ydot(3)-((sr+ss)/2.-dh0ds/h0-drds/r)*y(1)**2
      return
      end

SUBROUTINE RK4(Y,DYDX,N,X,H,YOUT,DERIVS)
  implicit none
integer nmax
PARAMETER (NMAX=3)
```

```
      integer i,n
      real h,hh,h6,xh,x

      real Y(N),DYDX(N),YOUT(N)
      real      YT(Nmax),DYT(Nmax),DYM(Nmax)
      HH=H*0.5
      H6=H/6.
      XH=X+HH
      DO 11 I=1,N
        YT(I)=Y(I)+HH*DYDX(I)
11    CONTINUE
      CALL DERIVS(XH,YT,DYT)
      DO 12 I=1,N
        YT(I)=Y(I)+HH*DYT(I)
12    CONTINUE
      CALL DERIVS(XH,YT,DYM)
      DO 13 I=1,N
        YT(I)=Y(I)+H*DYM(I)
        DYM(I)=DYT(I)+DYM(I)
13    CONTINUE
      CALL DERIVS(X+H,YT,DYT)
      DO 14 I=1,N
        YOUT(I)=Y(I)+H6*(DYDX(I)+DYT(I)+2.*DYM(I))
14    CONTINUE
      RETURN
      END

      subroutine sigone(sr,ss,s0)
      implicit none

      integer i
      real ds
      real alpha,b
      real ci
      real ri,vi

      real s0,r0,h0,zi
      real dh0ds,drds,dzds
      real d2rds,d2zds

      real nu,ra0,ro
      real ss,sr
      real bigt

      real l,ls,las,lar,ns,nr,ms,mr

      real y(3)
      real us0d,ut0d,p0d,dus0d,dut0d,dp0d
      real z(500),zd(500),zdd(500),r(500),rd(500),rdd(500),h(500),hd(500)

      common /step/ds
      common /geom/ z,zd,zdd,r,rd,rdd,h,hd
      common /zeroth/ us0d,ut0d,p0d,dus0d,dut0d,dp0d

      common b,vi
      common /all/ alpha,l,ls,ri,ci
      common /frione/ ns,nr,ms,mr                !friction for first order

      common /xnu/ nu

      i=(s0/ds)*2.+1.
      zi=z(i)
```

```
      dzds=zd(i)
      d2zds=zdd(i)
      r0=r(i)
      drds=rd(i)
      d2rds=rdd(i)
      h0=h(i)
      dh0ds=hd(i)

      y(1)=us0d
      y(2)=ut0d
      y(3)=p0d

      ra0=2*h0*ci*y(1)*vi/nu
      las=ns*ra0**ms*(1+(y(2)/b/y(1))**2)**((ms+1.)/2.)
      lar=nr*ra0**mr*(1+((y(2)-r0)/b/y(1))**2)**((mr+1.)/2.)
      ss=(ls/h0/ci)*las
      sr=(ls/h0/ci)*lar
      return
      end

      subroutine deriv1(s,y1,y1dot)
      implicit none

      integer i
      integer k,j
      real ds
      real alpha,b,ri,ci

      real s,r,h0,z
      real dh0ds,drds,dzds
      real d2rds,d2zds

      real us0,ut0,p0
      real bomeg,someg,f,bigt,eps,q0
      real y(3),ydot(3)
      real ls,l,las,lar,ns,nr,ms,mr,nsone,nrone,msone,mrone
      real sr,ss
      real beta0,beta1,bs1,bs2,bs3,bt1,bt2,bt3
      real als,a2s,a3s,alt,a2t,a3t
      real gamma,f1,f2,f3,g0
      real flag

      complex y1(3),y1dot(3)
      complex a(3,3),g(3)
      complex xj

      real us0d,ut0d,p0d,dus0d,dut0d,dp0d
      real pus0(500),put0(500),pp0(500),pus0d(500),put0d(500),pp0d(500)
      real pz(500),zd(500),zdd(500),pr(500),rd(500),rdd(500),h(500),hd(500)

      common /step/ds
      common /geom/ pz,zd,zdd,pr,rd,rdd,h,hd
      common /zeroth/ us0,ut0,p0,dus0d,dut0d,dp0d

      common /frione/ nsone,nrone,msone,mrone
      common /freq/bomeg,someg,f        !f=bomeg/someg,bomeg=whirlfreq,
c                                       !              someg=rotorfreq
      common b
      common /all/ alpha,l,ls,ri,ci,bigt,eps,q0

      common /pass/ pus0,put0,pp0,pus0d,put0d,pp0d
```

```
      xj=(0.,1.)
c     s is automatically updated by the main program
      i=(s/ds)*2.+1.
      z=pz(i)
      dzds=zd(i)
      d2zds=zdd(i)
      r=pr(i)
      drds=rd(i)
      d2rds=rdd(i)
      h0=h(i)
      dh0ds=hd(i)

      us0=pus0((i+1)/2)
      ut0=put0((i+1)/2)
      p0=pp0((i+1)/2)
      ydot(1)=pus0d((i+1)/2)
      ydot(2)=put0d((i+1)/2)
      ydot(3)=pp0d((i+1)/2)

c     perturbation coefficients
c
      call sigone(sr,ss,s)
c
      beta0=(ut0-r)/((b**2*us0)*(1+((ut0-r)/(b*us0))**2))
      beta1=ut0/b**2/(us0*(1+(ut0/b/us0)**2))
      a1s=(ss*(1.-msone)+sr*(1.-mrone))*us0**2/(2.*h0)
      a2s=-2.*ut0/r*drds/b**2+(sr*(mrone+1.)*beta0+ss*(msone+1.)*beta1)*us0/2.
      a3s=ydot(1)+((2.+mrone)*sr+(2.+msone)*ss)*us0/2.
      a3s=a3s-((1.+mrone)*sr*beta0*(ut0-r)+(1.+msone)*ss*beta1*ut0)/2.
c
      a1t=us0*((1.-mrone)*(ut0-r)*sr+(1.-msone)*ut0*ss+2.*ut0/r*drds)/h0/2.
      a2t=us0*(sr+ss)+sr*(mrone+1.)*(ut0-r)*beta0+2.*us0/r*drds
      a2t=(a2t+ss*(msone+1)*ut0*beta1)/2.
      a3t=sr*(ut0-r)*(mrone-(1.+mrone)*beta0*(ut0-r)/us0)
      a3t=(a3t+ss*ut0*(msone-(1.+msone)*beta1*ut0/us0))/2.

      gamma=someg*(f-ut0/r)
      g0=(1**2/ci/ls)*z*dzds+(ri**2/ci/ls)*r*drds
      f1=1**2/ci/ls*(dzds**2+z*d2zds)+ri**2/ci/ls*(drds**2+r*d2rds)
      f2=(us0/h0)*(d2zds-1./h0*dh0ds*dzds)
      f3=us0/h0*(f1-g0/h0*dh0ds)
      g(1)=1/ls*(f2+xj*gamma*bigt/h0*dzds)
      g(2)=1/ls*(-a1t/us0)*dzds
      g(3)=1/ls*(-a1s*dzds-y(1)*f2-xj*us0*gamma*bigt/h0*dzds)
      a(1,1)=(1./r*drds+1/h0*dh0ds)
      a(1,2)=-xj*someg*bigt/r
      a(1,3)=0.
      a(2,1)=a3t/us0
      a(2,2)=(a2t+xj*gamma*bigt)/us0
      a(2,3)=-xj*b/r/us0*(ls/ri)
      a(3,1)=a3s-us0*a(1,1)+xj*gamma*bigt
      a(3,2)=a2s+xj*someg*bigt*us0/r          !change
      a(3,3)=0.

100   continue
      do 11 k=1,3
      y1dot(k)=q0/eps*g(k)
      do 22 j=1,3
      y1dot(k)=y1dot(k)-a(k,j)*y1(j)
22    continue
11    continue
      y1dot(3)=y1dot(3)-us0*y1dot(1)
```

```
      return
      end


      SUBROUTINE RK4im(Y,DYDX,N,X,H,YOUT,DERIVS)
        implicit none
        integer nmax
      PARAMETER (NMAX=3)

        integer i,n
        real h,hh,h6,x,xh
        real flag

      complex Y(N),DYDX(N),YOUT(N)
      complex    YT(Nmax),DYT(Nmax),DYM(Nmax)
      HH=H*0.5
      H6=H/6.
      XH=X+HH
      DO 11 I=1,N
        YT(I)=Y(I)+HH*DYDX(I)
11    CONTINUE
      CALL DERIVS(XH,YT,DYT)
      DO 12 I=1,N
        YT(I)=Y(I)+HH*DYT(I)
12    CONTINUE
      CALL DERIVS(XH,YT,DYM)
      DO 13 I=1,N
        YT(I)=Y(I)+H*DYM(I)
        DYM(I)=DYT(I)+DYM(I)
13    CONTINUE
      CALL DERIVS(X+H,YT,DYT)
      DO 14 I=1,N
        YOUT(I)=Y(I)+H6*(DYDX(I)+DYT(I)+2.*DYM(I))
14    CONTINUE
      RETURN
      END
```